

University of Nevada, Reno

**Theoretical and Experimental Studies of Radiation
from Z-Pinch Complex Wire Arrays and Applications**

A dissertation submitted in partial fulfillment of the
requirements for the degree of Doctor of Philosophy in
Physics

by

Michael Eugene Weller

Dr. Alla S. Safronova/Dissertation Advisor

May 2014

Copyright © by Michael E. Weller 2014

All Rights Reserved



University of Nevada, Reno
Statewide • Worldwide

THE GRADUATE SCHOOL

We recommend that the dissertation
prepared under our supervision by

MICHAEL EUGENE WELLER

entitled

**Theoretical And Experimental Studies Of Radiation From
Z-Pinch Complex Wire Arrays And Applications**

be accepted in partial fulfillment of the
requirements for the degree of

DOCTOR OF PHILOSOPHY

Alla S. Safronova, Ph. D., Advisor

Victor L. Kantsyrev, Ph. D., Committee Member

Peter Beiersdorfer, Ph. D., Committee Member

Andrew Geraci, Ph. D., Committee Member

Hans Moosmüller, Ph. D., Graduate School Representative

Marsha H. Read, Ph. D., Dean, Graduate School

May, 2014

Abstract

In the research area of high energy density plasmas an ever increasing goal is searching for higher efficient radiators, particularly in z-pinch plasmas, and their applications. This goal is a major focus of this dissertation and implements both theoretical and experimental tools in the process. The theoretical tools involve the Wire Ablation Dynamics Model (WADM) to infer z-pinch implosion characteristics and various non-local thermodynamic equilibrium (LTE) kinetic models to understand the radiative properties of plasmas, including a new model for L-shell Ag. The experimental tools includes an advanced set of diagnostics, in particular a newly developed time-gated hard x-ray spectrometer to gain an understanding as to how these plasmas radiate in time, particularly in the 0.7 – 4.4 Å range. The experiments predominately took place on the 1.7 MA Zebra generator at the Nevada Terawatt Facility (NTF) at the University of Nevada, Reno (UNR). Traditional nested cylindrical wire arrays with mixed materials (brass and Al, Mo and Al) were tested to understand how the inner and outer arrays implode and radiate. Novel planar wire arrays, which have been shown to be very powerful radiation sources, arranged in single, double, and triple wire array configurations were tested with Mo and Ag materials, which have both been shown to be powerful radiators, and also mixed with Al to understand opacity effects and how a mixture of two different plasmas radiate. Radiation from the extreme ultraviolet (EUV) range has also been of recent interest due the substantial contribution into total radiation yields. Therefore EUV radiation of M-shell Cu was modeled and benchmarked with spheromak and laser-produced plasma data. Lastly, lasing gain from L-shell Ag is calculated as an application of the aforementioned model to evaluate whether lasing might be occurring in wire array z-pinches. In connection to creating a uniform plasma column to measure lasing lines, the split double planar wire array is introduced and preliminary results discussed.

This dissertation is dedicated to those who think they can't do it,
and to my late friend, Billy, who always kept it real

Acknowledgements

No dissertation is ever the product of solely one individual. I would like to thank my adviser Dr. Safronova for providing me with opportunity throughout these years, pushing me to better myself, and for seeing the theoretician that was in me. I would like to thank my co-adviser Dr. Kantsyrev for taking a chance with hiring me onto the group, and then teaching me all the experimental expertise that I know today. These two advisers exist first and foremost for their students and it was a pleasure working with both of them. I am thankful for Dr. Beiersdorfer from Lawrence Livermore National Laboratory (LLNL) for seeing me through the comprehensive exam and giving me guidance on the RSI paper, my second peer reviewed article. I am thankful for the rest of my committee members for seeing me through this process: Dr. Geraci and Dr. Moosmüller.

Throughout these years I believe I have worked with the best research team in the world. I would like to thank each person individually: Fatih Yilmaz for being the first to teach me theoretical models; Ken Williamson for teaching me the basics of z-pinch physics; Glenn Osborne for teaching me everything I know about optical systems; Nick Quart for helping me through my first non-LTE kinetic model; Ishor Shrestha for teaching me what hard work and dedication is and for building my very complex loads; Austin Stafford for helping me with all quantum and atomic physics questions; Steve Keim for all coding questions and theoretical installation of models; Veronica Shlyaptseva for help in all experimental campaigns; Heather Zunino for learning so quickly everything that has been taught to you; Dr. Esaulov for all the help you have provided me throughout the years; Dr. Ulyana Safronova for help with atomic

calculations; Dr. Faenov for help, insight, and suggestions with lasing; Kim Schultz for being a fantastic addition to the group; Augustus Merwin and Emil Petkov for being patient with me as I became your mentor; and Matt Cooper for the excellent conversations.

To all of my collaborators who helped me with presentations and papers, in particular Dr. Coverdale and Dr. Hansen from Sandia National Laboratories (SNL), Dr. Chuvatin from Ecole Polytechnique, Dr. Apruzese and Dr. Giuliani from Naval Research Laboratory (NRL), Dr. Clementson from LLNL, and Dr. Golovkin and Dr. MacFarlane from Prism.

My gratitude goes out to all staff at the University of Nevada, Reno Physics Department and the Nevada Terawatt Facility. In particular Dr. Derevianko for accepting me into the program, Mercy Balderrama and Marvin Wakefield for main office support, Dr. Covington, Alexey Astanovitskiy, Vidya Nalajala, Oleg Dmitriev, and Daniel Macaulay for providing support on Zebra, and Wade Cline for support on the time-gated hard x-ray spectrometer.

I would have never made it to UNR without previous educational experiences. To the Physics department at Arkansas Tech University, in particular Dr. Hemmati, Dr. Robertson, Dr. Musser, Dr. Kondrick, and Dr. Bullock, and to Michelle Justice, Steven Summer, and Taylor Duncan. To Lamar High School for providing me everything I needed to succeed and for having some of the best teachers in the state, and to my 3rd grade teacher Ms. Brandt.

I would like to thank my family; my amazing mother, Lora Rhinehart, for sacrificing everything for your two sons; my father, David Weller for teaching me valuable lessons

in life; my brother, Joshua Weller, for being the best big brother anybody could ask for; my stepfather, Wes Rhinehart, for teaching me hard work; and my grandparents for supporting me; and lastly my lovely girlfriend Lindsey for putting up with me over these years, particularly the last few months.

This work was supported by NNSA under DOE Cooperative Agreements DE-FC52-06NA27588, DE-FC52-06NA27586 and DE-NA001984 and in part by DE-FC52-06NA27616 and DE-NA0002075.

Outline

Chapter 1

Introduction and Motivation of Research	1
--	----------

Chapter 2

Theoretical and Experimental Tools	6
---	----------

2.1 – Non-LTE Kinetic Modeling of High Energy Density Plasmas	6
--	----------

2.1.1 – Non-LTE Kinetic Model of L-shell Ag	8
--	----------

2.1.2 – Non-LTE Kinetic Models of L-shell Mo, Cu, Zn, and K-shell Al and Mg	18
--	-----------

2.1.3 – Non-LTE Kinetic Modeling using Prism Atomic Data ATBASE and SPECT3D	22
--	-----------

2.2 – HELIOS-CR Radiation-Hydrodynamics Code	24
---	-----------

2.3 – Wire Ablation Dynamics Model	28
---	-----------

2.4 – The Zebra Generator	30
--	-----------

2.4.1 – The Zebra Optical System	33
---	-----------

2.4.2 – New Time-Gated Hard X-Ray Spectrometer on Zebra	36
--	-----------

2.5 – The Cobra Generator	41
--	-----------

2.6 – The Compact Laser Plasma Facility “Sparky” at UNR	42
--	-----------

2.7 – Sustained Spheromak Physics Experiment	43
---	-----------

Chapter 3

Radiative Properties of Uniform Mo and Mixed with Al Triple Planar Wire Arrays	45
---	-----------

3.1 – Introduction to Uniform Mo and Mixed with Al Triple Planar Wire Arrays.....	45
3.2 – Uniform Mo and Mixed with Al Triple Planar Wire Arrays with a 3.0 Inter-Planar Gap.....	46
3.2.1 – Implosion Characteristics and Temporal Radiation.....	47
3.2.2 – Radiative Characteristics	52
3.3 – Uniform Mo and Mixed with Al Triple Planar Wire Arrays with a Reduced Inter-Planar Gap of 1.5 mm	58
3.3.1 – Implosion Characteristics and Temporal Radiation of Triple Planar Wire Arrays with a Reduced Inter-Planar Gap of 1.5 mm	59
3.3.2 – Radiative Characteristics of Triple Planar Wire Arrays with a Reduced Inter-Planar Gap of 1.5 mm	65
3.4 – Conclusion of Uniform Mo and Mixed with Al Triple Planar Wire arrays at 3.0 mm and 1.5 mm inter-planar gap.....	71

Chapter 4

Implosion and Radiative Properties of Mixed Material Nested Cylindrical Wire Arrays

4.1 – Introduction and Motivation of Mixed Nested Cylindrical Wire Arrays	73
4.2 – Mixed Al and Brass Nested Cylindrical Wire Arrays on the Zebra Generator.....	74
4.2.1 – Time-integrated L-shell Cu and Zn and K-shell Al and Mg.....	76
4.2.2 – Time-gated Spectra of L-shell Cu and Zn and K-shell Al and Mg.....	81
4.2.3 – Wire Ablation Dynamics Modeling for Mixed NCWAs of L-shell Cu and Zn and K-shell Al and Mg	84
4.3 – Mixed Mo and Al Nested Cylindrical Wire Arrays on the Zebra and Cobra Generators.....	90
4.3.1 – Implosion Characteristics of Mo and Al NCWAs on Zebra.....	92
4.3.2 – Radiative Characteristics of Mo and Al NCWAs on Zebra.....	94

4.3.3 – Implosion Characteristics of Mo and Al NCWAs on Cobra	97
4.3.4 – Radiative Characteristics of Mo and Al NCWAs on Cobra	101
4.4 – Discussion and Conclusions of Mixed Material Nested Cylindrical Wire Array.....	103
Chapter 5	
Extreme EUV Spectroscopy and Modeling of Cu on the SSPX Spheromak and Laser Plasma “Sparky”	107
5.1 – Introduction.....	107
5.2 – Impurity Research on the Sustained Spheromak Physics Experiment	108
5.3 – Analysis of SSPX Impurity Spectra Dominated by M-shell Cu Emission.....	109
5.4 – Analysis of Laser Produced M-shell Cu Emission from “Sparky”	112
5.5 – Conclusions.....	113
Chapter 6	
Ag Planar Wire Arrays as Powerful Radiators	114
6.1 – Introduction and Motivation of Ag and Mixed Ag and Al Planar Arrays	114
6.2 – Comparison and Analysis of Ag SPWAs and Mixed Ag and Al DPWA.....	114
6.2.1 – Implosion Characteristics of Ag SPWA and Mixed Ag and Al DPWA.....	116
6.2.2 – Radiative Characteristics of Ag SPWA and Mixed Ag and Al DPWA.....	121
6.3 – Low-Aspect Ratio Ag DPWAs and their Signatures at Enhanced Current.....	127
6.4 – Conclusions.....	137
Chapter 7	
Potential for Lasing in Ne-like Ag on the Zebra Generator.....	139
7.1 – Introduction.....	139

7.2 – Lasing Gain Calculations for Ne-like L-shell Ag.....	140
7.3 – Split Double Planar Wire Array Load to Measure Lasing.....	146
7.4 – Conclusions.....	152
Chapter 8	
Conclusions.....	154
Appendix.....	159
References.....	162

List of Tables

Table 2.1. Ionization stages, line identification names, transitions, wavelengths, and spontaneous radiative decay rates of diagnostically useful L-shell Ag lines.....	12
Table 2.2. Wavelength ranges for the time-gated hard x-ray spectrometer as a function of crystal, crystal angle, and wedge angle	40
Table 3.1. List of considered shots and parameters for Mo and mixed Mo and Al TPWAs. The diameter is the diameter of the wires and the gap is the inter-planar gap.....	47
Table 3.2. List of considered shots and parameters for Mo and mixed Mo and Al TPWAs with reduced inter-planar gap	59
Table 4.1. List of considered shots and parameters for NCWAs. In Zebra shots 1790 and 1791 have brass on the inner array and Al in the outer array, while Zebra shots 1792 and 1793 have Al on the inner array and brass on the outer array.....	77
Table 4.2. List of considered shots and parameters for NCWAs of mixed Mo and Al on the Cobra and Zebra generators	90
Table 5.1. Diagnostically important transitions of Cu X – Cu XIII ions and theoretical wavelengths estimated with Spect3D and COWAN Code.....	111
Table 6.1: List of considered shots for pure Ag and mixed Ag and Al PWAs with load characteristics, total radiated energy output, PCD energy, and maximum current.....	115
Table 6.2. List of considered shots for pure Ag and mixed Ag and Al DPWAs with an increased gap of 6.0 mm; load characteristics, radiated energy output per length, PCD energy, implosion time, and maximum current	128
Table 7.1. List of considered lasing transitions for Ne-like Ag, along with wavelengths and gain calculations for two plasma conditions. Gain (a) is calculated using plasma	

conditions $T_e = T_{ion} = 1.8$ keV and $n_e = 10^{21}$ cm⁻³. Gain (b) is calculated using plasma conditions $T_e = T_{ion} = 2.4$ keV and $n_e = 10^{22}$ cm⁻³ 143

List of Figures

Figure 2.1. Energy level diagram of ground, singly, and doubly excited levels of adjacent ions. Collisional and radiative processes that transfer population between the levels are indicated by arrows and are color coordinated by the described processes 7

Figure 2.2. Synthetic L-shell Ag spectra demonstrating the electron temperature dependence at $T_e = 900$ eV, 1300 eV, 1800 eV, 2400 eV, and 3000 eV. The electron density was kept constant at $n_e = 10^{20}$ cm⁻³. The average ion charge, $\langle Z \rangle$, is also labeled to the left 13

Figure 2.3. Synthetic L-shell Ag spectra demonstrating the electron density dependence at $n_e = 10^{18}$ cm⁻³, 10^{19} cm⁻³, 10^{20} cm⁻³, 10^{21} cm⁻³, and 10^{22} cm⁻³. The electron temperature was kept constant at $T_e = 1800$ eV. The average ion charge, $\langle Z \rangle$, is also labeled to the left 15

Figure 2.4. Synthetic L-shell Ag spectra demonstrating the effect of fraction of hot electron dependence at 0%, 5%, 10%, and 15%. The electron temperature and density were kept constant at $T_e = 1800$ eV and $n_e = 10^{20}$ cm⁻³, respectively. The hot electron temperature was kept constant at $\varepsilon = 30$ keV with 100 eV FWHM. The average ion charge, $\langle Z \rangle$, is also labeled to the left 17

Figure 2.5. Synthetic L-shell Ag spectra demonstrating the contributions of different ionization stages. The electron temperature and density were kept constant at $T_e = 1800$ eV and $n_e = 10^{20}$ cm⁻³, respectively, while the fraction of hot electrons was 0% 18

Figure 2.6. Synthetic L-shell Mo spectra (left) with diagnostically important transitions (right). The synthetic spectra has $T_e = 1000$ eV and $n_e = 10^{20}$ cm⁻³ 19

- Figure 2.7.** Synthetic L-shell Cu and Zn spectra (left) with diagnostically important transitions (right). The synthetic spectra has $T_e = 350$ eV and $n_e = 5 \times 10^{19}$ cm⁻³. The synthetic spectra is weighted 70% Cu and 30% Zn, the same as the brass alloy20
- Figure 2.8.** Synthetic K-shell Al and Mg spectra (left) with diagnostically important transitions (right). The synthetic spectra has $T_e = 350$ eV and $n_e = 10^{20}$ cm⁻³. The synthetic spectra is weighted 95% Al and 5% Zn, the same as the Al 5056 alloy21
- Figure 2.9.** A comparison of L-shell Cu between two models: the blue is FAC run through SCRAM and the red is ATBASE run through SPECT3D. The calculations were run at $T_e = 300$ eV and $n_e = 5 \times 10^{19}$ cm⁻³22
- Figure 2.10.** Synthetic L-shell Kr spectra calculated through SPECT3D utilizing the atomic code ATBASE. a) L-shell Kr as a function of electron temperature with electron density constant at 10^{21} cm⁻³. b) L-shell Kr as a function of electron density with electron temperature constant at 400 eV23
- Figure 2.11.** A comparison of L-shell Ag radiation from a Single Planar Wire Array (top) and a Single Wire (bottom)25
- Figure 2.12.** Results from HELIOS-CR for a 30 μ m Ag single wire at 1.0 MA. a) Current pulse shape and zone radius as function of time, b) the electron temperature as a function of time and radius, c) electron density as a function of time and radius, and d) electron internal energy, kinetic energy, and magnetic energy as a function of time26
- Figure 2.13.** Results from HELIOS-CR for a) 50 μ m, b) 20 μ m, c) 10 μ m, and d) 5 μ m Ag single wire at 1.0 MA. For each simulation, the electron temperature is given as dependent on time and radius28
- Figure 2.14.** Example of a WADM simulation of an Al DPWA. The parameters were 10 wires in each plane, 6.0 mm interplanar gap, 1.0 interwire gap, and 12.5 μ m diameter wires29

Figure 2.15. The Zebra generator schematic, courtesy of University of Nevada, Reno (http://www.unr.edu/ntf/facility/zebra).....	32
Figure 2.16. The Zebra generator diagnostic layout for a general experiment.....	32
Figure 2.17. The schematic of the Load Current Multiplier on the Zebra generator.....	33
Figure 2.18. Optics schematic for the shadowgraphy system on the Zebra generator.....	34
Figure 2.19. Optics schematic for the ICCD system on the Zebra generator.....	35
Figure 2.20. a) Example of a shadowgraphy image. b) Example of an ICCD image.....	36
Figure 2.21. Diagram of a convex crystal spectrometer, with λ_{max} and λ_{min} shown along with the angle of incidence, Θ , and the radius of curvature of the crystal, r	37
Figure 2.22. Picture of a time-gated spectrometer body along with attached wedge.....	39
Figure 2.23. Schematic of the Cobra generator (Greenly <i>et al.</i> 2008).....	41
Figure 2.24. Schematic of the diagnostics used on the Cobra generator.....	42
Figure 2.25. a) The “Sparky” facility. “1” is the laser location, “2” is the vacuum chamber where the flat target is located, and “3” is where an EUV grazing spectrometer is located. b) An example of a flat target used.....	43
Figure 2.26. Schematic of the Sustained Spheromak Physics Experiment (from Wood <i>et al.</i> 2005a).....	44
Figure 2.27. Schematic of the Silver Flat Field Spectrometer on the SSPX (from Clementson <i>et al.</i> 2008).....	44
Figure 3.1. PCD and XRD signals, along with current and time-gated pinhole images of > 3.0 keV and > 1.0 keV, of Mo/Mo/Mo TPWA (a), Mo/Al/Mo TPWA (b), and	

Al/Mo/Al TPWA (c). The labels “a – f” denote the timings of the time-gated pinhole images49

Figure 3.2. Wire Ablation Dynamics Model implosion simulation of shot 1262, Mo/Al/Mo TPWA. The blue dots indicate initial starting positions of Mo wires, while the green dots indicate starting positions of Al wires. Light blue dots indicate ablating material from Mo wires and yellow dots indicate ablating material from Al wires50

Figure 3.3. (a) PCD and XRD signals from Al/Mo/Al along with current, timings from the time-gated spectrometer (labeled “1 – 6”), and K-shell Mg electron temperatures. (b) Spectra from time-gated spectrometer and (c) lineouts taken from spectra in (b) along with synthetic spectra52

Figure 3.4. (a) Time-integrated spatially resolved pinhole (left) and spectra (right) of Mo/Mo/Mo. (b) Time-integrated spatially resolved pinhole (left) and spectra (right) of Mo/Al/Mo. (c) Time-integrated spatially resolved pinhole (left) and spectra (right) of Al/Mo/Al54

Figure 3.5. Lineouts of L-shell Mo taken from Figure 3.4, Mo/Mo/Mo. The blue is experimental spectra, while the red is synthetic spectra. The distances from anode for each lineout are located to the right55

Figure 3.6. Lineouts of L-shell Mo taken from Figure 3.4, Mo/Al/Mo. The blue is experimental spectra, while the red is synthetic spectra. The distances from anode for each lineout are located to the right56

Figure 3.7. Lineouts of L-shell Mo taken from Figure 3.4, Al/Mo/Al. The blue is experimental spectra, while the red is synthetic spectra. The distances from anode for each lineout are located to the right57

Figure 3.8. PCD and XRD signals, along with current and time-gated pinhole images of > 3.0 keV and > 1.0 keV, of Mo/Mo/Mo TPWA (a), Mo/Al/Mo TPWA (b), and Al/Mo/Al TPWA (c) with an inter-planar gap of 1.5 mm. The labels “a – f” denote the timings of the time-gated pinhole images61

Figure 3.9. (a) PCD, XRD, and EUV signals from Mo/Al/Mo along with current, timings from the time-gated spectrometer (labeled “1 – 6”), and K-shell Al electron temperatures. (b) Spectra from time-gated spectrometer and (c) lineouts taken from spectra in (b) along with synthetic spectra.....63

Figure 3.10. (a) PCD, XRD, and EUV signals from Al/Mo/Al along with current, timings from the time-gated spectrometer (labeled “1 – 6”), and K-shell Al electron temperatures. (b) Spectra from time-gated spectrometer and (c) lineouts taken from spectra in (b) along with synthetic spectra.....64

Figure 3.11. (a) Time-integrated spatially resolved pinholes (left) and spectra (right) of Mo/Mo/Mo. (b) Time-integrated spatially resolved pinholes (left) and spectra (right) of Mo/Al/Mo. (c) Time-integrated spatially resolved pinholes (left) and spectra (right) of Al/Mo/Al.....66

Figure 3.12. Lineouts taken near the cathode from time-integrated spatially resolved spectra from **figure 3.11** of (a) Mo/Mo/Mo, (b) Mo/Al/Mo, and (c) Al/Mo/Al.....67

Figure 3.13. Lineouts of L-shell Mo taken from Figure 3.11, Mo/Mo/Mo. The blue is experimental spectra, while the red is synthetic spectra. The distances from anode for each lineout are located to the right68

Figure 3.14. Lineouts of L-shell Mo taken from Figure 3.11, Mo/Al/Mo. The blue is experimental spectra, while the red is synthetic spectra. The “a” and “c” represent anode and cathode, respectively. The distances from anode for each lineout are located to the right.....69

Figure 3.15. Lineouts of L-shell Mo taken from Figure 3.11, Al/Mo/Al. The blue is experimental spectra, while the red is synthetic spectra. The “a” and “c” represent anode and cathode, respectively. The distances from anode for each lineout are located to the right.....70

Figure 3.16. Electron temperature and density graphed as function of distance from anode. a) T_e of L-shell Mo and K-shell Al from Mo/Al/Mo. b) n_e of L-shell Mo and K-

shell Al from Mo/Al/Mo. c) T_e of L-shell Mo and K-shell Mg from Al/Mo/Al. d) n_e of L-shell Mo from Al/Mo/Al. Data points taken from Figures 3.14 and 3.15 71

Figure 4.1. Illustrations for Al-on-brass (a) and brass-on-Al (b). Picture of a nested cylindrical wire array (c)..... 77

Figure 4.2. X-ray time-integrated spatially resolved spectra (right) and pinhole images (left) of NCWAs for configurations of Al-on-brass (a) and brass-on-Al (b). The “a” and “c” refer to anode and cathode, respectively 79

Figure 4.3. Examples of K-shell Al/Mg and L-shell Cu/Zn experimental (blue) and synthetic (red) spectra of NCWAs for configurations of Al-on-brass (a) and brass-on-Al (b) taken from Figure 4.2, near anode..... 79

Figure 4.4. PCD signals with estimated electron temperatures (top) attained from TGSP (bottom) for Al-on-brass. The timings of the TGSP were changed from shot 1790 (a) to 1791 (b) to attain spectra from before, near, and after the main PCD peak 82

Figure 4.5. PCD signals with estimated electron temperatures (top) attained from time-gated spectra (bottom) for brass-on-Al for shot 1793..... 83

Figure 4.6. Comparison of data for mixed NCWA for shot 1790 with brass the inner array and Al the outer array (Al-on-brass). Shadowgraphy, time-gated spectra and pinhole images, as well as XRD, PCD, and EUV signals are shown with WADM calculations, where W_{Th} is the simulated thermalized kinetic energy 86

Figure 4.7. Comparison of data for mixed NCWA for shot 1793 with Al the inner array and brass the outer array (brass-on-Al). Shadowgraphy, time-gated spectra and pinhole images, as well as XRD, PCD, and EUV signals are shown with WADM calculations, where W_{Th} is the simulated thermalized kinetic energy..... 87

Figure 4.8. Illustrations for (a) Mo-on-Mo/Al (1043), (b) Mo/Al-on-Mo (1044), (c) Mo-on-Mo/Al (1795), and (d) Mo/Al-on-Mo (1794)..... 91

- Figure 4.9.** Signals, current, and time-gated pinhole images (a), shadowgraphy images (b), time-gated spatially integrated spectra (c), and in (d) a lineout taken from frame 6 (c) with experimental (blue) and synthetic spectra (red) of Mo-on-Mo/Al, Zebra shot 1795. The synthetic spectra is modeled K-shell Al at $T_e = 510$ eV93
- Figure 4.10.** Signals, current, and time-gated pinhole images (a), shadowgraphy images (b) of Mo/Al-on-Mo, Zebra shot 1794.....94
- Figure 4.11.** Time-integrated spatially resolved spectra (top-left) and pinhole (top-right) images of Mo-on-Mo/Al, Zebra shot 1795. Below is a lineout taken from the experimental spectra from above in blue and in red is modeled synthetic spectra of K-shell Al below that of L-shell Mo95
- Figure 4.12.** Time-integrated spatially resolved spectra (top-left) and pinhole (top-right) images of Mo/Al-on-Mo, Zebra shot 1794. Below are lineouts taken from the experimental spectra from above in blue and in red are modeled synthetic spectra of K-shell Al. The distances from anode for each lineout are located to the right.....96
- Figure 4.13.** Optical streak image (a), signals, current, and wire ablation dynamics modeling (b), EUV images (c), and shadowgraphy images (d) of Mo-on-Mo/Al, Cobra shot 1043. PCD_1 is filtered at > 0.2 keV and PCD_3 is filtered at > 0.9 keV99
- Figure 4.14.** Optical streak image (a), signals, current, and wire ablation dynamics modeling (b), EUV images (c), and shadowgraphy images (d) of Mo/Al-on-Mo, Cobra shot 1044. PCD_1 is filtered at > 0.2 keV and PCD_3 is filtered at > 0.9 keV 100
- Figure 4.15.** Time-integrated spatially resolved spectra (top-left) and pinhole (top-right) images of Mo-on-Mo/Al, Cobra shot 1043. Below is a lineout taken from the experimental spectra from above in blue and in red is modeled synthetic spectra of L-shell Mo with plasma parameters of $T_e = 1140$ eV and $n_e = 3 \times 10^{19}$ cm⁻³ 102
- Figure 4.16.** Time-integrated spatially resolved spectra (top-left) and pinhole (top-right) images of Mo/Al-on-Mo, Cobra shot 1044. Below are two lineouts taken, marked “1” and “2”, from the experimental spectra from above in blue and in red is modeled

synthetic spectra of L-shell Mo with plasma parameters of $T_e = 1130$ eV and $n_e = 9 \times 10^{18}$ cm^{-3} 103

Figure 5.1. Experimental results from the SSPX spheromak. EUV image shown along with respected lineouts for shots 20675, 20780, and 20801 110

Figure 5.2. Experimental spectrum of shot 20801 from SSPX at the top. Synthetic spectra calculated at $n_e = 10^{14}$ cm^{-3} for Cu at $T_e = 40$ eV (in the middle) and for O at $T_e = 15$ eV (at the bottom) 111

Figure 5.3. Experimental spectrum of Cu EUV produced on “Sparky” with two synthetic spectra calculated $T_e = 25$ eV and 90 eV and $n_e = 10^{19}$ cm^{-3} 112

Figure 6.1. Signals and time-gated pinhole images for shots (a) 2585 – Ag SPWA at standard current, (b) 2587 – Ag SPWA at standard current, (c) 2480 – Ag SPWA at enhanced current, and (d) 1928 – Ag and Al DPWA at standard current. The pinhole timings are shown with gray boxes and are listed “a-f” and are filtered at > 1.0 keV (bottom) and > 3.0 keV (top) 119

Figure 6.2. (a) Signals and timings for the TGHXR spectrometer for shot 2585 – Ag SPWA at standard current. In (b), images of spectra from the TGHXR spectrometer for shot 2585. The frames are listed as “1-4” and correspond with timings in (a). In (c), the third frame from (b) has enhanced contrast for clarity. (d) Signals and timings for the TGHXR spectrometer for shot 2587 – AG SPWA at standard current. In (e), images of spectra from the TGHXR spectrometer for shot 2587 and all frames have enhanced contrast for clarity the same as in (c). The frames are listed as “5-8” and correspond with timings in (d)..... 121

Figure 6.3. (a) Shot 2585 – Ag SPWA at standard current and (b) shot 2480 – Ag SPWA at enhanced current of x-ray time-integrated spatially resolved spectra (right) and pinhole images (left). The pinhole images are filtered at > 3.0 keV 123

Figure 6.4. (a) L-shell Ag spectra produced on Zebra in shot 2585 – Ag SPWA at standard current and (b) in shot 2480 – Ag SPWA at enhanced current. Lineouts taken from spectra in Figure 6.3..... 123

Figure 6.5. Shot 1928 – Ag and Al DPWA at standard current. (a) X-ray time-integrated spatially resolved spectra of K-shell Al and L-shell Ag and pinhole images. (b) Lineouts of the spectra in blue along with synthetic spectra in red for K-shell Al are shown in (b). In (c) K-shell Al T_e is plotted as a function of distance from cathode. In (d) K-shell Al and L-shell Ag n_e are plotted as functions of distance from cathode. Arrows numbered “1-3” correlate spectra with lineouts, as well as indicating bright spots that generate L-shell Ag radiation..... 126

Figure 6.6. Signals from PCD, XRD, and SiD, along with measured current (a) for Zebra shot 2986 (Ag DPWA with 6 mm gap). Time-gated spectra is shown in (b) with timings correlated with black triangles in (a) and numbered “1-4”. Shadowgraphy images are shown in (c) with timings correlated with grey circles in (a) and labeled “a-b”. Time-integrated spatially resolved pinhole images are shown in (d) at two different cutoff energies 130

Figure 6.7. Signals from PCD, XRD, and SiD, along with measured current (a) for Zebra shot 2985 (Ag DPWA with 6 mm gap). Time-gated spectra is shown in (b) with timings correlated with black triangles in (a) and numbered “1-4”. Shadowgraphy images are shown in (c) with timings correlated with grey circles in (a) and labeled “a-b”. Time-integrated spatially resolved pinhole images are shown in (d) at two different cutoff energies 131

Figure 6.8. Shadowgraphy images of Ag DPWAs with 6.0 mm gap at enhanced current. Images from three different identical loads with timings changed. Images show independently imploding planes along with “cone-like” structures developing in anode “a” and cathode “c”..... 132

Figure 6.9. Signals from PCD, XRD, and SiD, along with measured current and K-shell Mg electron temperatures (a) for Zebra shot 2988 (Ag and Al DPWA with 6 mm gap).

Time-gated hard x-ray spectra is shown in (b) with timings correlated with black triangles in (a) and numbered “1-4”. Shadowgraphy images are shown in (c) with timings correlated with grey circles in (a) and labeled “a-b”. Time-gated spectra is shown in (e) with timings correlated with black dots in (a) and labeled “a-f”. Lastly, (f) shows spectra in blue from (e) along with synthetic modeling of K-shell Mg in red..... 134

Figure 6.10. (a) Time-integrated spatially resolved spectra for Zebra shot 2988 (Ag and Al DPWA with 6 mm gap). (b) Experimental spectra (blue) taken from (a) and synthetic spectra (red) of K-shell Mg. (c) Time-integrated spatially resolved pinhole image (> 3.0 keV). (d) Electron temperature of K-shell Mg as a function of distance from anode..... 135

Figure 6.11. Shadowgraphy images of mixed Ag and Al DPWAs with 6.0 mm gap at enhanced current. The Ag plane is located on the left while the Al plane is located on the right in all images. Images from three different identical loads with timings changed. Images show independently imploding planes along with “cone-like” structures developing in anode “a” and cathode “c” 136

Figure 7.1. Lasing gain calculated as function of T_e and n_e for the Ne-like Ag transition of $2p_{1/2}^2 2p_{3/2}^3 3p_{3/2} \ ^3P_2 \rightarrow 2p_{1/2}^2 2p_{3/2}^3 3s \ ^3P_1$ at 99.2 \AA . In these calculations, $T_{ion} = T_e$ 145

Figure 7.2. Lasing gain calculated as function of T_e and n_e for the Ne-like Ag transition of $2p_{1/2}^2 2p_{3/2}^3 3p_{3/2} \ ^3P_0 \rightarrow 2p_{1/2}^2 2p_{3/2}^3 3s \ ^3P_1$ at 80.7 \AA . In these calculations, $T_{ion} = T_e$ 146

Figure 7.3. a) Structure of a split double planar wire array (perpendicular view) on the 1.7 MA Zebra generator. b) A reference shadowgraphy picture before the experiment (perpendicular view). c) Shadowgraphy taken approximately 50 ns into the shot after the current rise. The red dotted lines indicate where the wires originally began. An early and relatively uniform column has formed..... 147

Figure 7.4. Signals and time-gated pinhole images from a Mo split double planar wire array with 3.0 mm interplanar gap on the 1.7 MA Zebra generator. The pinhole timings are shown with gray boxes and are listed “a-f” and are filtered at > 1.0 keV (bottom) and > 3.0 keV (top)..... 148

Figure 7.5. a) Shadowgraphy from a split double planar wire array 50 ns into the shot after current rise, seen from a perpendicular view. b) Shadowgraphy from same shot as in a) 6 ns later. c) Shadowgraphy from a split double planar wire array 52 ns into the shot after current rise, seen from a parallel view, in between the planes. d) Shadowgraphy from same shot as in c) 6 ns later. The red dotted lines indicated were the wires originally began 149

Figure 7.6. Signals and time-gated pinhole images from a Mo split double planar wire array with 6.0 mm interplanar gap on the 1.7 MA Zebra generator. The pinhole timings are shown with gray boxes and are listed “a-f” and are filtered at > 1.0 keV (bottom) and > 3.0 keV (top)..... 150

Figure 7.7. Illustrations of EUV Spectrometer locations for the split double planar wire array experiments. The picture in the upper right shows the physical anode plate hardware with a hole in the middle for diagnostic access for an EUV spectrometer measure potential lasing lines radiating axially 152

Chapter 1

Introduction and Motivation of Research

For the better part of the last century major research has gone into creating a controllable and sustainable fusion power device. In order to overcome the Coulomb repulsion between positively charged nuclei, the fuel must be compressed and heated to thermonuclear temperatures, a process called inertial confinement fusion (ICF). The fuel used will more than likely be a mixture of deuterium (one proton and one neutron) and tritium (one proton and two neutrons). Some of the leading candidates for such a device include the use of lasers, tokamaks, and z-pinch. This dissertation will largely focus on z-pinch experiments at the university scale (1.0 MA) and further focuses on the study of the radiation from the plasma produced from such experiments. The main goal of performing experiments on university scale machines is not to attain fusion, but to maximize energy efficiency and power in considering load types and materials in a cost effective manner so that when larger machines are built in the future most of the knowledge of what “works” and what does not “work” is already known. A second goal for university scale machines, and of equal importance, is to teach new students experimental and theoretical physics.

The first experiments involving the use of z-pinch for ICF purposes took place in the 1950's, however magnetohydrodynamic instabilities within the pinch (Anderson *et al.* 1958) proved to be too great and interest quickly turned to other avenues. Though the idea of using z-pinch for ICF faded during this period, z-pinch continued to be

studied and in the 1960's single wire experiments were carried out, where very intense x-rays were observed. In order to achieve more hot and dense plasmas, single wires were replaced by cylindrical wire arrays (CWA) (Lieberman *et al.* 1999), which, as the name describes, is an array of wires oriented in a cylindrical manner equidistant from the center of the anode-cathode gap. The idea is that as current is flowing through the wires a magnetic field is created around the wires and a resulting $J \times B$ Lorentz force pulls the wires together towards the central z-axis (hence the name z-pinch). In a CWA, the wires pick up a tremendous amount of kinetic energy (ablation velocity measured to be up to 70 cm/ μ s in Jones *et al.* 2011), which helps in ionizing the plasma and increasing efficiency. With these advances, z-pinches produce plasmas with very high temperatures and densities and have been shown to be one the most efficient x-ray producers of any type of experiment (Spielman *et al.* 1998) and are currently thought to be a viable option for future possible ICF machines (Vesey *et al.* 2007). In 2005, the planar wire array (PWA) was introduced (Kantsyrev *et al.* 2006) and was shown to be a very powerful radiation source, producing much greater total radiation than CWAs, and a possible candidate to use on future ICF machines (Jones *et al.* 2010).

In this dissertation, PWAs are discussed in detail, as well as nested cylindrical wire arrays (NCWAs). This dissertation focuses on radiation from wire materials of mid-Z elements molybdenum (Mo), silver (Ag), copper (Cu), and zinc (Zn), and low-Z elements aluminum (Al) and magnesium (Mg).

One of the best ways to attain knowledge of the plasma parameters in z-pinch and other experiments is through plasma spectroscopy. In plasmas free electrons, ions, and photons interact with each other resulting in radiation that spans a large photon energy

spectrum. Spectrometers can be used to separate the radiation into spectral lines depending on the photon energy, which can be used as “fingerprints”, as each individual photon emitted depends on quantum mechanical probabilities, which can depend on various plasma parameters, such as electron temperature and density. With sufficient understanding of the probabilities and various rates involved, a theoretical model can be created to produce a synthetic spectrum to try and match the experimental spectrum. The first of these models (Gabriel 1972) involved K-shell plasmas, or plasmas involving transitions to the $n = 1$ shell of He-like and the surrounding ions. Advances in these models have added the inclusion of line shapes (Mancini *et al.* 1988) and effects of opacity (Apruzese *et al.* 1998). L-shell and M-shell models developed later as computer processors caught up to the complexity of Ne-like ion plasma environments and beyond. For instance, the first full collisional radiative models used to diagnose electron temperatures and densities that radiated in L-shell included selenium (Se) (Peyrusse *et al.* 1989), Mo, and Ag (Young *et al.* 1989). Each element presents different energy levels and a set of rates for similar K-shell, L-shell, or M-shell transitions.

Therefore, to help study this radiation many theoretical tools have been developed and utilized, which include non-local thermodynamic equilibrium (LTE) kinetic models, the wire ablation dynamic model (WADM), and the radiation-hydrodynamics model HELIOS-CR. Specifically, a new non-LTE kinetic model for L-shell Ag has been developed. The majority of the experimental data used comes from the Zebra generator at the University of Nevada, Reno (UNR). Other data comes from facilities that include the Z-pinch Cobra Generator at Cornell University, the Compact Laser Plasma Facility “Sparky” at UNR, and the Sustained Spheromak Physics Experiment (SSPX) at

Lawrence Livermore National Laboratory. The focus of Chapter 2 is the description of these theoretical and experimental tools.

A common theme throughout this dissertation is the constant search for more efficient radiators. In this search Mo triple planar wire arrays (TPWAs) are explored in Chapter 3 and are shown to be a very efficient radiator at > 25 kJ on the Zebra generator, and radiates at very high electron temperatures (> 1.4 keV) in the L-shell. The alloy Al 5056 (95% Al, 5% Mg) has been used in these experiments in two fashions; one as a tracer wire, the other to study how different plasmas mix (L-shell Mo and K-shell Al, for instance).

Brass (70% Cu, 30% Zn) and Al and Mo and Al nested cylindrical wire arrays (NCWAs) are investigated in Chapter 4 to understand how the inner and outer arrays radiate in this configuration, which had not been fully investigated to this point. It will be shown that the outer array radiates more greatly than the inner array. The thermalized kinetic energy of this implosion is estimated to be significantly less than the measured total energy, indicating there must be other mechanisms responsible for the radiation yields.

In certain plasma experiments, impurities can play a significant role. To more understand this, an investigation of Cu impurities on the Sustained Spheromak Physics Experiment (SSPX) facility was performed and is the focus of Chapter 5. To help in this, an EUV spectrometer was utilized to capture EUV Cu spectra, in which an M-shell Cu non-LTE model was used to diagnose the impurity plasma conditions.

Ag is explored in the continuation of the search for efficient radiators in Chapter 6. Ag was discovered to radiate at > 30 kJ on the Zebra generator, which currently is

near the record energy output recorded. A Ag non-LTE kinetic model was developed to help diagnose L-shell Ag plasma conditions. To help in understanding how L-shell Ag plasmas radiate in time, a time-gated hard x-ray spectrometer (TGHXR) was built and implemented. This spectrometer captured both hotter plasma L-shell Ag lines and cooler plasma characteristic L_{α} and L_{β} lines. Low aspect ratio DPWAs of uniform Ag and mixed with Al were tested attain a better diagnostic view with shadowgraphy to understand more how each plane in a DPWA implodes.

Furthermore, as an application, the potential for lasing in these L-shell Ag plasmas is discussed in Chapter 7, with a new load type considered with the goal of generating a uniform plasma column for a lasing medium, the split double planar wire array (SDPWA).

Lastly, Chapter 8 concludes and summarizes the dissertation with additional closing remarks.

Chapter 2

Theoretical and Experimental Tools

2.1 Non-LTE Kinetic Modeling of High Energy Density Plasmas

The majority of the plasmas studied in this dissertation are in the non-local thermodynamic equilibrium (non-LTE) state, which means that the plasma particles (ions, electrons, and photons) are not in equilibrium: the rate of each process does not equal the rate of the inverse process. LTE plasmas are generally created in high electron density regimes ($> 10^{23} \text{ cm}^{-3}$), where collisional effects dominate radiative ones, which is too high for the z-pinch plasmas predominately studied here, which have plasma electron densities $10^{18} - 10^{21} \text{ cm}^{-3}$. This makes any attempt to model radiation emitting from such plasmas complicated, as one has to consider a series of rate equations to account for all processes that populate and depopulate energy levels. These processes and their inverses include: collisional excitation and collisional de-excitation, collisional ionization and three-body recombination, dielectronic capture and Auger decay, radiative decay and resonant photo-absorption, and photoionization and radiative recombination. Figure 2.1 details these processes and the associated reactions. In this figure, $X_{Z,\eta}$ refers to an ion of charge Z and a set of quantum numbers symbolized by η . A single asterisk is used to denote a singly-excited state, while two asterisks indicate a doubly-excited state. The end goal of solving these rate equations is to attain level populations and create synthetic spectra to match and model experimental spectra to attain approximate plasma conditions, such as electron temperature and density.

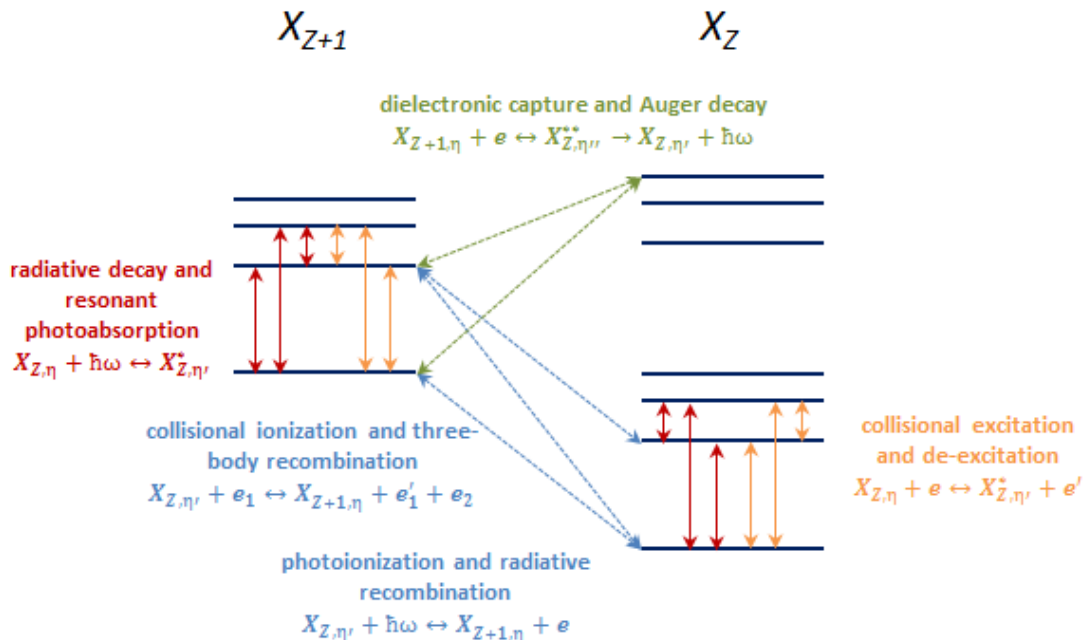


Figure 2.1. Energy level diagram of ground, singly, and doubly excited levels of adjacent ions. Collisional and radiative processes that transfer population between the levels are indicated by arrows and are color coordinated by the described processes.

There are many atomic models and codes in the scientific community that solve for these atomic rates with the goal of producing synthetic spectra to compare to experimental spectra. In this dissertation two such models are utilized; the first uses the Flexible Atomic Code (FAC) (Gu 2008) to calculate energy levels and various atomic rates, which are fed into the Spectroscopic Collisional-Radiative Atomic Model (SCRAM) (developed by Hansen 2003 and modified by Ouart 2010a) which calculates the rest of the rates and ultimately produces synthetic spectra as functions of various plasma parameters. Section 2.1.1 will discuss this process more and a new non-LTE kinetic model of L-shell Ag will be presented, while Section 2.1.2 will discuss other non-LTE models utilized in this dissertation that have already been developed. The second model, discussed in Section 2.1.3, is the Atomic Data ATBASE from PRISM

(MacFarlane et al. 2007) which calculates atomic rates and energy levels which get input into the PRISM code SPECT3D to generate synthetic spectra.

2.1.1 Non-LTE Kinetic Model of L-shell Ag

This section will discuss the new non-LTE kinetic model used for L-shell Ag plasmas. First, however, will be a brief description of how the models work. To begin with, the radiative decay and Auger decay rates are calculated using FAC. After these rates are attained, the data is sent to SCRAM to generate synthetic spectra. In order to calculate the collisional processes with free electrons, the cross-sections $\sigma(\varepsilon)$ are integrated over the electron distribution function $\mathcal{F}(\varepsilon)$:

$$n_e \langle v\sigma \rangle = n_e \int v(\varepsilon)\sigma(\varepsilon)\mathcal{F}(\varepsilon)d\varepsilon \quad (s^{-1}) \quad 2.1$$

In Equation 2.1, ε is the incident electron energy, v is the incident electron velocity ($v = \sqrt{2\varepsilon/m_e}$), n_e is the electron density, and the electron distribution function must be normalized to unity ($\int \mathcal{F}(\varepsilon)d\varepsilon = 1$). For three-body recombination, which involves two free electrons, Equation 2.1 simply would be integrated twice over the electron distribution function.

Ultimately, SCRAM calculates all the competing rates that populate and depopulate the population for each state, which can be written as:

$$\frac{dX_i}{dt} = \sum_{k=1}^N X_k R_{ki}^{tot} - X_i \sum_{k=1}^N R_{ik}^{tot} \quad 2.2$$

In Equation 2.2, i and k are energy level indices and R_{ik}^{tot} is the total rate from level i to level k . The solution, once set to unity ($\sum X_i = 1$), becomes fractional energy level populations. From here, the average charge state (Equation 2.3) and ion density (Equation 2.4) can be found:

$$\langle Z \rangle = \sum_Z X_Z Z \quad 2.3$$

$$n_{ion} = \frac{n_e}{\langle Z \rangle} \quad (cm^{-3}) \quad 2.4$$

Next, the electron distribution must be assumed to calculate collisional rates. Given the assumption that electron velocities are non-relativistic, have sufficient time to thermalize, and exchange effects are not important, the electron distribution can be described by the Maxwellian distribution:

$$\mathcal{F}_M(\varepsilon, T_e) = \frac{2}{\sqrt{\pi} T_e} \sqrt{\frac{\varepsilon}{T_e}} e^{-\varepsilon/T_e} \quad (eV^{-1}) \quad 2.5$$

In Equation 2.5, T_e is the electron temperature. This distribution is satisfied if there is enough time for the electrons to thermalize. The thermalization time is given by the electron self-collision time (Spitzer 1962):

$$t_c \approx 3.3(T_e/100 \text{ eV})^{3/2} (10^{20} \text{ cm}^{-3}/n_e \ln \Lambda) \text{ (ps)} \quad 2.6$$

where $\ln A$ is the Coulomb logarithm which varies with the temperature and density and is generally between five and fifteen. Using this equation for plasma conditions $T_e = 400$ eV and $n_e = 10^{20} \text{ cm}^{-3}$, the thermalization time is on the order of a few picoseconds. With this estimation, it is reasonable to assume that this Maxwellian distribution works for most of the electrons in the plasma, aside from areas of electric fields in the plasma, which occur in z-pinchs due to acceleration of electrons near Rayleigh-Taylor instabilities and can form “hot” electrons. To take this into account, the beam of electrons is approximated by a Gaussian centered at ε_0 with variance σ^2 at the tail of the Maxwellian distribution. The parameter α controls the fraction of hot electrons in Equation 2.7:

$$\mathcal{F}_{non-max}(\varepsilon, \alpha, T_e, \varepsilon_0, \sigma) = (1 - \alpha)\mathcal{F}_M(\varepsilon, T_e) + \alpha\mathcal{F}_G(\varepsilon, T_e) \quad 2.7$$

$$\mathcal{F}_G(\varepsilon, \varepsilon_0, \sigma) = \frac{1}{\sqrt{2\pi}\sigma} \exp\left(\frac{-(\varepsilon - \varepsilon_0)^2}{2\sigma^2}\right) \quad 2.8$$

Finally, line broadening of the spectra needs to be taken into consideration. In SCRAM, line broadening is taken into account in three ways (assuming optical thin conditions): temperature, natural, and instrumental broadening. SCRAM uses Voigt line profiles in order to take effects into account. For more information on SCRAM and more exact details of these calculations, see (Hansen 2003).

The atomic data for the new non-LTE Ag kinetic model was calculated by utilizing FAC, as described earlier in this section. The atomic data include the ground states from the bare to neutral atoms and the details from H-like to Al-like ions including singly and doubly excited states. The singly excited states are included up to $n = 6$ for H-like ions, where there are 30 total levels, $n = 5$ for He-ions, where there are 90 total levels, $n = 5$ for Li-like ions, where there are 101 total levels, $n = 4$ for Be-like ions, where there are 128 total levels, $n = 4$ for B-like ions, where there are 169 total levels, $n = 4$ for C-like ions, where there are 401 total levels, $n = 4$ for N-like, where there are 486 total levels, $n = 4$ for O-like, where there are 421 total levels, $n = 4$ for F-like, where there are 268 total levels, $n = 5$ for Ne-like, where there are 141 total levels, $n = 5$ for Na-like ions, where there are a total of 1029 levels, $n = 4$ for Mg-like, where there are 1273 total levels, and $n = 4$ for Al-like, where there are 385 total levels. The doubly excited states include up to $n = 3$ for He-, Li-, Na-, Mg-, and Al-like ions, and with $n = 2$ for Be-like ions. Total, 4957 energy levels are considered. This atomic data is input into the SCRAM code to generate synthetic spectra. This new Ag model can generate K- and L-shell synthetic spectra for a wide range of electron temperatures and densities, however has primarily been used for L-shell Ag studies (Chapter 6), as well as calculating lasing gain (described in Chapter 7).

Table 2.1 lists the ionization stages, line identification names, transitions, wavelengths, and spontaneous radiative decay rates of diagnostically useful L-shell Ag lines. The spontaneous radiative decay rate, A_r , is related to oscillator strength, f_{ki} , by the formula:

$$f_{ki} = \frac{A_r}{C} \left(\frac{g_i}{g_k} \right) \left(\frac{Ry}{\Delta E} \right)^2 \quad 2.9$$

In Equation 2.8, C is equal to $\alpha^3 Ry/\hbar = 8.033 \times 10^9 \text{ s}^{-1}$ (for electric multipole transitions), g_i and g_k are statistical weights of the upper and lower levels, respectively, and Ry is the Rydberg constant ($Ry = e^4 m_e / 2\hbar^2 = 13.605\,692 \text{ eV}$). This formula will be useful when calculating lasing gain, in Chapter 6.

Ion	Line	Transition	$\lambda(\text{\AA})$	$A_r(\text{s}^{-1})$
Ne	4C	$1s^2 2s^2 2p^5 4d \ ^1P_1 \rightarrow 1s^2 2s^2 2p^6 \ ^1S_0$	2.7693	8.21E+13
Ne	4D	$1s^2 2s^2 2p^5 4d \ ^3D_1 \rightarrow 1s^2 2s^2 2p^6 \ ^1S_0$	2.8803	1.37E+14
Ne	3A	$1s^2 2s 2p^6 3p \ ^1P_1 \rightarrow 1s^2 2s^2 2p^6 \ ^1S_0$	3.3992	5.99E+13
Ne	3B	$1s^2 2s 2p^6 3p \ ^3P_1 \rightarrow 1s^2 2s^2 2p^6 \ ^1S_0$	3.4452	2.18E+13
Ne	3C	$1s^2 2s^2 2p^5 3d \ ^1P_1 \rightarrow 1s^2 2s^2 2p^6 \ ^1S_0$	3.5485	2.74E+14
Ne	3D	$1s^2 2s^2 2p^5 3d \ ^3D_1 \rightarrow 1s^2 2s^2 2p^6 \ ^1S_0$	3.7197	3.29E+14
Ne	3F	$1s^2 2s^2 2p^5 3s \ ^1P_1 \rightarrow 1s^2 2s^2 2p^6 \ ^1S_0$	3.8026	1.60E+13
Ne	3G	$1s^2 2s^2 2p^5 3s \ ^3P_1 \rightarrow 1s^2 2s^2 2p^6 \ ^1S_0$	4.0214	1.82E+13
F	F1	$1s^2 2s^2 2p^4 3d \ ^2F_{5/2} \rightarrow 1s^2 2s^2 2p^5 \ ^2P_{3/2}$	3.4591	2.48E+14
Na	Na1	$1s^2 2s^2 2p^5 3s 3d \ ^2F_{5/2} \rightarrow 1s^2 2s^2 2p^6 3s \ ^2S_{1/2}$	3.7435	2.62E+14
Na	Na2	$1s^2 2s^2 2p^5 3s 3d \ ^2P_{1/2} \rightarrow 1s^2 2s^2 2p^6 3s \ ^2S_{1/2}$	3.5711	2.69E+14
Mg	Mg1	$1s^2 2s^2 2p^5 3s^2 3d \ ^1P_1 \rightarrow 1s^2 2s^2 2p^6 3s^2 \ ^1S_0$	3.7595	2.56E+14
Mg	Mg2	$1s^2 2s^2 2p^5 3s^2 3d \ ^3P_1 \rightarrow 1s^2 2s^2 2p^6 3s^2 \ ^1S_0$	3.5853	1.56E+14

Table 2.1. Ionization stages, line identification names, transitions, wavelengths, and spontaneous radiative decay rates of diagnostically useful L-shell Ag lines.

Understanding how the resulting spectra change as a function of various plasma parameters, such as T_e and n_e , as the next several figures will illustrate.

To understand how the new non-LTE kinetic model is dependent on electron temperature, the model was run keeping electron density ($n_e = 10^{20} \text{ cm}^{-3}$) and all other parameters constant, while changing only T_e , which ranged from 900 eV to 3000 eV. This range was chosen because the majority of the L-shell Ag plasmas in this research radiated in this range of electron temperatures, as will be discussed in Chapter 6. The most dominate features are of Ne-like Ag, and have a labeling scheme of Ne 3A, Ne 3C, Ne 3D, and so on, which follows the same labeling scheme as in Beiersdorfer *et al.* 1988 (see also Table 2.1).

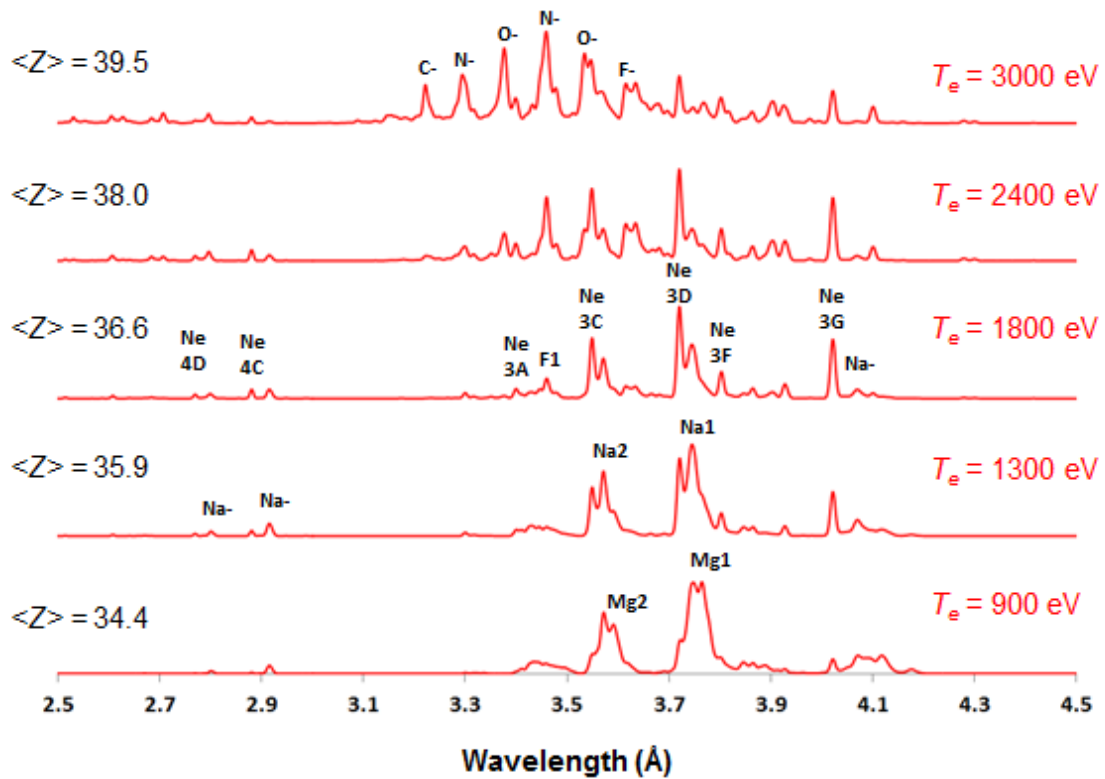


Figure 2.2. Synthetic L-shell Ag spectra demonstrating the electron temperature dependence at $T_e = 900 \text{ eV}$, 1300 eV , 1800 eV , 2400 eV , and 3000 eV . The electron density was kept constant at $n_e = 10^{20} \text{ cm}^{-3}$. The average ion charge, $\langle Z \rangle$, is also labeled to the left.

Figure 2.2 demonstrates the electron temperature dependency of the model. As seen in the average ion charge, $\langle Z \rangle$, in Figure 2.2, increasing electron temperature in the model leads to a significant increase in changing the ion charge state, which means higher electron temperatures indicates on average more electrons stripped from the individual ion. At 900 eV the spectra is dominated by Mg- (31.5%), Al- (18.3%), and Na-like (19.9%), while Ne-like (2.7%) contributes less. However, by 1800 eV the spectra is dominated now by Na- (38.3%), Ne-(35.4%), and F-like (13.4%), and has burned through most of Mg-like (8%). At 3000 eV, it's estimated that Ne-like (6.6%) has been burned mostly through and the plasma is now dominated by the higher ionization states of C- (16.5%), N- (26.2%), O- (24.4%), and F-like (15.4%). Due to this understanding of how electron temperature affects the ionization charge state, a useful diagnostic tool for estimating T_e among radiated L-shell Ag plasmas can be ratios between lines of different ionization stages, such as Mg1/Na1.

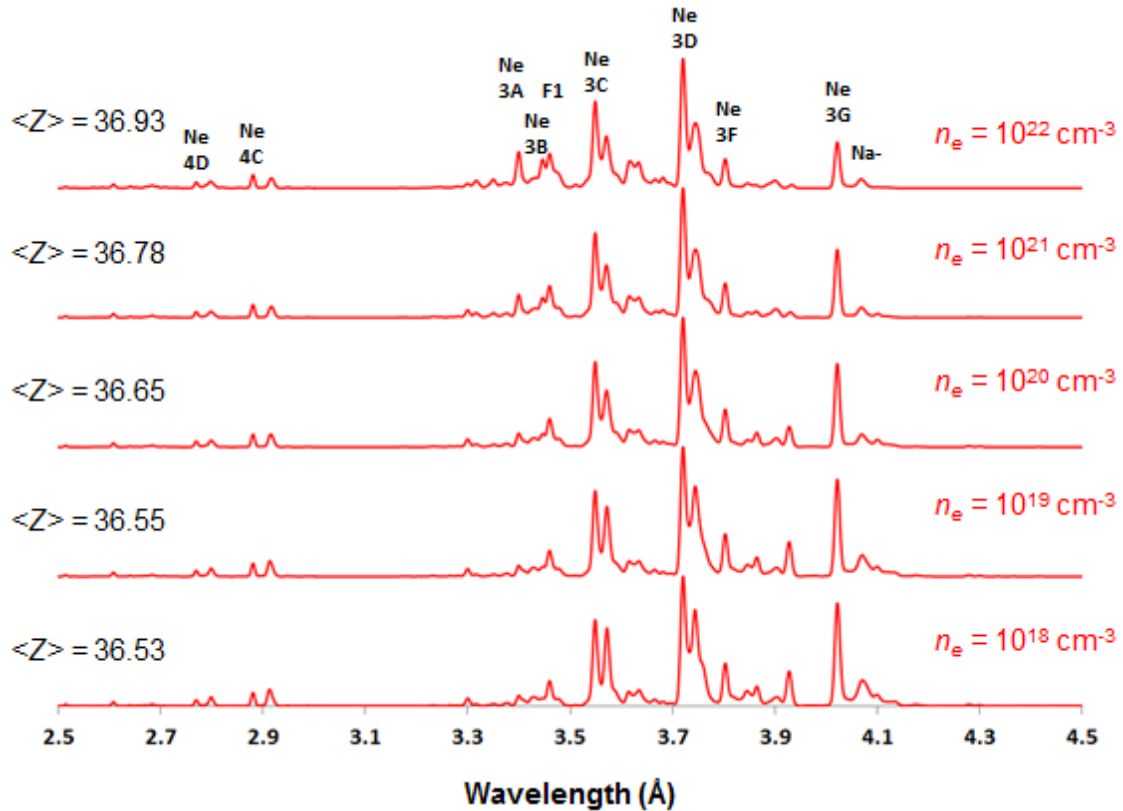


Figure 2.3. Synthetic L-shell Ag spectra demonstrating the electron density dependence at $n_e = 10^{18} \text{ cm}^{-3}$, 10^{19} cm^{-3} , 10^{20} cm^{-3} , 10^{21} cm^{-3} , and 10^{22} cm^{-3} . The electron temperature was kept constant at $T_e = 1800 \text{ eV}$. The average ion charge, $\langle Z \rangle$, is also labeled to the left.

Figure 2.3 demonstrates the electron density dependency of the spectra. One very instant noticeable effect of changing electron density in the model is how little the $\langle Z \rangle$ changes, going from $\langle Z \rangle = 36.53$ at $n_e = 10^{18} \text{ cm}^{-3}$ to $\langle Z \rangle = 36.93$ to $n_e = 10^{22} \text{ cm}^{-3}$, which is a relatively small increase of $\langle Z \rangle$ with an increase of n_e by four orders of magnitude. However, electron density plays a large role in affecting individual ion stages. For example in Figure 2.3, Ne 3G decreases with increasing electron density, while Ne 3A increases with increasing electron density. From this knowledge, a useful

diagnostic for estimating n_e in L-shell Ag plasmas is the ratio of (Ne 3A+ Ne 3B)/(Ne 3F + Ne 3G).

Figure 2.4 demonstrates the effect that fraction of hot electrons have in the model. In this figure, the electron temperature and density were kept constant at $T_e = 1800$ eV and $n_e = 10^{20}$ cm⁻³, respectively. The hot electron temperature was kept constant at $\varepsilon = 30$ keV with 100 eV full width at half maximum (FWHM). Increasing the fraction of hot electrons is similar to increasing T_e , as it increases $\langle Z \rangle$ substantially. Increasing the fraction of hot electrons also increases the spread of the ionization balance. For example, at 15% of hot electrons, the model predicts ionization stages ranging from Li- to Na-like, where at 0% the model predicts a spread ranging from N- to Mg-like.

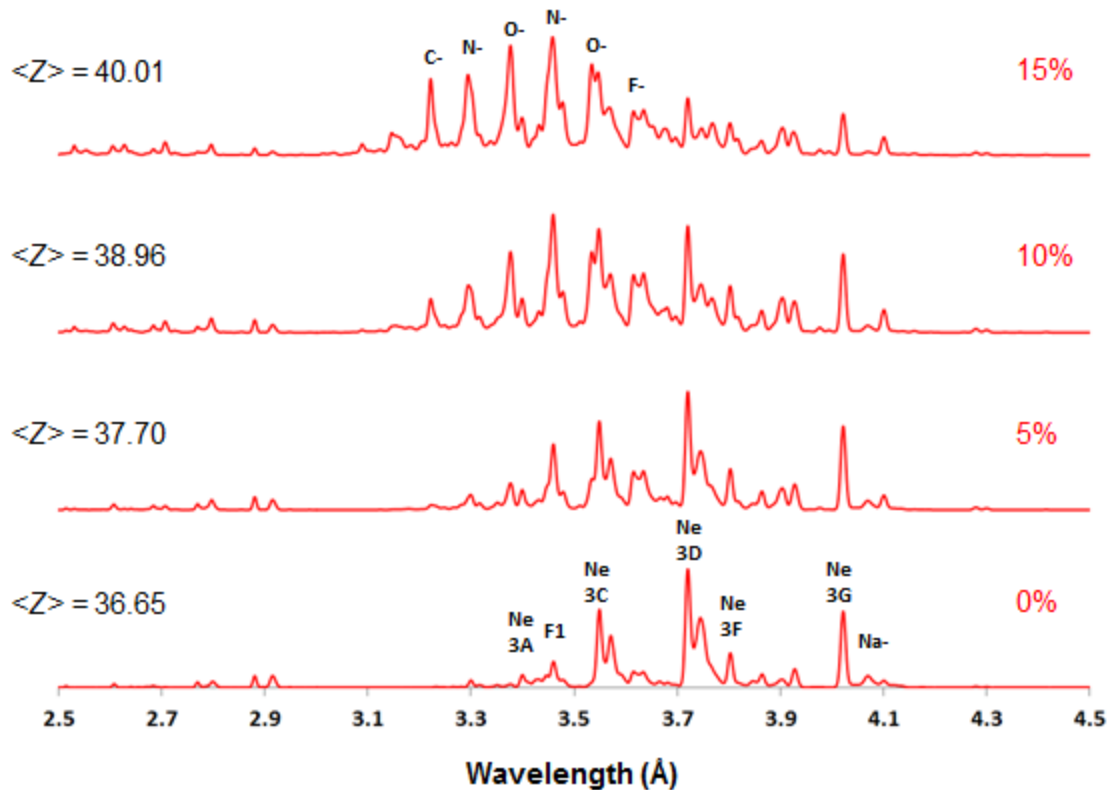


Figure 2.4. Synthetic L-shell Ag spectra demonstrating the effect of fraction of hot electron dependence at 0%, 5%, 10%, and 15%. The electron temperature and density were kept constant at $T_e = 1800$ eV and $n_e = 10^{20}$ cm $^{-3}$, respectively. The hot electron temperature was kept constant at $\varepsilon = 30$ keV with 100 eV FWHM. The average ion charge, $\langle Z \rangle$, is also labeled to the left.

To help better understand the individual ion contributions to the model of L-shell Ag, Figure 2.5 shows the ion contributions of N- through Mg-like for $T_e = 1800$ eV and $n_e = 10^{20}$ cm $^{-3}$. In this figure, each ionization stage was run to normalize the synthetic spectra to 1, to get a better picture of the contribution to each ionization stage. This allows an easy way to understand which individual lines come from what ionization stage, which helps in line identifications.

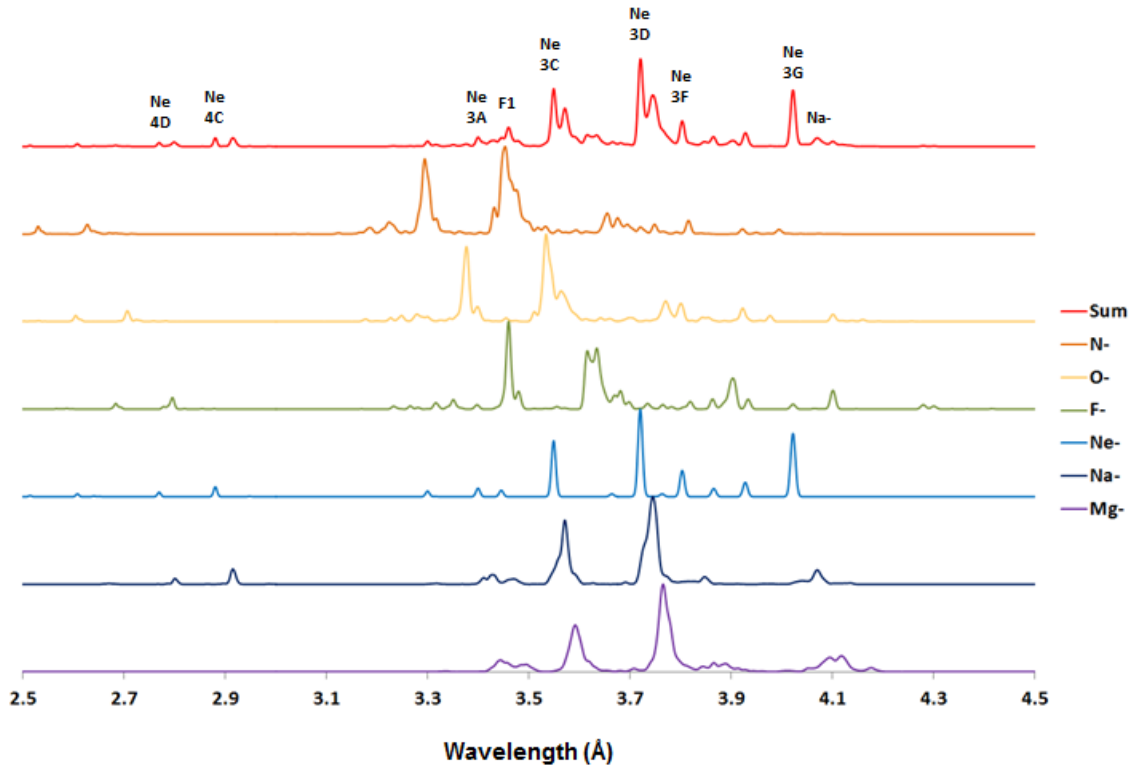


Figure 2.5. Synthetic L-shell Ag spectra demonstrating the contributions of different ionization stages. The electron temperature and density were kept constant at $T_e = 1800$ eV and $n_e = 10^{20} \text{ cm}^{-3}$, respectively, while the fraction of hot electrons was 0%.

2.1.2 Non-LTE Kinetic Models of L-shell Mo, Cu, Zn, and K-shell Al and Mg

Throughout this dissertation many non-LTE kinetic models will be utilized to derive plasma parameters from different materials. These models are similar to the non-LTE kinetic model of L-shell Ag described in Section 2.1.1 and include L-shell Mo (Hansen 2003), Cu, and Zn (Ouart 2010a) and K-shell Al and Mg (Yilmaz 2009). It will be beneficial to briefly detail these models along with some diagnostically important lines that will be useful for electron temperature and density estimations in later chapters.

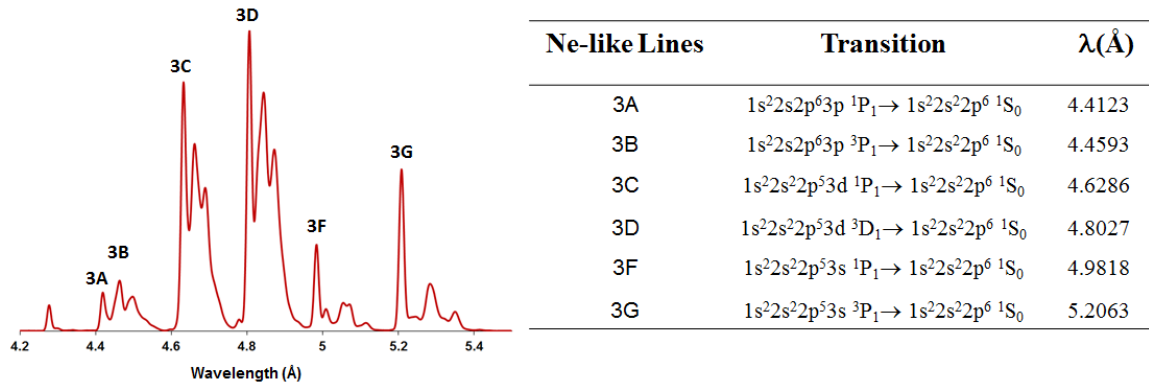


Figure 2.6. Synthetic L-shell Mo spectra (left) with diagnostically important transitions (right). The synthetic spectra has $T_e = 1000$ eV and $n_e = 10^{20} \text{ cm}^{-3}$.

The L-shell Mo non-LTE kinetic model uses the Hebrew University Lawrence Livermore Atomic Code (HULLAC) (Bar-Shalom *et al.* 1988) to calculate energy levels, spontaneous and collisional rates, collisional excitation, collisional ionization, and photoionization cross sections. Extra energy levels and spontaneous rates Ne-, Na-, and Mg-like Mo were calculated by Ulyana Safronova using a relativistic many-body perturbation theory (RMBPT) code. Singly excited states of O-like to Mg-like Mo ions up to $n = 7$ and singly and doubly excited states of Na-like and Mg-like up to $n = 5$ are included. The atomic data is input into SCRAM to generate synthetic spectra. Figure 2.6 illustrates a sample of L-shell Mo synthetic spectra calculated at $T_e = 1000$ eV and $n_e = 10^{20} \text{ cm}^{-3}$ with a list of diagnostically important Ne-like Mo lines. This model is predominately used in Chapter 3. For more information for this model see Hansen 2003.

The L-shell Cu and Zn non-LTE kinetic models use FAC to calculate the set of atomic data. The atomic data include the ground states from the bare to neutral atoms and the details from Al-like down to H-like ions including singly and doubly excited states. The doubly excited states include up to $n = 3$ for He-, Li-, Na-, Mg-, and Al-like

ions, and with $n = 2$ for Be-like ions. The singly excited states are included up to $n = 6$ for H-like ions, $n = 5$ for He- to Li-like ions, Ne- and Na-like ions, and $n = 4$ for Be- to F-like ions, and Mg- and Al-like ions. In Chapter 4, brass wire alloys are utilized, which is comprised of 70% Cu and 30% Zn. In order to correctly model the experimental L-shell Cu and Zn spectra produced from this alloy, the two non-LTE kinetic models are utilized using the same plasma parameters. Once the synthetic spectra are produced, the Cu spectrum is weighted 70% and the Zn spectrum is weighted 30%, after which the spectra is added together. Figure 2.7 gives an example of the end result with synthetic spectra calculated at $T_e = 350$ eV and $n_e = 5 \times 10^{19} \text{ cm}^{-3}$, along with diagnostically important lines. For more information for these models see Quart 2010a.

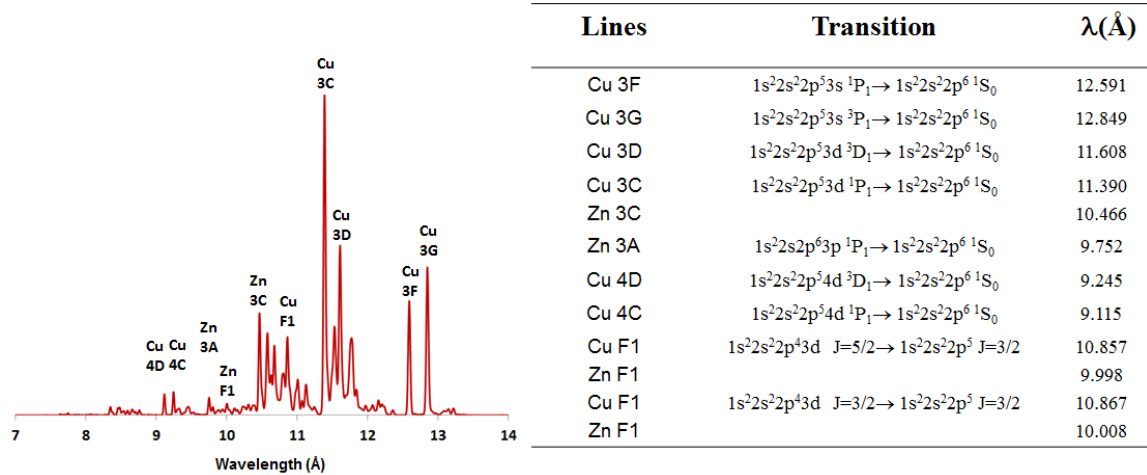


Figure 2.7. Synthetic L-shell Cu and Zn spectra (left) with diagnostically important transitions (right). The synthetic spectra has $T_e = 350$ eV and $n_e = 5 \times 10^{19} \text{ cm}^{-3}$. The synthetic spectra is weighted 70% Cu and 30% Zn, the same as the brass alloy.

The K-shell Al and Mg non-LTE kinetic models use FAC to calculate the set of atomic data. The atomic data include singly excited states of H-like up to $n = 6$, He-like up to $n = 5$, Li like up to $n = 4$ were included. Al wires have recently been used as tracer wires to provide additional information for x-ray diagnostics (Safronova *et al.* 2008a), and specifically Al 5056 alloy (95% Al, 5% Mg) wires have been used due to the K-shell Mg lines being much less influenced by opacity because of their relatively low concentration and therefore are helpful in diagnosis of optically thick K-shell plasmas. Figure 2.8 demonstrates a sample of K-shell Al and Mg synthetic spectra calculated at $T_e = 1000$ eV and $n_e = 10^{20}$ cm $^{-3}$, with Al weighted at 95% and Mg weighted at 5%, along with diagnostically important lines. For more information of these models see Yilmaz 2009.

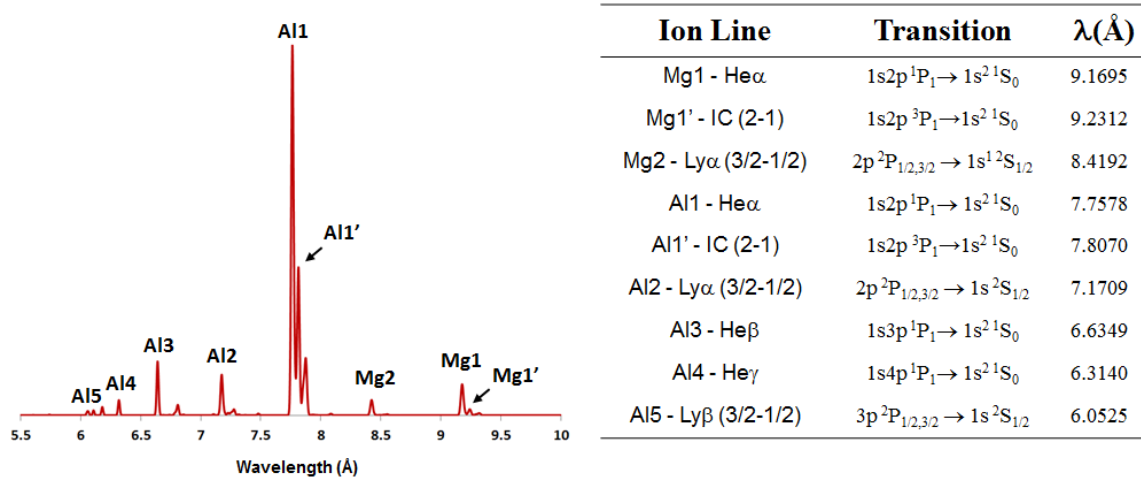


Figure 2.8. Synthetic K-shell Al and Mg spectra (left) with diagnostically important transitions (right). The synthetic spectra has $T_e = 350$ eV and $n_e = 10^{20}$ cm $^{-3}$. The synthetic spectra is weighted 95% Al and 5% Zn, the same as the Al 5056 alloy.

2.1.3 Non-LTE Kinetic Model using Prism Atomic Data ATBASE and SPECT3D

Prism Computational Sciences, Inc. has developed a new atomic data code named ATBASE. ATBASE has many applications, but most importantly for this dissertation has applications in studying non-LTE generated plasmas by generating a set of atomic data for all low- to mid-z elements, which include atomic data for all ionization stages. This atomic data includes: atomic energy levels and oscillator strengths, photoionization cross-sections, electron collisional excitation and ionization cross-sections, autoionization rates, and dielectronic recombination rate coefficients. ATBASE also generates equation of state and multigroup opacity data that goes into the PRISM OPACITY and Equation Of State (PROPCEOS) code. ATBASE makes it very easy to pick and choose different ionization stages to study, and from there pick and choose different energy levels.

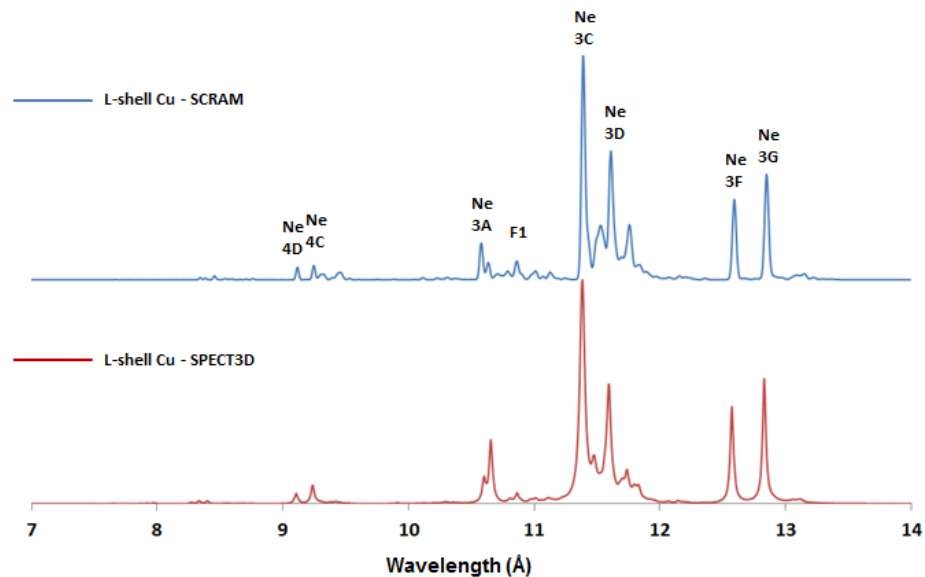


Figure 2.9. A comparison of L-shell Cu between two models: the blue is FAC run through SCRAM and the red is ATBASE run through SPECT3D. The calculations were run at $T_e = 300$ eV and $n_e = 5 \times 10^{19} \text{ cm}^{-3}$.

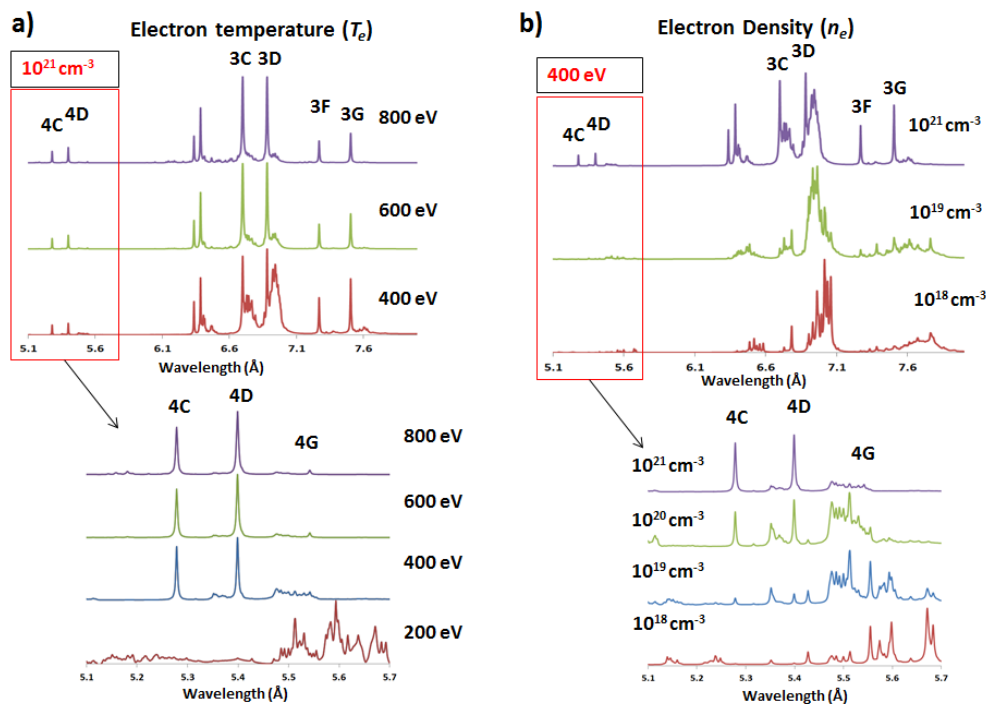


Figure 2.10. Synthetic L-shell Kr spectra calculated through SPECT3D utilizing the atomic code ATBASE. a) L-shell Kr as a function of electron temperature with electron density constant at 10^{21} cm^{-3} . b) L-shell Kr as a function of electron density with electron temperature constant at 400 eV.

To help in creating synthetic spectra based off of the ATBASE atomic code, SPECT3D (MacFarlane *et al.* 2007) is used. In SPECT3D, plasma conditions can be set, such as electron temperature and plasma density, then as an input the atomic code one wishes to run is set, along with the spectral range one wishes to view. The results are synthetic spectra similar to what SCRAM produces. There are two major advantages to using these codes: first, it offers the ability to compare results from other atomic codes, such as FAC run through SCRAM as discussed in the previous section. For example, Figure 2.9 gives a comparison of L-shell Cu (Ouart 2010a) from SCRAM and SPECT3D,

secondly, it's very user friendly to set up and choose what atomic data one wishes to calculate, such as, M-shell Cu (see Chapter 5) or L-shell Kr (see Figure 2.10).

SPECT3D can also be used as a post-processing tool for other PRISM codes, such as HELIOS-CR (discussed in Section 2.2), where it can be used to calculate spectra and ionization distributions for various geometries, including 1D, 2D, and 3D Cartesian, and includes many useful graphical interfaces, such as 2D grids for T_e and n_e .

2.2 HELIOS-CR Radiation-Hydrodynamics Code

The Prism code HELIOS is a 1-D radiation-hydrodynamics code that can be used to simulate dynamics of laser produced plasmas, z-pinches, radiatively-heated plasmas, and shock propagation in materials. Because HELIOS is a 1-D model, it's very limited in its applications, however when upgraded to HELIOS-CR (MacFarlane *et al.* 2006), it includes the option to simulate non-LTE plasmas using an inline collisional-radiative (CR) model and utilizes ATBASE to calculate atomic level and transition energies, photoionization cross-sections, oscillator strengths, and dielectronic recombination, autoionization, and electron capture rates. The simulations can be calculated using planar, cylindrical, and spherical geometries.

Using HELIOS-CR, it's possible to set up a z-pinch simulation of a single wire using the cylindrical geometry and setting up a discharge current with the appropriate conditions, such as 1.0 MA maximum with a 100 ns rise time. Single wire z-pinch experiments of Ag have recently been accomplished and they were shown to have similar radiative properties of L-shell Ag as Ag planar wire arrays (discussed in Chapter 6), as Figure 2.11 indicates, so it will be beneficial to look into some of the results from single wire Ag simulations.

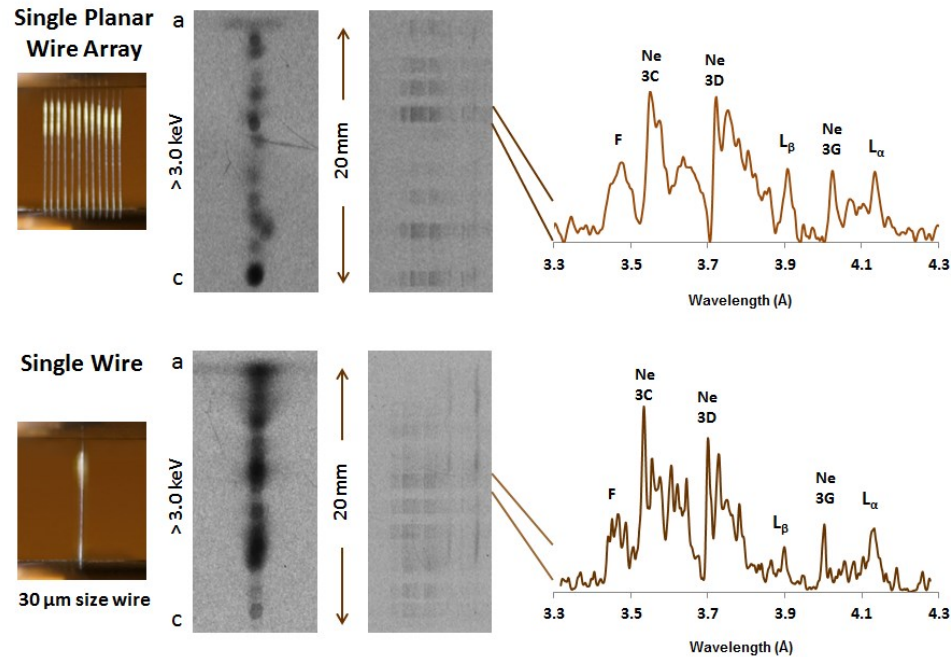


Figure 2.11. A comparison of L-shell Ag radiation from a Single Planar Wire Array (top) and a Single Wire (bottom).

Before each simulation, HELIOS-CR offers a series of input options. The Geometry input option is first and the cylindrical geometry was used for these simulations. The next series of inputs is the Spatial Grid tab. Here the region thickness can be changed and in these series of simulations the thickness was changed from 5 μm to 50 μm in diameter. The next important input is in the Magnetic tab. Here magnetohydrodynamics (MHD) effects can be included and there is an option to “supply discharge current”. With this option a current discharge can be manually set up. A basic current setup is to go from 0.0 MA to 1.0 MA in 100 ns of time with a sinusoidal dependence. The next several figures show the results of these simulations of Ag single wires.

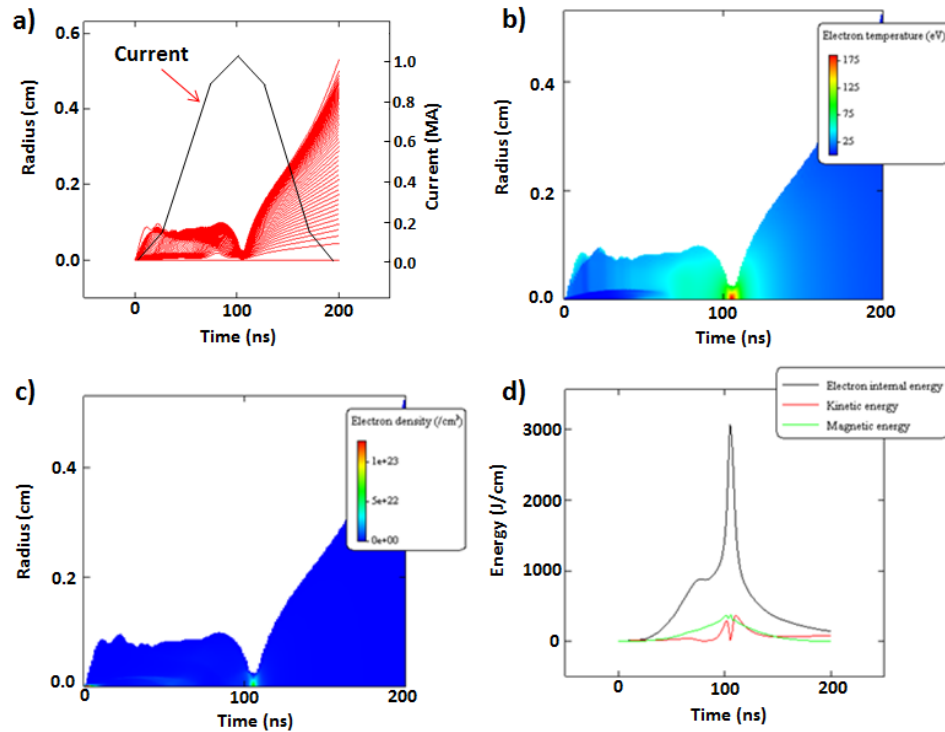


Figure 2.12. Results from HELIOS-CR for a 30 μm Ag single wire at 1.0 MA. a) Current pulse shape and zone radius as function of time, b) the electron temperature as a function of time and radius, c) electron density as a function of time and radius, and d) electron internal energy, kinetic energy, and magnetic energy as a function of time.

Figure 2.12 demonstrates the first results from HELIOS-CR for a 30 μm Ag single wire at 1.0 MA with 100 ns rise time. Figure 2.12(a) depicts the current pulse shape along with the zone radius as a function of time. In the simulation, fifty individual zones were chosen. Fifty zones were chosen to be an optimal number, as too little zones the resolution of the implosion is lost, and too many zones the simulation becomes too computationally expensive. Going back to the results, the 30 μm Ag wire is shown to expand to 0.1 cm within several ns of time with a single implosion just after 100 ns, after which the material expands as current drops. In Figure 2.12(b), the electron temperature plot shows just over 180 eV, which initially appears to be too low of an estimate, as

experiments for single wire implosions give L-shell Ag up to $T_e = 1800$ eV. A possible explanation for this low estimation of T_e will be shown in Figure 2.13. Where T_e appears to be underestimated, Figure 2.12(c) gives electron density dependence with an estimate $> 10^{22}$ cm⁻³ at stagnation, which may be an overestimation, however at all other times $n_e < 10^{21}$ cm⁻³, which is more realistic and gives assuredness in the simulation. Figure 2.12(d) gives energy dependencies of electron internal energy, kinetic energy, and magnetic energy in J/cm. Interestingly the electron internal energy shows a possible radiation pre-pulse at roughly 80 ns in time.

To understand more of the electron temperature question, Figure 2.13 shows results of the same simulations with different initial wire thickness, specifically 50 μ m, 20 μ m, 10 μ m, and 5 μ m. The results show that with decreasing wire thickness the maximum electron temperature increases. Figure 2.13(a) suggests that at 50 μ m thickness, the wire is too thick and there is no “pinch”, just a wire expansion to approximately 0.1 cm, with a maximum $T_e > 50$ eV. Figure 2.13(b) shows that at 20 μ m there are multiple “pinches”, a slightly smaller wire expansion to 0.07 cm, and a maximum $T_e > 250$ eV, higher than for the 30 μ m wire. Figure 2.13(c) gives a maximum $T_e > 600$ eV with a 10 μ m diameter, and finally Figure 2.13(d) gives a maximum $T_e > 1800$ eV with a 5 μ m diameter. An explanation to this behavior in the code is that with smaller diameter thicknesses, the results more and more approach “bright” or “hot” spot conditions seen in z-pinch plasmas, and as shown in the previous sections, L-shell Ag only radiates at > 1800 eV electron temperatures in these “bright” spot formations.

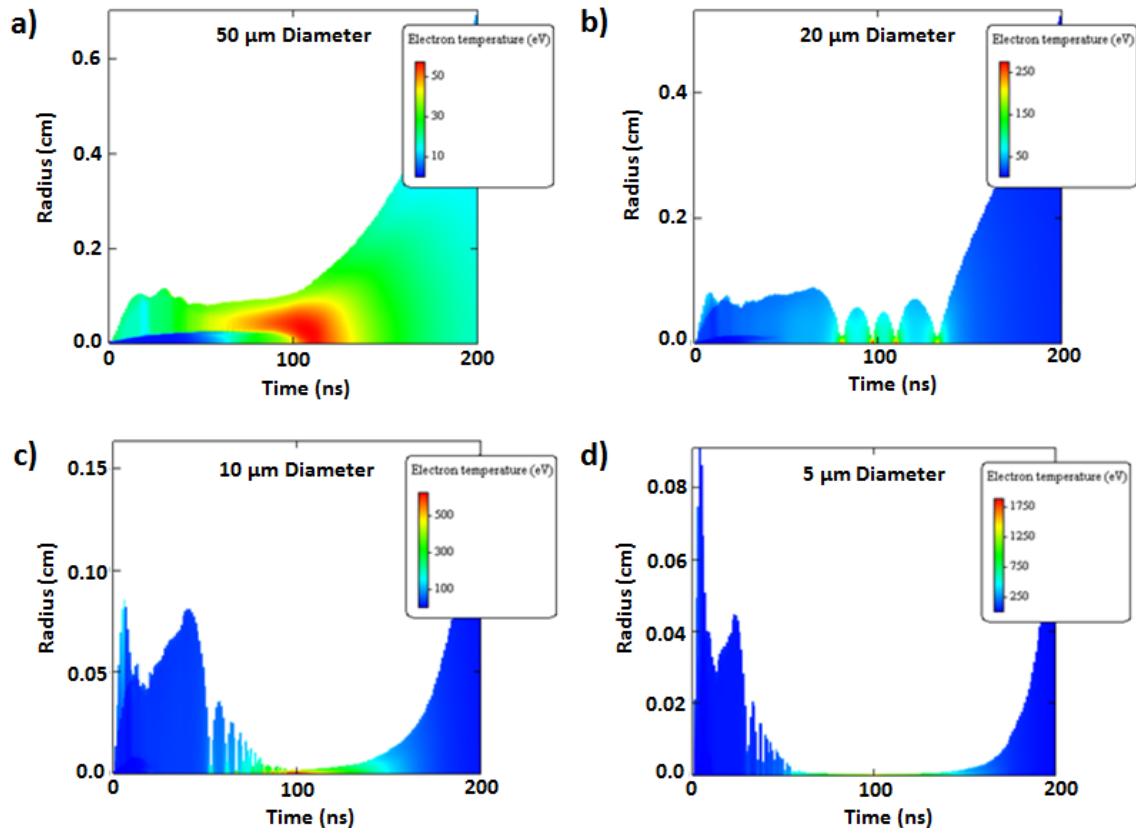


Figure 2.13. Results from HELIOS-CR for a) 50 μm , b) 20 μm , c) 10 μm , and d) 5 μm Ag single wire at 1.0 MA. For each simulation, the electron temperature is given as dependent on time and radius.

2.3 Wire Ablation Dynamics Model

For z-pinch experiments of wire arrays, it's important to have a theoretical understanding of how well certain wire array types perform compared to others, how the implosion dynamics of the wire array work, at what point in time the wire array implodes, and at what energies, velocities, densities, and other plasma properties in which the wire array can be expected to have. Having such information is critical in not only choosing the best load types to perform experiments on, but also to understand, for instance, how thick the wires need to be, how many wires to include, and to understand

where to “position” the time-gated diagnostics to attain as much information as possible. For these reasons, the Wire Ablation Dynamics Model (WADM) (Esaulov *et al.* 2009) was created, which is an ablation modified version of the Wire Dynamics Model (WDM) (Esaulov *et al.* 2006).

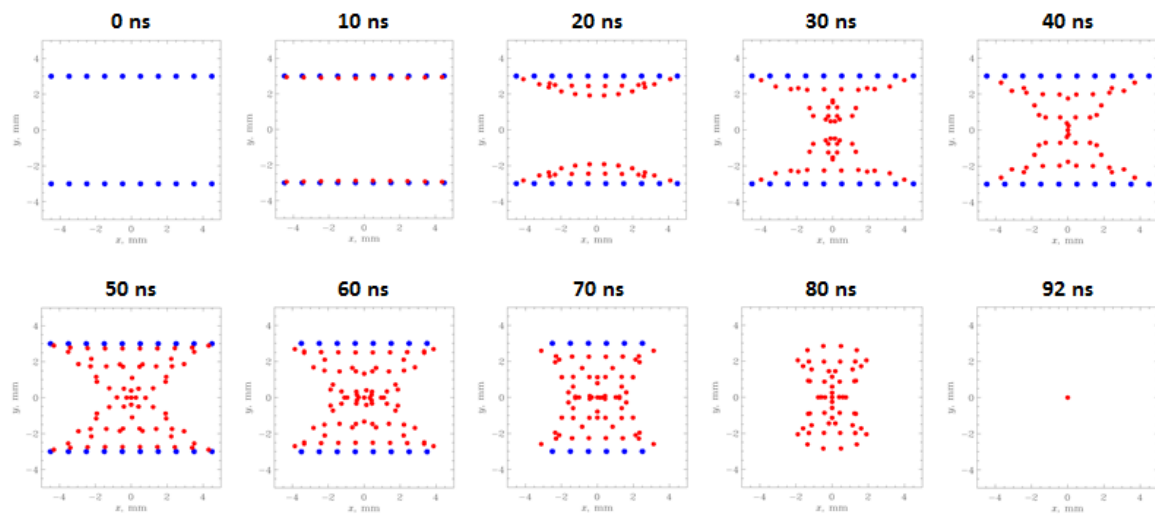


Figure 2.14. Example of a WADM simulation of an Al DPWA. The parameters were 10 wires in each plane, 6.0 mm interplanar gap, 1.0 interwire gap, and 12.5 μm diameter wires.

The WADM is used throughout this dissertation. The model works by inputting the desired parameters, which include the intrinsic properties of the pulsed power generator (such as the Zebra generator in Section 2.4), and exact wire array specifications. The wire array specifications include the wire array type (cylindrical, single planar, double planar, etc.), wire array spacing (interplanar gap, interwire gap, etc.), total wire mass, and ablation rate coefficient. The ablation rate coefficient is dependent on the properties of the wire material (Esaulov *et al.* 2009). Some wire materials have faster ablation rates (Al), while others have slower ablation rates (Mo and Ag). Once the proper

specifications are met, the WADM self-consistently calculates the inductive current distribution between the wires and the magnetic field contribution for each wire for each time step (every ns, generally up to 150 ns for Zebra simulations). The wires are then split apart into individual current filaments at rates proportional to the ablation coefficient. From this, the WADM simulates ablated coronal plasma with kinetic energy and acceleration for each filament depending on the net magnetic field, which contributes to the evolution of the simulated plasma. Figure 2.14 depicts an example of a WADM simulation of an Al DPWA. In this example there were ten 12.5 μm diameter wires in each plane for a total of twenty wires, a 6.0 mm interplanar gap, and a 1.0 mm interwire gap. The predicted implosion time is 92 ns.

The WADM is also capable of simulating mixed wire load types. Outside of providing implosion times, the WADM provides information on change in thermalization energy, energy in precursor region, kinetic energy, energy per length, and contour information for mass density, current density, and plasma velocities for each time step.

2.4 The Zebra Generator

The Zebra generator is a pulsed power machine located at the Nevada Terawatt Facility (NTF) (Bauer *et al.* 1997, and see Kantsyrev *et al.* 2009 for experimental setup), which is a branch of the Physics Department at the University of Nevada, Reno. The Zebra generator is capable of delivering up to 1.0 MA of current in 100 ns of time (or alternatively, 0.6 MA in 200 ns), or up to 1.5 TW of power. This is accomplished by charging thirty two 1.3 μF Marx capacitors in parallel up to 85 kV with a stored energy of 150 kJ. For clarification of the layout of the Zebra generator, see Figure 2.15. The vast

majority of the experimental results in this dissertation were produced on the Zebra generator.

Figure 2.16 shows the diagnostic layout for a general Zebra experiment. Individual diagnostics can change from campaign to campaign depending on the need for the experiments.

For a more detailed look into the various diagnostics that are fielded on the Zebra generator, see (Osborne 2012 and Williamson 2011). Recently, the Zebra generator was upgraded to achieve currents up to 1.7 MA with the use of the Load Current Multiplier (LCM) (Chuvatin *et al.* 2010). Figure 2.17 shows how the LCM is implemented in the Zebra chamber. Increasing the current gives excellent opportunity to compare experimental results from two different current regimes (~ 1.0 MA and ~ 1.7), which provides much needed current scaling. A few side effects of the LCM is that the anode to cathode gap is lowered from 2.0 cm to 1.0 cm, and also, due to the added eight return current posts, a few diagnostic ports are blocked from line of site to the plasma.

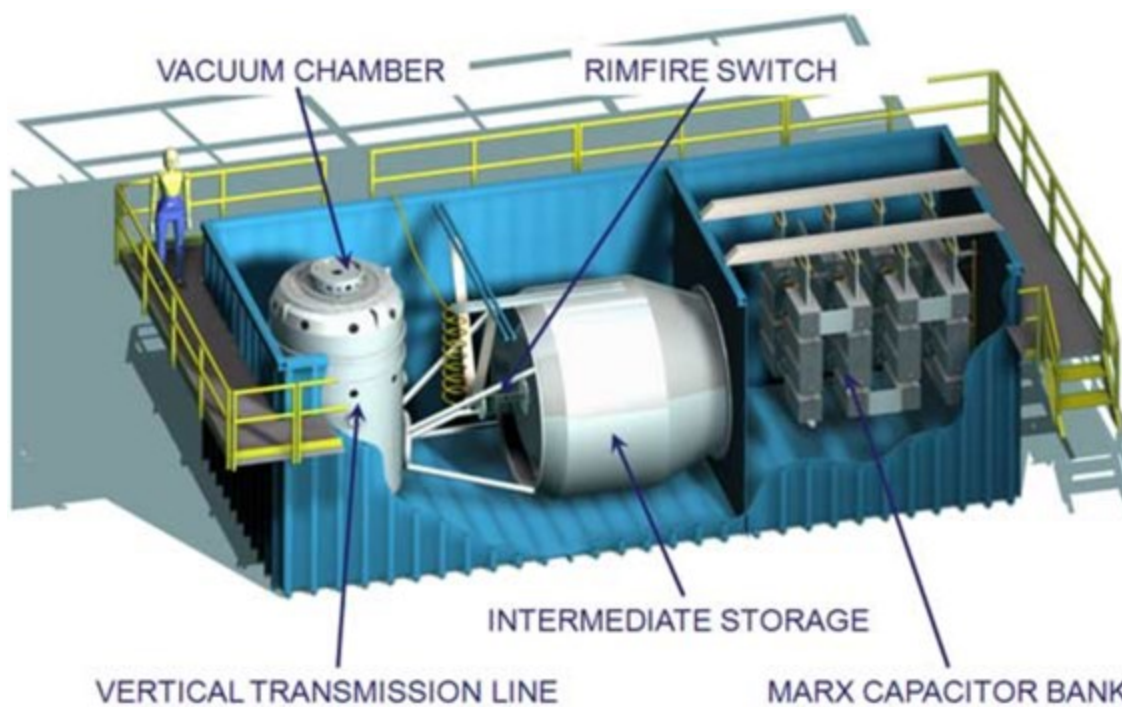


Figure 2.15. The Zebra generator schematic, courtesy of University of Nevada, Reno (<http://www.unr.edu/ntf/facility/zebra>).

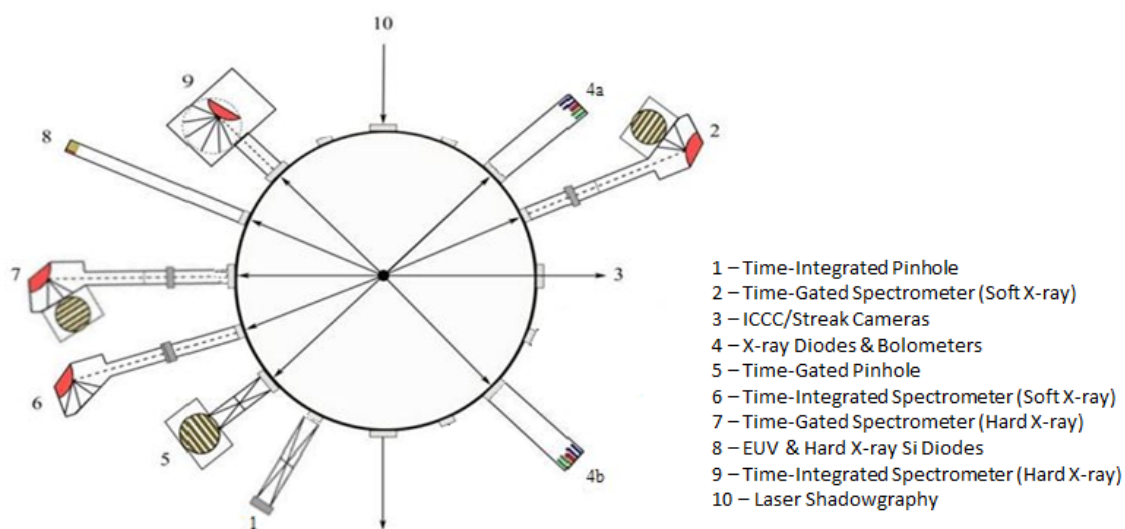


Figure 2.16. The Zebra generator diagnostic layout for a general experiment.

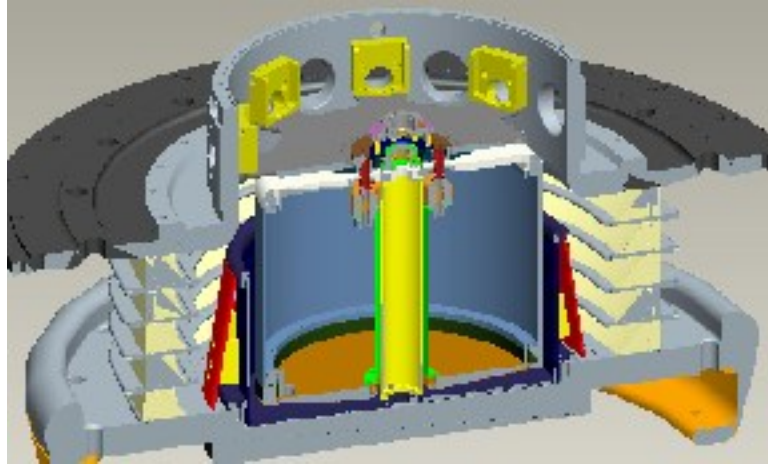


Figure 2.17. The schematic of the Load Current Multiplier on the Zebra generator.

The next two sections will cover two specific diagnostic systems that are pertinent to this dissertation: the Zebra shadowgraphy and optical system and a description of a new time-gated hard x-ray spectrometer fielded on Zebra.

2.4.1 The Zebra Optical System

As part of the experimental side of the research, approximately two Zebra campaigns were accomplished every year. Each individual for each campaign is generally responsible for a set number of tasks for each experiment, including setting up the suite of diagnostics beforehand. One very complicated set of diagnostics, which I became responsible for during experiments, is the Zebra optical system, which includes a laser shadowgraphy setup and an intensified charge-coupled device (ICCD) camera.

The shadowgraphy system works by firing a second harmonic 150 ps pulse from a Nd:YAG laser named EKSPLA ($\lambda = 532 \text{ nm}$) during the z-pinch experiment. The laser refracts from density gradients in the plasma up to a critical electron density (for 532 nm, the critical electron density is $3.9 \times 10^{21} \text{ cm}^{-3}$), in which the refraction becomes too intense and the light is no longer able to be collected by the CCD cameras, or essentially

the light penetrates up to the critical density creating a “shadow”. It’s advantageous to have a temporal understanding of the wire ablation process, and to achieve this goal the laser is polarized and then split into two paths, one called Channel 1 (Ch1) and the other Channel 2 (Ch2), separated by 22.5° . To see orientations and to have a better understanding of where the laser is polarized and split, see Figure 2.18. Ch1 and Ch2 have an intrinsic ~ 3 ns between them, while the delay adds an extra ~ 6 ns, giving four frames of knowledge of the plasma separated by 3 ns each. It’s important to note the LCM configuration has return current posts that usually block Ch2, so only Ch1 is available for LCM configuration experiments. Also, for safety purposes, due to the wavelength and brightness of the laser, proper laser safety goggles are required during any usage of the EKSPLA laser.

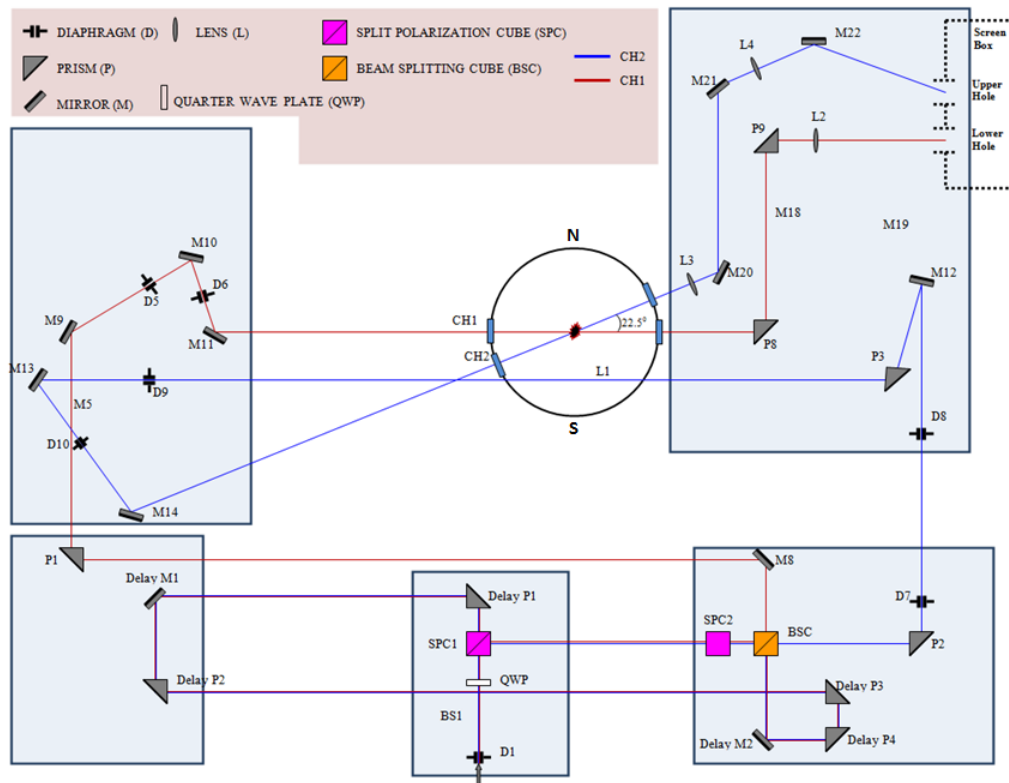


Figure 2.18. Optics schematic for the shadowgraphy system on the Zebra generator.

The other separate optical path on the Zebra generator heads north out of the chamber and eventually to the ICCD camera, as illustrated in Figure 2.19. The ICCD camera has two main components; a focusing system and an MCP used to intensify and capture the image. The settings of the ICCD camera are usually set to 3 ns duration with an MCP gain of 70, though these settings can be changed if desired. Figure 2.20 shows examples of both a shadowgraphy image and an ICCD image.

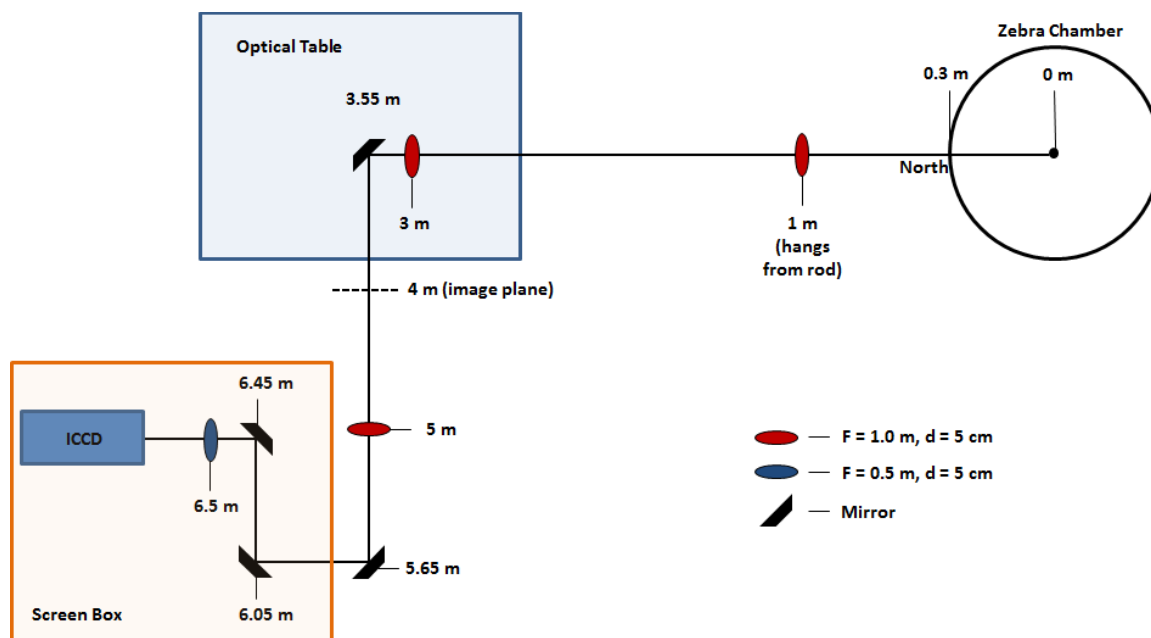


Figure 2.19. Optics schematic for the ICCD system on the Zebra generator.

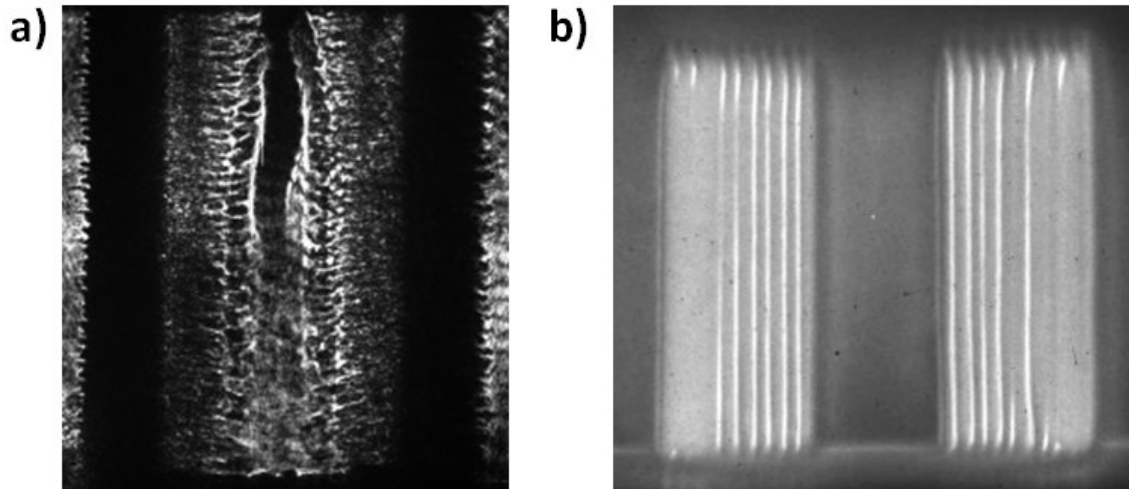


Figure 2.20. a) Example of a shadowgraphy image. b) Example of an ICCD image.

2.4.2 New Time-Gated Hard X-Ray Spectrometer on Zebra

Over the years there has grown an increasing demand to understand how L-shell and K-shell plasmas radiate in time, such as L-shell Mo and Ag and K-shell Mo and Cu. Not only this, but for such a mid-Z element as Cu, where a z-pinch experiment can ionize easily into both L- and K-shell, it has become important to understand how both simultaneously radiate in time. One way to understand these plasmas is through spectroscopy, which utilizes Bragg's Law to diffract x-ray spectra:

$$2d \sin \theta = m\lambda \quad 2.10$$

where d is the atomic spacing in the crystal lattice, θ is the angle of incidence, m is the order of diffraction, and λ is the diffracted wavelength. In this dissertation, convex crystals, such as potassium hydrogen phthalate (KAP, $2d = 26.634 \text{ \AA}$), α -quartz ($2d =$

6.687), and LiF ($2d = 4.028$), are used in both time-integrated and time-gated spectrometers. Because of the direct relationship, the lower the crystal $2d$ spacing, the lower the wavelength range, Λ , one can attain. Λ is defined as:

$$\Lambda = \frac{2(\lambda_{max} - \lambda_{min})}{(\lambda_{max} + \lambda_{min})} \quad 2.11$$

See Figure 2.21 for clarity. The spectral resolution, R , is defined by:

$$R = \frac{\lambda}{\Delta\lambda} \quad 2.12$$

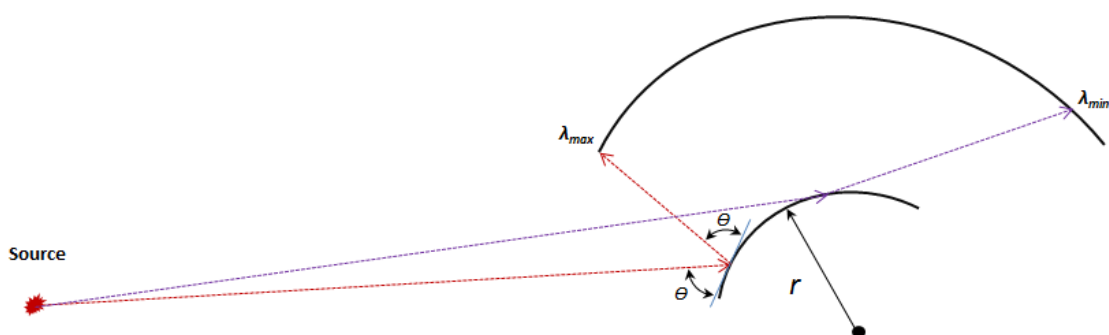


Figure 2.21. Diagram of a convex crystal spectrometer, with λ_{max} and λ_{min} shown along with the angle of incidence, Θ , and the radius of curvature of the crystal, r .

R is essentially a ratio of λ to the minimum difference between simultaneously resolved features and is generally a result of source size and imperfections in the diffraction crystal.

In previous years, two main spectrometers have been fitted simultaneously for experiments on the Zebra generator, one a time-integrated spatially resolved (TISP) spectrometer and the other a time-gated spatially integrated spectrometer (TGSP). Both traditionally use a KAP crystal. The TISP spectrometer utilizes a horizontal slit (0.5 mm) to attain spatial resolution along the length of the pinch (from anode to cathode, though the slit can be moved to a vertical position to have radial resolution) and has a wavelength range of approximately 1 – 15 Å (when using the KAP crystal), however lacks time-resolution. Bio-max MS Kodak x-ray film is used and is put alongside the inner wall of the spectrometer which allows for such a wide spectral range to be measured. The TGSP is very similar to the TISP, except for a few differences: it has a microchannel plate (MCP) attached to the main body of the spectrometer, allowing for time-resolved images. Briefly, an MCP has six gold strips and a pulsed bias to obtain time-resolved images, with each gold strip acting as a photocathode, where incident photons are converted to electrons via the photoelectric effect and are accelerated through plate capillaries. This causes a cascading emission of secondary electrons that impact a phosphor screen, which in turn is exposed to visible wavelength film. The timings of the gates on the MCP are spaced depending on the cable length differences, generally 5 ns, and each gate is gated to last between 1 – 6 ns, generally 3 ns. The TGSP also doesn't have a slit to add for spatial resolution, partially due to the limited exposure time on the film, so a slit is not put in place in order to capture as many photons as possible. Lastly,

due to the small size of the MCP (< 2 inches) the Λ is reduced from that of the TISP, from $1 - 15 \text{ \AA}$ to $6.5 - 10 \text{ \AA}$ (using KAP crystal). This reduced Λ is out of range of many important transitions, including L-shell Mo ($4 - 5.5 \text{ \AA}$) and L-shell Ag ($3 - 4.5 \text{ \AA}$). The Λ can be adjusted on the TGSP by a few ways. For one, the crystal can either be changed to a new crystal, or the crystal angle can be adjusted inside the spectrometer (see Figure 2.21). Secondly, the wedge, which attaches to the body of the spectrometer and where the MCP mounts, can be replaced with a different wedge angle which allows for a different Λ . Each process takes time and requires the spectrometer to be open, which is problematic because the MCP requires high vacuum ($\sim 10^5$ Torr) at all times to function properly. Each time the MCP is exposed to air it needs to be pumped at high vacuum for 24 hours to remove atmospheric particles. The other solution, of course, is to have a second TGSP capable of attaining the proper Λ one needs. This was the motivation for building and piecing together a new TGSP, with the goal of attaining time-resolved images of “harder” x-rays. This would also allow for simultaneous measurements of two different Λ regimes.

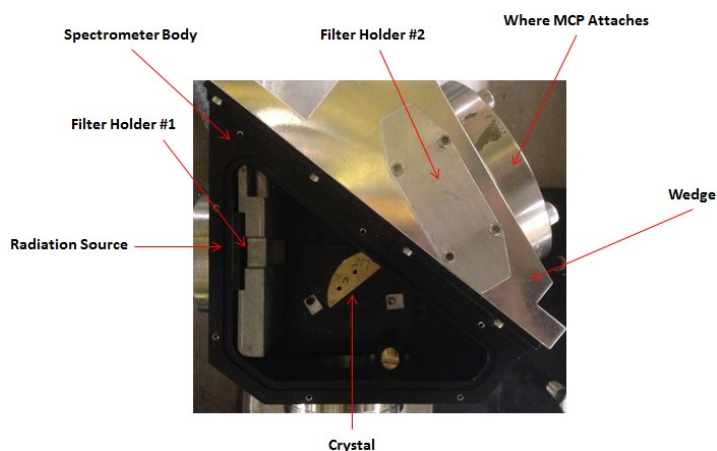


Figure 2.22. Picture of a time-gated spectrometer body along with attached wedge.

Figure 2.22 shows the body of the new time-gated hard x-ray (TGHXR) spectrometer, along with a wedge where the MCP attaches, the crystal, and where filters are placed. There are two locations where filters, used to block unwanted light, are located, one in front of the crystal and the second in front of the MCP. Table 2.2 lists different Λ as a function of crystal, crystal angle, and wedge angle. The wedge angles 76° and 32° are actually the same wedge just rotated 180° to create two different angles. The wedge angle 45° is a brand new wedge specially designed to capture the Λ of $1.1 - 1.85 \text{ \AA}$. This new TGHXR spectrometer has recently been used to measure L-shell Ag lines (see Chapter 6) using the α -quartz crystal (crystal angle = 35° , wedge angle = 76°) and K-shell Cu ($\text{He}\alpha \sim 1.5 \text{ \AA}$) and Mo ($\text{He}\alpha \sim 0.7 \text{ \AA}$) using LiF crystal (crystal angle = 15° , wedge angle = 32°).

Crystal (Crystal Angle)	Wedge 76°	Wedge 45°	Wedge 32°
α -quartz (35°)	3.8 - 4.4 \AA	-	-
α -quartz (25°)	-	2.0 - 3.1 \AA	-
α -quartz (15°)	-	-	1.2 - 2.3 \AA
LiF (30°)	2.1 - 2.7 \AA	-	-
LiF (20°)	-	1.1 - 1.85 \AA	-
LiF (15°)	-	-	0.7 - 1.5 \AA
KAP (35°)	14 - 18 \AA	-	-
KAP (20°)	-	8.0 - 12.5 \AA	-
KAP (15°)	-	-	6.5 - 10 \AA

Table 2.2. Wavelength ranges for the time-gated hard x-ray spectrometer as a function of crystal, crystal angle, and wedge angle.

2.5 The Cobra Generator

A few experiments in this dissertation were accomplished on the Cobra generator, which is a generator similar to the Zebra generator and is located at Cornell University. Cobra utilizes thirty two $1.3 \mu\text{F}$ Marx capacitors that charge up to 70 kV with a stored energy of 100 kJ and delivers up to 1.0 MA of current. A main difference from the Zebra generator is that the Marx capacitor bank is stored from two banks that travel through four laser-triggered transmission lines (see Figure 2.23) which allow for current rise times from 85 – 250 ns (Greenly *et al.* 2008). Another difference is that Cobra is sensitive to load inductance and was designed primarily for low-inductance cylindrical wire arrays (see Chapter 4) and x-pinch. Figure 2.24 shows the schematic of the diagnostics used on Cobra.

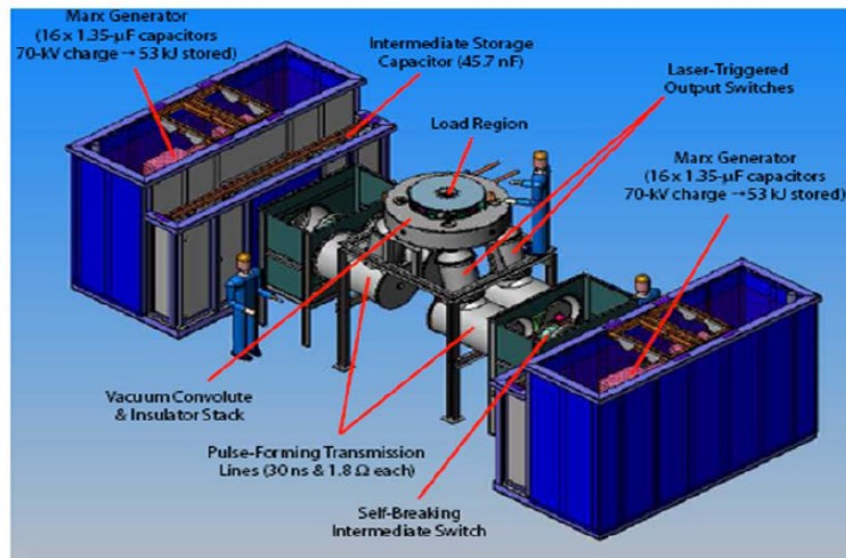


Figure 2.23. Schematic of the Cobra generator (Greenly *et al.* 2008).

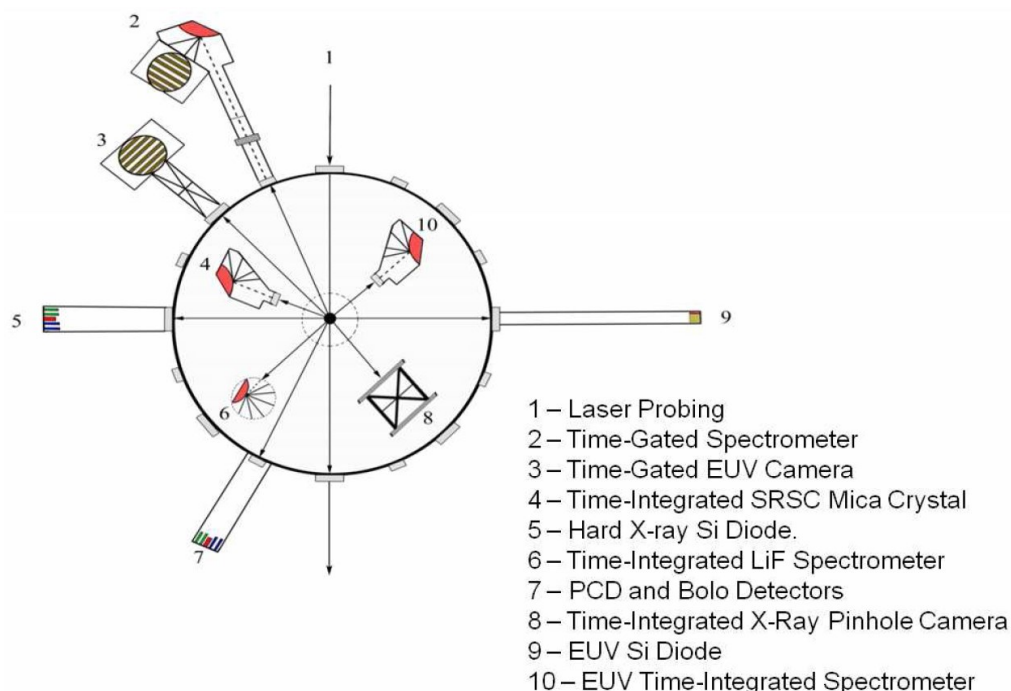


Figure 2.24. Schematic of the diagnostics used on the Cobra generator.

2.6 The Compact Laser Plasma Facility “Sparky” at UNR

In order to test and calibrate diagnostics the compact laser plasma facility “Sparky” was developed at the University of Nevada, Reno (Kantsyrev *et al.* 2008a). The facility was also partially developed to study extreme ultraviolet radiation from different materials (which is a focus of Chapter 5). The facility utilizes a neodymium-doped yttrium aluminum garnet (Nd:YAG) solid state laser ($\lambda = 1.06 \mu\text{m}$, 0.4 J, 3 ns, 10 Hz) that focuses and strikes solid flat targets multiple times (see Figure 2.25). To avoid cratering of the target, the target is manually moved via a control scheme. An EUV grazing spectrometer (Shevelko *et al.* 1998) is used to collect EUV radiation to study and calibrate complicated EUV lines (capable between 40 – 300 Å), such as M-shell Cu and Mo.

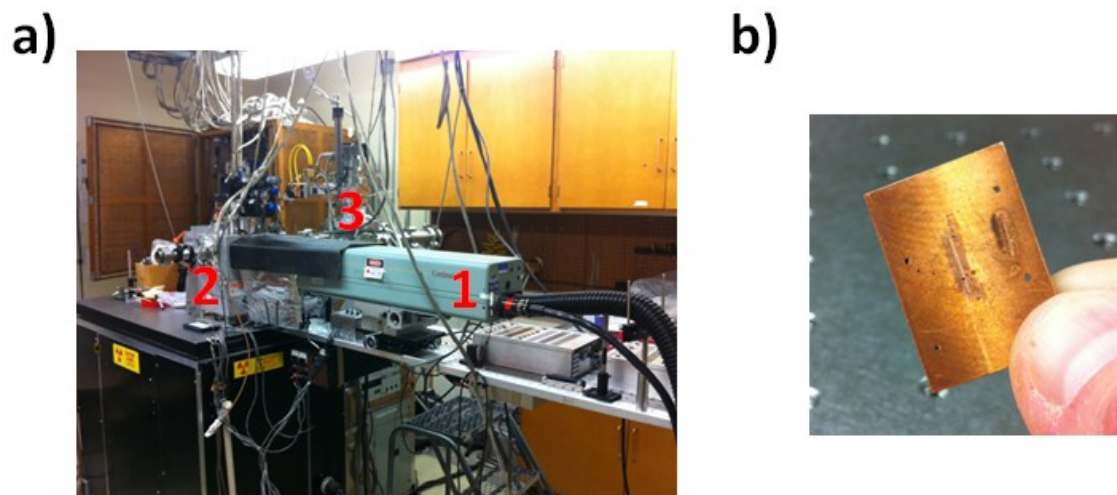


Figure 2.25. a) The “Sparky” facility. “1” is the laser location, “2” is the vacuum chamber where the flat target is located, and “3” is where an EUV grazing spectrometer is located. b) An example of a flat target used.

2.7 Sustained Spheromak Physics Experiment

The Sustained Spheromak Physics Experiment (SSPX) at the Lawrence Livermore National Laboratory (LLNL) was a facility to explore innovative confinement concepts to explore energy confinement and current drive in spheromaks (Wood *et al.* 2005a). The term spheromak refers to an arrangement of plasma formed into a toroidal shape. SSPX plasma currents achieved up to 1 MA, creating around 4 ms of plasma, with electron densities around 10^{14} cm^{-3} and electron temperatures exceeding 500 eV (Hudson *et al.* 2008). Figure 2.26 shows the schematic of the SSPX. For this dissertation (Chapter 5), the interest stems from impurities, such as O or Cu from the inner chamber, which could dilute the plasma. For the purpose of studying these impurities, the Silver Flat Field Spectrometer (SFFS) (Clementson *et al.* 2008) was developed (Figure 2.27). The spectral range is 25 – 400 Å with a 200 Å bandwidth and resolution up to 0.3 Å FWHM.

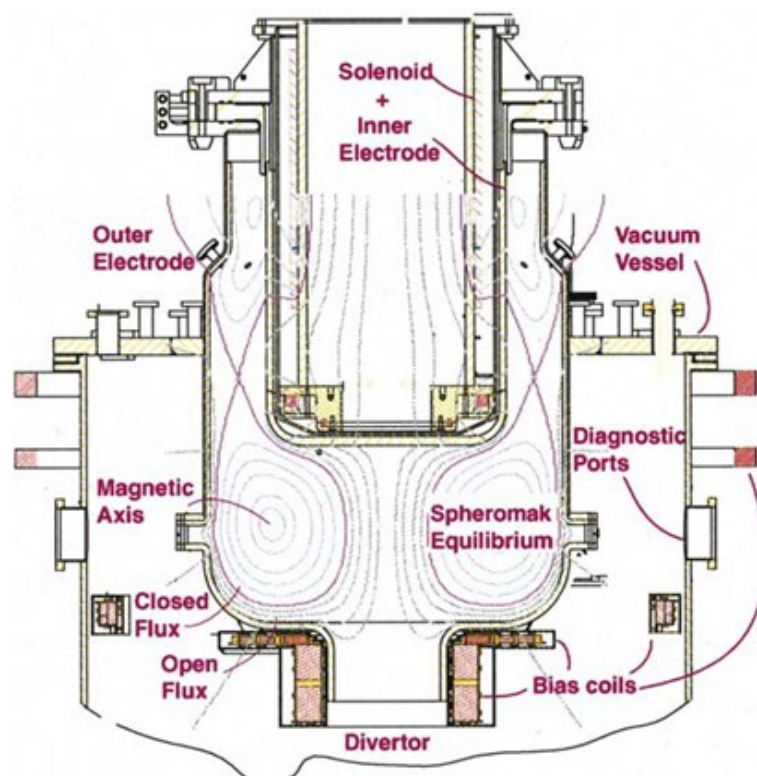


Figure 2.26. Schematic of the Sustained Spheromak Physics Experiment (from Wood *et al.* 2005a).

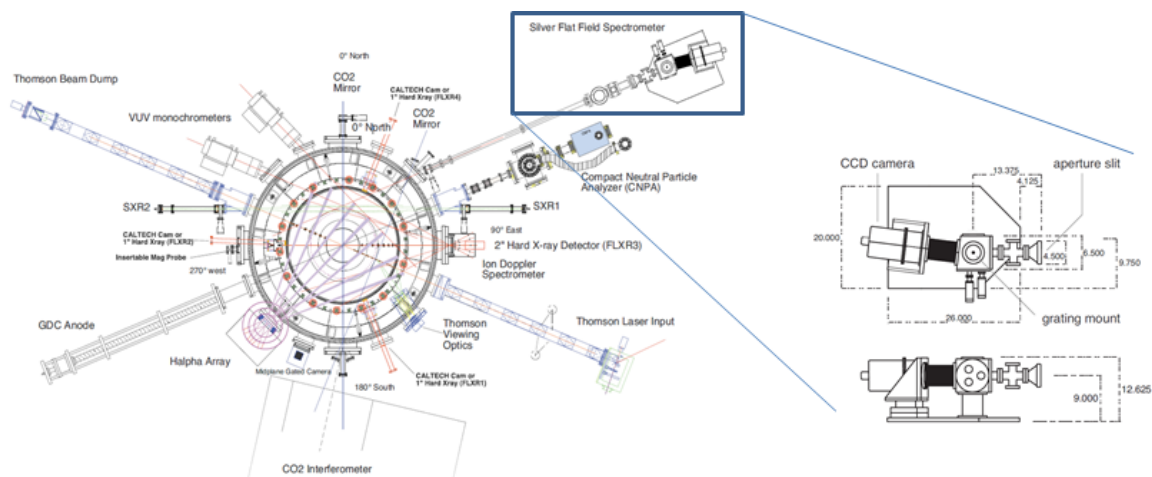


Figure 2.27. Schematic of the Silver Flat Field Spectrometer on the SSPX (from Clementson *et al.* 2008).

Chapter 3

Radiative Properties of Uniform Mo and Mixed with Al Triple Planar Wire Arrays

3.1 Introduction to Uniform Mo and Mixed with Al Triple Planar Wire Arrays

Planar wire arrays (single and multi-planar) have previously shown to be very efficient x-ray radiators (Kantsyrev *et al.* 2006, Kantsyrev *et al.* 2008b) on university scale z-pinch generators, such as the 1.7 MA Zebra generator at UNR. In particular, single and double planar wire arrays of Mo were studied (Yilmaz *et al.* 2008) and it was shown that Mo SPWAs produced very high T_e at > 1300 eV for heavier loads (150 μg) and moderately high electron density (n_e at $> 10^{21}$ cm^{-3}) for lighter loads (90 μg) with total radiated energies > 18 kJ. Mo double planar wire arrays (DPWAs), however, produced lower electron temperature (T_e at > 1100 eV) but with higher total radiated energies > 21 kJ. This chapter will largely focus on the radiative and implosion characteristics of Mo and mixed Mo and Al triple planar wire arrays (TPWAs), in particular how geometry and inter-planar gaps play a role in efficiency of energy conversion to x-rays, and also how placement and mass concentration of different Mo and Al wires influence overall radiation of, for example, K-shell Al and L-shell Mo, and how this affects opacity of the plasmas.

Section 3.2 will cover results and analysis of Mo and mixed Mo and Al TPWAs with an inter-planar gap of 3.0 mm, while Section 3.3 will highlight results and analysis of these Al TPWAs with a smaller inter-planar gap of 1.5 mm, and Section 3.4 concludes.

3.2 Uniform Mo and Mixed with Al Triple Planar Wire Arrays with a 3.0 Inter-Planar Gap

Implosion dynamics of three different triple planar wire arrays that were performed on Zebra generator will be compared in this section: the first consisting of uniform Mo (Mo/Mo/Mo), the second consisting of 68% Mo and 32 % Al (5056, 95% Al, 5% Mg) (Mo/Al/Mo), with Mo planes on the outside, and the third consisting of 35% Mo and 65% Al (5052) (Al/Mo/Al), with Al planes on the outside. In particular, experimental results for x-ray time-integrated, spatially-resolved spectra and pinhole images, x-ray time-gated pinhole and spectra images, PCD and XRD signals, and total radiated energy will be fully compared and analyzed. Table 3.1 lists the load characteristics of the shots considered in this section. The anode-cathode gap for all loads considered was 20 mm. Each plane consisted of six wires, and the Mo and Al wires had diameters such that each plane would have approximately the same mass of around 90 $\mu\text{g}/\text{cm}$, which, according to Wire Ablation Dynamics Model (WADM) calculations, would have implosion times estimated to be around 100 ns, or the maximum of the current, which allows maximum efficiency of x-ray radiation and total energy output. The total radiated energy for the Mo/Mo/Mo and Mo/Al/Mo loads were comparable at 16.2 and 16.9 kJ, respectively. The total radiated energy for Al/Mo/Al load, however, was less at 13.1 kJ. This is to be expected as Al is a less efficient radiator as Mo, and these results also suggest that the outer planes carry a higher distribution of current (as suggested in Safronova *et al.* 2014 for mixed Cu and Al TPWAs) and contribute more to the total radiation than the inner plane, perhaps due to increased kinetic energy the outer planes have relative to the inner plane. These energies are still less than for the Mo DPWAs (> 21 kJ) previously studied.

Shot #	Material # Wires	Diameter (μm) Gap (mm)	Linear Mass ($\mu\text{g/cm}$)	Al (%)	Total Energy (kJ)
1261	Mo/Mo/Mo 6/6/6	7.9/7.9/7.9 3.0	90	-	16.2
1262	Mo/Al/Mo 6/6/6	7.9/15.0/7.9 3.0	89	32	16.9
1263	Al/Mo/Al 6/6/6	15.0/7.9/15.0 3.0	87	65	13.1

Table 3.1. List of considered shots and parameters for Mo and mixed Mo and Al TPWAs. The diameter is the diameter of the wires and the gap is the inter-planar gap.

3.2.1 Implosion Characteristics and Temporal Radiation

This section will analyze the implosion characteristics of the TPWA loads considered. Figure 3.1 shows signals and time-gated pinhole (TGPH) images of Mo/Mo/Mo, Mo/Al/Mo, and Al/Mo/Al. Briefly, the TGPH utilized a microchannel plate (MCP) consisting of six gates with 6 ns spacing between gates and 3 ns frame duration, allowing two images of energies > 1.0 keV and > 3.0 keV. The signals include a $5 \mu\text{m}$ Kimfoil filtered x-ray diode (XRD, > 0.2 keV) and an $8 \mu\text{m}$ Be filtered PCD (> 0.8 keV). Looking at Figure 3.1(a) and 3.1(b), the implosion times of Mo/Mo/Mo and Mo/Al/Mo are roughly the same at 101 and 99 ns, respectively. The XRD signals indicate a sharp rise just before the implosion, followed by a series of bursts after the main pinch lasting for approximately 40 ns. The PCD signals show interesting results where, similar to the XRD signals, there are a series of bursts; however the most intense bursts come later in time, at ~ 120 ns. Now looking to Figure 3.1(c), the implosion time of Al/Mo/Al is 97 ns, which is slightly earlier than the other two configurations, but within experimental jitter. The XRD and PCD signals, however, are different than the other two loads. The XRD

signal is characterized by a sharp peak, followed by only a few, much smaller bursts lasting for approximately 40 ns. The PCD signal is characterized by a sharp rise around implosion time, in contrast to the Mo/Mo/Mo and Mo/Al/Mo loads, followed by a few bursts. The TGPH images indicate many random bright spot formations for both > 1.0 and > 3.0 keV images for Mo/Mo/Mo and Mo/Al/Mo, and for the > 3.0 keV for Al/Mo/Al. K-shell Al approximately radiates > 1.0 keV and the random bright spot formations for Mo/Al/Mo in the > 1.0 keV TGPH image indicate that K-shell Al is not radiating completely in a column-like manner, however the > 1.0 keV TGPH image for Al/Mo/Al shows a very intense column-like structure around implosion time, on frame “b” on the film, which indicates K-shell Al is radiating in a column-like structure. Later in Section 3.2.2 this structure will be compared to the time-integrated spatially resolved results.

To understand how the wires in this TPWA configuration implode, the Wire Ablation Dynamics Model was applied to shot 1262 for Mo/Al/Mo, and the results are shown in Figure 3.2. The simulation shows results from a top down perspective of how the individual wires implode in time. By 43 ns the Mo wires on the outside are well into the ablation process towards the central axis, while the Al wires on the inside have started to ablate as well. By 82 ns the outside Mo wires have fully ablated away from their initial positions, while the innermost four Al wires are still ablating. Finally by 98 ns the WADM predicts the load will fully implode, which agrees with experiment well.

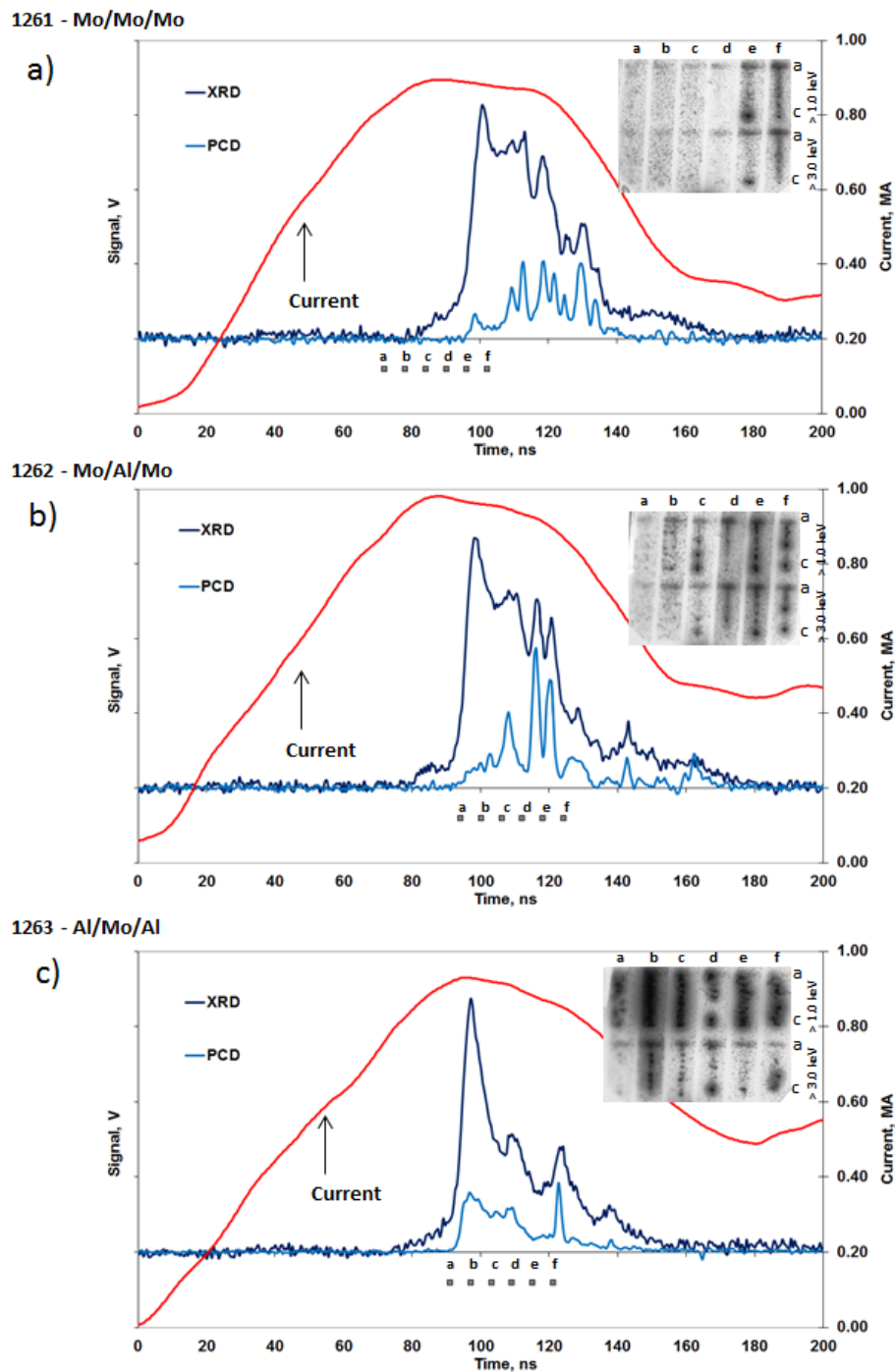


Figure 3.1. PCD and XRD signals, along with current and time-gated pinhole images of > 3.0 keV and > 1.0 keV, of Mo/Mo/Mo TPWA (a), Mo/Al/Mo TPWA (b), and Al/Mo/Al TPWA (c). The labels “a – f” denote the timings of the time-gated pinhole images.

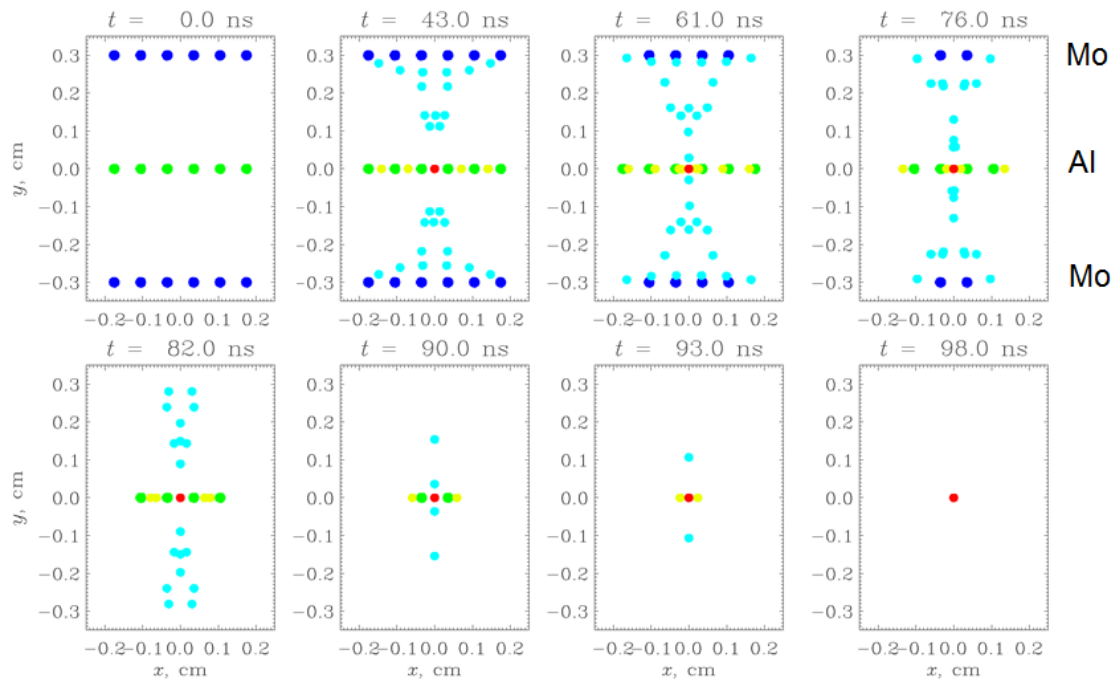


Figure 3.2. Wire Ablation Dynamics Model implosion simulation of shot 1262, Mo/Al/Mo TPWA. The blue dots indicate initial starting positions of Mo wires, while the green dots indicate starting positions of Al wires. Light blue dots indicate ablating material from Mo wires and yellow dots indicate ablating material from Al wires.

To understand how K-shell Al radiates in time, a time-gated spectrometer (TGSP) was fielded for Al/Mo/Al. The TGSP utilized a KAP crystal ($2d = 26.63 \text{ \AA}$) which allowed for viewing of wavelengths between 6.2 and 11 \AA , wide enough to cover most of K-shell Al and Mg spectra. Bio-max MS Kodak x-ray film was implemented in this work. The spacing between gates was 5 ns , while the MCP was gated to last for 3 ns . Figure 3.3 shows the results of the K-shell Al and Mg spectra along with XRD and PCD signals. The spectra were collected starting at 110 ns after current rise, or 13 ns after the main implosion. Frame 1 in Figure 3.3(b) indicates very strong emissions from K-shell Al and the emergence of K-shell Mg, which is in general an indicator of high opacity in

the K-shell Al plasma, as Mg in the Al 5056 alloy is only 5%. Due to such high opacity in K-shell Al, a non-LTE kinetic model of Mg is used to derive T_e from the K-shell Mg spectra (Yilmaz 2009). Frame 1, which corresponds to a peak in the PCD signal, shows a K-shell Mg $T_e = 360$ eV. The ratio of Mg2/Mg1 is used to estimate T_e . Usually, the electron density is estimated by the ratio of Mg1 and inter-combination line Mg1', however the intensity of the Mg1' here is too low and an estimate of 10^{20} cm⁻³ is used, which is an appropriate electron density for PWA plasmas. Frame 2, 5 ns later, which corresponds to a “valley” in the PCD signal, shows a K-shell Mg T_e of 300 eV, and stays constant in Frame 3 at 300 eV, again corresponding to the “valley” in the PCD signal. Frame 4 corresponds to another peak in the PCD signal, and the K-shell Mg modeling shows an increase in T_e to 340 eV from the previous two time frames. By Frame 5 the PCD signal has dissipated and the K-shell Al is reduced and the K-shell Mg has disappeared. By Frame 6 there is no spectra and corresponds to a PCD signal that is nearly zero. This shows excellent correlation between K-shell Mg electron temperature and PCD signal where generally the greater the PCD signal the higher the K-shell Mg electron temperature is. These results are in agreement with previous results of correlation of PCD signals with electron temperature, see, for example (Weller *et al.* 2012a), where PCD signals correlated not only for K-shell Al and Mg, but also L-shell Cu and Zn. It would be interesting to have time-gated results of L-shell Mo, however, as discussed in Chapter 2, the time-gated spectrometer used in these experiments didn't have the proper spectral range to attain L-shell Mo lines.

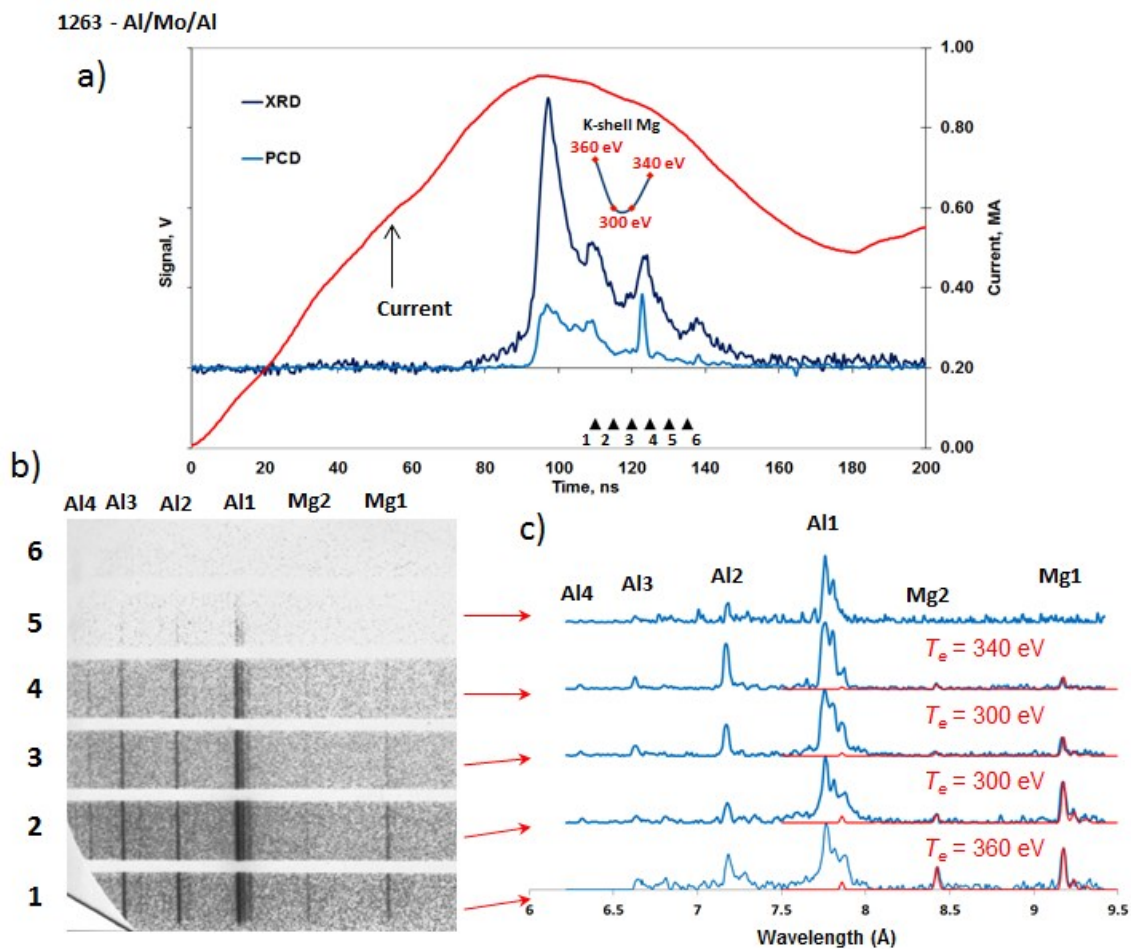


Figure 3.3. (a) PCD and XRD signals from Al/Mo/Al along with current, timings from the time-gated spectrometer (labeled “1 – 6”), and K-shell Mg electron temperatures. (b) Spectra from time-gated spectrometer and (c) lineouts taken from spectra in (b) along with synthetic spectra.

3.2.2 Radiative Characteristics

The radiative characteristics of the Mo TPWA experiments are explored in detail in this section. Figure 3.4 shows the results of time-integrated spatially resolved pinhole (TIPH) and spectra (TISP) from Mo/Mo/Mo, Mo/Al/Mo, and Al/Mo/Al. The spectra were taken with a KAP convex crystal spectrometer while the pinhole images were filtered to study L-shell Mo emissions > 3.0 keV. Both diagnostics are axially resolved

to study variations along the length of the pinch from anode “a” to cathode “c”. Diagnostically important L-shell Mo lines, along with K-shell Al and K-shell Mg lines are indicated. It’s important to note that in these experiments, the TIPH and TISP diagnostics were located on opposite beam lines, a full 180° from each other. This is important when analyzing bright spot formations and the corresponding spectra. For Mo/Mo/Mo, L-shell Mo radiates from 4-5 bright spots, and is most prevalent near the cathode. For Mo/Al/Mo, L-shell Mo radiates again from bright spots, this time approximately 3, and K-shell Al appears to radiate mostly where L-shell Mo is seen, except for near the anode. It’s interesting for Mo/Al/Mo near the middle a bright spot is shown to radiate to the left in the TIPH image, and this can be seen in the spectra, which gives evidence of radiation from two sources. Moving to Al/Mo/Al, L-shell Mo again appears to radiate from bright spots, roughly 3-4, however K-shell Al and Mg appear to radiate in a column-like manner. This likely has two explanations: one, the initial mass of Al constitutes 65% of the total mass, where in the previous Mo/Al/Mo load Al constituted 32% of the total mass, and two, the Al is located on the outer planes, which likely contribute more to radiation than the inner plane. Interestingly, a similar bright spot seen in Mo/Al/Mo is produced in Al/Mo/Al in the TGPH image, and can be seen in the spectra, indicating two sources. More experiments need to be accomplished to understand if this is purely coincidence or if it is reproducible.

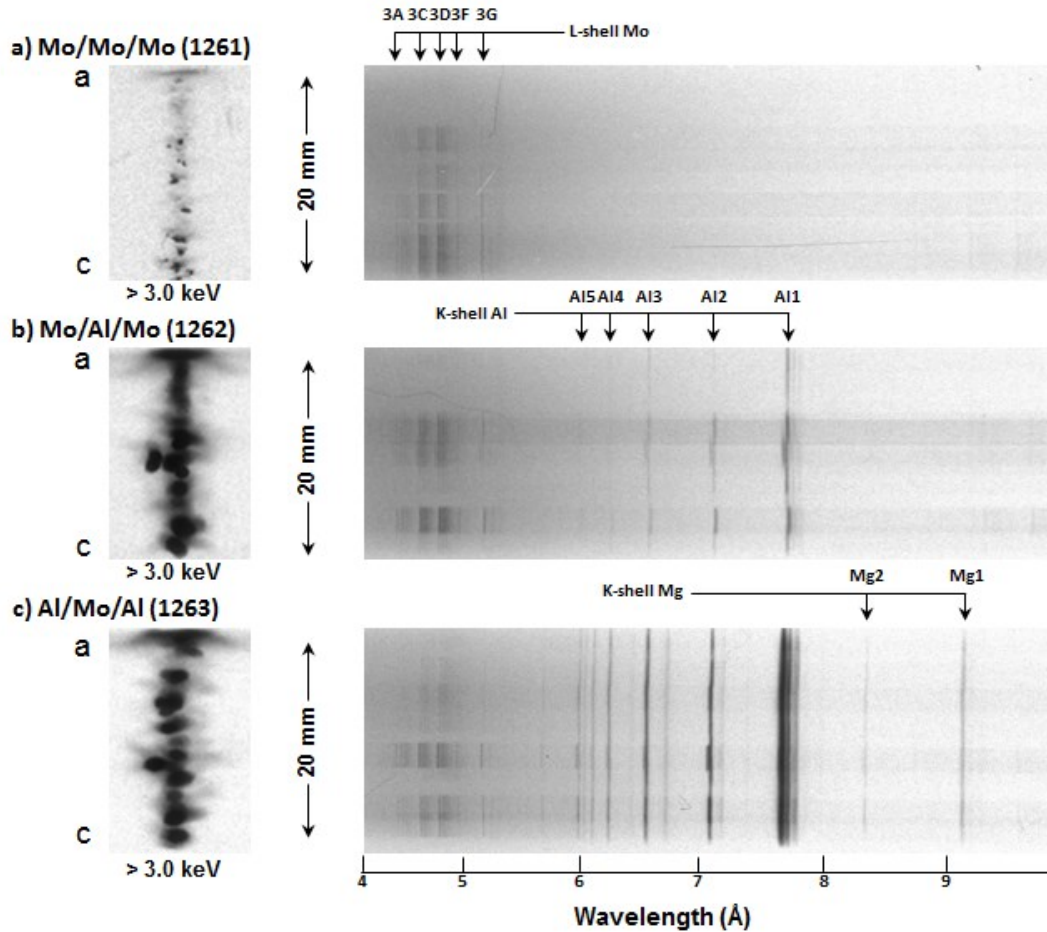


Figure 3.4. (a) Time-integrated spatially resolved pinhole (left) and spectra (right) of Mo/Mo/Mo. (b) Time-integrated spatially resolved pinhole (left) and spectra (right) of Mo/Al/Mo. (c) Time-integrated spatially resolved pinhole (left) and spectra (right) of Al/Mo/Al.

Lineouts were taken from the spectra in Figure 3.4 and non-LTE kinetic modeling was applied for both L-shell Mo and K-shell Al/Mg. Figure 3.5 shows three lineouts taken from Mo/Mo/Mo. The spectra show an increase in intensity of 3A, 3B, 3F, and 3G lines the closer to the cathode. The lineout taken near the anode was successfully modeled with $T_e = 1050$ eV and $n_e = 10^{20}$ cm⁻³. The ratio $(3A+3B)/(3F+3G)$ has been

shown to be a good indicator of n_e , while the ratios of Mg1/Na1 and F1/Mg1 can be used as an T_e diagnostic.

Figure 3.6 shows five lineouts taken from Mo/Al/Mo. L-shell Mo again shows very high intensities of 3A, 3B, 3F, and 3G closer to the anode. In particular the lineout taken closest to the anode indicates relatively high optically thick L-shell Mo plasma due to the thickness of the line shapes. K-shell Al, however, is produced relatively optically thin (K-shell Mg is not apparent), and modeling of plasma parameters of K-shell Al was accomplished. K-shell Al T_e ranged from 330 to 420 eV, with higher T_e corresponding to intense L-shell Mo spectra, and lower T_e with less intense to no L-shell Mo spectra. A possible explanation is that K-shell Al T_e may possibly being affected by the presence of the L-shell Mo through radiative cooling from the Mo ions. K-shell Al n_e was nearly constant ranging from $2 \times 10^{20} \text{ cm}^{-3}$ to $3 \times 10^{20} \text{ cm}^{-3}$.

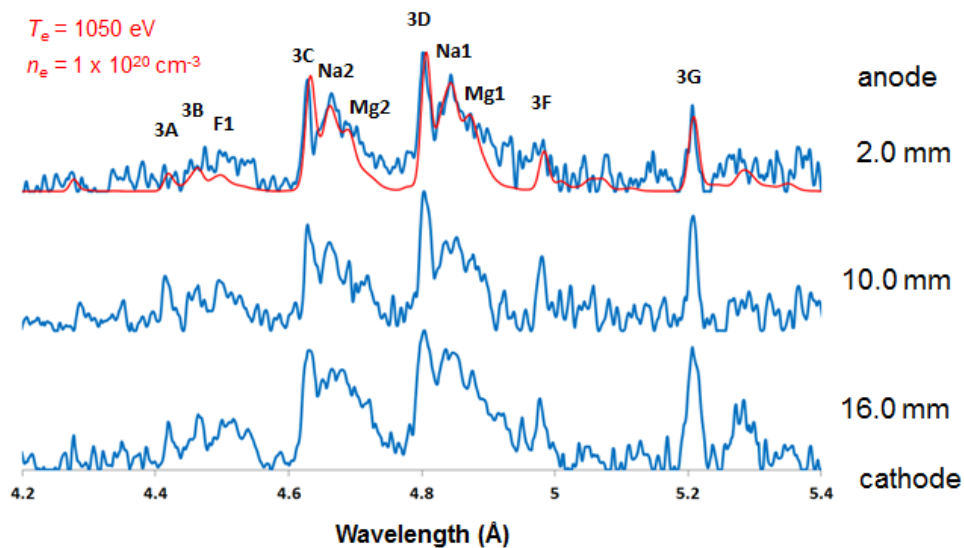


Figure 3.5. Lineouts of L-shell Mo taken from Figure 3.4, Mo/Mo/Mo. The blue is experimental spectra, while the red is synthetic spectra. The distances from anode for each lineout are located to the right.

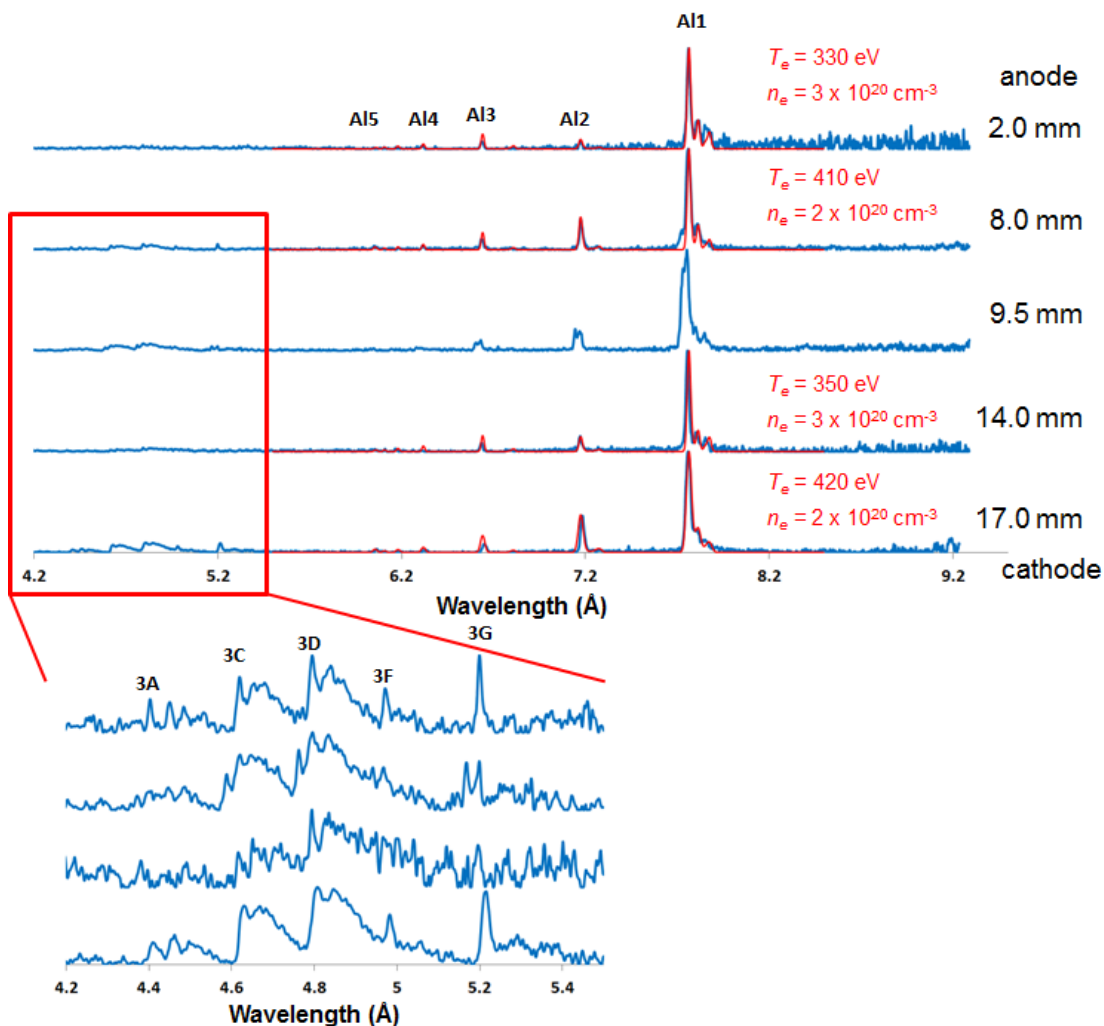


Figure 3.6. Lineouts of L-shell Mo taken from Figure 3.4, Mo/Al/Mo. The blue is experimental spectra, while the red is synthetic spectra. The distances from anode for each lineout are located to the right.

Figure 3.7 shows four lineouts from Al/Mo/Al. L-shell Mo is less intense as before while K-shell Al is much more intense and broad (in particular Al1) and K-shell Mg appears which indicates K-shell Al is optically thick. The lineout near the cathode for L-shell Mo was modeled and produced $T_e = 1020$ eV and $n_e = 5 \times 10^{19}$ cm⁻³. K-shell Mg was modeled for all lineouts. K-shell Mg T_e ranged from 320 to 340 eV, with higher T_e

corresponding to intense L-shell Mo spectra, and lower T_e with less intense to no L-shell Mo spectra, though the difference in T_e is smaller than observed for Mo/Al/Mo. It's also important to note that K-shell Al/Mg and L-shell Mo plasmas radiate at much different T_e , as the results suggest here and as concluded in Safronova *et al.* 2007. K-shell Al n_e was nearly constant ranging from $2 \times 10^{20} \text{ cm}^{-3}$ to $3 \times 10^{20} \text{ cm}^{-3}$.

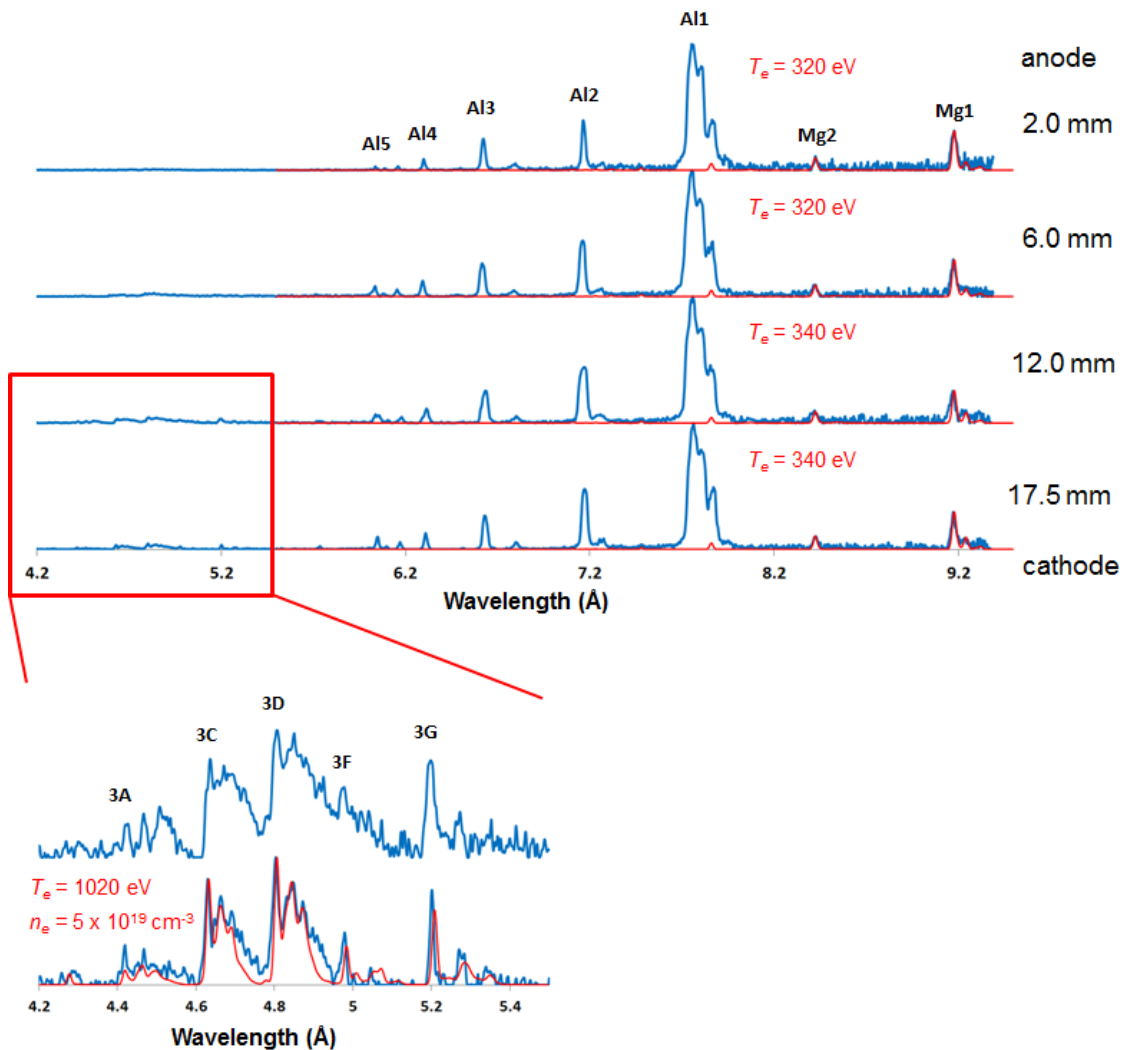


Figure 3.7. Lineouts of L-shell Mo taken from Figure 3.4, Al/Mo/Al. The blue is experimental spectra, while the red is synthetic spectra. The distances from anode for each lineout are located to the right.

3.3 Uniform Mo and Mixed with Al Triple Planar Wire Arrays with a Reduced Inter-Planar Gap of 1.5 mm

Results from early TPWA experiments with an inter-planar gap of 3.0 mm yielded powers and energies that were 20-30% lower than double planar wire array (DPWA) (Kantsyrev et al. 2009). It is important to note, though, that because of the open magnetic configuration of the TPWA and DPWA, the placement of the outer wires can significantly change the dynamics and efficiency of the implosion. Comparing to DPWAs with inter-row gaps of 6.0 mm and not 3.0 mm, the TPWAs had a 20% increase in energy output. The logical step then was to field TPWAs with a reduced inter-row gap of 1.5 mm, thus making the outer-row gap 3.0 mm, comparable to the highest yielding DPWAs.

All shots considered in this section are uniform Mo and mixed with Al TPWAs. The mixed loads consisted of either two Mo planes on the outside with Al in the center or two Al planes on the outside with Mo in the center. Different wire diameters of Mo and Al were used to keep the planes approximately the same mass, with a total mass of ~ 115 $\mu\text{g/cm}$. The change of inter-row gap is investigated: decreasing the inter-row gap from 3.0 mm to 1.5 mm led to a higher yield of 25 kJ (a 40-50% increase), close to the highest yield from Mo DPWAs. Table 3.2 lists the load characteristics of the shots considered in this section. All experiments were performed on the Zebra generator at UNR at 1.0 MA.

Shot #	Material # Wires	Diameter (μm) Gap (mm)	Linear Mass ($\mu\text{g/cm}$)	Al (%)	Total Energy (kJ)
1969	Mo/Mo/Mo 6/6/6	8.9/8.9/8.9 1.5	114	-	25.5
1932	Mo/Mo/Mo 6/6/6	8.9/8.9/8.9 1.5	114	-	24.5
1968	Mo/Al/Mo 6/6/6	8.9/17.8/8.9 1.5	116	35	22.2
1933	Mo/Al/Mo 6/6/6	8.9/17.8/8.9 1.5	116	35	22.5
1953	Al/Mo/Al 6/6/6	17.8/8.9/17.8 1.5	116	68	23.1
2166	Al/Mo/Al 6/6/6	17.8/8.9/17.8 1.5	116	68	24.0
2167	Al/Mo/Al 6/6/6	17.8/8.9/17.8 1.5	116	68	21.1

Table 3.2. List of considered shots and parameters for Mo and mixed Mo and Al TPWAs with reduced inter-planar gap.

3.3.1 Implosion Characteristics and Temporal Radiation of Triple Planar Wire Arrays with a Reduced Inter-Planar Gap of 1.5 mm

This section will analyze the implosion characteristics of the TPWA loads considered. Figure 3.8 shows signals and time-gated pinhole (TGPH) images of Mo/Mo/Mo, Mo/Al/Mo, and Al/Mo/Al. The signals include a 5 μm Kimfoil filtered x-ray diode (XRD, > 0.2 keV), an 8 μm Be filtered PCD (> 0.8 keV), and a 0.2 μm Al filtered Si diode to capture extreme ultraviolet radiation (EUV, > 17 eV). The EUV diode was added due to a significant amount of radiation emitting from the EUV region (M-shell Mo, for example), which has previously gone relatively unexplored. Looking at Figure 3.8(a-c), the implosion times of Mo/Mo/Mo, Mo/Al/Mo, and Al/Mo/Al are 95, 103, and 95 ns respectively.

Similar to the signals from Mo and mixed Mo and Al TPWAs with a 3.0 mm inter-planar gap, the XRD signals indicate a sharp rise just before the implosion, followed by a series of bursts after the main pinch lasting for approximately 40 ns. The PCD signals show interesting results where, similar to the XRD signals, there are a series of bursts; however the most intense bursts come later in time, between 100 – 120 ns. The TGPH images indicate many random bright spot formations for both > 1.0 and > 3.0 keV images for Mo/Mo/Mo and Mo/Al/Mo, and for the > 3.0 keV for Al/Mo/Al. K-shell Al approximately radiates > 1.0 keV and the random bright spot formations for Mo/Al/Mo in the > 1.0 keV TGPH image indicate that K-shell Al is not radiating completely in a column-like manner, however the > 1.0 keV TGPH image for Al/Mo/Al shows a very intense column-like structure around implosion time, on image b) on the film, which indicates K-shell Al is radiating in a column-like structure, again, similar to the 3.0 mm inter-planar counterparts. The EUV signals for all shots indicate > 17 eV radiation starting as early as 20 ns into the current rise and continuing to well after the XRD and PCD signals have dissipated and continuing past 200 ns. It's clear that a great deal of interesting physics is occurring in this region and is the subject of current studies (Safronova *et al.* 2011).

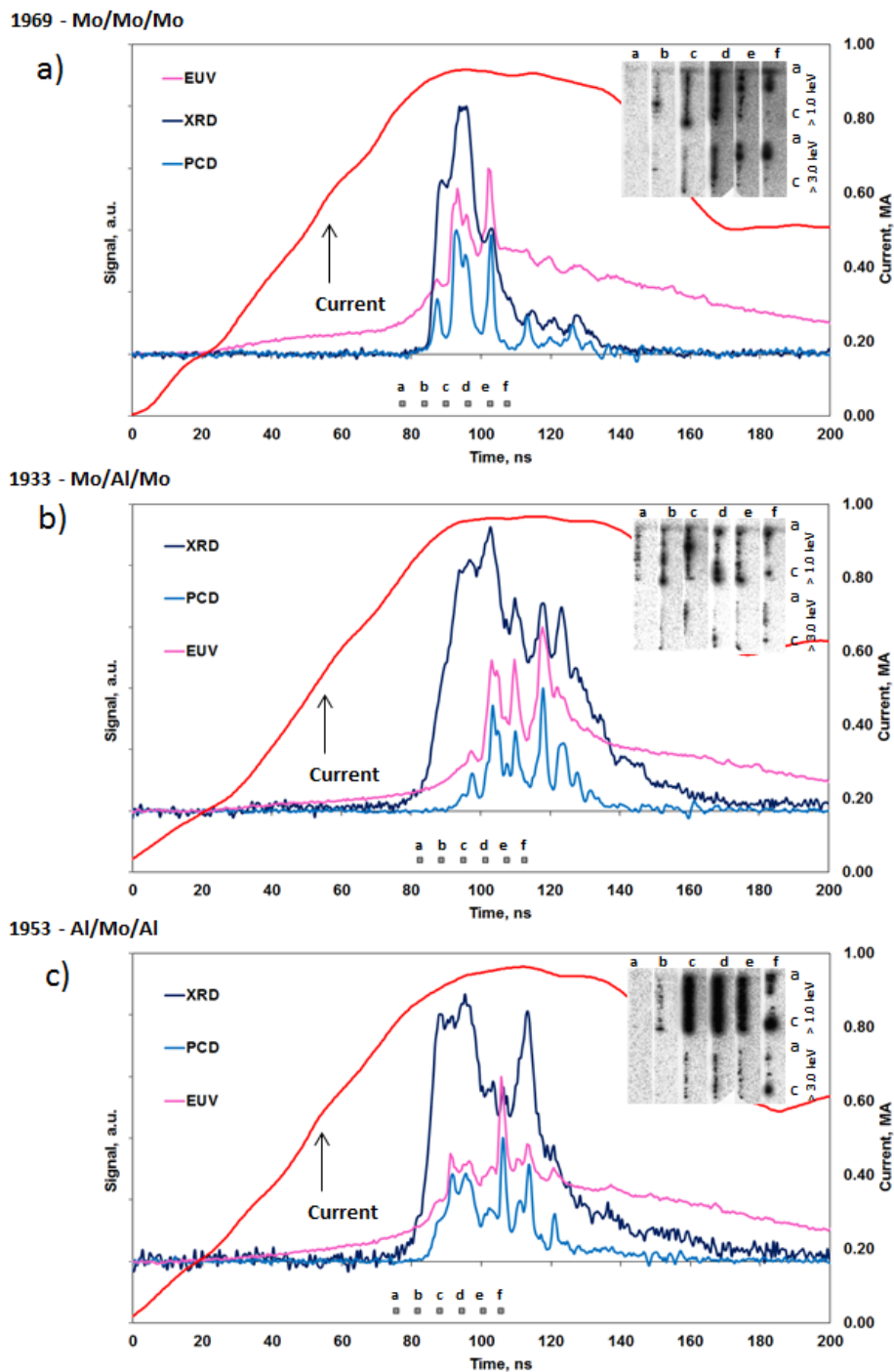


Figure 3.8. PCD and XRD signals, along with current and time-gated pinhole images of > 3.0 keV and > 1.0 keV, of Mo/Mo/Mo TPWA (a), Mo/Al/Mo TPWA (b), and Al/Mo/Al TPWA (c) with an inter-planar gap of 1.5 mm. The labels “a – f” denote the timings of the time-gated pinhole images.

To understand how K-shell Al radiates in time, a time-gated spectrometer (TGSP) was fielded for Mo/Al/Mo and Al/Mo/Al. The TGSP utilized a potassium hydrogen phthalate (KAP) crystal ($2d = 26.63 \text{ \AA}$) which allowed for viewing of wavelengths between 6.2 and 11 \AA , wide enough to cover most of K-shell Al spectra. Bio-max MS Kodak x-ray film was implemented in this work. The spacing between gates was 5 ns, while the MCP was gated to last for 3 ns. Figure 3.9 shows the results of the K-shell Al spectra along with signals of Mo/Al/Mo. The spectra were collected starting at 73 ns after current rise, or 22 ns before the main implosion. Frame 2 in Figure 3.9(b) indicates the presence of background, perhaps bremsstrahlung radiation or recombination, however very weak K-shell Al radiation, and corresponds to a spike in PCD signal. This may indicate that L-shell Mo, from the outer planes, is radiating just slightly before K-shell Al, from the inner plane, however without time resolution of L-shell Mo itself this is purely speculation and points to the importance of understanding time evolution of L-shell Mo. Frame 3, which corresponds to a “valley” in the PCD signal and little background, shows definitive appearance of K-shell Al, with an estimated T_e of 425 eV. The ratio of Al₂/Al₁ is used to estimate T_e . Usually, the electron density is estimated by the ratio of Al₁ and inter-combination line Al₁’, however here the intensity of the Al₁’ is too low and the electron density 10^{20} cm^{-3} is used. Frame 4, 5 ns later, which corresponds just before the main implosion and re-emergence of background, shows a K-shell Al T_e of 430 eV. Frame 5, which corresponds to just after the main implosion, shows very intense background and a maximum of K-shell Al T_e of 450 eV. The final frame 6 corresponds to another “valley” in the PCD signal and significant reduction of background, along with reduction of K-shell Al T_e with an estimation of 350 eV. This shows excellent

correlation between K-shell Al electron temperature and PCD signal, and it's also important to note that K-shell Al radiated relatively optically thin, with no presence of K-shell Mg. This is likely do to the Al wires being in the inner plane and also starting out with a low percentage of initial mass (35%), and shows an advantage of having mixed materials.

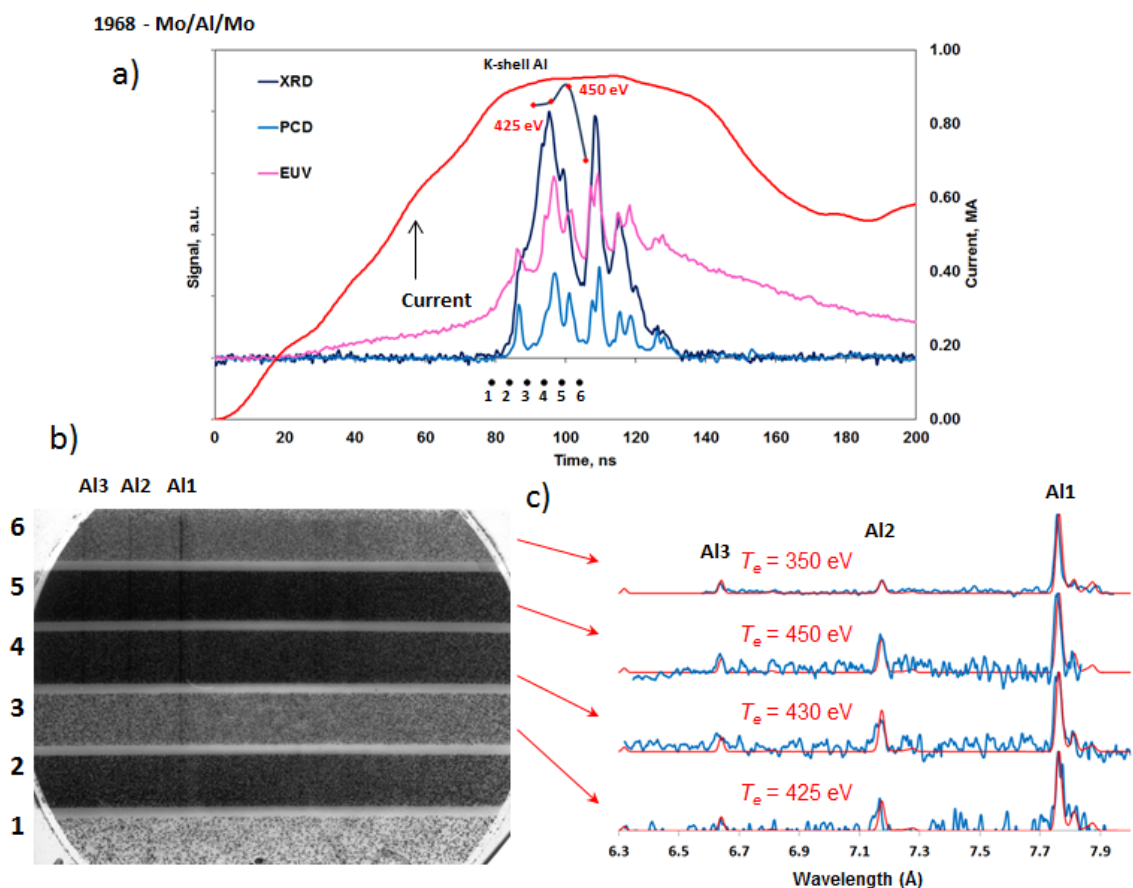


Figure 3.9. (a) PCD, XRD, and EUV signals from Mo/Al/Mo along with current, timings from the time-gated spectrometer (labeled “1 – 6”), and K-shell Al electron temperatures. (b) Spectra from time-gated spectrometer and (c) lineouts taken from spectra in (b) along with synthetic spectra.

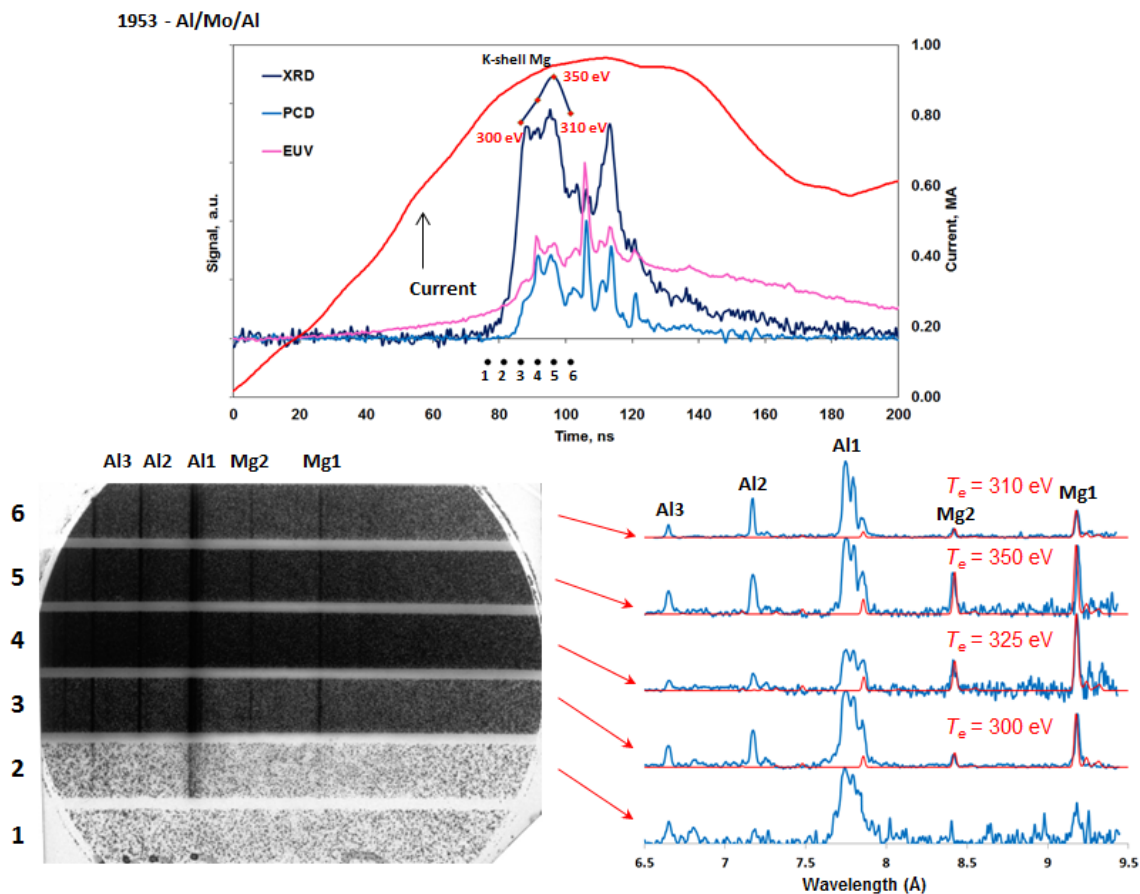


Figure 3.10. (a) PCD, XRD, and EUV signals from Al/Mo/Al along with current, timings from the time-gated spectrometer (labeled “1 – 6”), and K-shell Al electron temperatures. (b) Spectra from time-gated spectrometer and (c) lineouts taken from spectra in (b) along with synthetic spectra.

Figure 3.10 shows the results of the K-shell Al and Mg spectra along with signals from the Al/Mo/Al configuration. Similar to the previous Mo/Al/Mo case, the first frame 1 is taken before any PCD signal and no K-shell Al or Mg was measured. By frame 2, however, K-shell Al is measured, with very weak evidence of K-shell Mg and very little background on the film. The corresponding lineout indicated that K-shell Al lines Al 1 and Al 2 are optically thick. Frame 3 corresponds to a rapid rise in PCD signal, strong background on the film, and strong K-shell Al and Mg lines. Due to the high opacity of

K-shell Al, K-shell Mg was modeled and had an estimated T_e of 300 eV. Frames 4-6 proceed to follow the PCD signal to just before to just after the main implosion, characterized by strong K-shell Al and Mg emissions, strong background, and modeled K-shell Mg T_e of 325, 350, and 310 eV, respectively. As previously for Mo/Al/Mo, the modeled T_e follows the PCD signal well.

3.3.2 Radiative Characteristics of Triple Planar Wire Arrays with a Reduced Inter-Planar Gap of 1.5 mm

Figure 3.11 shows the results of time-integrated spatially resolved pinhole (TIPH) and spectra (TISP) from Mo/Mo/Mo, Mo/Al/Mo, and Al/Mo/Al. The spectra were taken with a KAP convex crystal spectrometer while the pinhole images were filtered to study L-shell Mo emissions > 3.0 keV and K-shell Al and Mg emission (along with L-shell Mo) > 1.0 keV. Both diagnostics are axially resolved to study variations along the length of the pinch from anode “a” to cathode “c”. Diagnostically important L-shell Mo lines, along with K-shell Al and K-shell Mg lines are indicated. The pure Mo/Mo/Mo load shows increased hard x-ray formation and less bright spot formation than the mixed loads. The mixed Mo/Al/Mo load produces optically thin K-shell Al radiation with no presence of K-shell Mg lines and radiates not in a column-like manner, but follows L-shell Mo radiation, which correlate with “bright” spot formations. The Al/Mo/Al load produces optically thick K-shell Al and has a strong presence of K-shell Mg and radiates more in a column-like manner than for the Mo/Al/Mo load, though there still appears to be an influence in K-shell Al and Mg electron temperatures (as discussed below) wherever L-

shell Mo along with “bright” spots in the film appear. For all cases, L-shell Mo radiates from many bright spots (7 – 10).

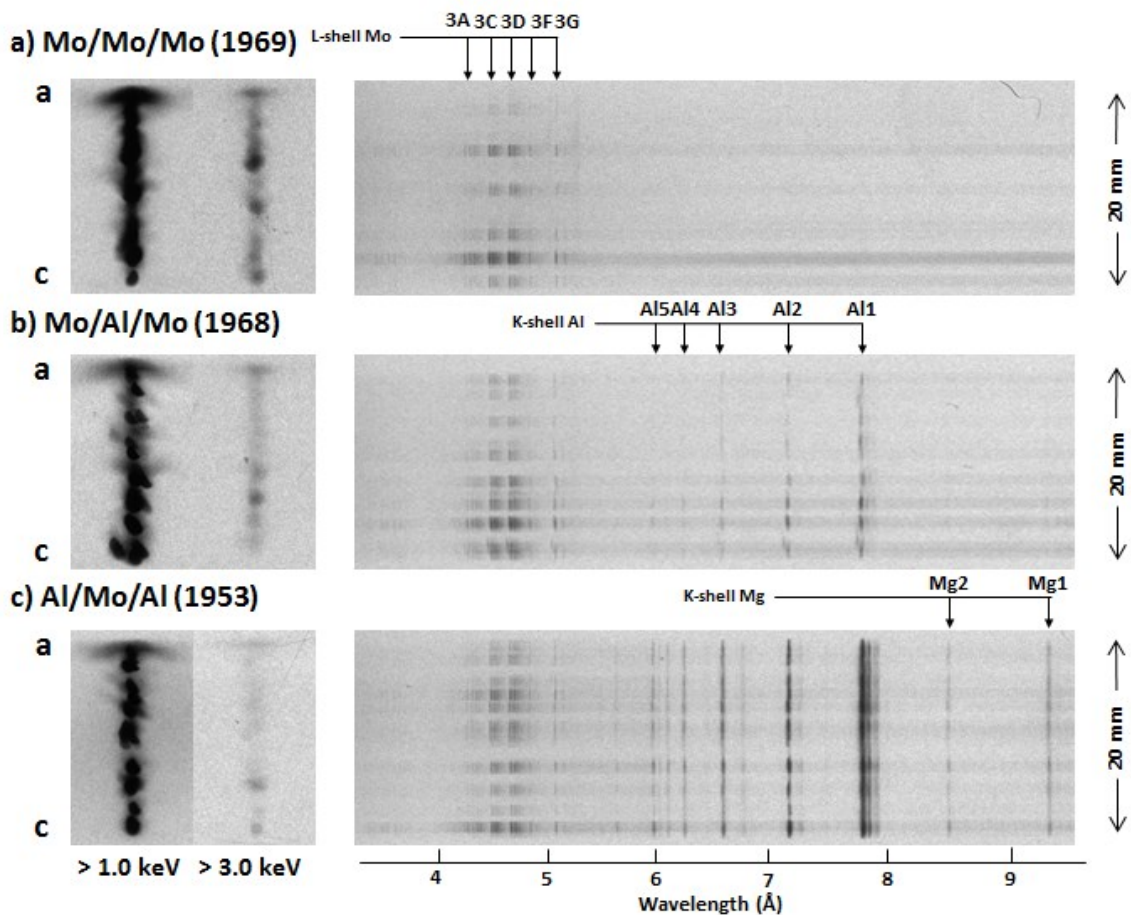


Figure 3.11. (a) Time-integrated spatially resolved pinholes (left) and spectra (right) of Mo/Mo/Mo. (b) Time-integrated spatially resolved pinholes (left) and spectra (right) of Mo/Al/Mo. (c) Time-integrated spatially resolved pinholes (left) and spectra (right) of Al/Mo/Al.

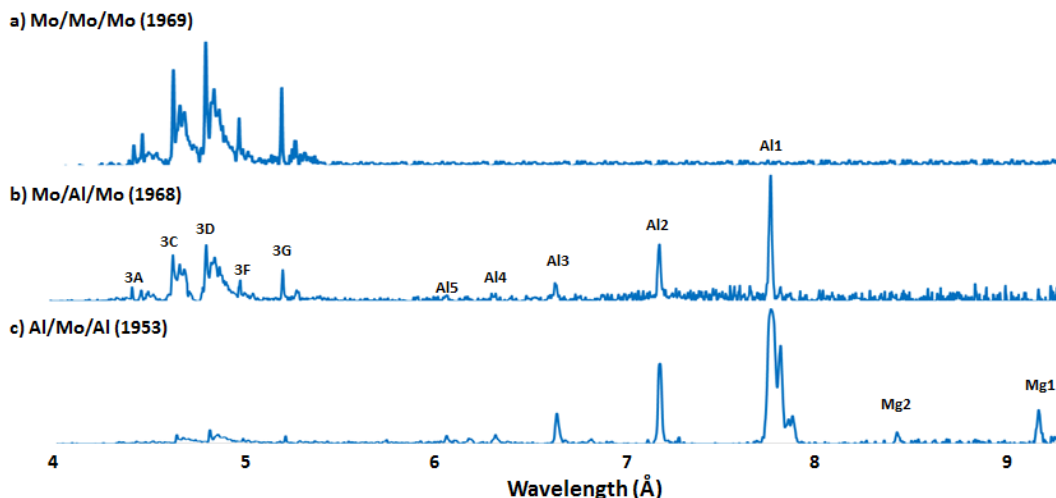


Figure 3.12. Lineouts taken near the cathode from time-integrated spatially resolved spectra from Figure 3.11 of (a) Mo/Mo/Mo, (b) Mo/Al/Mo, and (c) Al/Mo/Al.

Figure 3.12 shows the example of experimental lineouts (taken near the cathode in all cases) of the TISP spectra. This is to very clearly show how different mass concentrations and wire placement can effect radiation output and that despite the fact that the mass of Al increased by twice and of Mo decreased by twice for Al/Mo/Al, the ratio of K-shell Al/L-shell Mo radiated energy went from 1 to 12, indicating again that the outer planes are likely contributing more to the total radiation than the inner plane. To compare to similar loads of Mo/Al/Mo and Al/Mo/Al at 3.0 inter-planar gap discussed in Section 3.2, the ratio of K-shell Al/L-shell Mo radiated energy went from approximately 3 to 26, which indicates the loads with a smaller inter-planar gap radiated L-shell Mo more efficiently than for the larger inter-planar gaps, which is evident by the increased total radiated energies. The next three figures, Figure 3.13-15, show more detailed lineouts, along with non-LTE kinetic modeling, of the spectra shown in Figure 3.11. Despite substantially different mass and plane position of Mo for each shot, the

electron temperatures and densities did not significantly change for L-shell Mo: electron temperatures were estimated to be between 950 and 1200 eV while electron densities were estimated to be between 10^{19} and 10^{20} cm^{-3} . On opposite, substantial gradients occur for K-shell Al plasmas: electron temperatures were estimated to be between 370 and 500 eV while electron densities were estimated to be between 6×10^{19} and 5×10^{20} cm^{-3} for Mo/Al/Mo (Figure 3.14), indicating a very non-uniform implosion. For Al/Mo/Al (Figure 3.15), Mg plasma temperatures were estimated to be between 300 and 360 eV while electron densities were estimated to be between 9×10^{19} and 2×10^{20} cm^{-3} , indicating a much more uniform implosion, yet cooler, than for Mo/Al/Mo.

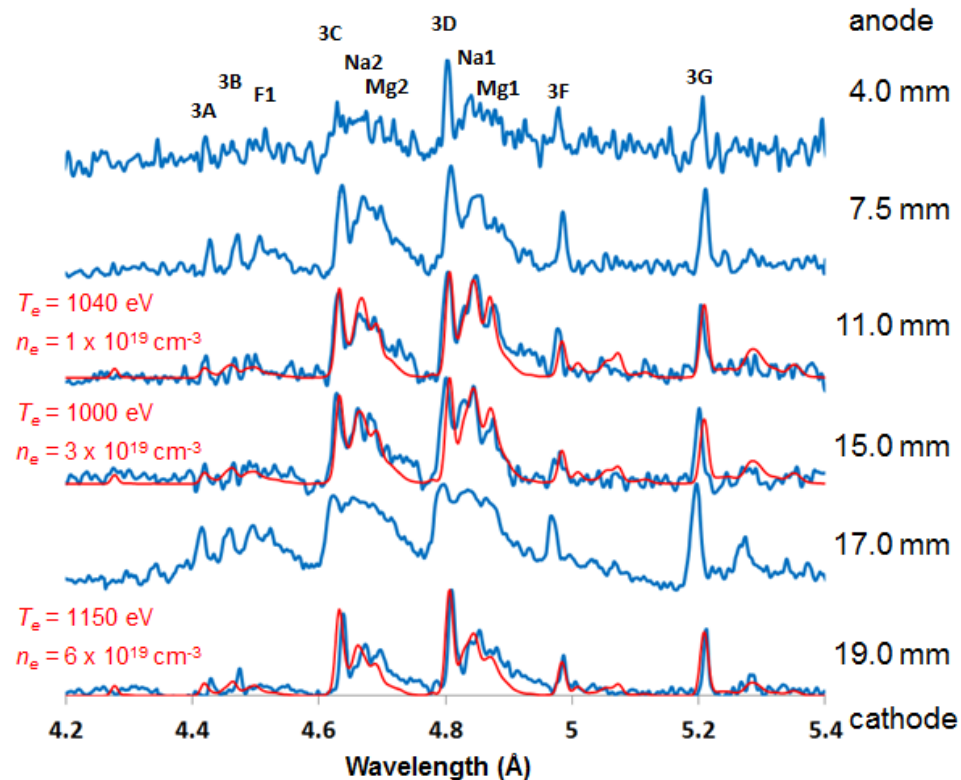


Figure 3.13. Lineouts of L-shell Mo taken from Figure 3.11, Mo/Mo/Mo. The blue is experimental spectra, while the red is synthetic spectra. The distances from anode for each lineout are located to the right.

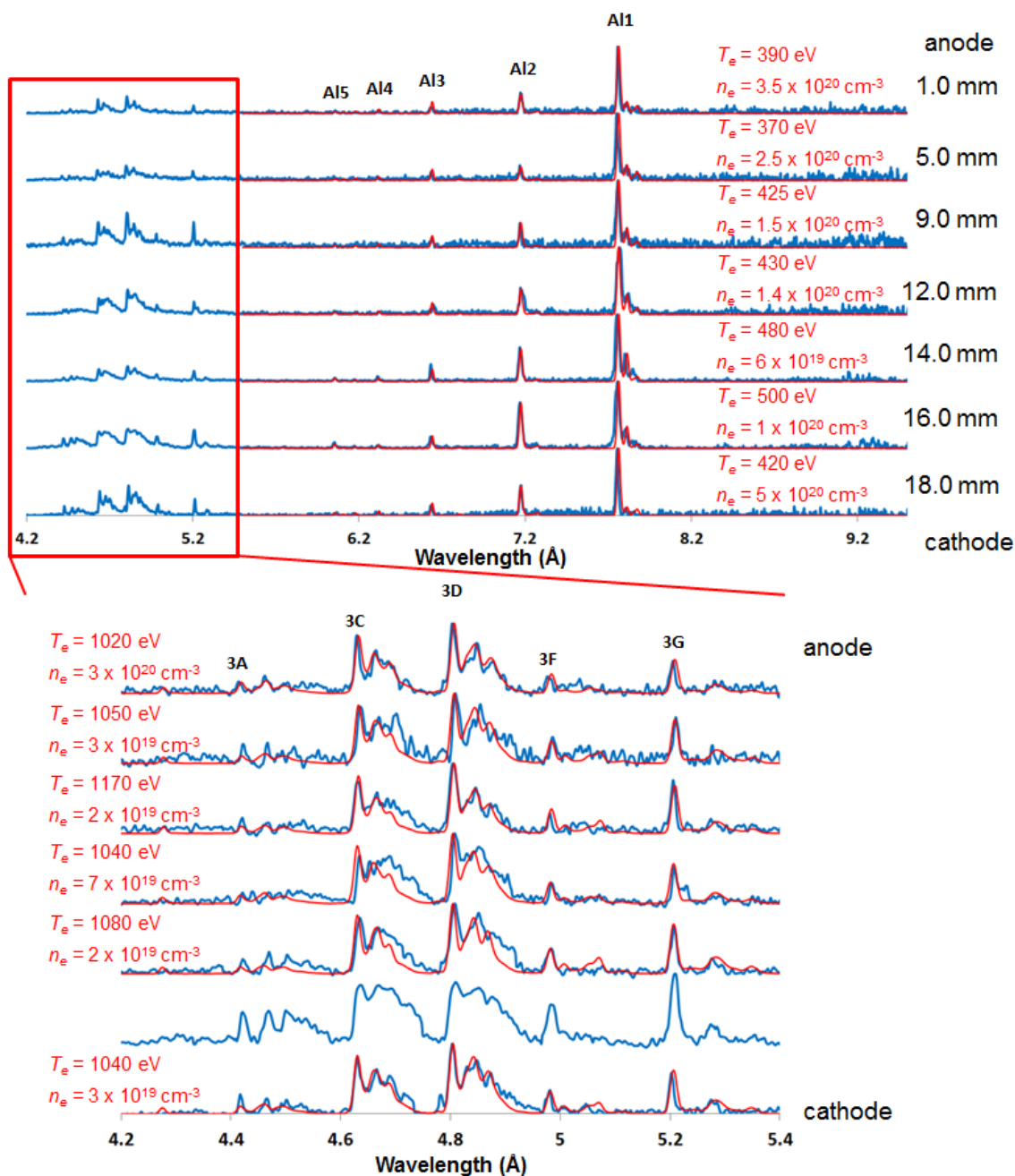


Figure 3.14. Lineouts of L-shell Mo taken from Figure 3.11, Mo/Al/Mo. The blue is experimental spectra, while the red is synthetic spectra. The “a” and “c” represent anode and cathode, respectively. The distances from anode for each lineout are located to the right.

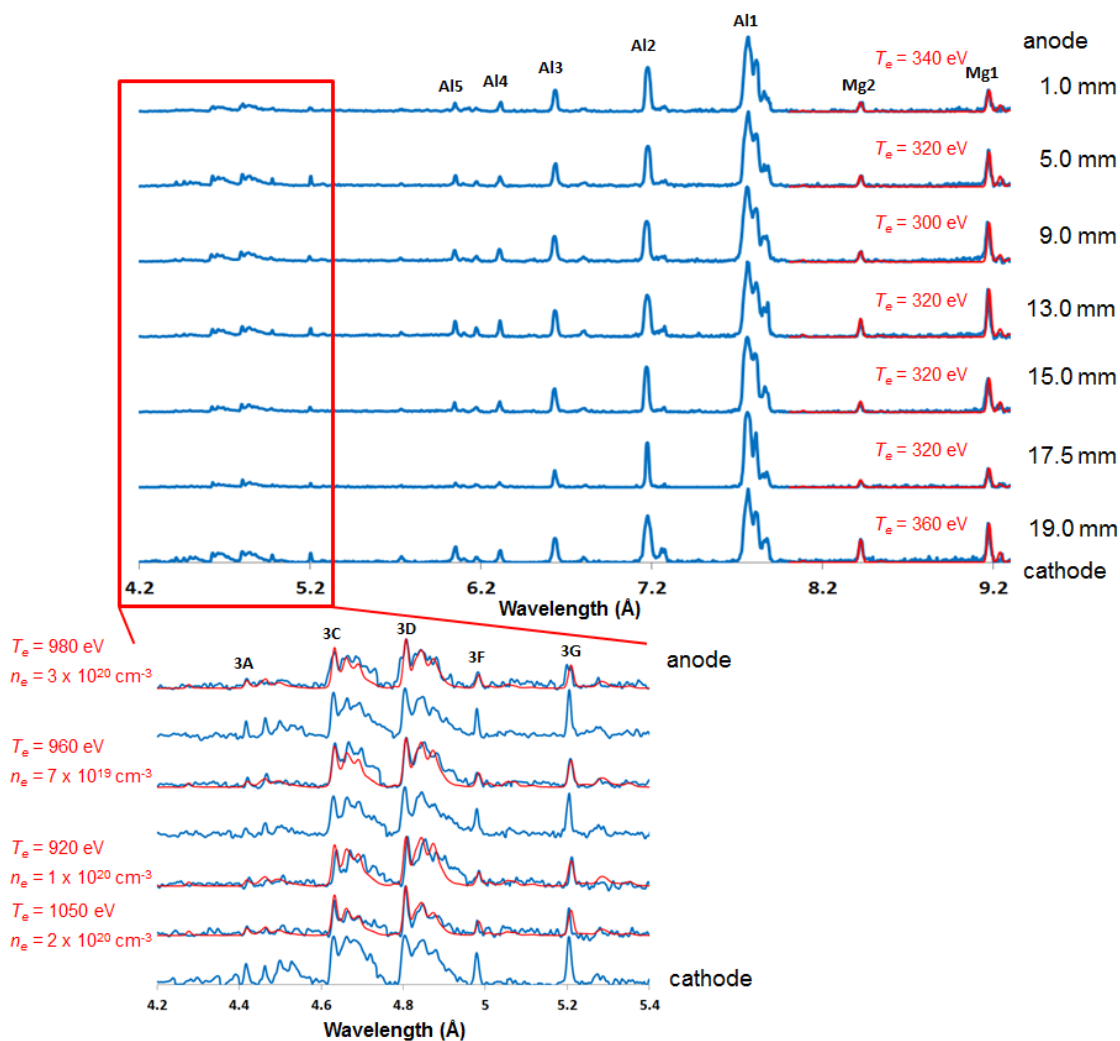


Figure 3.15. Lineouts of L-shell Mo taken from Figure 3.11, Al/Mo/Al. The blue is experimental spectra, while the red is synthetic spectra. The “a” and “c” represent anode and cathode, respectively. The distances from anode for each lineout are located to the right.

Figure 3.16 gives a clear summary of electron temperature and density of L-shell Mo and K-shell Al/Mg as function of distance from anode. Again, L-shell Mo radiates at clearly much higher electron temperatures than for K-shell Al and Mg.

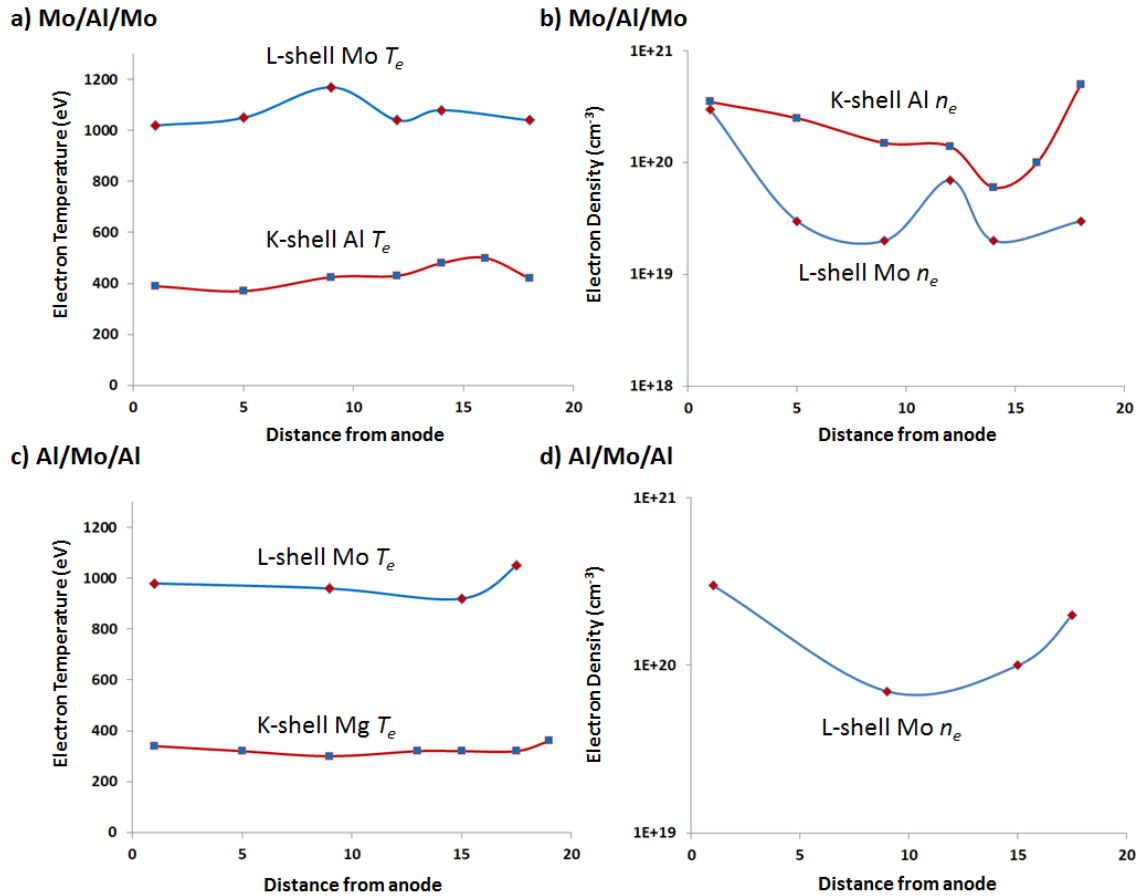


Figure 3.16. Electron temperature and density graphed as function of distance from anode. a) T_e of L-shell Mo and K-shell Al from Mo/Al/Mo. b) n_e of L-shell Mo and K-shell Al from Mo/Al/Mo. c) T_e of L-shell Mo and K-shell Mg from Al/Mo/Al. d) n_e of L-shell Mo from Al/Mo/Al. Data points taken from Figures 3.14 and 3.15.

3.4 Conclusion of Uniform Mo and Mixed with Al Triple Planar Wire arrays at 3.0 mm and 1.5 mm inter-planar gap

Experiments and analysis of data for triple planar wire arrays of Mo and mixed Mo and Al at 3.0 mm inter-planar gap and reduced 1.5 mm inter-planar gap was accomplished for the first time. The reduced gap size of TPWA's (3 mm to 1.5 mm)

produced higher energy output (from ~ 16 kJ to ~ 25 kJ for pure Mo) for all configurations. Time-gated spectrometer modeling of K-shell Al and Mg followed PCD and XRD signals well for the Mo/Al/Mo and Al/Mo/Al configurations. The radiative properties of L-shell Mo and K-shell Al agree well with previously reports results from Safronova *et al.* 2007 with the investigation of mixed Mo and Al single planar wire arrays where L-shell Mo radiated from randomly generated bright spot formations between the anode and cathode. For both 3.0 mm and 1.5 mm interplanar gap Mo/Al/Mo configurations, K-shell Al lines were optically thin and followed Mo L-shell radiation from bright spot pattern, likely due to initial placement inside and small initial Al concentration ($\sim 35\%$ total mass). For both Al/Mo/Al configurations, K-shell Al lines were optically thick and followed a column-like structure, likely due to initial placement outside and large initial Al concentration ($\sim 70\%$ total mass). The importance and advantage of using mixed wire material loads was shown.

Chapter 4

Implosion and Radiative Properties of Mixed Material Nested Cylindrical Wire Arrays

4.1 Introduction and Motivation of Mixed Nested Cylindrical Wire Arrays

Nested Cylindrical Wire Arrays (NCWAs) have been studied extensively at Sandia National Laboratories on the 20 MA, 100 ns rise time Z-machine and have demonstrated an increase in x-ray power and reduction of pulse width (Deeney *et al.* 1998) as compared to single wire arrays, producing pulse shapes required for inertial confinement fusion (Cuneo *et al.* 2006, Cuneo *et al.* 2005). An important issue for NCWAs is understanding how the inner and outer arrays radiate and implode. To this end, other experiments at lower current facilities (Deeney *et al.* 2004, Safronova *et al.* 2008b) have sought to study the dynamics and radiative characteristics of nested arrays. In Deeney *et al.* 2004, tracer spectroscopy was utilized by switching Al (5056, 5% Mg) and pure Al (1100) between inner and outer arrays; it was shown that the outer array material reached the highest temperature plasma. It was shown in Safronova *et al.* 2008b, using mixed Al (5056) and SS (304, 69% Fe, 19% Cr, 9% Ni) NCWAs on the 1 MA, 100 ns rise time Cobra generator at Cornell University (Douglass *et al.* 2007), that the outer wire array radiates more intensely than the inner wire array. This was explained as the outer array having more kinetic energy than the inner array (due to its larger radius), though the complexity of nested arrays due to current switching and varying levels of inner-penetration of the outer array to the inner array makes this difficult to estimate (Terry *et*

al. 1999, Sanford *et al.* 2007). In this chapter, we present an extension of the work presented in Safronova *et al.* 2008b by comparing K-shell Al and other L-shell mid-Z's, specifically fielding mixed brass (70% Cu, 30 % Zn) and Al (5056) NCWAs on the 1.0 MA, 100 ns rise time Zebra generator at UNR (Kantsyrev *et al.* 2009), which will be presented in Section 4.2, and also fielding mixed Mo and Al NCWAs on both the Zebra and Cobra (Glidden *et al.* 2003) generators, which will be presented in Section 4.3. The advantage of studying NCWAs from both mixed brass and Al and mixed Mo and Al experiments is that L-shell Cu/Zn and K-shell Al/Mg radiate at approximately the same T_e (300 – 500 eV), while L-shell Mo and K-shell Al/Mg radiate at very different T_e (900 – 1400 eV for L-shell Mo), which can provide valuable extra information in how the inner and outer arrays radiate. Section 4.4 will conclude the chapter. The majority of the results showed in this chapter were published in High Energy Density Physics (Weller *et al.* 2012a).

4.2 Mixed Al and Brass Nested Cylindrical Wire Arrays on the Zebra Generator

The dynamics of mixed nested cylindrical wire arrays were studied at the UNR Zebra generator with existing theoretical and experimental tools to better understand the contributions of each array to the emitted radiation. In particular in this section, experimental results of mixed brass (70% Cu, 30% Zn) and Al (5056, 5% Mg) nested cylindrical wire arrays are analyzed and compared. The loads used brass in the inner array and Al in the outer array, or alternately, Al in the inner array and brass in the outer array, with a mass ratio of 1:1 (outer to inner). Consequently, radiative properties of K-shell Al and Mg ions and L-shell Cu and Zn ions are compared as functions of the placements of the brass and Al wires on the inner and outer arrays. Results show that the

placement of brass and Al, whether on the inner or outer array, dramatically affects the intensity of the x-ray emission. Specifically, the ratio of Cu L-shell to Al K-shell emissions changed from 4 when Al is in the outer array to 40 when brass is in the outer array, and the total radiated yield was highest when the brass was on the outer array (18 kJ, versus 15 kJ when brass is on the inner array). Each load was fielded twice to vary the timing of the time-gated imaging and spectral diagnostics. This provides a more complete understanding of the evolution of the plasma parameters over the x-ray pulse and highlights the importance of the time-gated diagnostics.

The outer and inner arrays were kept uniform with 8 wires of either brass (7.62 μm dia.) or Al (12.7 μm dia.) in the outer and inner arrays; the mass was the same ($\sim 30 \mu\text{g}/\text{cm}$) for all the arrays. The 1:1 mass ratio (outer to inner) is different than many of the load configurations in previous nested array studies, where the ratio ranged from 2:1 to 4:1 (outer to inner) (see, for instance, Coverdale *et al.* 2008 and Jones *et al.* 2008). The radius of the outer array was 13 mm, while the radius of the inner array was 6 mm, with interwire gaps of 5.1 and 2.4 mm, respectively. These gaps are relatively large compared to other work, but result from the desired mass loading of the arrays for optimal coupling to the Zebra generator and limitations on available wire sizes. For each experiment, the outer array was kept aligned with the inner array. Each load was fielded twice to vary the timing of the time-gated pinhole and x-ray spectrometers and obtain a more complete understanding of the evolution of the plasma parameters. K-shell Al and Mg emissions and L-shell Cu and Zn emissions were studied extensively via spectroscopy to evaluate the emissions as a function of time and original placement of the materials in the array. An extensive diagnostic suite, which included more than ten different beam-lines, was

fielded with the emphasis to study emissions from K-shell Al/Mg and L-shell Cu/Zn. These diagnostics are described throughout the text in the upcoming sections.

4.2.1 Time-integrated L-shell Cu and Zn and K-shell Al and Mg

Table 4.1 lists the mixed NCWAs of brass and Al discussed in this section. Shots 1790 and 1791 were performed with brass in the inner array and Al in the outer array and will be referred to as the Al-on-brass array. Shots 1792 and 1793 were the opposite configuration, with Al in the inner array and brass in the outer array and will be referred to as the brass-on-Al array (see Figure 4.1 for clarity). In all cases, the linear mass of the Al and brass alloys were kept approximately the same with $27 \mu\text{g}/\text{cm}$ for Al and $31 \mu\text{g}/\text{cm}$ for brass. The pinch length was 20 mm for all cases. A bare nickel bolometer was used to measure the total radiated energy, while a photoconducting diode (PCD) is used to derive energy $> 0.8 \text{ keV}$. The PCD was filtered using an $8 \mu\text{m}$ Be filter ($>0.8 \text{ keV}$, 0.5 ns resolution), measuring only the hottest part of plasmas in the experiments, which is approximately the region in which K-shell Al and Mg and L-shell Cu and Zn radiate. It is interesting to note that when brass is in the outer array, the total energy, E_{tot} , measured is higher than when brass is on the inner array, that is, $E_{\text{tot}}(\text{brass-on-Al}) \approx 18 \text{ kJ}$ and $E_{\text{tot}}(\text{Al-on-brass}) \approx 15 \text{ kJ}$. PCD energy, E_{PCD} , is also listed, with $E_{\text{PCD}}(\text{brass-on-Al}) \approx 0.39 \text{ kJ}$ and $E_{\text{PCD}}(\text{Al-on-brass}) \approx 0.36 \text{ kJ}$. It has been shown (Ouart *et al.* 2009) that for similar configurations the brass wire arrays radiate more total energy than Al wire arrays, which suggests in this case that the outer array contributes more to the total radiation than the inner array. Implosion times are also listed and are all between 110 and 120 ns. Zero time refers to the start of the current rise. In general, load parameters, such as wire diameter, are chosen to give an estimated implosion time of around peak current (100 ns).

Figure 4.2 shows time-integrated spatially resolved (TISR) spectra and pinhole (TIPH) images of shots 1790 (Al-on-brass) and 1793 (brass-on-Al). The spectra were taken with a KAP ($2d = 26.63 \text{ \AA}$) convex crystal spectrometer while the pinhole images were filtered to study emissions $>1.0 \text{ keV}$. Both diagnostics are axially resolved to study variations along the length of the pinch from anode to cathode. The spectra obtained on the other identical shots provided similar results to those shown here. Diagnostically important K-shell Al and Mg and L-shell Cu and Zn lines are indicated in Figure 4.2 (see Safronova *et al.* 2007 and Quart *et al.* 2010b for more information).

Shot #	Material outer-on-inner	Diameter (μm) outer-on-inner	Total energy (kJ)	PCD energy (kJ) ($> 0.8 \text{ keV}$)	Implosion time (ns)
1790	Al-on-brass	12.7-on-7.6	15.0	0.34	110
1791	Al-on-brass	12.7-on-7.6	14.5	0.37	112
1792	brass-on-Al	7.6-on-12.7	17.5	0.38	111
1793	brass-on-Al	7.6-on-12.7	17.5	0.39	118

Table 4.1. List of considered shots and parameters for NCWAs. In Zebra shots 1790 and 1791 have brass on the inner array and Al in the outer array, while Zebra shots 1792 and 1793 have Al on the inner array and brass on the outer array.

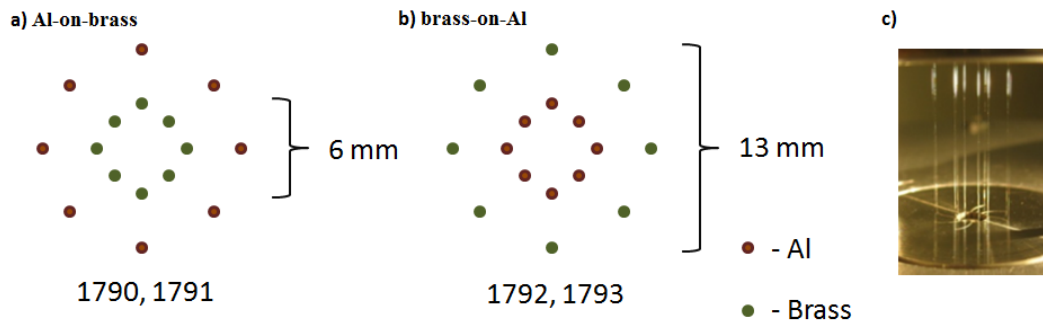


Figure 4.1. Illustrations for Al-on-brass (a) and brass-on-Al (b). Picture of a nested cylindrical wire array (c).

The Al-on-brass array produces optically thick K-shell Al and relatively optically thin L-shell Zn and Cu, with well-defined column like structures for both. This is strengthened by the corresponding pinhole image that shows only a few bright spots along the axis. Conversely, the brass-on-Al array produces almost optically thin K-shell Al and more optically thicker L-shell Zn and Cu, with radiation that is more defined by the respective bright spot formations seen from the pinhole image. In general, the optical thickness, or opacity effects, will be seen first in lines with higher radiative decay rates (Al1 and Al2 for K-shell Al and Cu 3C for L-shell Cu, for example), provided that a large enough ion density or plasma thickness exists. Therefore, when the material is on the outer array, the respective lines have higher opacity, which is an indicator of more intense radiation in those lines. These results agree with previous observations of mixed NCWA loads which indicate that the outer array contributes more to the radiated energy than in the inner array; this is discussed further in the final paragraph of this section.

Figure 4.3 shows example lineouts of the TISR spectra overlaid with the non-LTE kinetic models of Cu, Zn, Al, and Mg (Safronova *et al.* 2006a) used to derive electron temperatures and densities (T_e and n_e). The Cu and Zn models are used for L-shell radiation while the Al and Mg models are used for K-shell radiation. Generally speaking, the Al model is used to model lines that originate from high Rydberg states when the plasma is optically thin, in which case the 5% Mg in the alloy shows virtually no trace of lines. When Mg lines do appear in the spectra, Al is presumed optically thick, and thus the Mg model is used to estimate T_e and n_e . The models average over a uniform plasma slab that is used to obtain an escape factor for each transition.

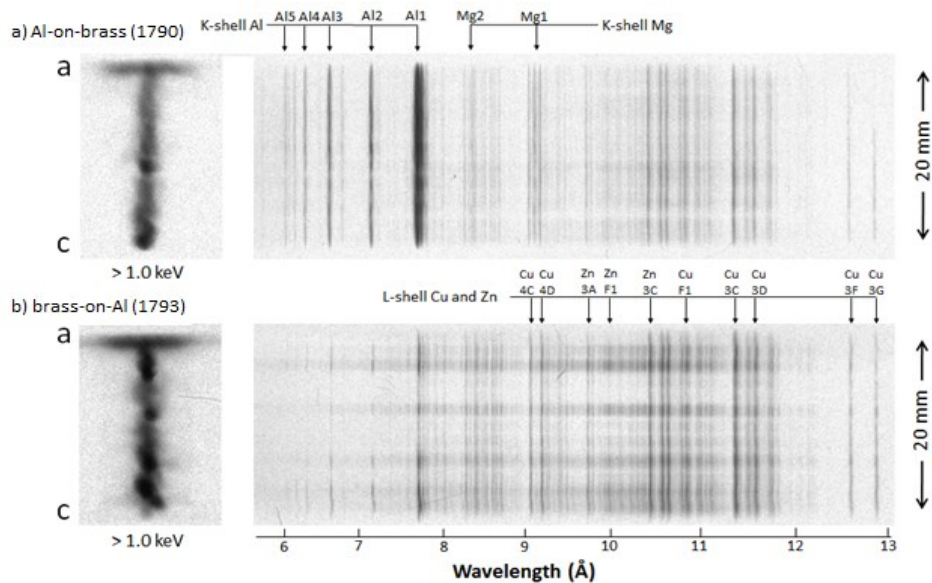


Figure 4.2. X-ray time-integrated spatially resolved spectra (right) and pinhole images (left) of NCWAs for configurations of Al-on-brass (a) and brass-on-Al (b). The “a” and “c” refer to anode and cathode, respectively.

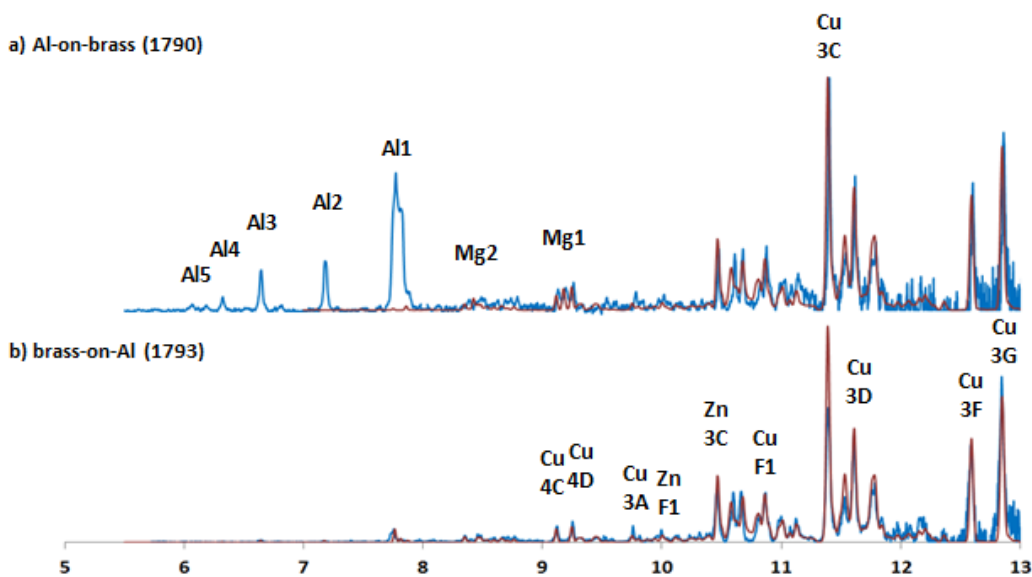


Figure 4.3. Examples of K-shell Al/Mg and L-shell Cu/Zn experimental (blue) and synthetic (red) spectra of NCWAs for configurations of Al-on-brass (a) and brass-on-Al (b) taken from Figure 4.2, near anode.

For the Al-on-brass load, the modeling shows that the L-shell Cu and Zn and K-shell Mg had similar electron temperatures, ranging from 320 to 370 eV. Electron density shows a different trend, however. The density for K-shell Mg remains relatively constant at $5 \times 10^{19} \text{ cm}^{-3}$ while L-shell Cu and Zn ranges from $5 \times 10^{19} \text{ cm}^{-3}$ near the anode to $5 \times 10^{18} \text{ cm}^{-3}$ near the cathode, a significant drop in density. For the brass-on-Al array, the electron temperatures for the L-shell Cu and Zn and K-shell Al are again similar, ranging from 310 eV to 380 eV, which is a slightly broader variation than observed for the Al-on-brass array. This variation is also evidenced in the respective pinhole images, which show non-uniformities in emissions for this same photon energy range. The electron densities for the brass-on-Al array range from $1.8 \times 10^{20} \text{ cm}^{-3}$ to $2 \times 10^{20} \text{ cm}^{-3}$ for K-shell Al while L-shell Cu and Zn varies from $1 \times 10^{19} \text{ cm}^{-3}$ near the anode to $5 \times 10^{18} \text{ cm}^{-3}$ near the cathode. As before, the Cu and Zn density is lower than the Al and Mg density, and decreases along the length of the pinch. For both configurations, the density from L-shell Cu and Zn is similar; however the K-shell Al and Mg density increases by a significant factor when the Al alloy is on the inner array compared to the outer array. Since the K-shell Al and Mg and L-shell Cu and Zn radiate at very similar electron temperatures, it is difficult to spot a clear trend on how T_e changes as a function of initial placement of the alloys. This will be discussed further in section 4.6.

While there is no obvious trend in T_e with initial alloy placement, it is clear that the intensity of the radiation is dramatically affected by the initial position of the wires. Analysis of the intensity of spectral lines shows that the ratio of the L-shell Cu/Zn to K-shell Al/Mg increases from 4 to 40 when the configuration changes from Al-on-brass to brass-on-Al, while at the same time the energy derived from the PCD signal, E_{PCD} , gives

comparable values. This ratio was estimated by integrating the intensity of the K-shell Al/Mg and L-shell Cu/Zn taken from various lineouts of the spectra and averaged. This result is another indicator of the importance of the material on the outer array in determining the overall emissions from the plasma.

4.2.2 Time-gated Spectra of L-shell Cu and Zn and K-shell Al and Mg

One of the goals in fielding each load twice was to attain a more complete picture of the time evolution of the plasma as well as assess overall reproducibility of the pulse shape and radiated output. To accomplish this, the timing of the time-gated spatially integrated spectrometer (TGSP) was varied for the shots, ranging from a start immediately before the main pulse peak to immediately after the main pulse peak. Figures 4.4 and 4.5 illustrate how the plasma evolves by plotting electron temperature of L-shell Cu/Zn and K-shell Al/Mg alongside a PCD signal with timing beginning from the start of the current rise. The electron temperatures shown in Figures 4.3 and 4.4 were inferred from the spectroscopic modeling.

For the Al-on-brass array (Figure 4.4), the L-shell Cu and Zn emissions have slightly higher T_e than the K-shell Al and Mg emissions, by an average of about 30 eV through the duration of both shots. The L-shell Cu and Zn show 350 eV 15 ns before the PCD peak, climbing to 390 eV near the PCD peak, dropping off to 340 eV 10 ns after the PCD peak. For identical timings, the K-shell Al and Mg emissions have T_e of 300, 350, and 310 eV. Electron densities were estimated to be approximately $5 \times 10^{19} \text{ cm}^{-3}$ for L-shell Cu and Zn and $1 \times 10^{20} \text{ cm}^{-3}$ for K-shell Al and Mg. This is different from the time-integrated results of Section 4.3, which showed nearly identical T_e , which suggests the evolution of the plasma is different for the brass and Al alloys.

For the brass-on-Al array (Figure 4.5), the results were slightly different; the K-shell Al emissions have a slightly higher electron temperature than the L-shell Cu and Zn emissions. The K-shell Al was estimated to be 380, 370, and 350 eV, while L-shell Cu and Zn were estimated to be 360, 350, and 320 eV for the same timings. Again, the temperatures follow the PCD signal. These measurements were obtained at times well after the main implosion, however, as opposed to during the main implosion as for the Al-on-brass array. This could explain the differences in plasma parameters observed, and highlights the need for more information on the evolution of these plasmas. Detailed measurements well before, during, and after the main implosion phase are needed to garner a more complete understanding of how these plasmas develop and radiate.

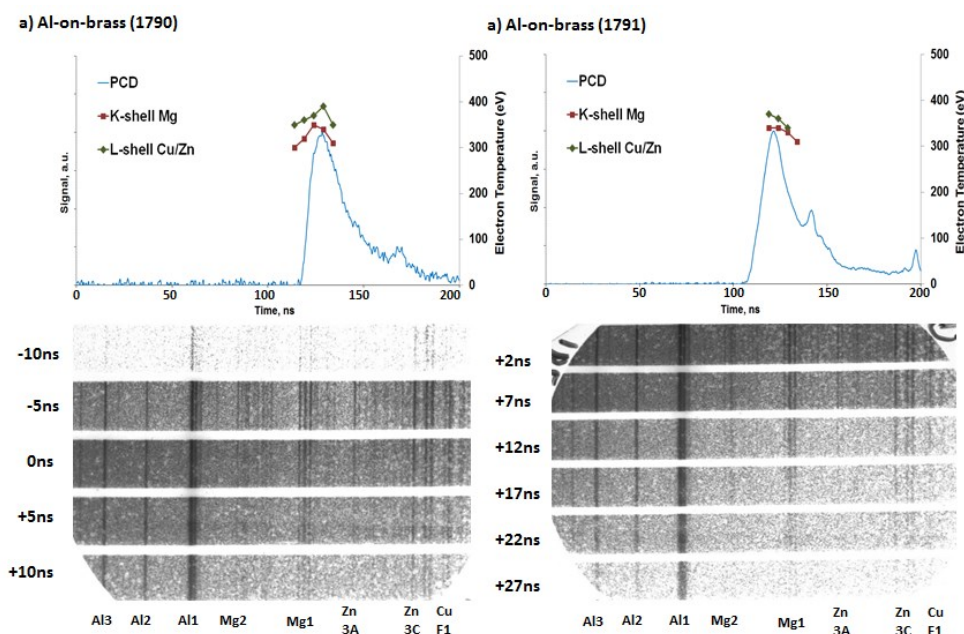


Figure 4.4. PCD signals with estimated electron temperatures (top) attained from TGSP (bottom) for Al-on-brass. The timings of the TGSP were changed from shot 1790 (a) to 1791 (b) to attain spectra from before, near, and after the main PCD peak.

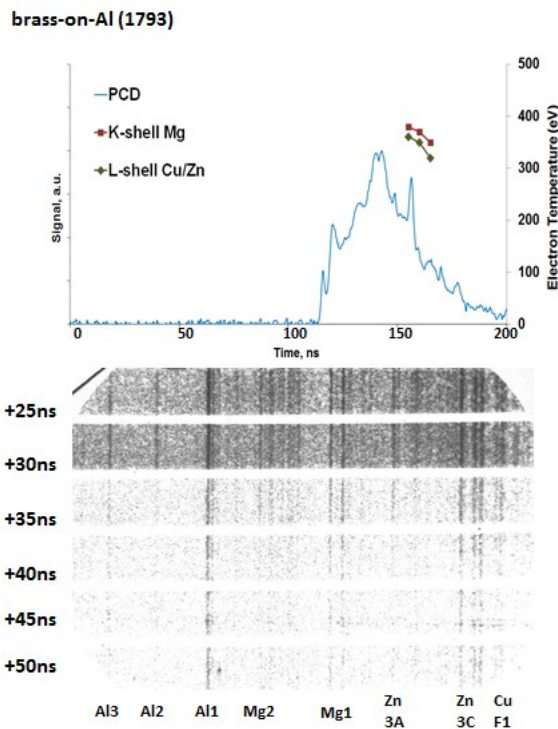


Figure 4.5. PCD signals with estimated electron temperatures (top) attained from time-gated spectra (bottom) for brass-on-Al for shot 1793.

It is also important to note the change in the PCD signal when changing configurations from Al-on-brass to brass-on-Al. For the Al-on-brass array, the signal for both shots has one primary pulse followed by one or two small secondary pulses, producing a narrow x-ray pulse. Looking back to Figure 4.2, this narrow x-ray pulse corresponds to a pinhole image which shows few bright spots and a relatively tight pinch. For the brass-on-Al array, however, the signal is more random, producing many pulses after the main pulse and is not as narrow as for the brass-on-Al array. Again, going back to Figure 4.2, formation of this many pulses corresponds to a pinhole image that shows many bright spots and not as tight of a pinch. For the Al-on-brass array, the average power was ~ 20 GW, while for the brass-on-Al array the average power was ~ 21 GW.

Even though the total energy radiated for the Al-on-brass array was significantly less than that of the brass-on-Al array, the narrower x-ray pulse for the Al-on-brass array resulted in a similar radiated power.

4.2.3 Wire Ablation Dynamics Modeling for Mixed NCWAs of L-shell Cu and Zn and K-shell Al and Mg

Figures 4.6 and 4.7 show the Wire Ablation Dynamics Model (Esaulov *et al.* 2009) (WADM) results for the Al-on-brass and brass-on-Al arrays. For the complicated case of NCWAs, the model is able to describe the uneven current distribution through the array wires and the inductive current transfer that changes the current distribution as the array implodes. In the nested wire array configuration there are two main competing factors when calculating the wire mass ablation rate described as follows in Equation 4.1:

$$\frac{dm_n}{dt} = -G_n I_n^2 \quad 4.1$$

where m_n is the ablated mass per unit length of the n^{th} wire, I_n is the electric current carried by the n^{th} wire, G_n is the ablation rate coefficient (Lebedev *et al.* 2001, Lebedev *et al.* 2002). The model of inductive current partition implemented in the WADM predicts uneven current distribution between the outer (larger current fraction) and inner (smaller current fraction) arrays. Thus, in a single wire material nested array load the outer array always implodes first. The scenario, however, may be different for mixed wire material nested arrays. For example, the ablation rate coefficient for Al is larger than for most other materials, including brass (see Esaulov *et al.* 2009), which can affect the overall

initiation and implosion of the different materials in the array. In the case of a NCWA, it was shown that on COBRA generator the inner Al array implodes first, contrary to a conventional implosion scenario for NCWA, when the outer array is built of SS wires of the matching mass (Williamson *et al.* 2009). Since our arrays also used Al, we have examined this effect with the WADM here as well.

Figures 4.6 and 4.7, the TGSP spectra (also shown in Figures 4.4 and 4.5), time-gated pinhole (TGPH) and shadowgraphy images are shown correlated with the measured current, PCD (mentioned in Sections 4.2.1 and 4.2.2), x-ray diode (XRD), and extreme ultraviolet (EUV) signals. The XRD was filtered using a 5 μm Kimfoil filter ($E > 0.18$ keV, 0.5 ns resolution). The EUV was filtered using a 0.2 μm Al filter ($E > 17$ eV, 0.5 ns resolution). The two rows of images produced with the TGPH camera had different filters with cutoff energies of 1 keV (bottom) and 3 keV (top). The WADM produced the thermalized kinetic energy, W_{Th} , and the inner and outer array position as a function of time.

For both cases considered, the outer array is estimated to implode before the inner array. Also, the thermalized kinetic energy for both cases is less than 8 kJ, which is significantly less than the total energy measured by the bare Ni bolometer, indicating there is another mechanism in addition to thermalized kinetic energy that is responsible for the total radiation yields, perhaps Ohmic heating (Safronova *et al.* 2011).

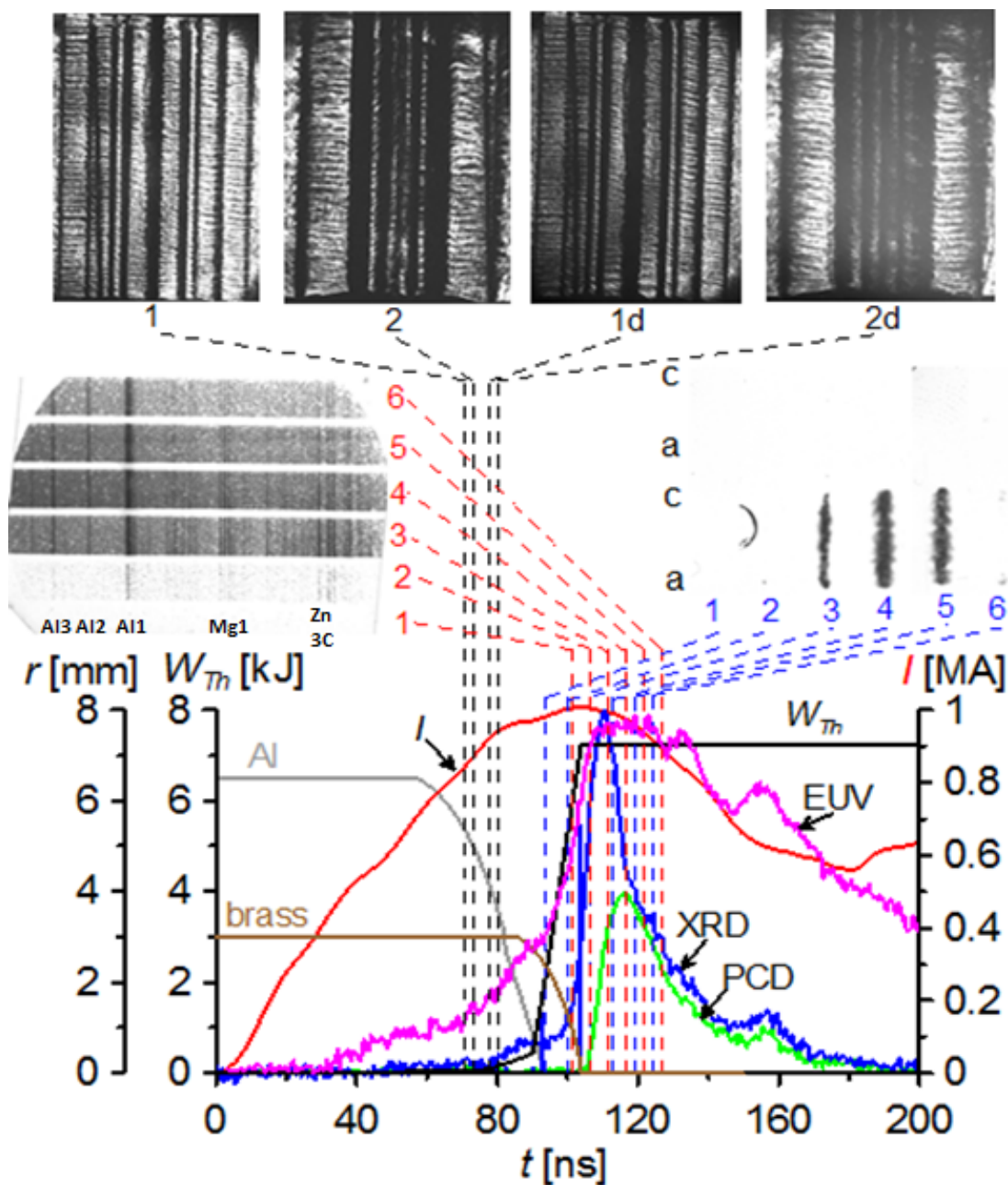


Figure 4.6. Comparison of data for mixed NCWA for shot 1790 with brass the inner array and Al the outer array (Al-on-brass). Shadowgraphy, time-gated spectra and pinhole images, as well as XRD, PCD, and EUV signals are shown with WADM calculations, where W_{Th} is the simulated thermalized kinetic energy.

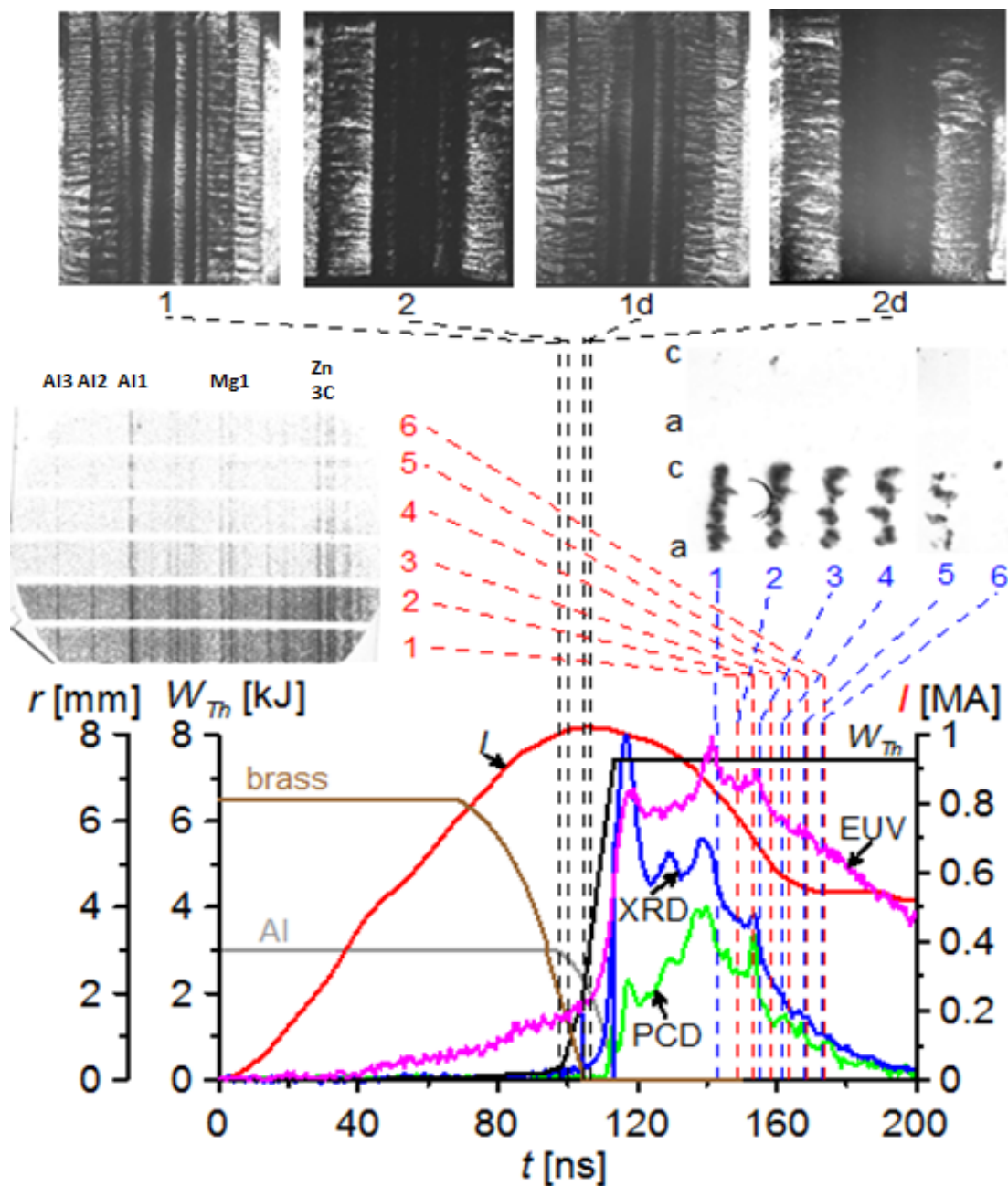


Figure 4.7. Comparison of data for mixed NCWA for shot 1793 with Al the inner array and brass the outer array (brass-on-Al). Shadowgraphy, time-gated spectra and pinhole images, as well as XRD, PCD, and EUV signals are shown with WADM calculations, where W_{Th} is the simulated thermalized kinetic energy.

The XRD signal for the Al-on-brass array shows similar structure as the PCD signal discussed in Section 4.2.2, with a narrow main pulse width and one small secondary pulse after. The EUV signal is interesting to discuss. The EUV radiation is noticeable virtually from the start of the current rise and continues well after the both the PCD and XRD signals have dissipated. The narrow pulse width of the PCD and XRD signal is not seen due to continued strong EUV radiation after the main pulse. For the brass-on-Al array, the XRD signal again yielded similar results than that of the corresponding PCD signal, producing many pulses after the main pulse and is not as narrow as for the Al-on-brass array. The EUV signal for this configuration again shows very early signal and continuation well after the PCD and XRD signals have dissipated, which is not unexpected due to the EUV diode capturing softer x-rays. For more information of about EUV signals in Z-pinch plasmas see Whitney *et al.* 2004 and Velikovich *et al.* 1998.

The shadowgraphy is taken early in the implosion and show four frames of timing. The EKSPLA laser was used, which operates at 532 nm with a 0.15 ns pulse. The 1, 2, 1d, and 2d labeling refer to where and when the laser passed through during the experiment. Two channels are used, channel 1 and channel 2 and are angled 22.5 degrees from one another. The “d” in 1d and 2d refer to a 6 ns delay from the non-delay counterparts. Channel 2 also has an intrinsic 3 ns delay from channel 1. Here, shadowgraphy is a useful diagnostic for seeing the evolution of the ablation process. For the Al-on-brass array, frame 1 is taken about 75 ns after current start (35 ns before implosion peak) and shows that the outer Al array has already begun the implosion. The WADM for this load predicts that the outer Al array will begin to implode about 60 ns after current start, in agreement with the shadowgraphy observations. For the brass-on-

Al array, the frame 1 is taken about 98 ns after current start (20 ns before implosion peak) and shows the outer brass array well into the implosion. The WADM for this load predicts that the outer brass array will begin to implode about 75 ns after current rise, again, in agreement. The difficulty in shadowgraphy images with NCWAs, however, is that it is very difficult to distinguish between the outer and the inner array when looking within the diameter of the inner array (in this case, 6 mm). In turn, this makes it difficult to see the ablation process of the inner array compared to the outer array.

For the TGPH images, different timings were captured for the two loads. The six frames of the TGPH had 6 ns of delay from the previous frame, with each frame capturing between 3 and 5 ns. For the Al-on-brass array, the TGPH camera captured frames during the middle of the implosion. For > 1 keV, the first two frames (-15 ns and -9 ns relative to implosion peak) show no evidence of radiation. The third, fourth, and fifth frames (-3 ns, +3 ns, and +9 ns relative to implosion peak) show strong radiation with a nice column-like structure, similar to the one seen in the in the TIPH image from Figure 4.2 with the same cutoff energy. The sixth frame (+15 ns relative to implosion peak) again shows no evidence of radiation for > 1 keV. For the brass-on-Al array, the TGPH camera captured frames late in the implosion, starting from +24 ns relative to implosion peak. For such late timings, the > 1 keV frames show very unstable and non-uniform structures. Unfortunately, due to the different timings, the TGPH images for the two loads cannot be directly compared.

4.3 Mixed Mo and Al Nested Cylindrical Wire Arrays on the Zebra and Cobra Generators

Results of experiments with nested cylindrical wire arrays of Mo and Al that were performed on the 1.0 MA, 100 ns Zebra generator and the 1.0 MA, 100 ns Cobra generator are presented. The loads on both the Zebra and Cobra generators utilized Al tracer wires with different concentrations (~30% Al for Zebra and ~15% Al for Cobra), which were in either the inner or outer array. Data are fully compared and analyzed from a set of diagnostics, which included fast, filtered x-ray diodes; a Ni bolometer; laser shadowgraphy and streak setups; time-gated and time-integrated x-ray pinhole cameras; and spatially resolved, time-integrated and spatially-integrated, time resolved x-ray spectrometers. Implosion dynamics are analyzed with the Wire Ablation Dynamics Model. Non-LTE kinetic modeling of L-shell Mo and K-shell Al and Mg was utilized to derive plasma electron temperature and density and to estimate opacity effects.

Shot # Generator	Material # Wires	Diameter (μm)	Linear Mass ($\mu\text{g/cm}$)	Al (%)	Total Energy (kJ)
1043 Cobra	Al/Mo-on-Mo 2/6-on-8	16.8/8.9-on-8.9	101	15	5.8
1044 Cobra	Mo-on-Al/Mo 8-on-2/6	8.9-on-16.8/8.9	101	15	7.0
1794 Zebra	Mo-on-Al/Mo 8-on-4/4	8.9-on-17.8/8.9	103	30	19.4
1795 Zebra	Al/Mo-on-Mo 4/4-on-8	17.8/8.9-on-8.9	103	30	18.5

Table 4.2. List of considered shots and parameters for NCWAs of mixed Mo and Al on the Cobra and Zebra generators.

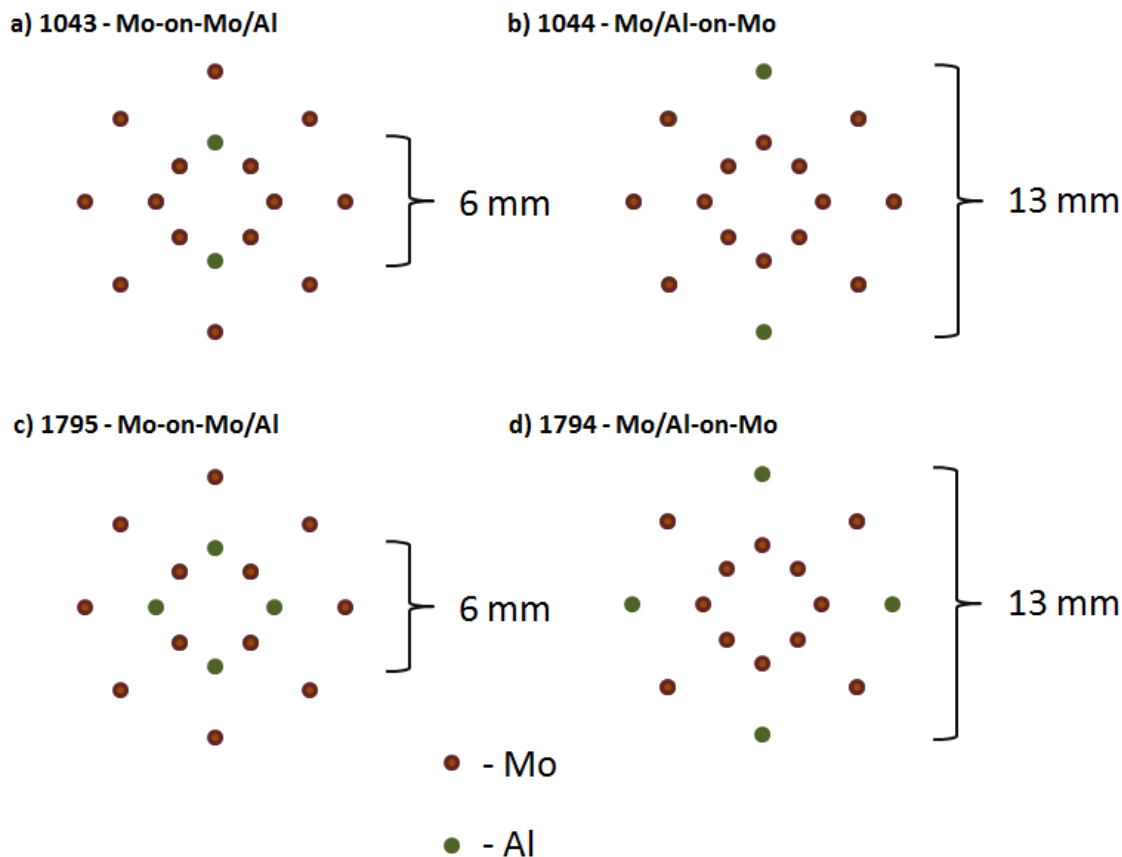


Figure 4.8. Illustrations for (a) Mo-on-Mo/Al (1043), (b) Mo/Al-on-Mo (1044), (c) Mo-on-Mo/Al (1795), and (d) Mo/Al-on-Mo (1794).

Table 4.2 lists the mixed NCWAs of Mo and Al discussed in this section. Shots 1043 and 1044 were performed on the 1.0 MA Cobra generator with shot 1043 having two Al tracer wires in the inner array and shot 1044 having two Al tracer wires in the outer array. Shots 1794 and 1795 were performed on the 1.0 MA Zebra generator with shot 1794 having four Al tracer wires in the outer array and shot 1795 having four Al tracer wires in the inner array. The NCWAs with Al tracer wires in the outer array will be referred to as Mo/Al-on-Mo and with Al tracer wires in the inner array will be referred to as Mo-on-Mo/Al (see Figure 4.8 for clarification). In all cases, the linear mass of the loads were

kept approximately the same at $\sim 100 \mu\text{g}/\text{cm}$. The pinch length was 20 mm for all cases and the inner array had a 6.0 mm diameter while the outer array had a 13 mm diameter. A bare nickel bolometer was used to measure the total radiated energy, while a photoconducting diode (PCD) is used to derive energy $> 0.8 \text{ keV}$. Two PCD's were fielded for the Cobra experiments, one was filtered using a $2 \mu\text{m}$ Kimfoil filter ($>0.2 \text{ keV}$) to capture soft x-ray radiation, the other was filtered using a $12 \mu\text{m}$ Be filter ($>0.9 \text{ keV}$) measuring only the hottest part of plasmas in the experiments, which is approximately the region in which K-shell Al and L-shell Mo radiate. An XRD and PCD were fielded for the Zebra experiments, the XRD using a $5 \mu\text{m}$ Kimfoil filter ($>0.2 \text{ keV}$) to capture soft x-ray radiation, the PCD was filtered using an $8 \mu\text{m}$ Be filter ($>0.8 \text{ keV}$) measuring only the hottest part of plasmas in the experiments, which is approximately the region in which K-shell Al and L-shell Mo radiate.

4.3.1 Implosion Characteristics of Mo and Al NCWAs on Zebra

This section will explore results of the implosion characteristics of the experiments from Mo and Al NCWAs performed on the Zebra generator. Figure 4.9 shows results from Zebra shot 1795 Mo-on-Mo/Al of signals, which include PCD and XRD signals and current, shadowgraphy images, time-gated spatially resolved pinhole and spatially integrated spectra images, and a lineout along with synthetic spectra from the spectra. The signals in Figure 4.9(a) show an implosion time of 122 ns on the XRD, however the PCD signal doesn't appear until 140 ns with a sharp rise and fall, similar to the Cobra shot 1043 seen in Figure 4.9(b), except with similar events occurring roughly 20 ns earlier in time. The XRD shows a very faint increase around the 60 ns mark; however it's too small to be compared to the pre-pulse shapes seen in the Cobra experiments. The

TGPH images at > 3.0 keV are relatively weak, except for a column-like structure which corresponds to the narrow PCD pulse at 140 ns. The TGSP in Figure 4.9(c) begins timing at 140 ns, and the first image corresponds to the PCD pulse, and produced K-shell Al with $T_e = 510$ eV, which is quite hot. After this only faint K-shell Al lines are seen after stagnation.

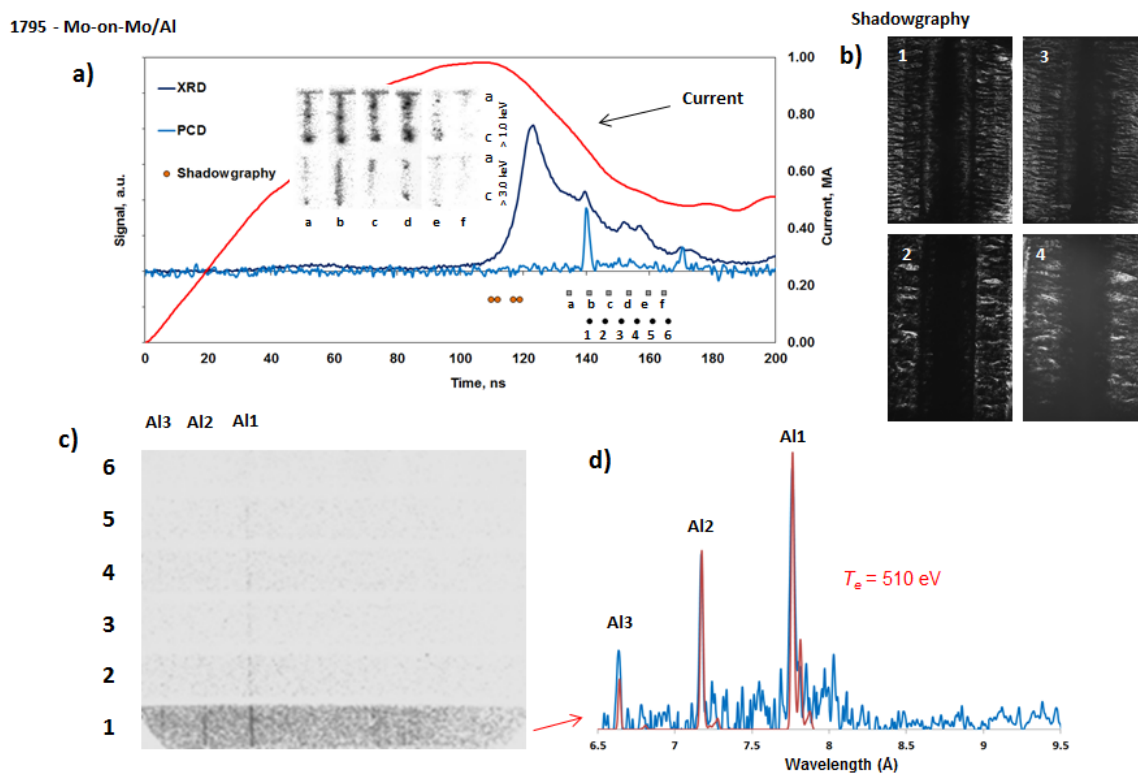


Figure 4.9. Signals, current, and time-gated pinhole images (a), shadowgraphy images (b), time-gated spatially integrated spectra (c), and in (d) a lineout taken from frame 6 (c) with experimental (blue) and synthetic spectra (red) of Mo-on-Mo/Al, Zebra shot 1795. The synthetic spectra is modeled K-shell Al at $T_e = 510$ eV.

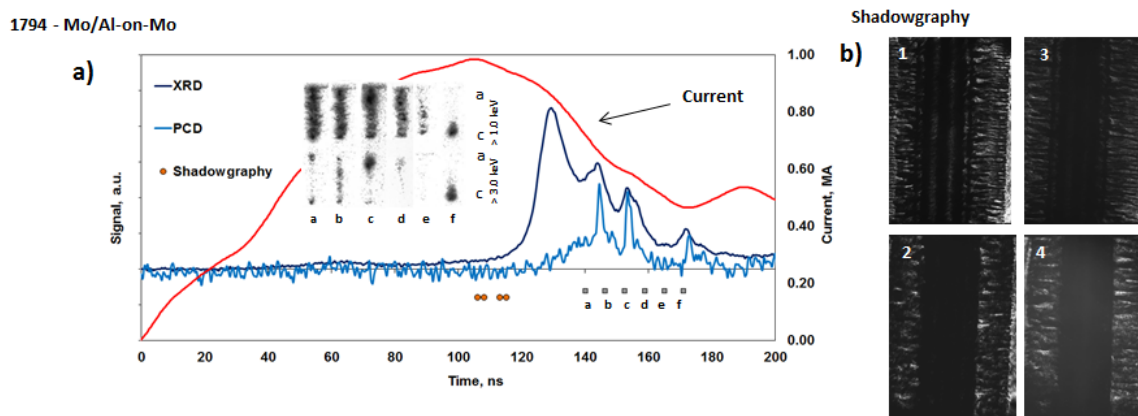


Figure 4.10. Signals, current, and time-gated pinhole images (a), shadowgraphy images (b) of Mo/Al-on-Mo, Zebra shot 1794.

Figure 4.10 shows results from Zebra shot 1794 Mo/Al-on-Mo of signals, which include PCD and XRD signals and current and shadowgraphy images. The PCD and XRD signals appear similar to the signal from shot 1795, which had the four Al tracer wires on the inside, with an implosion time of 128 ns and a few PCD signal bursts at 144 and 153 ns. The biggest difference from shot 1795 is in the TGPH images at > 1.0 keV, which is in the similar energy range of K-shell Al radiation. The first four frames in Figure 4.10(a) show very intense and column-like radiation, as opposed to in Figure 4.9(a), where the TGPH image > 1.0 keV shows relatively weaker and less column-like structure.

4.3.2 Radiative Characteristics of Mo and Al NCWAs on Zebra

This section focuses on the radiative characteristics of the Mo and Al NCWAs on the Zebra generator. Figure 4.11 shows TISP spectra and pinhole TIPH images of Zebra shot 1795 (Mo-on-Mo/Al). These experiments contained twice the number of Al tracer wires than the Cobra experiments, and the results are seen here. K-shell Al and L-shell Mo

radiation are both measured, most prevalent near the cathode, on the TISP spectra image and lineouts were taken and modeling was accomplished. L-shell Mo was modeled to have plasma parameters of $T_e = 1075$ eV and $n_e = 9 \times 10^{19} \text{ cm}^{-3}$ while K-shell Al was modeled to have plasma parameters of $T_e = 535$ eV and $n_e = 9 \times 10^{18} \text{ cm}^{-3}$. L-shell Mo is seen to radiate from two bright spots, while K-shell Al can be seen from possibly three, though both are very faint.

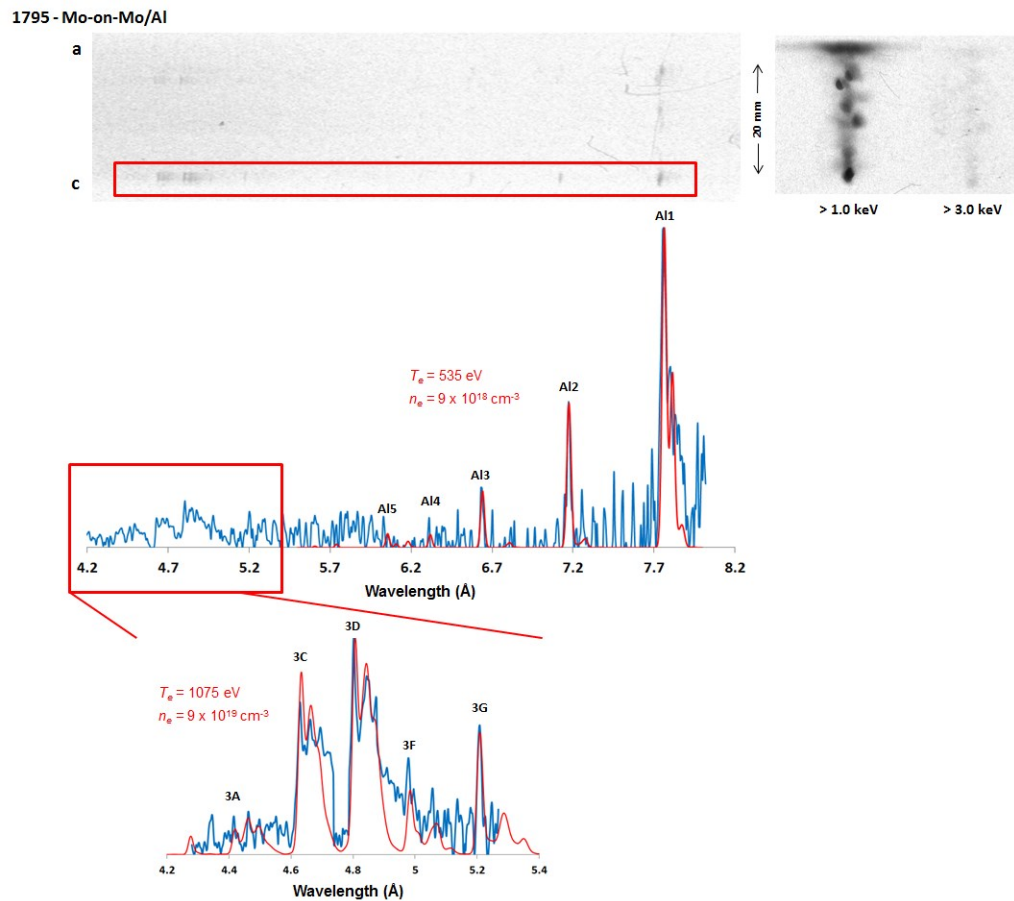


Figure 4.11. Time-integrated spatially resolved spectra (top-left) and pinhole (top-right) images of Mo-on-Mo/Al, Zebra shot 1795. Below is a lineout taken from the experimental spectra from above in blue and in red is modeled synthetic spectra of K-shell Al below that of L-shell Mo.

Contrast these results to Figure 4.12, where TISP spectra and pinhole TIPH images of Zebra shot 1794 (Mo/Al-on-Mo) are shown. In this experiment the Al tracer wires are located on the outside rather than on the inside. The results show K-shell Al radiating in a column-like structure with little to no L-shell Mo measured. With the absence of L-shell Mo, K-shell Al, though more prevalent, radiated at less electron temperature than for shot 1795. Lineouts were taken from the anode to cathode with results shown in Figure 4.12. The K-shell plasma parameters, from anode to cathode, are as follows: $T_e = 410$ eV and $n_e = 4 \times 10^{19} \text{ cm}^{-3}$, $T_e = 375$ eV and $n_e = 1 \times 10^{19} \text{ cm}^{-3}$, $T_e = 360$ eV and $n_e = 3 \times 10^{18} \text{ cm}^{-3}$, $T_e = 375$ eV and $n_e = 1 \times 10^{19} \text{ cm}^{-3}$.

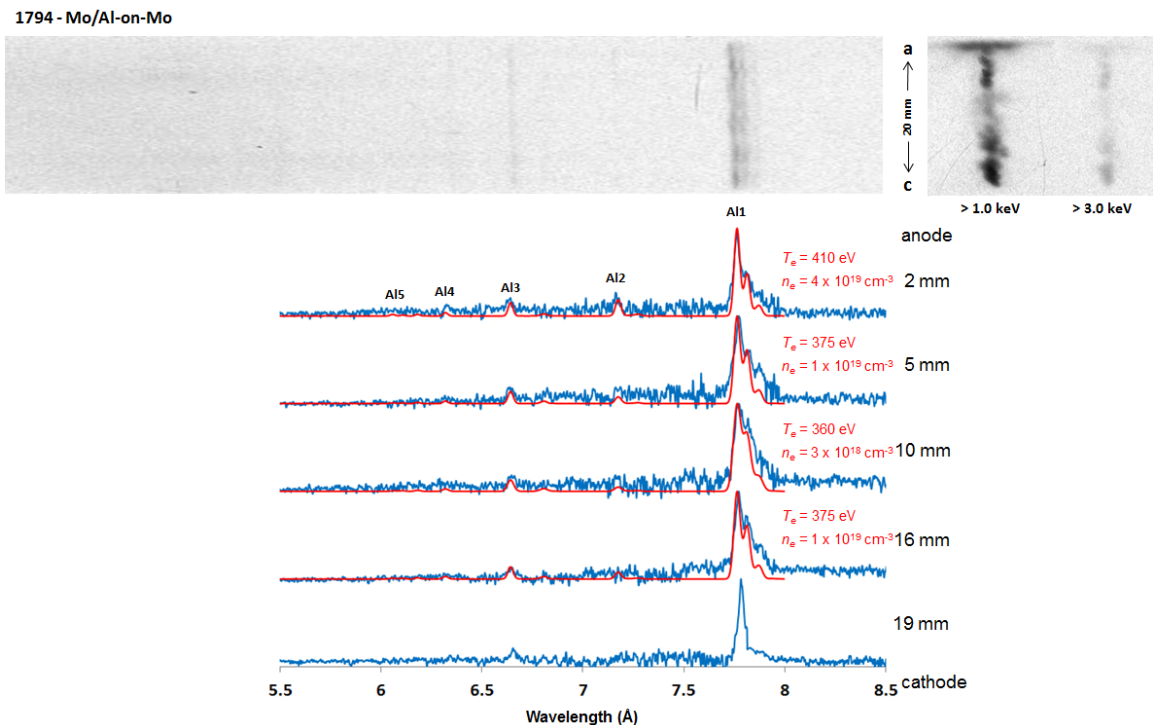


Figure 4.12. Time-integrated spatially resolved spectra (top-left) and pinhole (top-right) images of Mo/Al-on-Mo, Zebra shot 1794. Below are lineouts taken from the experimental spectra from above in blue and in red are modeled synthetic spectra of K-shell Al. The distances from anode for each lineout are located to the right.

4.3.3 Implosion Characteristics of Mo and Al NCWAs on Cobra

This section focuses on the implosion characteristics of the Mo and Al NCWAs on the Cobra generator. Figure 4.13 shows results from Cobra shot 1043 Mo-on-Mo/Al of an optical streak image, signals, which include two PCD signals of different energy regimes (>0.2 keV and >0.9 keV) and current, WADM showing how the inner and outer wires radiate, EUV images, and shadowgraphy images. First, the optical streak image in Figure 4.13(a), which is taken with a radially resolved optical streak camera with 4 ns resolution and 200 ns duration, shows how and when the inner and outer arrays implode. What's very interesting here is that the two inner Al wires appear to implode before the outer Mo wires, which was originally unexpected. Modeling was accomplished with the WADM (Figure 4.13(b)) and showed results are in good agreement in with the optical streak results of the inner two Al wires imploding before the outer and inner Mo wires. This could be explained by the faster ablation rate of Al compared to Mo. Looking at the two PCD signals, the > 0.2 keV signal shows a strong pre-pulse shape at around 75 ns into the current rise which is possibly early Al wire radiation, followed by a main implosion around 150 ns, and two to three pulses following lasting for another 60 ns of time. A main implosion at 150 ns indicates poor correlation with the current maximum at 100 ns and could explain the weak L-shell Mo radiation seen in Figure 4.9. The > 0.9 keV signal showed no signal until 175 ns into current rise and is very narrow, which again could explain the weak L-shell Mo radiation. EUV and shadowgraphy images shown in Figure 4.13 (c-d) show results around the 100 ns current rise time and show a well-defined pre-cursor column in the middle with original wires still ablating, which correlates well with the PCD signals. Figure 4.14 shows similar data as Figure 4.13, but

from Cobra shot 1044 Mo/Al-on-Mo. The optical streak image in Figure 4.14(a) shows the two outer Al wires clearly imploding before the outer and inner Mo wires, which is again predicted well by the WADM in Figure 4.14(b). The two PCD signals showed similar results as before, with a well-defined pre-pulse shape near 75 ns into the current rise, again, possible Al early radiation, and a main implosion around 175 ns, instead of 150 ns. Instead there appears to be a pulse-foot shape at 150 ns where the main implosion was before for Mo-on-Mo/Al. The EUV and shadowgraphy images in Figure 4.14(c-d) show images taken later in time than the previous experiment and shows destruction of the wires at around 125 ns in time.

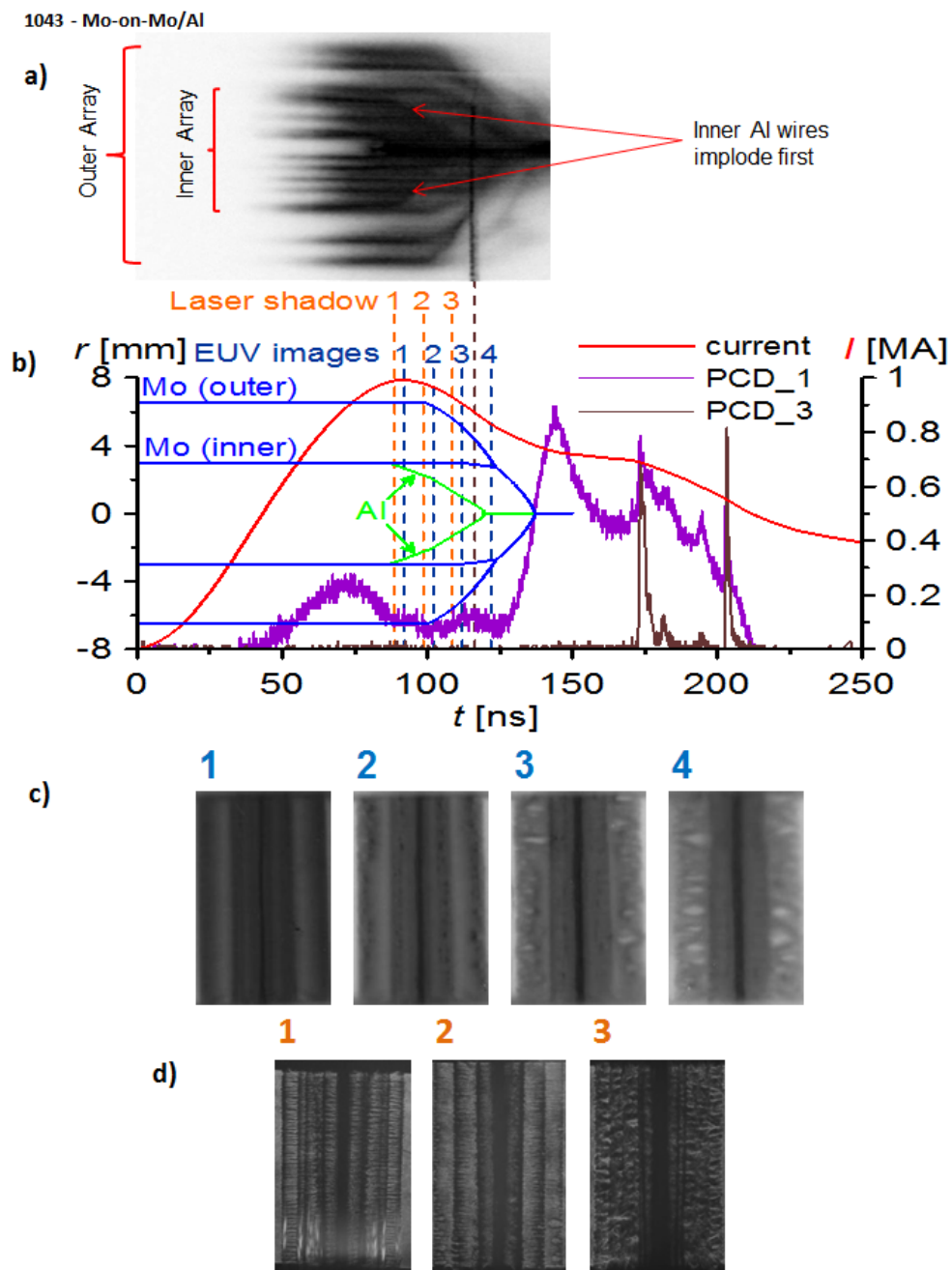


Figure 4.13. Optical streak image (a), signals, current, and wire ablation dynamics modeling (b), EUV images (c), and shadowgraphy images (d) of Mo-on-Mo/Al, Cobra shot 1043. PCD_1 is filtered at > 0.2 keV and PCD_3 is filtered at > 0.9 keV.

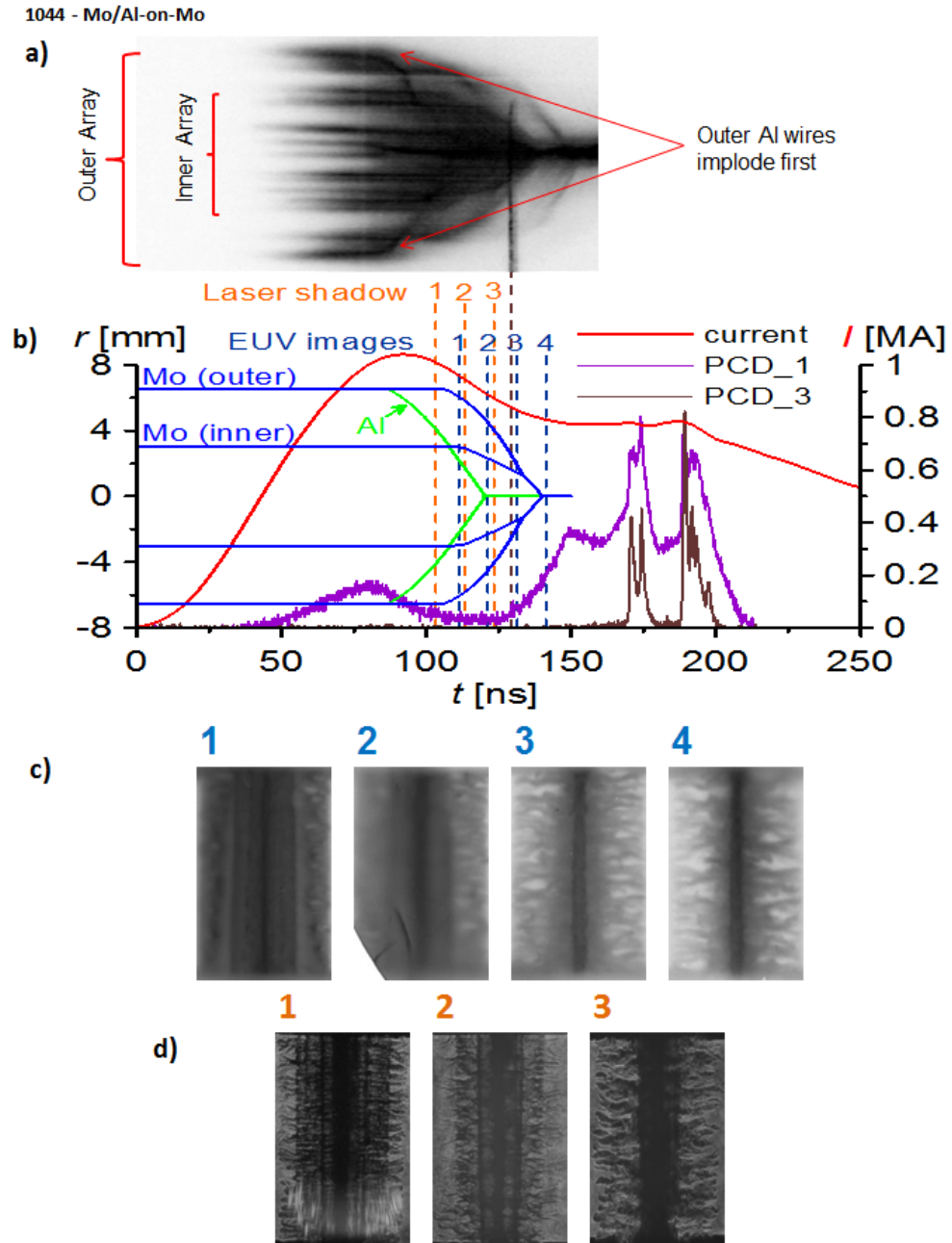


Figure 4.14. Optical streak image (a), signals, current, and wire ablation dynamics modeling (b), EUV images (c), and shadowgraphy images (d) of Mo/Al-on-Mo, Cobra shot 1044. PCD_1 is filtered at > 0.2 keV and PCD_3 is filtered at > 0.9 keV.

4.3.4 Radiative Characteristics of Mo and Al NCWAs on Cobra

This section focuses on the radiative characteristics of the Mo and Al NCWAs on the Cobra generator. Figure 4.15 shows time-integrated spatially resolved spectra (TGSP) and pinhole (TIPH) images of Cobra shot 1043 (Mo-on-Mo/Al). The spectra was taken with a potassium hydrogen phthalate (KAP) ($2d = 26.63 \text{ \AA}$) convex crystal spectrometer while the pinhole image was filtered to study emissions $>1.0 \text{ keV}$. Both diagnostics are axially resolved to study variations along the length of the pinch from anode to cathode. Diagnostically important L-shell Mo lines are indicated. Despite multiple bright spots measured, only one bright spot seen on the TIPH image located in the middle of the pinch produced any noticeable L-shell Mo radiation. From this, no K-shell Al radiation is measured on the film, likely due to the two wires located on the inner array and contributing only 15% of the total mass. In the same figure, a lineout was taken of the L-shell Mo radiation and a non-LTE kinetic L-shell Mo model was used to derive plasma parameters of $T_e = 1140 \text{ eV}$ and $n_e = 3 \times 10^{19} \text{ cm}^{-3}$.

1043 - Mo-on-Mo/Al

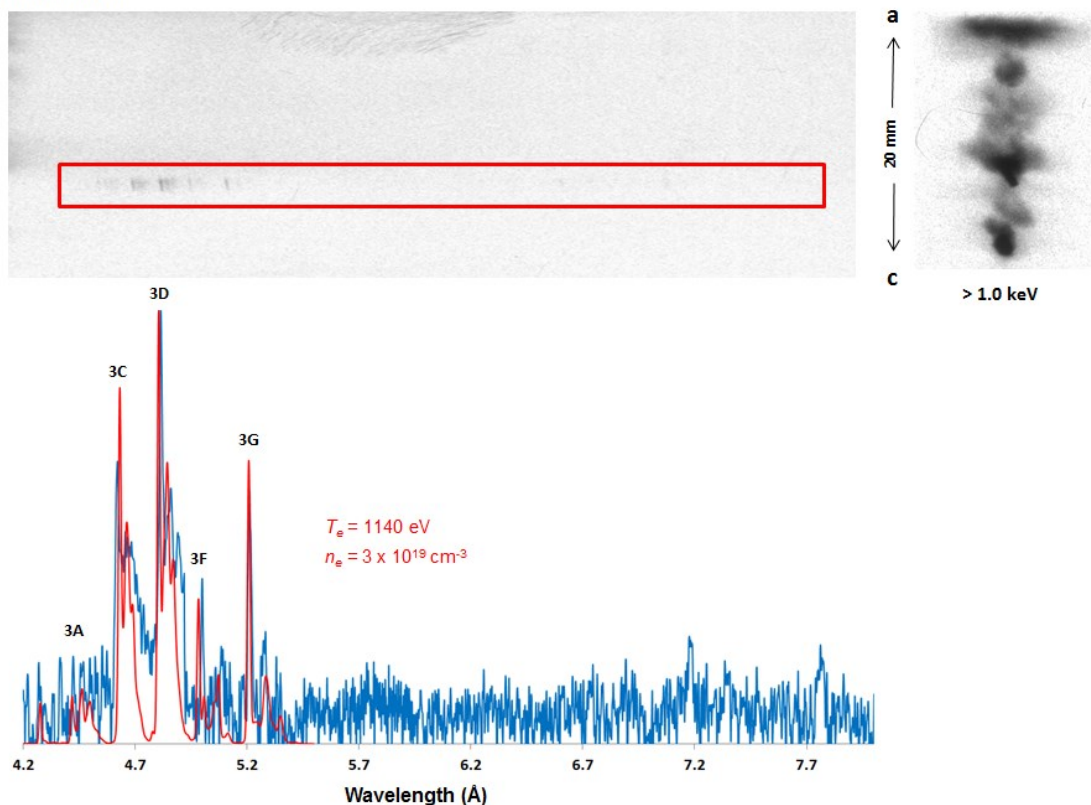


Figure 4.15. Time-integrated spatially resolved spectra (top-left) and pinhole (top-right) images of Mo-on-Mo/Al, Cobra shot 1043. Below is a lineout taken from the experimental spectra from above in blue and in red is modeled synthetic spectra of L-shell Mo with plasma parameters of $T_e = 1140$ eV and $n_e = 3 \times 10^{19} \text{ cm}^{-3}$.

Figure 4.16 shows TISP and TIPH images of Cobra shot 1044 (Mo/Al-on-Mo). With the Al tracer wires on the outer array for this shot compared to the previous shot, K-shell Al is measured from three locations along the pinch, and L-shell Mo is produced from two of those locations, near the middle to cathode area. It's clear that where L-shell Mo radiates the Al $_{2\alpha}$ line ($\text{Ly}\alpha$) appears, indicating hotter electron temperatures for K-shell Al than where K-shell Al radiates without significant L-shell Mo radiation, near the anode. In the same figure, lineouts were taken from the TISR spectra and successful modeling

was accomplished for L-shell Mo for the lineout taken near the middle with plasma parameters $T_e = 1130$ eV and $n_e = 9 \times 10^{18} \text{ cm}^{-3}$, which suggest a relatively hot but low dense plasma, compared to other L-shell Mo plasmas studied in chapter 3.

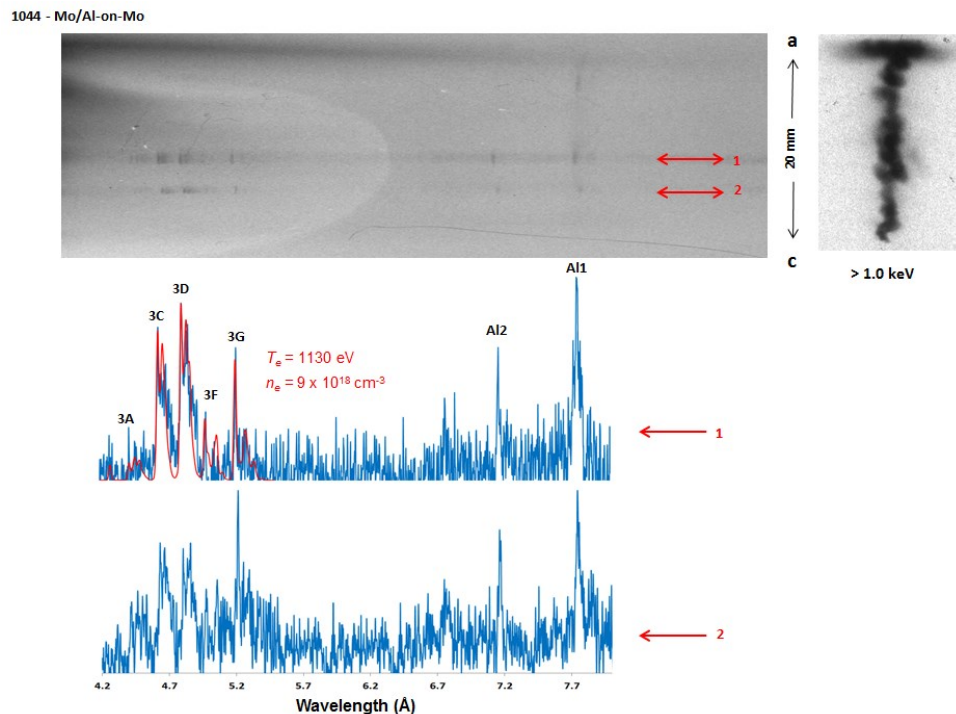


Figure 4.16. Time-integrated spatially resolved spectra (top-left) and pinhole (top-right) images of Mo/Al-on-Mo, Cobra shot 1044. Below are two lineouts taken, marked “1” and “2”, from the experimental spectra from above in blue and in red is modeled synthetic spectra of L-shell Mo with plasma parameters of $T_e = 1130$ eV and $n_e = 9 \times 10^{18} \text{ cm}^{-3}$.

4.4 Discussion and Conclusions of Mixed Material Nested Cylindrical Wire Arrays

In this chapter, experiments and analysis of data for mixed Al and brass nested cylindrical wire arrays were accomplished for the first time. The Al and brass wires were switched between experiments to compare how the inner and outer arrays radiate and see

how each contributes to the stagnated plasma. In addition, time-gated spectroscopy was utilized to provide a more complete understanding of the evolution of the plasma by changing the timing between identical shots. Results show that, in agreement with previous observations, the outer array contributes more to the emissions than the inner array. This is evidenced by analysis of time-integrated spectroscopy of the L-shell Cu and Zn and K-shell Al and Mg radiation, where it was observed that the L-shell Cu/Zn to K-shell Al/Mg ratio increased by a factor of 10 when switching from the Al-on-brass to the brass-on-Al configuration. The opacity of the emission lines was also affected by the initial wire array position, with the outer array wires producing significantly more optically thick lines as compared to the inner array wires, most easily seen in the K-shell Al radiation. The pulse shapes from the signals, such as the PCD signal, also seem to be affected by the initial wire array position (easily seen in Figures 4.6 and 4.7). When comparing the brass-on-Al and Al-on-brass arrays, the brass-on-Al array gives higher total energy (18 kJ to 15 kJ) in a wider pinch diameter with a broader, multiple pulse PCD signal than the Al-on-brass array (see Figures 4.4 and 4.5).

One of the key questions in this study is how does changing wire array position from the outer to inner array affect plasma parameters, such as electron temperature and density. The theoretical modeling of the measured spectra plays an important role in this analysis. For example, time-integrated spectral analysis in Deeney *et al.* 2004 showed that the highest temperature plasma is produced by the material on the outer array. In Safronova *et al.* 2008b the spectral analysis indicated that the plasma from the outer array of a mixed NCWA can be cooler than the inner array by having unequal masses between the inner and outer arrays (about 2:1 mass ratio, outer to inner). Here, the results aren't

quite as clear. This is due to the fact that L-shell Cu and Zn and K-shell Al and Mg radiate at nearly identical electron temperatures for the time-integrated spectral results. The time-gated spectral results, however, show a possible different pattern. When the Al array is the outer array, the T_e for the K-shell Al and Mg is less (300 – 350 eV) than when the alloy is the inner array (350 – 380 eV). When the brass array is the outer array, the T_e for the L-shell Cu and Zn is less (320 – 360 eV) than when the alloy is the inner (340 – 390 eV). For electron density, L-shell Cu and Zn doesn't change much moving from the inner array to the outer array, however there is a significant change for K-shell Al and Mg, which is a topic for further study. This provides a more complete understanding of the evolution of the plasma parameters over the x-ray pulse, though much more information can be attained since the timings of the gates were different relative to the implosion time of the shot (see Figure 4.4), indicating the importance of time-gated diagnostics for future studies. A final conclusion that can be made is that the evolutions of the plasmas for the brass and Al arrays are different, depending on whether they are the inner or the outer arrays, and have different influences on the final implosion; for instance the Al-on-brass configuration produced a narrow pulse shape that could be beneficial for ICF studies, whereas the brass-on-Al configuration produced higher total energy. Future work will focus on a broader range of time-gated spectra from well before and well after the main burst with the goal of achieving specific pulse features and improved radiative performance optimized for ICF loads on multimegaampere machines (Velikovich *et al.* 1998).

In addition, a comparison of nested cylindrical wire arrays of Mo and Al from both the Cobra and Zebra generators was accomplished for the first time. These experiments

provided valuable information due to L-shell Mo and K-shell Al/Mg radiating at much different electron temperatures, unlike the brass and Al NCWAs. For the Cobra experiments, it was shown that the two Al tracer wires implode before Mo wires regardless of the placement of Al wires, and resulted in a pre-cursor formation on the PCD signal > 0.2 keV which could be radiation from the Al wires. For the Zebra experiments with four Al tracer wires, the Al K-shell radiation follows Mo L-shell bright spot radiation pattern when inside, however when Al wires are outside, it follows a column-like pattern. Modeling of Al K-shell radiation was shown to have less T_e when the Al wires were outside when compared to inside. K-shell Al lines are optically thin in all experiments regardless its percentage in the total mass, which is a very important feature for plasma diagnostics.

Chapter 5

EUV Spectroscopy and Modeling of Cu on the SSPX Spheromak and Laser Plasma “Sparky”

5.1 Introduction

In Chapter 4, L-shell Cu plasmas were studied (among L-shell Zn and Mo); however a significant contribution to radiation comes from M-shell Cu transitions, which radiate predominately in the EUV spectrum. This EUV radiation has recently become of great interest in z-pinch (Safronova *et al.* 2011) due to this major contribution to yield. Because of this, non-LTE kinetic M-shell models have been developed to help study this radiation. This chapter explores first results from a non-LTE kinetic model of M-shell Cu from Spect3D (see Section 2.2).

Radiation from two different experiments was used to help benchmark the new model: the first being from the Sustained Spheromak Physics Experiment (SSPX) (see Section 2.7) at Lawrence Livermore National Laboratory (LLNL), which, among other research, studied M-shell Cu impurities. Details from these experiments will be explored in Section 5.2 and results presented in Section 5.3. A second set of experiments were carried out on the compact laser-plasma x-ray/EUV facility “Sparky” at UNR, with Cu flat targets used. The EUV spectra were recorded between 40-300 Å and compared with results from SSPX. Results from these experiments will be presented in Section 5.4. Section 5.5 concludes the chapter.

5.2 Impurity Research on the Sustained Spheromak Physics Experiment

The SSPX at LLNL was a facility to explore innovative confinement concepts to explore energy confinement and current drive in spheromaks (Wood *et al.* 2005a). SSPX plasma currents achieved up to 1 MA, creating around 4 ms of plasma, with electron densities around 10^{14} cm^{-3} and electron temperatures exceeding 500 eV (Hudson *et al.* 2008). A critical component of the spheromak is the flux conserver, which is used to confine the plasma, and was made of Cu and coated with W to avoid sputtering of the wall material (Wood *et al.* 2005b). Impurities can play a beneficial role in plasmas, acting like a tracer, providing key information on plasma conditions through spectroscopical analysis (Stratton *et al.* 2008). However, impurities with high enough concentrations can cause issues, effectively cooling and diluting the plasma, posing problems for ignition and magnetic stability (Wesson 1997)). In Clementson *et al.* 2008, EUV plasma spectroscopy was utilized to study impurities on SSPX. The diagnostic included an EUV grazing-incident spectrometer, known as the Silver Flat Field Spectrometer (SFFS), which was developed at the LLNL EBIT facility (Graf *et al.* 2008). The SFFS has a spherical 1200 lines/mm grating with a resolution of 0.3 \AA full width at half maximum over the spectral range of 25 – 450 \AA . Imaging is accomplished with a back-illuminated Photometrics CCD camera, giving a wavelength range of around 200 \AA per image. In Clementson *et al.* 2008, impurities of B, C, N, O, Ti, Cu, and W were identified. One campaign was described in which the SSPX flux conserver was extended by inserting uncoated copper rods between the upper and lower sections. This led to a high influx of Cu into the plasmas and Cu spectra dominated the EUV emission in many

discharges. Work remained on diagnosing the M-shell Cu transitions in these spectra, notably Cu X – Cu XIII transitions, which is addressed in the next section.

5.3 Analysis of SSPX Impurity Spectra Dominated by M-shell Cu Emission

During the experimental campaign on the SSPX spheromak in which the flux conserver was altered by inserting uncoated Cu rods, images were taken by the SFFS with a wavelength range between 115 – 315 Å. The field of view was through the magnetic axis at the midplane of the plasma torus. The images are time- and spatially integrated. Figure 5.1 shows spectra from three SSPX shots, 20675, 20780, and 20801, of varying levels of contributions of M-shell Cu. Oxygen is also abundantly present in the spectra, as well as a few W lines. From analysis it is found that the most abundant transition is Cu X ($3p^5 3d^3 \ ^3F_3 \rightarrow 3p^6 3d^2 \ ^3F_3$) at 138.75 Å, followed by Cu XI ($3p^5 3d^2 \ ^2D_{5/2} \rightarrow 3p^6 3d \ ^2D_{5/2}$) at 135.23 Å. Other notable transitions include Cu X ($3p^5 3d^3 \ ^3D_3 \rightarrow 3p^6 3d^2 \ ^3F_4$) at 132.32 Å, Cu X ($3p^5 3d^3 \ ^3G_5 \rightarrow 3p^6 3d^2 \ ^3F_4$) at 153.67 Å, and Cu XIII ($3p^4 3d \ ^2D_{5/2} \rightarrow 3p^5 \ ^2P_{3/2}$) at 143.27 Å (compare to Ryabtsev *et al.* 2009, Shirai *et al.* 1991). Wavelengths were estimated both from Cowan’s code (Cowan 1981) and with the atomic code ATBASE run through Spect3D (see Table 5.1) and compared with recommended NIST (<http://physics.nist.gov/asd3>) data. Figure 5.2 displays theoretical calculations for shot 20801 on SSPX. EUV Cu spectra were calculated with Spect3D, while those of O (Wilcox *et al.* 2008) were calculated from SCRAM, with an atomic model based on FAC calculations. The plasma parameters needed for best agreement with the observed Cu spectra were found to be an electron temperature $T_e = 40$ eV and an electron density $n_e = 10^{14} \text{ cm}^{-3}$. For the O spectrum T_e was found to be somewhat lower, of about 15 eV, with the same $n_e = 10^{14} \text{ cm}^{-3}$. Similar simulations were run for the other two shots. For shot

20675, the Cu spectrum was modeled to have $T_e = 35$ eV, while the O spectrum was modeled to have $T_e = 15$ eV and for shot 20780, the Cu spectrum gave $T_e = 35$ eV while the O spectrum gave $T_e = 13$ eV: all calculated at the electron density were of $n_e = 10^{14}$ cm^{-3} . A possible explanation for cooler O plasma compared to Cu is that the O emission is from the outer cooler plasma whereas the Cu emission is from the inner hotter region.

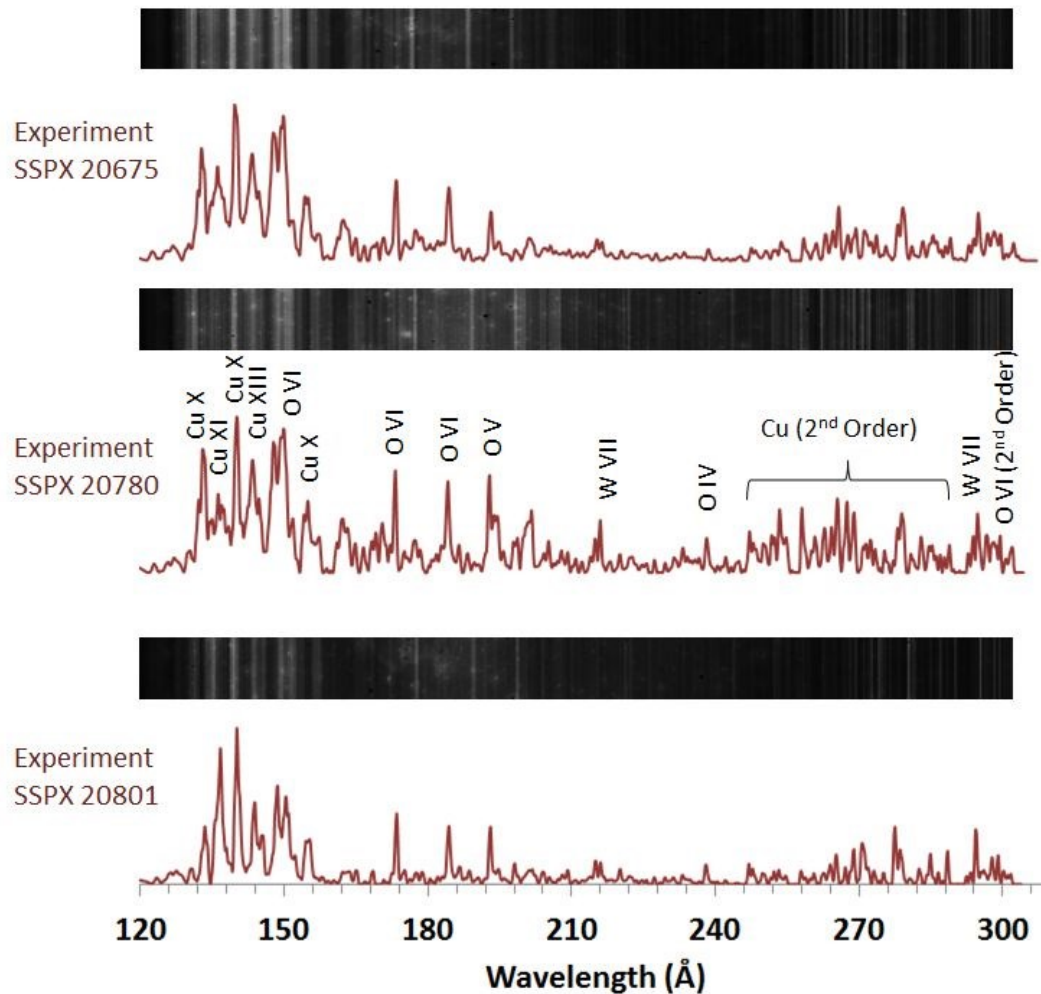


Figure 5.1. Experimental results from the SSPX spheromak. EUV image shown along with respected lineouts for shots 20675, 20780, and 20801.

Ion	Transition	Spect3D λ (Å)	COWAN λ (Å)
Cu X	$3p^5 3d^3 D_3 \rightarrow 3p^6 3d^2 F_4$	132.71	132.32
Cu X	$3p^5 3d^3 F_3 \rightarrow 3p^6 3d^2 F_3$	139.85	138.75
Cu X	$3p^5 3d^3 H_5 \rightarrow 3p^6 3d^2 G_4$	150.59	153.96
Cu X	$3p^5 3d^3 G_5 \rightarrow 3p^6 3d^2 F_4$	153.80	152.67
Cu XI	$3p^5 3d^2 D_{5/2} \rightarrow 3p^6 3d^1 D_{5/2}$	135.41	135.23
Cu XI	$3p^5 3d^2 F_{7/2} \rightarrow 3p^6 3d^1 D_{5/2}$	148.48	147.18
Cu XI	$3p^5 3d^2 P_{3/2} \rightarrow 3p^6 3d^1 D_{5/2}$	136.09	137.14
Cu XII	$3p^5 3d^1 P_1 \rightarrow 3p^6 S_0$	139.18	139.27
Cu XIII	$3p^4 3d^1 D_{5/2} \rightarrow 3p^5 P_{3/2}$	143.16	143.27

Table 5.1. Diagnostically important transitions of Cu X – Cu XIII ions and theoretical wavelengths estimated with Spect3D and COWAN Code.

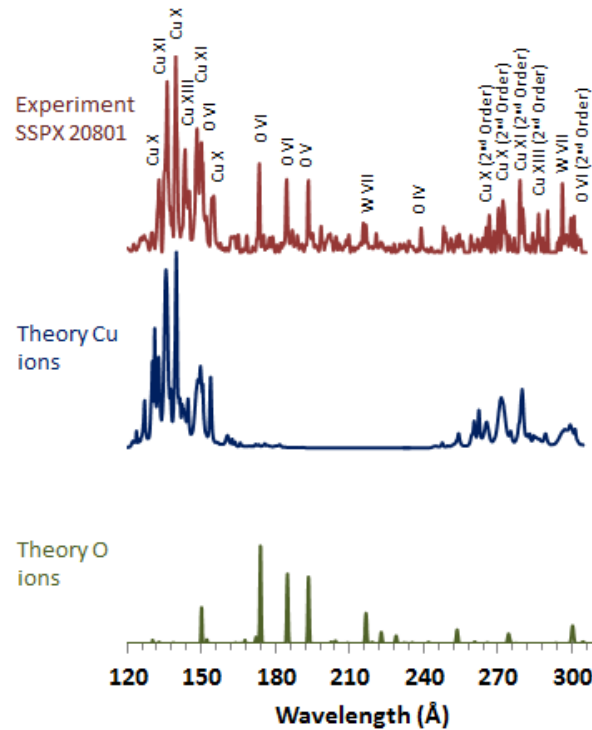


Figure 5.2. Experimental spectrum of shot 20801 from SSPX at the top. Synthetic spectra calculated at $n_e = 10^{14} \text{ cm}^{-3}$ for Cu at $T_e = 40 \text{ eV}$ (in the middle) and for O at $T_e = 15 \text{ eV}$ (at the bottom).

5.4 Analysis of Laser Produced M-shell Cu Emission from “Sparky”

The second set of experiments was performed on the compact laser-plasma x-ray/EUV facility “Sparky” at UNR. The EUV/soft x-ray laser plasma source operates with a 0.4 J, 3 ns, 10 Hz solid state laser. An EUV grazing incidence spectrometer was implemented to study the EUV spectra. The resolution of this spectrometer was $\lambda/\Delta\lambda = 100$ (Shevelko *et al.* 1998). A Cu slab was used as the target and shot multiple times (ranging from a few hundred to a few thousand) at different laser intensities. Figure 5.3 displays the results of a Cu slab shot approximately 220 times at maximum laser intensity. As with Kantsyrev *et al.* 2008a, the EUV spectra indicate a non-uniform, likely two-temperature, plasma. A possible explanation is that the laser produces plasma with a hot inner core and with a relatively cooler outer shell. Moreover, the spectrum is not only integrated in space but also in time, so it collects the EUV radiation from different plasma conditions throughout time. Modeling from Spect3D indicates two plasma conditions, one at lower $T_e = 25$ eV, and one at higher $T_e = 90$ eV, with $n_e = 10^{19}$ cm⁻³.

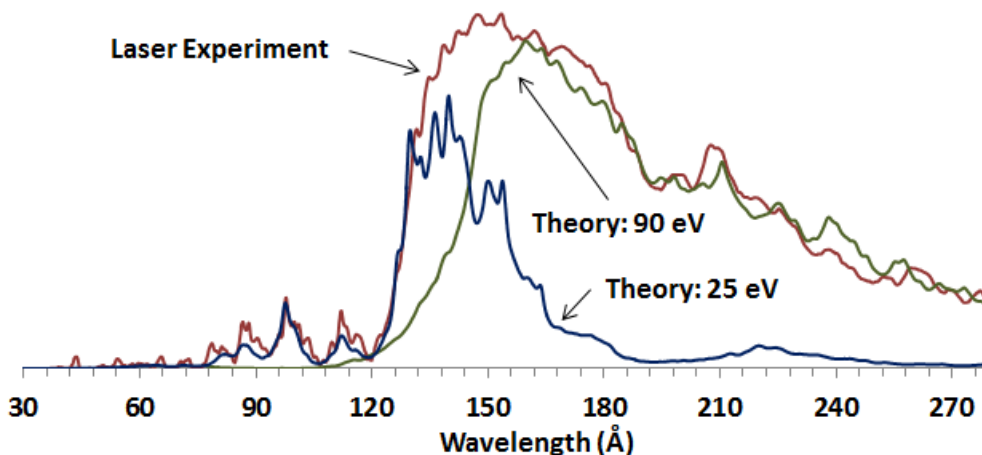


Figure 5.3. Experimental spectrum of Cu EUV produced on “Sparky” with two synthetic spectra calculated $T_e = 25$ eV and 90 eV and $n_e = 10^{19}$ cm⁻³.

5.5 Conclusions

EUV Cu spectra have been studied from two different sets of experiments in the range between 40-300 Å. The first set of experiments on the SSPX spheromak studied Cu impurities from rods inserted to extend the flux conserver. Results included a detailed analysis of Cu X – XIII transitions with an electron temperature up to 40 eV and electron density on the order of 10^{14} cm^{-3} , while O was modeled to be cooler at 15 eV. The second set of experiments on the laser-plasma facility “Sparky” studied EUV Cu at much different plasma conditions than that from SSPX. Such conditions indicate a non-uniform, two-temperature plasma, one with lower electron temperature of 25 eV emitting from the cooler outer shell, and another with a higher electron temperature of 90 eV emitting from the hotter inner core, and density of the order of 10^{19} cm^{-3} . The majority of the results from this chapter were published in Weller *et al.* 2012b.

Chapter 6

Ag Planar Wire Arrays as Powerful Radiators

6.1 Introduction and Motivation of Ag and Mixed Ag and Al Planar Arrays

Silver (Ag) wire arrays were recently introduced as efficient x-ray radiators and have been shown to create L-shell plasmas that have the highest electron temperature (> 1.8 keV) observed on the Zebra generator so far and upwards of 30 kJ of energy output (Safronova *et al.* 2011). In this chapter, results of single planar wire arrays (SPWAs) and double planar wire arrays (DPWAs) of Ag and mixed Ag and Al that were tested on the UNR Zebra generator are presented and compared (Sections 6.2 and 6.3). To further understand how L-shell Ag plasma evolves in time, a time-gated x-ray spectrometer was designed and fielded (see Section 2.4.2), which has a spectral range of approximately 3.5 – 5.0 Å. With this, L-shell Ag as well as cold L_{α} and L_{β} Ag lines were captured and analyzed along with PCD signals (> 0.8 keV). Along with PCD signals, other signals, such as filtered XRD (> 0.2 keV) and Si-diodes (SiD) (> 9 keV), are analyzed covering a broad range of energies from a few eV to greater than 53 keV. The observation and analysis of cold L_{α} and L_{β} lines show possible correlations with electron beams and SiD signals. Section 6.4 will discuss and conclude the chapter.

6.2 Comparison and Analysis of Ag SPWAs and Mixed Ag and Al DPWA

Planar wire array (PWA) configurations in z-pinch experiments have been shown to be very efficient radiators (Kantsyrev *et al.* 2006). As part of this research, different wire materials have been tested in search for more efficient radiation sources. With this in

mind, a series of Z-pinch experiments were performed at the UNR Zebra generator that focused on radiation from Ag planar wire arrays. This section presents some of the major results of these experiments. It was also shown that Ag radiated from many “bright” spots along the pinch, with “cold” L_α and L_β lines observed in more “column-like” features along the pinch, between the bright spot formations. Many of the early Ag experiments were performed on the Zebra generator in what is now referred to as the “standard” 1.0 MA configuration with a 100 ns rise time. The new LCM (see Section 4.2) allows for experiments to be performed at currents as high as 1.7 MA which provides many useful comparisons, such as energy scaling with current, efficiency of radiating into L-shell Ag, and analyzing different plasma parameters, such as electron temperature and density. Experiments in this section include both standard current and enhanced current LCM results. The majority of the results from this section have recently been published (Weller *et al.* 2014).

Shot #	Configuration - Wire Material	Wire #	Diameter of Wire (μm)	Array Mass ($\mu\text{g/cm}$)	Total Energy (kJ)	PCD Energy (J)	Maximum Current (MA)
2585	SPWA - Ag	8	17.8	209	30.6	314	0.84
2587	SPWA - Ag	8	17.8	209	30.4	317	0.89
2480	SPWA - Ag	10	25	515	16.5	405	1.60 (LCM)
1928	DPWA - Ag/Al	8/8	10/19	131	21.0	224	0.98

Table 6.1: List of considered shots for pure Ag and mixed Ag and Al PWAs with load characteristics, total radiated energy output, PCD energy, and maximum current.

Table 6.1 lists the pure Ag and mixed Ag and Al PWA experiments that are discussed in this section. “Shot #” refers to the Zebra shot number. The configuration refers to either single planar wire arrays or double planar wire array, followed by the wire material. All aluminum wires listed were Al 5056 alloy, which is 95% Al and 5% Mg. The number of wires refers to the number of total wires in the SPWAs and number of wires in each plane for the DPWA. For the mixed Ag and Al DPWA, one plane is Ag while the other plane is Al. The diameter of the wires refers to the thickness, which is then followed by the array mass, in mass per unit length. The array mass is listed this way due to the different anode to cathode gap length between the standard (2.0 cm) and LCM (1.0 cm) configurations. The total radiated energy is also listed and was measured with a bare nickel bolometer. The photoconducting diode (PCD, filtered with 8 μm Be, > 0.8 keV, 0.5 ns resolution) signal has been calibrated and provides energies for the given cutoff range, which are also listed in the table. The maximum current refers to the current peak, measured with calibrated B-dots.

6.2.1 Implosion Characteristics of Ag SPWA and Mixed Ag and Al DPWA

SPWAs of Ag and a DPWA of mixed Ag and Al were tested on the UNR Zebra generator. Table 6.1 lists the load configurations for the shots considered in this section. Shot 2585 and 2587 were identical SPWAs that had eight 17.8 μm diameter Ag wires spaced 0.7 mm apart and had a current maximum of 0.84 MA and 0.89 MA, respectively. Shot 2480 was a SPWA that had ten 25.0 μm diameter Ag wires spaced 0.7 mm apart and had a current maximum of 1.60 MA (LCM). Lastly, shot 1928 was a mixed Ag and Al DPWA with one plane consisting of eight 10 μm diameter Ag wires (66 $\mu\text{g}/\text{cm}$) and the other plane consisting of eight 19 μm diameter Al (5056) wires (61 $\mu\text{g}/\text{cm}$). The

thickness of the wires was chosen to keep each plane approximately the same mass. The interplanar gap was 3.0 mm with wires spaced 0.7 mm apart. Total array mass needs to be considered to allow for maximum x-ray signals, which coincide with implosion times listed, to be around 100 ns, or maximum of current as well as for maximum efficiency of x-ray radiation and total energy output. Because of this the array mass per length for the enhanced current configuration is more than twice that at standard configuration. The total radiated energy per length for the SPWAs at standard and enhanced current was comparable, with 15.3 kJ/cm (30.6 kJ total) for shot 2585, 15.2 kJ/cm (30.4 kJ total), and 16.5 kJ/cm for shot 2480. One explanation for this comparable radiated energy per length for two different current regimes is likely due to the anisotropy of SPWA Ag loads as reported in Kantsyrev *et al.* 2013, where bolometer detectors were systematically shown to measure more radiated energy when the bolometer was pointed perpendicular to the plane as opposed to parallel to the plane, by a factor of 1.2 or greater. In this data, shots 2585 and 2587 at standard current were oriented perpendicular to the bolometer while shot 2480 at enhanced current was oriented parallel to the bolometer. The total radiated energy per length for the mixed DPWA was 10.5 kJ/cm (21.0 kJ total), less than the pure Ag SPWA configurations. The PCD energies are also listed and were filtered to include L-shell Ag and K-shell Al radiation. The PCD energies for shots 2585 and 2587 were 315 J and 317 J, respectively, while the PCD energy for shot 2480, was 405 J. This may indicate that, though the total overall energies are comparable, the enhanced current shot 2480 was more efficient at radiating in L-shell Ag than the standard current shots. The PCD energy for shot 1928 was 224 J, again, less than the pure Ag SPWA configurations. One possible explanation that the total radiated energy is less for the

mixed Ag and Al DPWA is the inclusion of the Al plane itself; given that Al traditionally is a less efficient radiator than other materials, especially compared to Ag.

In the interest of studying implosion characteristics, signals and time-gated pinholes (TGPH) of all shots considered are shown in Figure 6.1. The TGPH provided two images of energies > 1.0 keV and > 3.0 keV. The signals include an XRD (> 0.2 keV), a PCD (> 0.8 keV), a SiD, > 53 keV, and a $25\ \mu\text{m}$ Cu filtered Faraday Cup (> 93 keV electron cutoff energy). The Faraday Cup was utilized to measure electron beams and was oriented directly above the pinch. Looking at Figures 6.1(a) and 6.1(b) of shots 2585 and 2587, the Ag SPWAs have main implosions that occur between 96 and 99 ns, followed by a series of bursts after the main pinch lasting for approximately 60 ns. This corresponds with TGPH images which show very many random bright spot formations, which indicate a non-uniform implosion. Figure 6.1(c) provides the implosion characteristics of shot 2480, the Ag SPWA at enhanced current. The implosion time was 90 ns, followed by a series of bursts after the main pinch lasting for approximately 50 ns, which have very similar implosion characteristics of the SPWAs at standard current. The TGPH images again show random bright spot formations, though perhaps indicating a more uniform pinch in frame “c” than the standard current SPWA counterparts. Finally, Figure 6.1(d) shows the implosion characteristics of shot 1928, the mixed Ag and Al DPWA. Here, the advantage of the mixed Ag and Al DPWA configuration becomes evident, with a main implosion at 100 ns that consists of a clear main pulse, followed by only a few smaller secondary pulses, producing much narrower XRD, SiD, and PCD signals. This corresponds with TGPH images in the last three frames which indicate a much more uniform pinch.

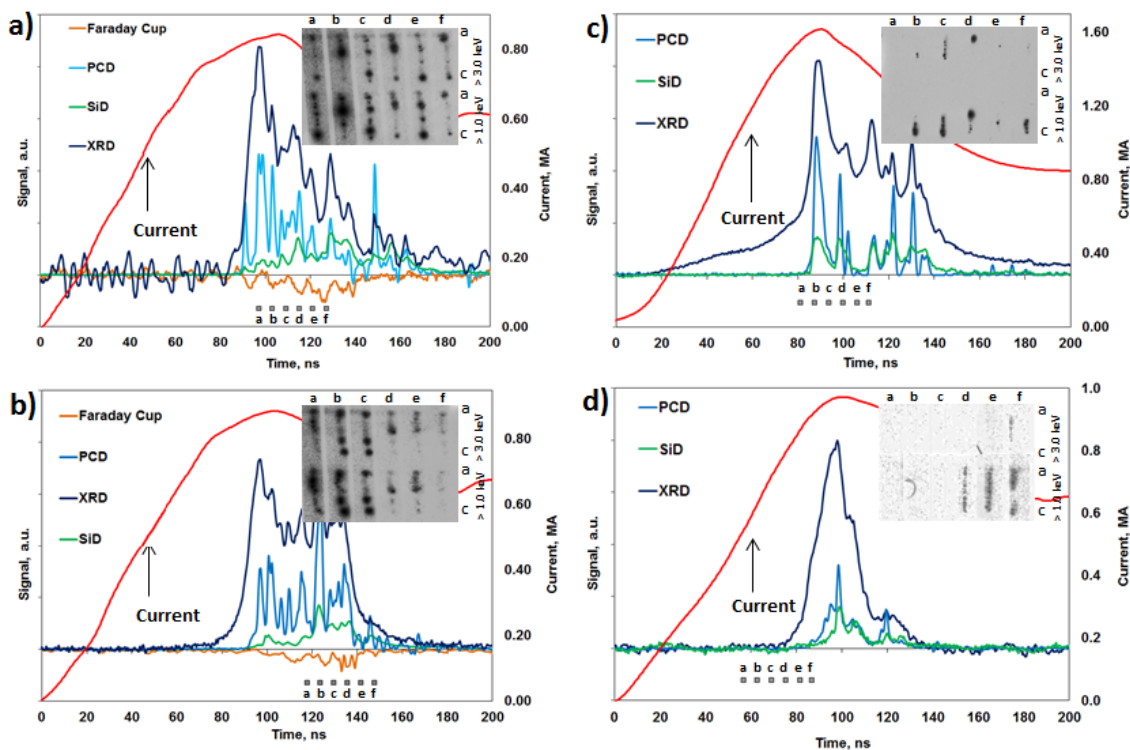


Figure 6.1. Signals and time-gated pinhole images for shots (a) 2585 – Ag SPWA at standard current, (b) 2587 – Ag SPWA at standard current, (c) 2480 – Ag SPWA at enhanced current, and (d) 1928 – Ag and Al DPWA at standard current. The pinhole timings are shown with gray boxes and are listed “a-f” and are filtered at > 1.0 keV (bottom) and > 3.0 keV (top).

To further understand the implosion characteristics of L-shell Ag, a time-gated hard x-ray (TGHXR) spatially integrated spectrometer was fielded for the first time for shots 2585 and 2587. The TGHXR used a convex α -quartz crystal ($2d = 6.687 \text{ \AA}$) with a 4” diameter, which allowed for viewing of wavelengths between 3.8 and 4.5 \AA . The spacing between gates was 5 ns, while the MCP was gated to last for 3 ns. The first analysis of the time-gated L-shell Ag, shown in Figure 6.2, yields interesting results; for shot 2585, Figure 6.2(a-c), the first two frames show what appear to be L_{α} and L_{β} lines, with no

evidence of L-shell radiation from hot plasmas. The third frame, however, shows very strong background, the disappearance of the L_α and L_β lines, and the appearance of Ne-like 3G and Na-like Ag lines. The background may possibly be continuum caused by either bremsstrahlung radiation or recombination. By the fourth frame the background has dissipated along with the Ne- and Na-like lines, and the reappearance of the L_α and L_β occurs. The L_α and L_β lines are likely caused by excitation of low ionization stages of Ag ions by electron beams, which have been shown to have correlation with SiD signals (Ouart *et al.* 2011), which is the case here. The spectra were captured during the middle of the x-ray burst signals and indicate just how drastically plasma conditions can change in the ns time scale. Careful observation shows that the background along with the L-shell lines corresponds well with a sharp spike in XRD and PCD signals, which in general has correlated with hotter plasma conditions (Weller *et al.* 2012a, Safronova *et al.* 2008b). Due to the nature of these results, an identical experiment was performed (shot 2587) which is presented in Figure 2(d-e). In this particular experiment, all four frames yielded strong background, along with the L-shell Ne- and Na-like lines, consistent with previous results. More research needs to be completed on the nature of this background to further understand if this is continuum emission or some other mechanism, such as an instrumental artifact. No L_α and L_β lines were measured, likely due to the timing of the gates being earlier than shot 2585 and coinciding with very weak SiD and Faraday cup signals.

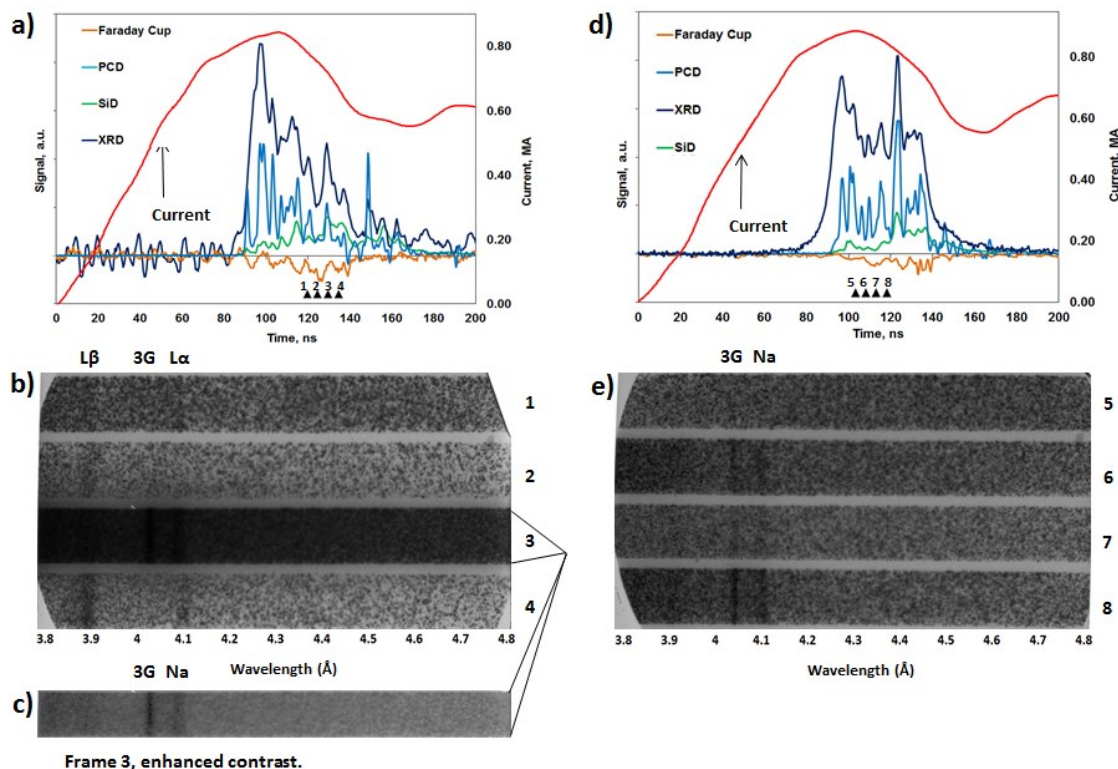


Figure 6.2. (a) Signals and timings for the TGHXR spectrometer for shot 2585 – Ag SPWA at standard current. In (b), images of spectra from the TGHXR spectrometer for shot 2585. The frames are listed as “1-4” and correspond with timings in (a). In (c), the third frame from (b) has enhanced contrast for clarity. (d) Signals and timings for the TGHXR spectrometer for shot 2587 – AG SPWA at standard current. In (e), images of spectra from the TGHXR spectrometer for shot 2587 and all frames have enhanced contrast for clarity the same as in (c). The frames are listed as “5-8” and correspond with timings in (d).

6.2.2 Radiative Characteristics of Ag SPWA and Mixed Ag and Al DPWA

The radiative characteristics of the experiments described in the earlier sections are explored in detail in this section. Figure 6.3 shows time-integrated spatially resolved (TISP) spectra and pinhole (TIPH) images of shots 2585 and 2480. The spectra were taken with a potassium hydrogen phthalate (KAP) ($2d = 26.63 \text{ \AA}$) convex crystal

spectrometer while both pinhole images were filtered to study L-shell Ag emissions > 3.0 keV. Both diagnostics are axially resolved to study variations along the length of the pinch from anode “a” to cathode “c”. Bio-max MS Kodak x-ray film was implemented in this work. Diagnostically important L-shell Ag lines, along with characteristic lines L_α and L_β , are indicated in Figure 6.4, which are F- through Mg-like Ag, with Ne-like Ag being the predominate features (for more information on L-shell line identification, see Safronova *et al.* 2007 and Quart *et al.* 2010b). Both shots produce very many “bright” spots, roughly 4-5 per cm, as seen on the TIPH images and correlate well with the TISP spectra, however there are a few striking differences. The first is that the enhanced current shot (2480) had substantially increased intensity of the Ag L-shell radiation, which is seen up to fourth order reflection on the film. This result is in agreement with the fact that shot 2480 also had increased PCD energy output, as opposed to the standard current shots, indicating again that the enhanced current was more efficient at radiating in L-shell Ag. Also from this shot higher Rydberg state transitions of Ne-like 4C and 4D can be seen between 2.8 and 3.0 Å. A second difference is that the standard current shot (2585) produced very well defined “cold” L_α and L_β features along the length of the pinch, indicating strong electron beam presence (for more information on electron beams see Shrestha *et al.* 2010), as seen from Figure 6.4, while the enhanced current shot had relatively weaker L_α and L_β lines. The presence of strong F-like features indicate electron temperature on the order of 1.4 – 1.8 keV in this plasma (Safronova *et al.* 2011). A main similarity of the standard and enhanced current shots, however, is that L-shell Ag is being produced optically thick.

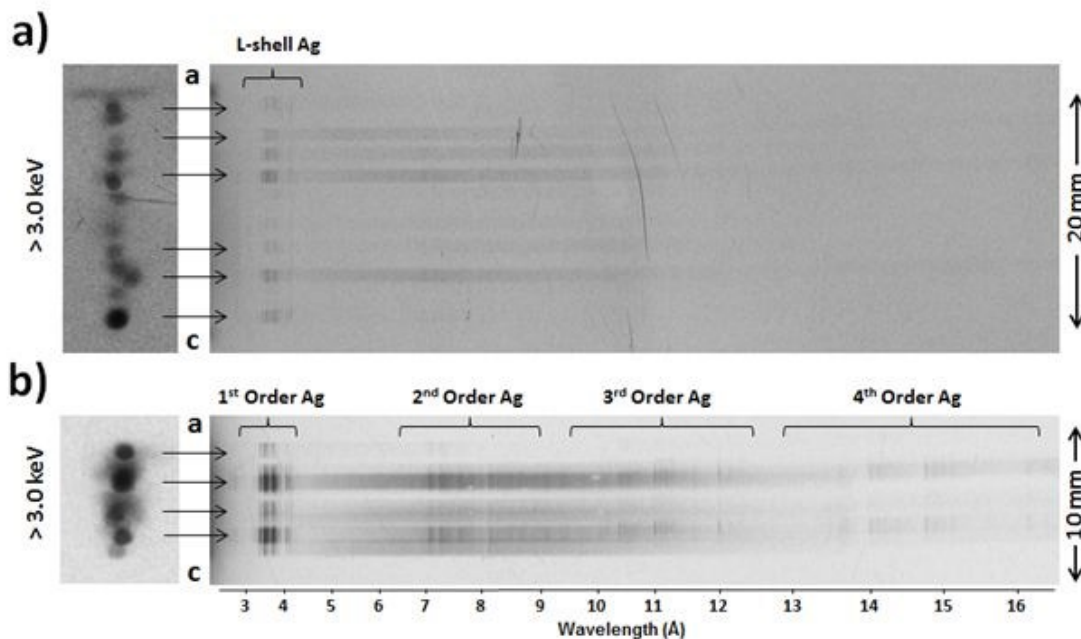


Figure 6.3. (a) Shot 2585 – Ag SPWA at standard current and (b) shot 2480 – Ag SPWA at enhanced current of x-ray time-integrated spatially resolved spectra (right) and pinhole images (left). The pinhole images are filtered at > 3.0 keV.

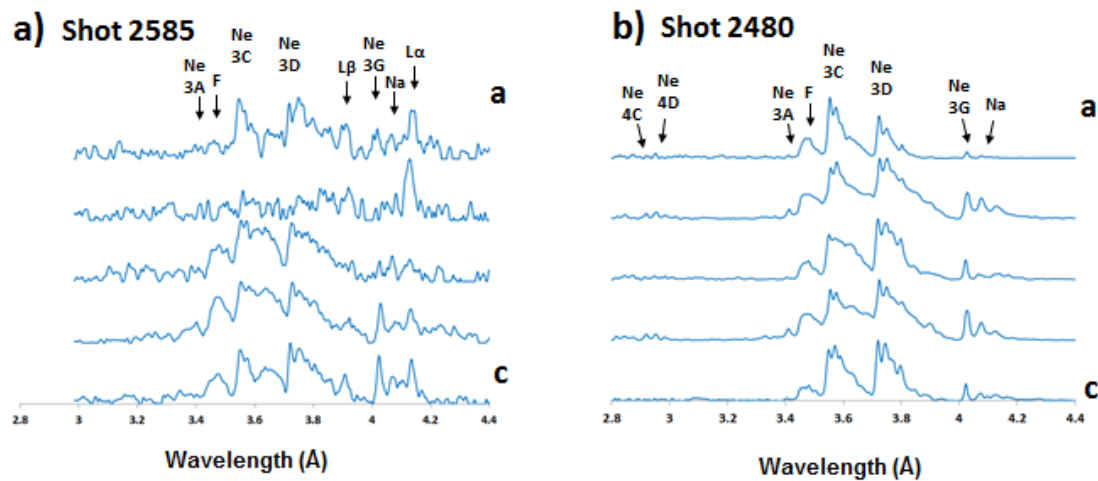


Figure 6.4. (a) L-shell Ag spectra produced on Zebra in shot 2585 – Ag SPWA at standard current and (b) in shot 2480 – Ag SPWA at enhanced current. Lineouts taken from spectra in Figure 6.3.

Analysis of the time-integrated results for shot 1928 is presented in Figure 6.5. The TISP spectra demonstrate that, while Al radiates mostly along the column of the pinch (K-shell Al lines are labeled Al1, Al2, etc., for more information on K-shell Al line identification, see Section 2.1.1), Ag only radiates from 3-4 main bright spots. It's likely that L-shell Ag is radiating only from relatively hotter portions of the plasma, compared to what K-shell Al can radiate from. It's also very important to point out that the mixture of Al and Ag wires produced not only optically thin K-shell Al (no K-shell Mg lines), but almost optically thin L-shell Ag, which is in contrast to the pure Ag SPWA loads, which produced optically thick L-shell Ag plasma. The TIPH images agree with the results of the TISP spectra. The pinhole image of > 1.0 keV includes both radiation from K-shell Al and L-shell Ag and appears to be more column-like, though with noticeable bright spots. The pinhole image of > 3.0 keV includes radiation mostly from L-shell Ag, and correlates well with the L-shell spectra. As mentioned earlier, Biomax-MS film is used to capture the experimental spectra and the intensity (normalized to 1) is calculated by the method reported in Knauer *et al.* 2006 with measurement errors within 20% as reported in Chandler *et al.* 2005 (within the accuracy of the atomic data, see Safronova *et al.* 2008a). Non-LTE kinetic modeling was performed for the K-shell Al spectra and the synthetic spectra results are overlaid in dashed black on top of the experimental spectra in gray in Figure 6.5(b). In Figure 6.5(c), electron temperatures (T_e) of K-shell Al are plotted as function of distance from cathode in mm. The T_e ranges from $T_e = 360$ eV to 580 eV. Higher K-shell Al T_e seems to correlate with the L-shell Ag radiation, indicating that the presence of the hotter L-shell Ag plasma may be affecting the K-shell Al plasma. The Al2 ($\text{Ly}\alpha$) to Al1 ($\text{He}\alpha$) ratio is used to estimate K-shell Al T_e with an estimated

uncertainty of $\pm 10\%$. It's important to take note, that although 5% Mg was present in the Al alloy, no Mg K-shell spectra were recorded, and that Al K-shell spectra were optically thin, even with very high T_e . In Figure 6.5(d), the K-shell Al electron densities (n_e) are plotted and range from $n_e = 7 \times 10^{18} \text{ cm}^{-3}$ to $7 \times 10^{20} \text{ cm}^{-3}$, with the higher n_e being near the cathode. The ratio of the inter-combination transition ($1s2p \ ^3P_1 \rightarrow 1s^2 \ ^1S_0$) to the resonate line AlI ($\text{He}\alpha$) is used to estimate K-shell Al n_e with an estimated uncertainty within an order of magnitude. Also in Figure 6.5(d) are n_e estimates of L-shell Ag from two bright spot formations (indicated by arrows "1" and "2"). The estimations are $n_e = 1 \times 10^{20} \text{ cm}^{-3}$ and $n_e = 7 \times 10^{20} \text{ cm}^{-3}$, roughly an order of magnitude higher than the K-shell Al n_e from the same bright spot region. The ratio of Ne-like lines $(3A+3B)/(3F+3G)$ is used to estimate L-shell Ag n_e (for an example of this ratio being used, see Ref (Hansen *et al.* 2005)). The estimations were also made possible due to L-shell Ag being optically thin, an advantage that this mixed Ag and Al DPWA load had over the pure Ag SPWA loads. The lines connecting the points in Figures 6.5(c) and 6.5(d) are for visual representations only and are not designed to represent trends in between the points.

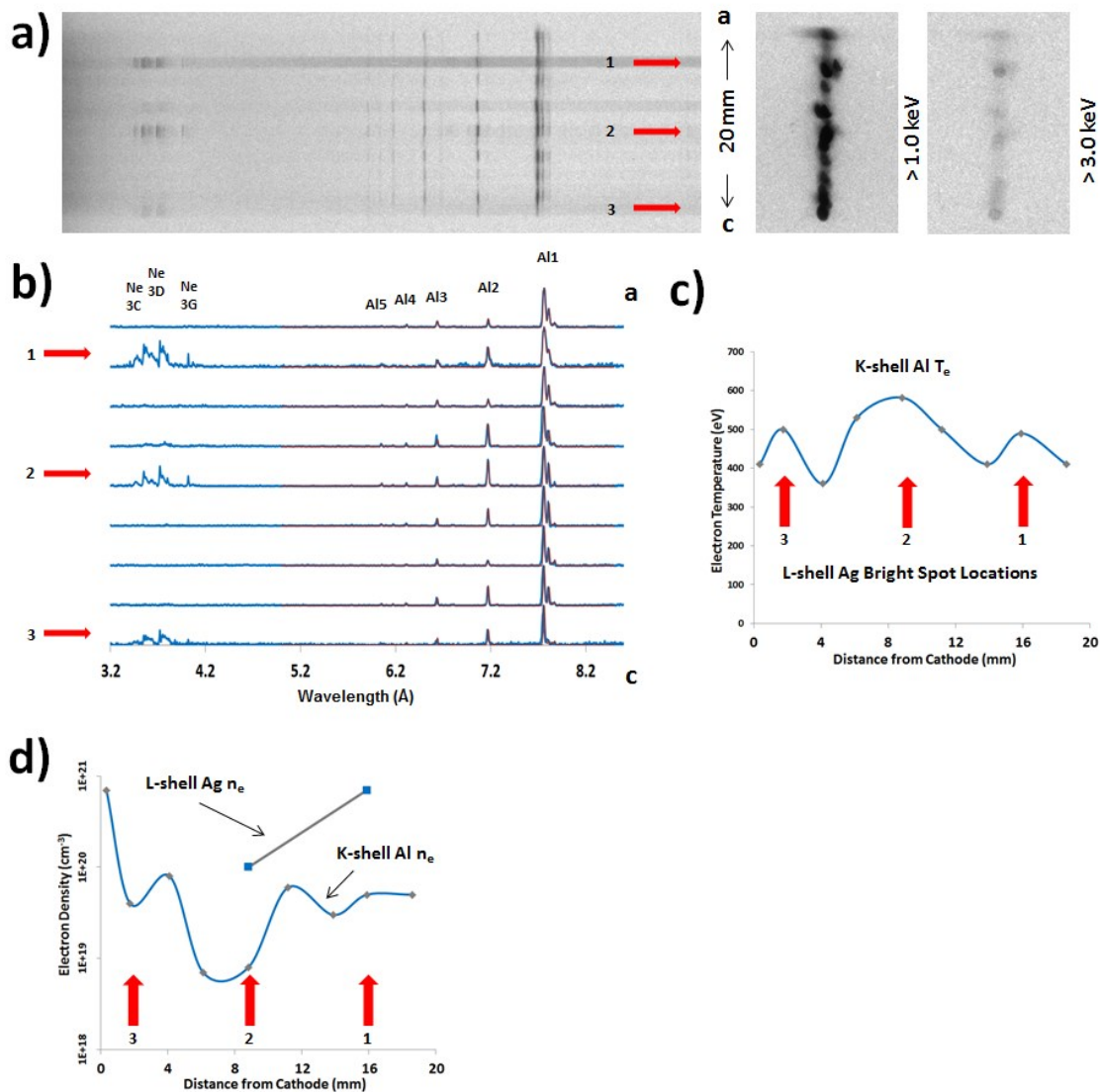


Figure 6.5. Shot 1928 – Ag and Al DPWA at standard current. (a) X-ray time-integrated spatially resolved spectra of K-shell Al and L-shell Ag and pinhole images. (b) Lineouts of the spectra in blue along with synthetic spectra in red for K-shell Al are shown in (b). In (c) K-shell Al T_e is plotted as a function of distance from cathode. In (d) K-shell Al and L-shell Ag n_e are plotted as functions of distance from cathode. Arrows numbered “1-3” correlate spectra with lineouts, as well as indicating bright spots that generate L-shell Ag radiation.

6.3 Low-Aspect Ratio Ag DPWAs and their Signatures at Enhanced Current

The DPWA of mixed Ag and Al discussed in the previous sections had a 3.0 mm interplanar gap, which proved to be too small of a gap to allow shadowgraphy images to view in between the planes, which provides useful information as to how the planes are imploding. Because of this limitation, DPWAs of Ag and mixed Ag and Al with a 6.0 mm interplanar gap were designed and implemented on the Zebra generator at 1.7 MA. The pure Ag loads contained five wires of 25 μm diameter Ag in each plane, for a total of ten wires, with a 0.7 mm interwire gap. The mixed Ag and Al loads contained five wires of 25 μm diameter Ag in one plane and five wires of 49.8 μm diameter Al in the other plane. The diameters of the Ag and Al wires were chosen to keep both planes approximately the same mass. For both configurations, each plane was approximately 2.8 mm wide, creating an aspect ratio of $\phi = 0.47$. The aspect ratio (ϕ) (Williamson *et al.* 2010) in DPWAs is the width (w) of the planes divided by the interplanar gap (g). Low aspect ratios loads are defined as $\phi < 0.7$, and allow for the global field to magnetically isolate each plane until the final implosion with only off-axis mass accumulation, or in other words, each plane individually implodes as if it was initially a SPWA. Table 6.2 lists the load characteristics, as well as the implosion time and total radiated energy. The total radiated energy of the three pure Ag loads averaged 9.7 kJ/cm, while the total radiated energy of the three mixed Ag and Al loads averaged 8.7 kJ/cm, both of which have total radiated energy less than shot 1928 that had a mixed Ag and Al DPWA at standard current, which radiated 10.5 (see Table 6.1). This is likely due to the increased gap from 3.0 mm to 6.0 mm, as concluded in chapter 3 studying Mo/Al TPWAs, which suggests doing so decreases load efficiency.

Shot #	Material # Wires	Diameter (μm) Gap (mm)	Linear Mass ($\mu\text{g/cm}$)	Implosion Time (ns)	Radiated Energy (kJ/cm)
2984	Ag/Ag	25.5/25.5	515	105	9.9
DPWA	5/5	0.7/6.0			
2985	Ag/Ag	25.5/25.5	515	99	9.5
DPWA	5/5	0.7/6.0			
2986	Ag/Ag	25.5/25.5	515	97	9.6
DPWA	5/5	0.7/6.0			
2987	Ag/Al	25.5/49.8	521	112	8.1
DPWA	5/5	0.7/6.0	258/263		
2988	Ag/Al	25.5/49.8	521	120	8.9
DPWA	5/5	0.7/6.0	258/263		
2989	Ag/Al	25.5/49.8	521	111	9.2
DPWA	5/5	0.7/6.0	258/263		

Table 6.2. List of considered shots for pure Ag and mixed Ag and Al DPWAs with an increased gap of 6.0 mm; load characteristics, radiated energy output per length, PCD energy, implosion time, and maximum current.

Figure 6.6 shows the signals, TGHRX spectra, TIPH images, and shadowgraphy images of shot 2986. Looking at signals first, there is a main x-ray burst at approximately 96 ns into the current rise, followed by an almost equal burst 6-7 ns later, followed by a smaller burst in radiation in the XRD signal only around 35 ns later. This suggests that after each plane independently implodes (within 10 ns of each other), the two planes then ablate together towards the central z-axis and a secondary and smaller implosion occurs. Shadowgraphy images, taken at 63 and 69 ns, are shown to the right. The EKSPLA laser was used, which operates at 532 nm with a 0.2 ns pulse. The laser is polarized before reaching the Zebra chamber, where one half of the polarization is taken on a 6 ns delay path. Images were then taken with a CCD camera. The images were taken parallel to the planes, providing a view in between the two planes. A few features

are observed; first, the planes appear to be independently imploding, just as expected with the low aspect ratio loads. Second, there are cone-like structures seen on the anode and cathode, but predominately near the anode. This is likely due to electron beam interaction with the anode and cathode plate material, which is made of stainless steel. The TIPH images, taken 45° from the shadowgraphy images, also show evidence of two independently imploding planes, especially in the > 3.0 keV image. The > 1.0 keV image shows evidence that after the planes imploded separately, the plasma imploded again on axis. In both TIPH images there is a cone-like structure of no radiation > 1.0 keV, which correlates well with the cone-like structure in the shadowgraphy images, and also indicates that the cone-like structure is cooler plasma, again, caused by electron beams. Also in the TIPH images, it's clear in > 1.0 keV the plasma connects in the central z-axis, where in > 3.0 keV there is very little radiation in the center. The TGHXR images show evidence of L_α and L_β lines, which appear only in the presence of harder x-ray signals. For more information about the correlation of electron beams and hard x-ray signals, see Shrestha *et al.* 2010.

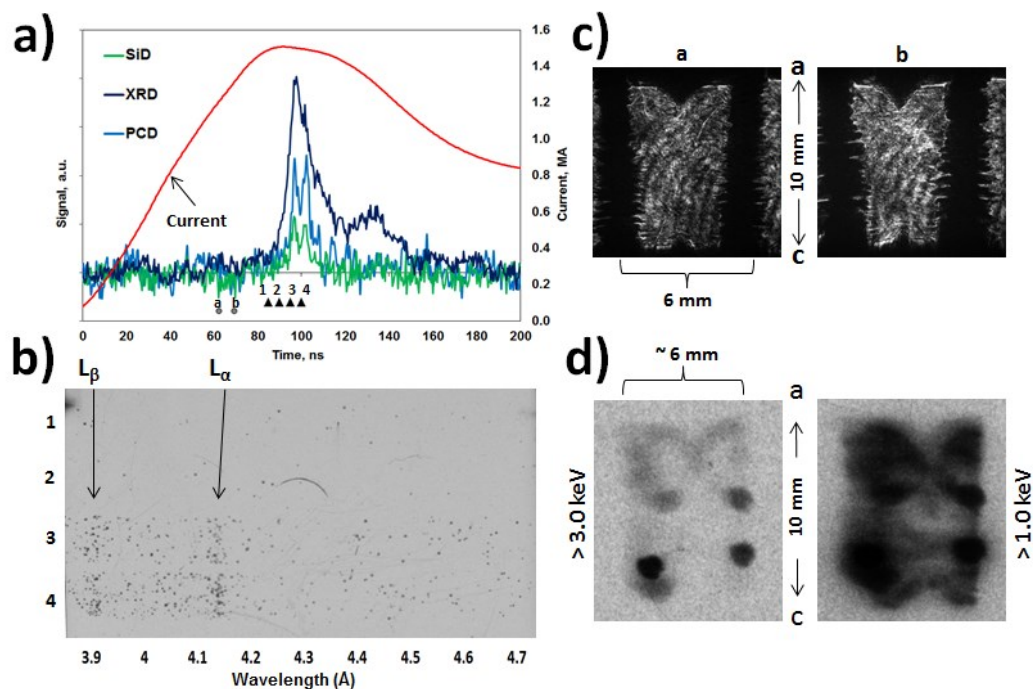


Figure 6.6. Signals from PCD, XRD, and SiD, along with measured current (a) for Zebra shot 2986 (Ag DPWA with 6 mm gap). Time-gated spectra is shown in (b) with timings correlated with black triangles in (a) and numbered “1-4”. Shadowgraphy images are shown in (c) with timings correlated with grey circles in (a) and labeled “a-b”. Time-integrated spatially resolved pinhole images are shown in (d) at two different cutoff energies.

Figure 6.7 shows the signals, TGHRX spectra, TIPH images, and shadowgraphy images of shot 2985, which is similar data from the identical shot 2986 shown in Figure 6.6, but with later the timings of the gates of the TGHRX spectrometer after the main SiD and PCD burst. Consequently, no L_{α} and L_{β} lines were measured on the TGHRX spectrometer, which confirm more the findings and conclusions taken from shot 2985, where L_{α} and L_{β} lines were measured during the same time harder x-ray signals of PCD and SiD were measured. Looking into shadowgraphy, the cone-like structures were again reproduced.

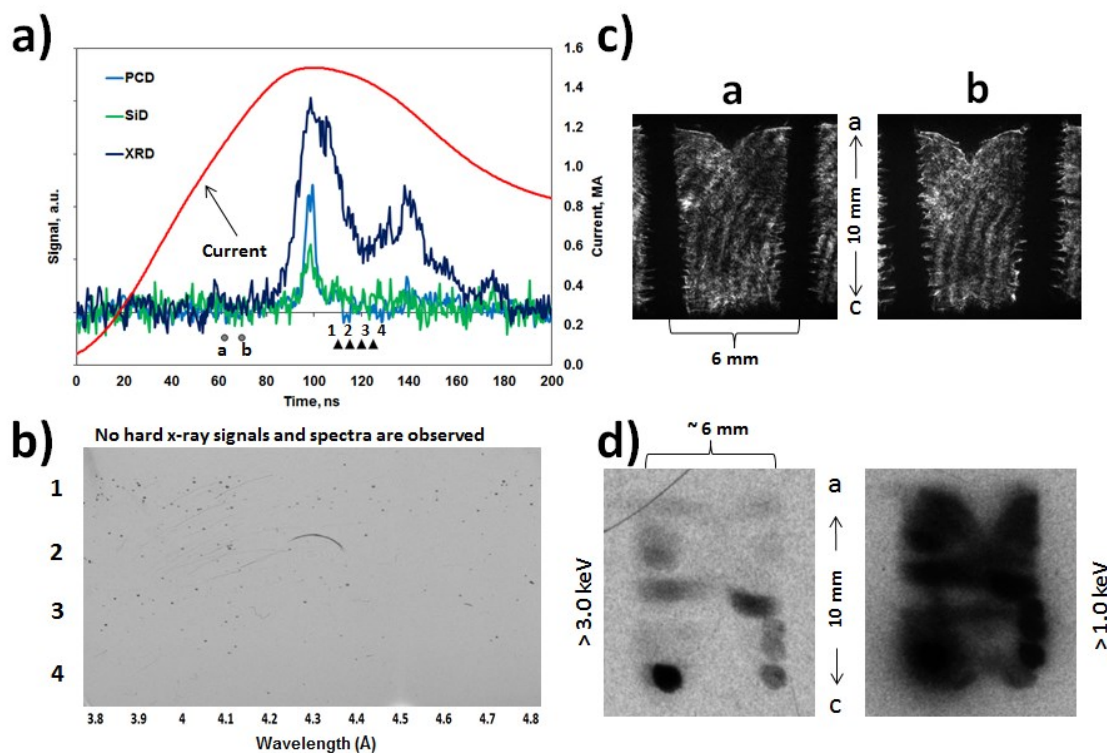


Figure 6.7. Signals from PCD, XRD, and SiD, along with measured current (a) for Zebra shot 2985 (Ag DPWA with 6 mm gap). Time-gated spectra is shown in (b) with timings correlated with black triangles in (a) and numbered “1-4”. Shadowgraphy images are shown in (c) with timings correlated with grey circles in (a) and labeled “a-b”. Time-integrated spatially resolved pinhole images are shown in (d) at two different cutoff energies.

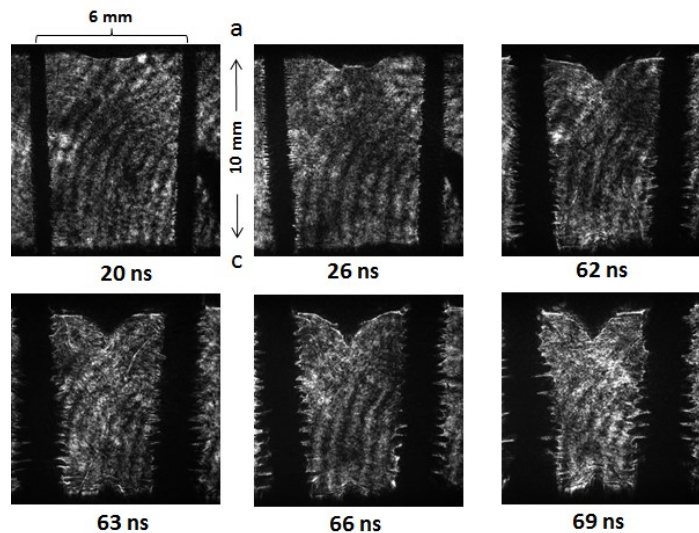


Figure 6.8. Shadowgraphy images of Ag DPWAs with 6.0 mm gap at enhanced current. Images from three different identical loads with timings changed. Images show independently imploding planes along with “cone-like” structures developing in anode “a” and cathode “c”.

For all three identical Ag DPWAs, the timings of the shadowgraphy images changed from each shot. The result of this time-evolution of the wire planes is shown in Figure 6.8. As early 20 ns into the current rise, the cone-like structure appears to be developing. These images show consistency in the cone-like structure development, as well as consistency in which both planes independently implode. It’s also apparent that each plane not only implodes independently, but do so at approximately the same time (within 10 ns), followed by a secondary implosion in which the two planes implode towards the central z-axis. Although the total radiated energy was relatively low compared to other Ag DPWAs and little to no L-shell Ag radiation was observed, this load configuration has shown interesting results in plasma generation and the evolution thereof, as well as possible electron beam interaction with the anode and cathode surfaces.

Next will be results of the mixed Ag and Al DPWAs with an increased gap of 6.0 mm. Traditionally, Al is a much quicker ablator than other wire materials, so the results of shadowgraphy looking between the two planes with an increased gap should prove very interesting. Figure 6.9 shows the implosion characteristics of shot 2988 from a mixed Ag and Al DPWA. First, the signals paint a different picture than for the pure Ag loads, showing a few step-like pre-pulse features at 90 ns and 105 ns in time, followed by the main implosion at 120 ns. The two shadowgraphy images, taken at 95 and 101 ns, show two planes, the Ag plane on the left and the Al plane on the right, with the Al plane clearly ablating towards the central z-axis before the Ag plane. This could explain why the signals are very different than from the pure Ag loads, where one plane has much different implosion characteristics than the other. The cone-like structure again is apparent near both the anode and cathode. In Figure 6.9(b), the TGHXR spectrometer shows very faint L_{α} and L_{β} lines in frames “3” and “4”, which correspond to increase in the hard SiD signal. The TGPH image in Figure 6.9(d) shows radiation only coming from > 1.0 keV and very little to none from > 3.0 keV, which is likely coming from the Al plane. Finally, the TGSP in Figure 6.9(e) shows very strong spectra from K-shell Al and Mg. The fact that K-shell Mg appears in the Al 5056 allow (95% Al, 5% Mg) suggests that K-shell Al is optically thick, so non-LTE kinetic modeling was accomplished for K-shell Mg and attained electron temperatures of 320 and 340 eV, which correspond well to the step-like pre-pulse features seen in the XRD and PCD signals.

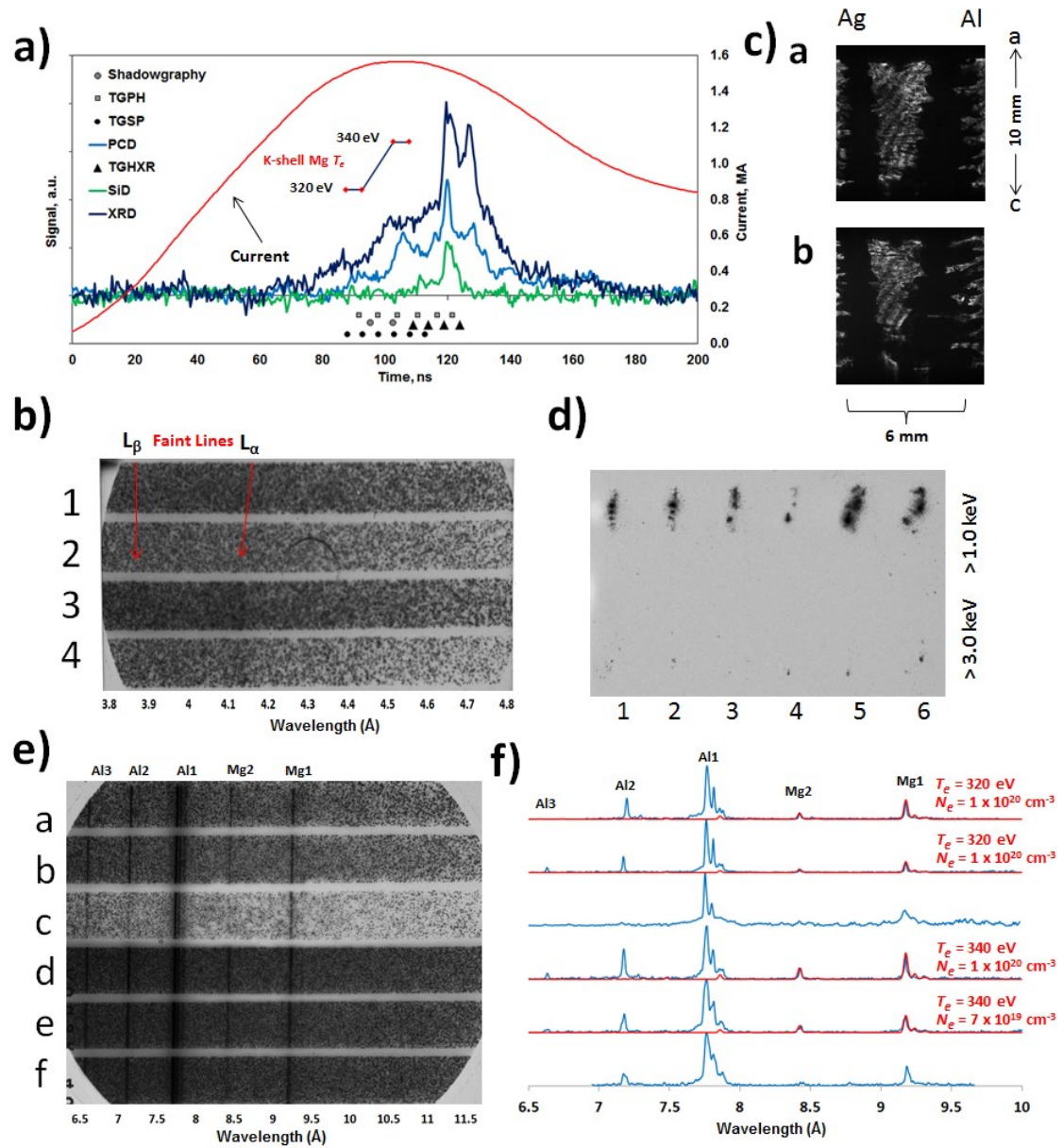


Figure 6.9. Signals from PCD, XRD, and SiD, along with measured current and K-shell Mg electron temperatures (a) for Zebra shot 2988 (Ag and Al DPWA with 6 mm gap). Time-gated hard x-ray spectra is shown in (b) with timings correlated with black triangles in (a) and numbered “1-4”. Shadowgraphy images are shown in (c) with timings correlated with grey circles in (a) and labeled “a-b”. Time-gated spectra is shown in (e) with timings correlated with black dots in (a) and labeled “a-f”. Lastly, (f) shows spectra in blue from (e) along with synthetic modeling of K-shell Mg in red.

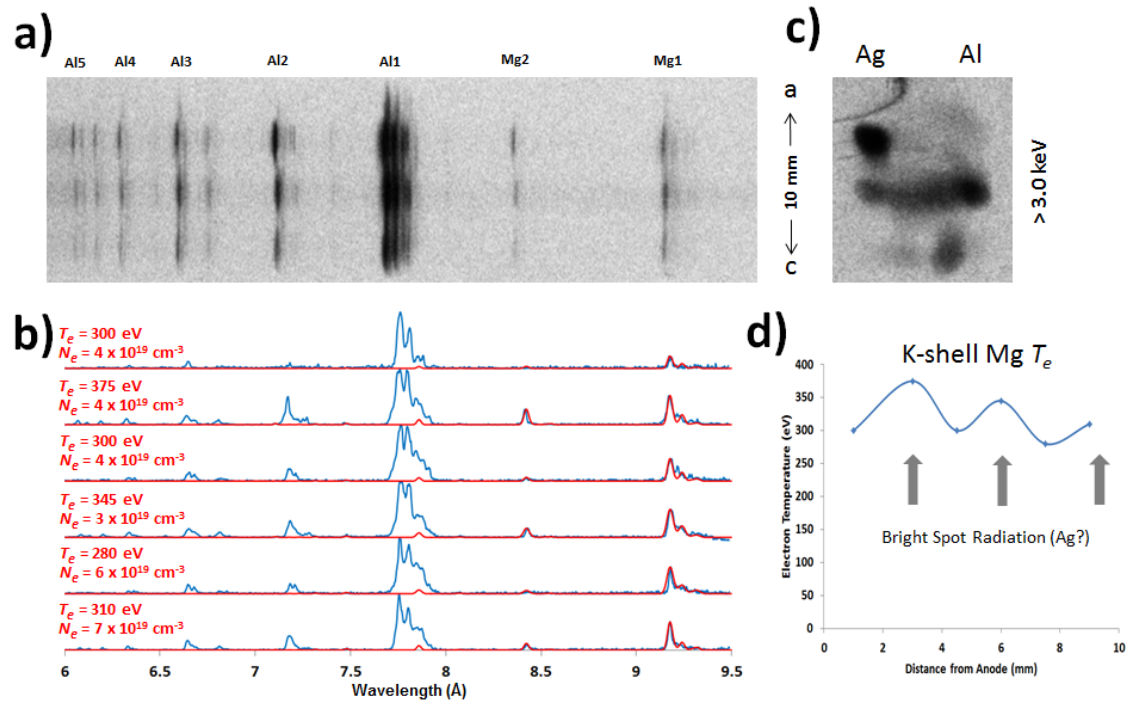


Figure 6.10. (a) Time-integrated spatially resolved spectra for Zebra shot 2988 (Ag and Al DPWA with 6 mm gap). (b) Experimental spectra (blue) taken from (a) and synthetic spectra (red) of K-shell Mg. (c) Time-integrated spatially resolved pinhole image (> 3.0 keV). (d) Electron temperature of K-shell Mg as a function of distance from anode.

Figure 6.10 highlights the radiative characteristics of shot 2988 from a mixed Ag and Al DPWA. Looking at the time-integrated spectra, it's clear that K-shell Al and Mg radiate along a column-like manner and mostly optically thick, and no discernable L-shell Ag was measured in the spectra, though there are at least three bright spots which correlate to increased intensity of K-shell Al and Mg, and modeling of K-shell Mg indicates that there is also an increase in electron temperature, from approximately 300 eV to over 375 eV. Looking to the pinhole image (> 3.0 keV), there is evidence of Ag radiation where Ag's initial position was, so it's interesting that this doesn't correlate with L-shell Ag spectra on the film. Even still, where this Ag is radiating in the pinhole

image, there seems to be an effect in the K-shell Mg electron temperatures, which agrees with earlier results from previous sections.

Figure 6.11 presents a clear picture the time evolution of the Ag and Al wire planes. By 67 ns there is a strong distinction between the Ag and Al planes, Al moving towards the central z-axis. The Al plane is shown to implode towards the central axis from the anode and then moves this imploding process to the anode, and this appears to have some effect of the cone-like structure.

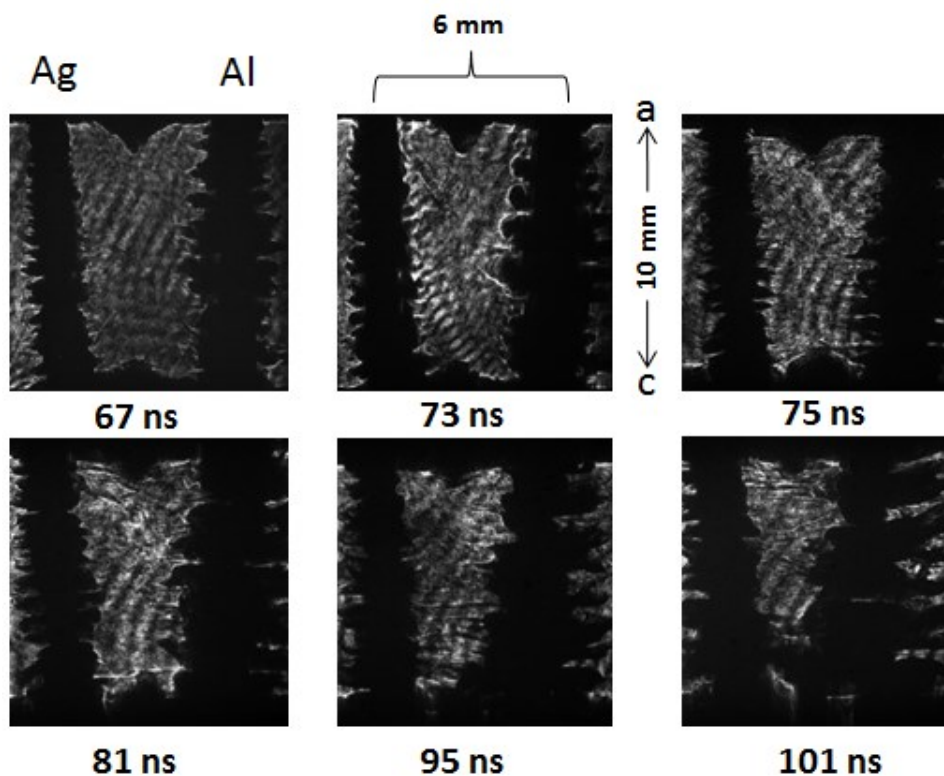


Figure 6.11. Shadowgraphy images of mixed Ag and Al DPWAs with 6.0 mm gap at enhanced current. The Ag plane is located on the left while the Al plane is located on the right in all images. Images from three different identical loads with timings changed. Images show independently imploding planes along with “cone-like” structures developing in anode “a” and cathode “c”.

6.4 Conclusions

In this chapter, pure Ag and mixed with Al PWAs and potential for lasing are discussed in detail for the first time. Ag wire arrays were explored due to their past and present performance as a very efficient radiator on the Zebra generator, producing near record energies of greater than 30 kJ. For the comparison between Ag SPWAs with standard (1.0 MA) and enhanced (1.7 MA) configurations, it was shown that Ag SPWAs produce very many bright spots along the pinch, corresponding with x-ray signals with a main burst, followed by very many bursts, and optically thick L-shell Ag plasmas. In particular, at standard configuration, the time-evolution of L-shell Ag was measured, resulting in what appeared to be cold L_α and L_β lines that likely correspond to electron beams and SiD measurements, and Ne-like 3G and Na-like satellite Ag lines that correlate with strong background generated in hotter plasma. The experiment at enhanced current produced very intense L-shell Ag radiation that manifested up to fourth order in the TISP spectra. Both configurations produced high energy output (> 15 kJ/cm for the standard configuration and > 16 kJ/cm for the enhanced configuration), both near records for the Zebra generator. For the mixed Ag and Al DPWA, it was shown that, while K-shell Al radiated along the length of the pinch in a column like manner, L-shell Ag radiated from only a few bright spots. Both K-shell Al and L-shell Ag radiated optically thin. Modeling of the K-shell Al indicated optically thin yet relatively hot T_e (> 500 eV), with the T_e being possibly affected by the presence of the L-shell Ag through radiative cooling from the Ag ions. This suggests that, while the K-shell Al and L-shell Ag may not be perfectly mixed in the plasma, they still have influence on each other in T_e . This may be explained by the fact that L-shell Ag requires much hotter T_e to radiate

than K-shell Al does (roughly three times). Modeling of the n_e of both K-shell Al and L-shell Ag indicate that L-shell Ag is an order of magnitude greater than that of K-shell Al and in the range of 10^{20} cm^{-3} to $7 \times 10^{20} \text{ cm}^{-3}$. The pulse shape for the mixed Ag and Al DPWA was also different than those of the Ag SPWAs, producing one main x-ray burst, followed by only a few smaller bursts, indicating a much more uniform pinch.

To better understand the implosion dynamics between planes in a double planar wire array, experiments were accomplished at 1.6 MA on Zebra of Ag and mixed Ag and Al DPWAs with an increased interplanar gap of 6.0 mm. The results produced independently imploding planes (similar to having two single planar wire arrays) before the two planes come together to form a secondary implosion. Again, time-gated hard x-ray spectra measured cold L_α and L_β lines showing correlation to harder x-ray SiD ($> 9 \text{ keV}$), showing a possible correlation to electron beams. For mixed Ag and Al loads, the Al implodes first, however still shows evidence of imploding independently before moving towards the central axis.

Chapter 7

Potential for Lasing in Ne-like Ag on the Zebra Generator

7.1 Introduction

In the previous chapter, z-pinch produced Ag plasmas were shown to radiate at very high electron temperatures ($T_e > 1.8$ keV). Electron densities have also been shown to be produced as high as 10^{21} cm⁻³ for z-pinch produced plasmas, particularly from x-pinches (Safronova *et al.* 2006b). Under these plasma conditions, Ag radiates predominantly in the Ne-like ionization stage, and could be conducive to population inversions between the 3p and 3s levels. In these transitions, the upper levels do not decay rapidly to the Ne-like ground state, while the lower levels have rapid dipole allowed decays to the Ne-like ground state (Apruzese *et al.* 1983), giving rise to inversion and lasing. The lower levels give rise to the 3F ($2p_{1/2}2p_{3/2}^43s^1P_1 \rightarrow 2p_{1/2}^22p_{3/2}^4^1S_0$) and 3G ($2p_{1/2}^22p_{3/2}^33s^3P_1 \rightarrow 2p_{1/2}^22p_{3/2}^4^1S_0$) lines. Under LTE conditions, the ratio of the number of electrons in each level can be characterized by the Boltzmann factor: $X_i/X_k = e^{-(E_i-E_k)/kT}$, where X_n are populations of the levels and E is the energy of the levels. Looking at this equation, X_i never exceeds X_k no matter how high T gets, therefore to achieve population inversion, the system needs to be in a non-LTE state, where three-body, radiative, and dielectric recombination from the F-like state (one ionization stage below Ne-like) and collisional excitation from the ground state can drive electrons to the upper level of the inversion. The electron temperature component is important in maintaining the Ne-like stage, and also increases collisional excitation rates. Therefore, under proper conditions in non-LTE

plasma with high enough T_e , population inversions can occur. So the question remains, does lasing occur on the Zebra generator for Ne-like L-shell Ag, and if so, at what gains? To help answer this question, a non-LTE kinetic model of L-shell Ag was utilized to calculate theoretical lasing gains (see Section 2.1.1). Much research has been accomplished both theoretically (Apruzese *et al.* 1983, Hansen *et al.* 2005) and experimentally (MacGowan *et al.* 1987, Fields *et al.* 1992) concerning these Ne-like ions and lasing. MacGowan *et al.* 1987 the Nova laser was used to create gain among Ne-like Mo and later Fields *et al.* 1992 for Ne-like Ag. It was proposed (Davis *et al.* 1988) to develop a pulsed power-driven laboratory x-ray laser using a Kr gas puff Z-pinch; however the experiments proved to be too non-uniform to achieve adequate lasing, though the intrinsically high gains of Ne-like Ag (9.4 cm^{-1} has been experimentally demonstrated (Fields *et al.* 1992)) may allow detection of amplification even under non-ideal conditions of significant non-uniformity. Lastly, due to the recent advances in creating more uniform pinches (Deeney *et al.* 1998 and Davis *et al.* 1997), and success at lower currents through the use of capillary discharges (Rocca *et al.* 1995), it's feasible that lasing at high gains are occurring at university scale Z-pinch devices.

Section 7.2 calculates theoretical lasing gain for Ne-like Ag for various plasma conditions, while Section 7.3 explores a new load type, the split double planar wire array, designed for uniform plasma conditions that are suitable for lasing, and Section 7.4 concludes the chapter.

7.2 Lasing Gain Calculations for Ne-like L-shell Ag

Fourteen transitions were shown to produce population inversions and are listed in Table 7.1. Of the fourteen transitions, nine are $3p \rightarrow 3s$, three are $4p \rightarrow 3s$, and two are

5p \rightarrow 5s. The wavelengths (\AA) and gain factors are also included. The gain factors are calculated using the negative of the absorption coefficient, k , of a Doppler-broadened transition, at line center, and is given by:

$$k(\text{cm}^{-1}) = 1.08 \times 10^{-16} f \lambda \sqrt{\frac{M_{ion}(\text{amu})}{T_{ion}(\text{eV})}} \left(X_k - \frac{g_k}{g_i} X_i \right) \quad 7.1$$

where f is the absorption oscillator strength, λ is the transition wavelength in \AA , M_{ion} is the mass of the ion, T_{ion} is the ion temperature, X_n are the populations of the respective levels in cm^{-3} , and g_n are the statistical weights of the levels. The absorption oscillator strength is calculated using Equation 2.8. Lasing can occur when $X_i > \left(\frac{g_i}{g_k}\right)X_k$ for decay transition from level i to k . The level populations are calculated using a non-LTE kinetic model of Ag, which utilizes the FAC atomic data. Ne-like Ag lasing has already been reported (Fields *et al.* 1992) on the Nova laser under comparable plasma conditions to Z-pinch. However there is a significant difference in T_{ion} when comparing laser produced plasma sources and Z-pinch plasma sources, as reported in Hansen *et al.* 2005 where potential for lasing in Ne-like Mo was discussed. In laser plasmas, the $T_{ion} \sim T_e$, however for Z-pinch plasmas it is estimated that $T_{ion} \geq T_e$, where the T_{ion} can be significantly greater than that of T_e (Haines *et al.* 2006), which in effect can broaden and detune the lasing transitions through Doppler effects. Another consideration are the effects of refraction of lasing emission due to large radial density gradients present in the z-pinch plasma column, which can reduce gain by as much as 20-40% (Hansen *et al.* 2005). One

final consideration is effect of hyperfine splitting in the Ne-like lines due to the coupling with the dipole magnetic moment of the nucleus. If the splitting is significant enough, the linewidth of the level increases, thereby lowering the gain. This effect has been measured previously (Nilsen *et al.* 1993) and was a possible explanation for low laser emissions for Ne-like ions in odd numbered Z elements, such as Ag ($Z = 47$). In Scofield *et al.* 1994 the contribution for gain lowering by hyperfine splitting as a function of ion temperature was assessed, and it was found that for Ag, the ion temperature would have to be as low as 10 eV to cause any significant drop in gain. As mentioned earlier in this section, T_{ion} is estimated to be greater than or equal to T_e , and given the estimated T_e is on the order of 1.4 – 1.8 keV for Ne-like L-shell Ag plasmas, it is highly unlikely that T_{ion} is on the order of 10 eV. Even if this were the case, this process would be offset by the fact that with low T_{ion} the Doppler broadening is minimized, and gain is substantially increased. Also, it was shown that the hyperfine splitting was only significant for the states with the $2p_{1/2}$ vacancy and not for states with the $2p_{3/2}$ vacancy due to the electron's spin and orbital angular momentum contributing with opposite sign and adds together for the $2p_{1/2}$ case while subtracting for the $2p_{3/2}$ case. Half of the transitions considered here have the $2p_{3/2}$ vacancy, and thus hyperfine splitting shouldn't be a concern for those transitions. The conclusion is that the effect of hyperfine splitting in general for Ne-like Ag isn't significant enough to affect lasing gains in z-pinch produced plasmas.

Upper Level i	Lower Level k	λ (Å)	Gain (a) (cm ⁻¹)	Gain (b) (cm ⁻¹)
$2p_{1/2}2p_{3/2}^43p_{3/2}^1D_2$	$2p_{1/2}^22p_{3/2}^33s^3P_1$	41.2	2.0×10^{-4}	7.0×10^{-4}
$2p_{1/2}^22p_{3/2}^33p_{3/2}^3P_0$	$2p_{1/2}^22p_{3/2}^33s^3P_1$	80.7	3.9	18.5
$2p_{1/2}^22p_{3/2}^33p_{3/2}^3P_2$	$2p_{1/2}^22p_{3/2}^33s^3P_1$	99.2	5.9	28.2
$2p_{1/2}^22p_{3/2}^33p_{3/2}^1P_1$	$2p_{1/2}^22p_{3/2}^33s^3P_1$	105.1	3.7	14.7
$2p_{1/2}^22p_{3/2}^33p_{1/2}^3D_2$	$2p_{1/2}^22p_{3/2}^33s^3P_1$	167.5	6.6	29.2
$2p_{1/2}^22p_{3/2}^33p_{1/2}^3D_1$	$2p_{1/2}^22p_{3/2}^33s^3P_1$	174.0	1.0	3.9
$2p_{1/2}2p_{3/2}^43p_{3/2}^1D_2$	$2p_{1/2}2p_{3/2}^43s^1P_1$	100.2	3.7	22.6
$2p_{1/2}2p_{3/2}^43p_{1/2}^1S_0$	$2p_{1/2}2p_{3/2}^43s^1P_1$	102.0	1.1	5.9
$2p_{1/2}2p_{3/2}^43p_{1/2}^3P_0$	$2p_{1/2}2p_{3/2}^43s^1P_1$	120.4	3.8	18.9
$2p_{1/2}2p_{3/2}^44p_{1/2}^3P_0$	$2p_{1/2}^22p_{3/2}^34s^3P_1$	56.7	3.0×10^{-4}	2.0×10^{-3}
$2p_{1/2}^22p_{3/2}^34p_{3/2}^3P_0$	$2p_{1/2}^22p_{3/2}^34s^3P_1$	201.0	0.3	2.8
$2p_{1/2}2p_{3/2}^44p_{1/2}^3P_0$	$2p_{1/2}2p_{3/2}^44s^1P_1$	318.5	0.1	1.4
$2p_{1/2}^22p_{3/2}^35p_{3/2}^3P_0$	$2p_{1/2}^22p_{3/2}^35s^3P_1$	406.1	0.1	1.1
$2p_{1/2}2p_{3/2}^45p_{1/2}^3P_0$	$2p_{1/2}2p_{3/2}^45s^1P_1$	646.6	6×10^{-2}	0.6

Table 7.1. List of considered lasing transitions for Ne-like Ag, along with wavelengths and gain calculations for two plasma conditions. Gain (a) is calculated using plasma conditions $T_e = T_{ion} = 1.8$ keV and $n_e = 10^{21}$ cm⁻³. Gain (b) is calculated using plasma conditions $T_e = T_{ion} = 2.4$ keV and $n_e = 10^{22}$ cm⁻³.

Looking back to Table 7.1, gains are calculated for two different plasma conditions. The first is calculated using conditions that have proven to be attainable for L-shell Ag on the Zebra generator, which is $T_e = 1.8$ keV and $n_e = 10^{21}$ cm⁻³. In these calculations, it is assumed $T_{ion} = T_e$, which, from discussion above, probably underestimates T_{ion} . The $2p_{1/2}^22p_{3/2}^33p_{1/2}^3D_2 \rightarrow 2p_{1/2}^22p_{3/2}^33s^3P_1$ transition at 167.5 Å has the largest calculated gain at 6.6 cm⁻¹, followed by the $2p_{1/2}^22p_{3/2}^33p_{3/2}^3P_2 \rightarrow 2p_{1/2}^22p_{3/2}^33s^3P_1$ transition at 99.2 Å with a gain of 5.9 cm⁻¹. The lowest wavelength with an appreciable gain is the $2p_{1/2}^22p_{3/2}^33p_{3/2}^3P_0 \rightarrow 2p_{1/2}^22p_{3/2}^33s^3P_1$ transition at 80.7 Å with a gain of 3.9 cm⁻¹.

For interest, the lowest wavelength transition that showed any positive gain at all was the $2p_{1/2}2p_{3/2}^43p_{3/2}^1D_2 \rightarrow 2p_{1/2}^22p_{3/2}^33s^3P_1$ transition at 41.2 Å with a small gain of $2.0 \times 10^{-4} \text{ cm}^{-3}$. The second set of gain calculations were using conditions $T_e = 2.4 \text{ keV}$ and $n_e = 10^{22} \text{ cm}^{-3}$. Again, the highest gain calculated is the $2p_{1/2}^22p_{3/2}^33p_{1/2}^3D_2 \rightarrow 2p_{1/2}^22p_{3/2}^33s^3P_1$ transition at 167.5 Å with a gain of 29.2 cm^{-3} . Beyond $T_e = 3.0 \text{ keV}$, the plasma is estimated to quickly burn through Ne-like, and considerably drop the level populations of the levels, while beyond $n_e \sim 10^{23} \text{ cm}^{-3}$, the collisional processes become too intense and consequentially destroy the population inversions. Figures 7.1 and 7.2 show plots of how both T_e and n_e affect lasing gain for the transitions $2p_{1/2}^22p_{3/2}^33p_{3/2}^3P_2 \rightarrow 2p_{1/2}^22p_{3/2}^33s^3P_1$ at 99.2 Å and $2p_{1/2}^22p_{3/2}^33p_{3/2}^3P_0 \rightarrow 2p_{1/2}^22p_{3/2}^33s^3P_1$ at 80.7 Å, respectively. Gains were calculated for $T_e = T_{\text{ion}}$ in the range of 900 – 3000 eV and n_e in the range of $10^{19} - 10^{24} \text{ cm}^{-3}$. From these figures it becomes clear that, with reasonably high density, between $10^{21} \text{ cm}^{-3} \leq n_e \leq 10^{23} \text{ cm}^{-3}$, T_e can be anywhere between 1200 and 3000 eV and produce high gains between 1.0 cm^{-1} and 60 cm^{-1} for the $2p_{1/2}^22p_{3/2}^33p_{3/2}^3P_2 \rightarrow 2p_{1/2}^22p_{3/2}^33s^3P_1$ transition at 99.2 Å and gains between 1.0 cm^{-1} and 30 cm^{-1} for the $2p_{1/2}^22p_{3/2}^33p_{3/2}^3P_0 \rightarrow 2p_{1/2}^22p_{3/2}^33s^3P_1$ transition at 80.7 Å. As expected at $n_e = 10^{24} \text{ cm}^{-3}$ the calculations show negative lasing gain and are plotted as 0.0 cm^{-1} on the graph. This wide range of plasma conditions that potentially produce high gain in Ne-like Ag indicates that there is a good chance that lasing is occurring, at least in some regions, within z-pinch plasmas.

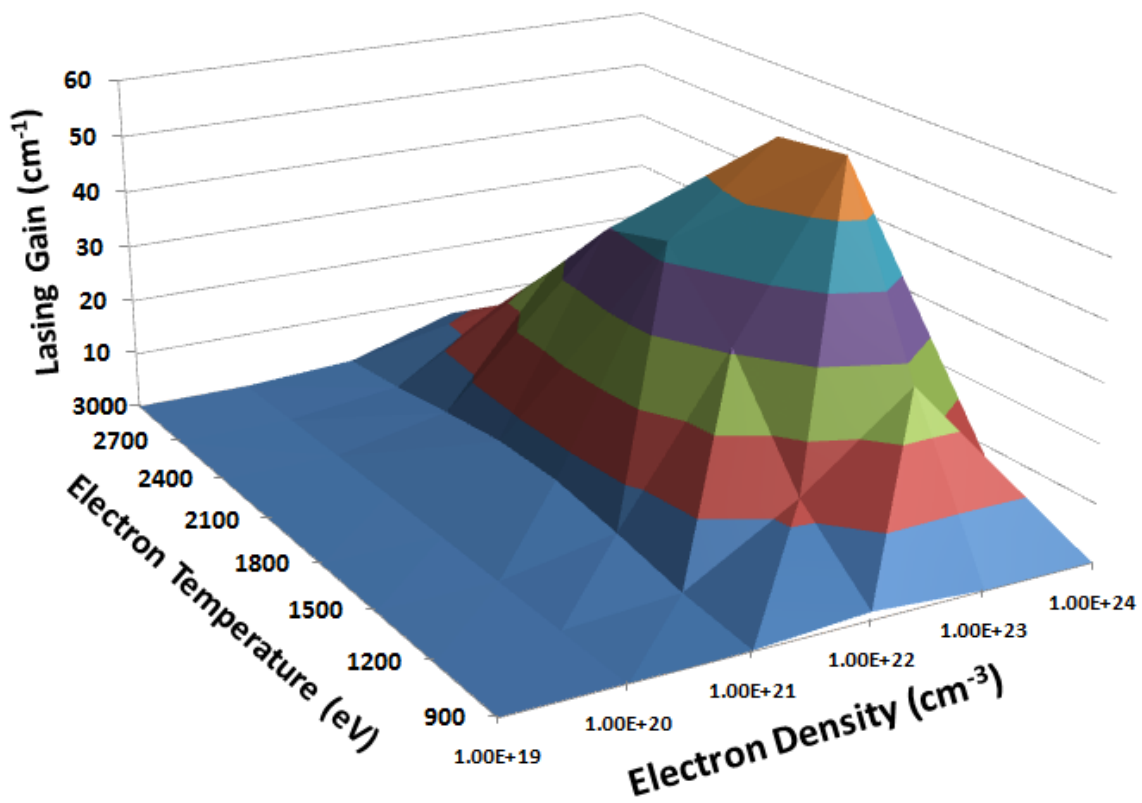


Figure 7.1. Lasing gain calculated as function of T_e and n_e for the Ne-like Ag transition of $2p_{1/2}^2 2p_{3/2}^3 3p_{3/2} \ ^3P_2 \rightarrow 2p_{1/2}^2 2p_{3/2}^3 3s \ ^3P_1$ at 99.2 Å. In these calculations, $T_{ion} = T_e$.

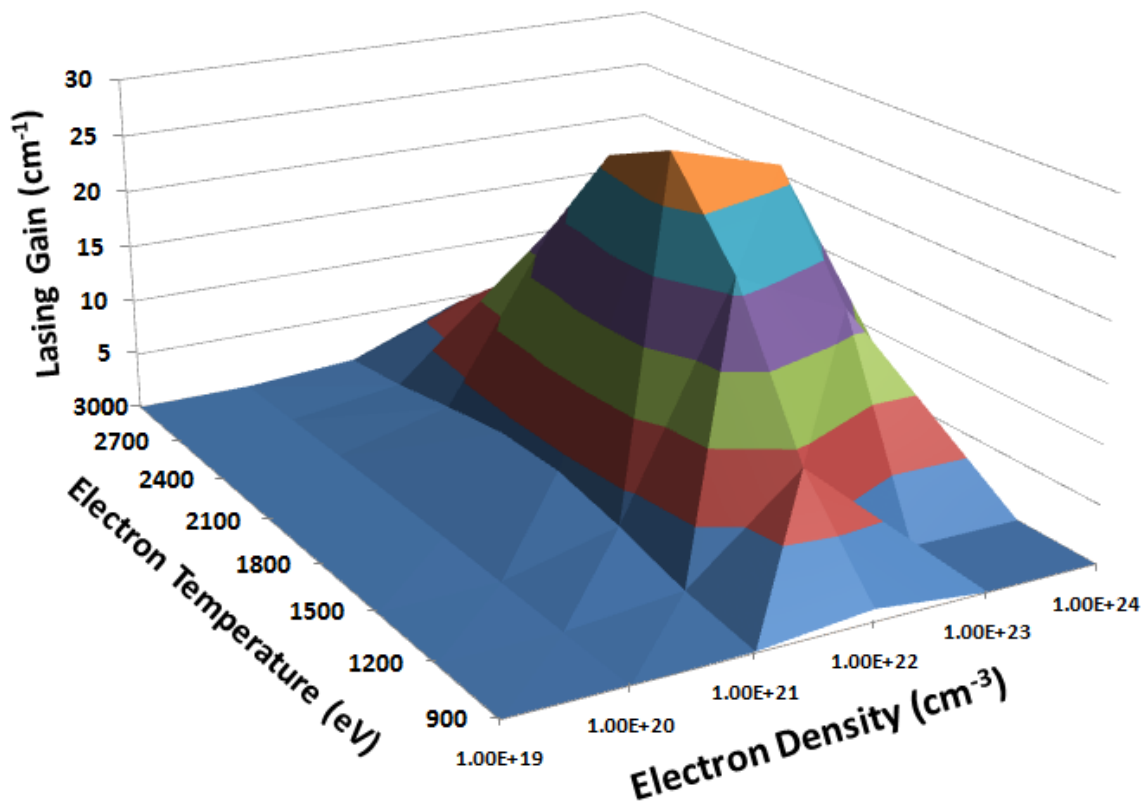


Figure 7.2. Lasing gain calculated as function of T_e and n_e for the Ne-like Ag transition of $2p_{1/2}^2 2p_{3/2}^3 3p_{3/2} \ ^3P_0 \rightarrow 2p_{1/2}^2 2p_{3/2}^3 3s \ ^3P_1$ at 80.7 Å. In these calculations, $T_{ion} = T_e$.

7.3 Split Double Planar Wire Array to Measure Lasing

The first preliminary results on the creation of a more uniform plasma column for the purpose of measuring lasing on the Zebra generator will be discussed in this section. The new wire array scheme used for these experiments is the split double planar wire array (SDPWA). The configuration consists of two DPWAs split by 3.5 mm (which can be adjusted). The experiments used twenty 10.16 μm diameter Mo wires (2x5/5 wires) that had an interplanar gap of either 3.0 mm or 6.0 mm and interwire gap of 0.7 mm. Mo wires were used instead of Ag to avoid potential issues, such as hyperfine splitting, for initial experiments. Future experiments include Ag wires. These experiments were taken

with the implementation of the LCM at 1.7 MA. The first results of shadowgraphy are shown in Figure 7.3, which display images from a SDPWA with a 3.0 mm gap. It's evident that as early as 50 ns into the current rise, a column-like plasma structure has formed, possibly a precursor before the main implosion. This particular structure is of interest for a possible medium for lasing, and further research is required. Figure 7.4 shows signals and time-gated pinhole images (TGPH) from this experiment. The signals include a filtered x-ray diode (XRD, > 0.2 keV), a photoconducting diode (PCD, > 0.8 keV), and a silicon diode (SiD, > 9 keV). Frame (b) on the TGPH image was taken at the maximum of the signals (~ 100 ns) and indicates a very uniform and column-like structure at implosion, which again, can be good conditions for lasing.

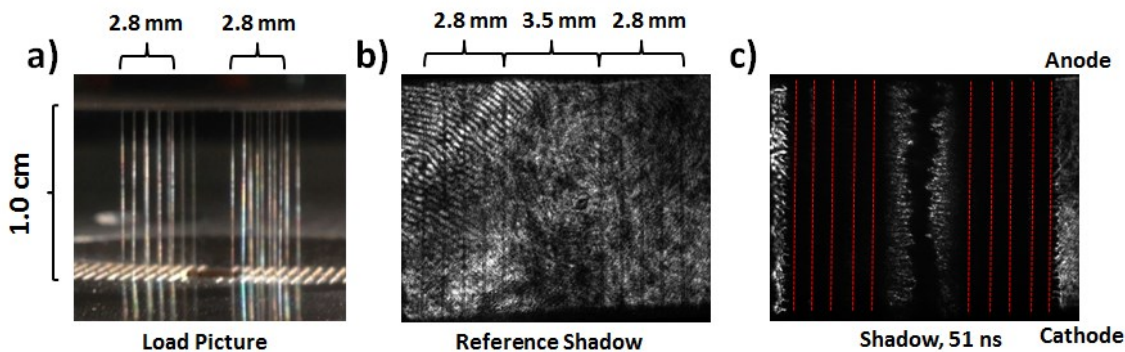


Figure 7.3. a) Structure of a split double planar wire array (perpendicular view) on the 1.7 MA Zebra generator. b) A reference shadowgraphy picture before the experiment (perpendicular view). c) Shadowgraphy taken approximately 50 ns into the shot after the current rise. The red dotted lines indicate where the wires originally began. An early and relatively uniform column has formed.

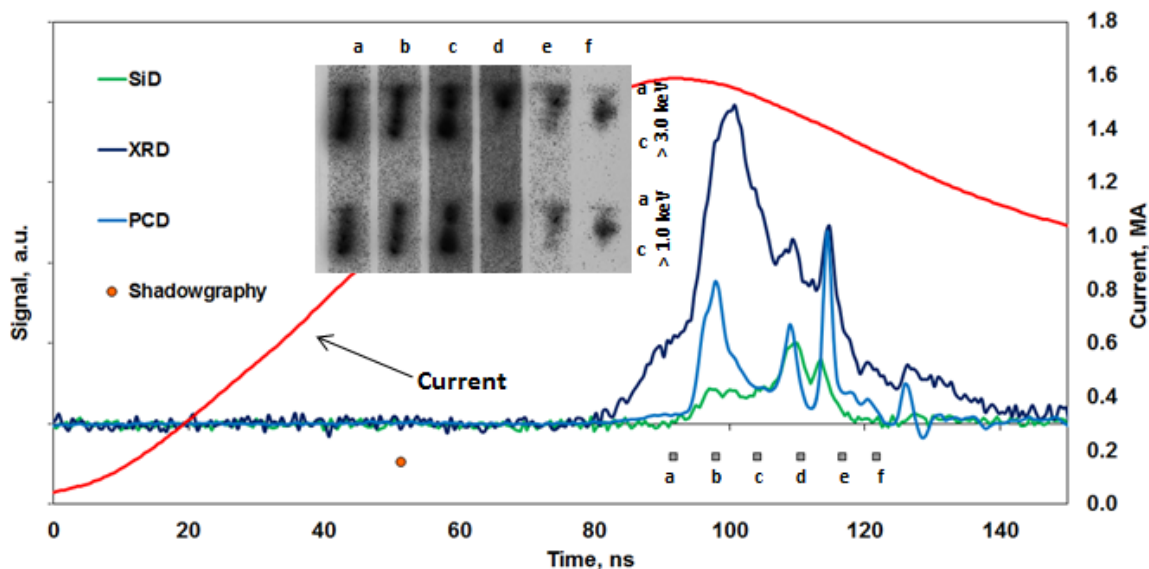


Figure 7.4. Signals and time-gated pinhole images from a Mo split double planar wire array with 3.0 mm interplanar gap on the 1.7 MA Zebra generator. The pinhole timings are shown with gray boxes and are listed “a-f” and are filtered at > 1.0 keV (bottom) and > 3.0 keV (top).

The new SDPWA load was also carried out with a 6.0 mm interplanar gap to see how the gap changes the dynamics of the plasma flow early in the implosion. This also allowed for excellent diagnostic access in between the planes, so two experiments were performed, one in which the laser probe had a perpendicular view as before, and the other in which the laser probe had a parallel view between the planes. The results of these experiments are illustrated in Figure 7.5. These experiments were carried out with the same Mo wires as before. Figure 7.5(a) shows the development of a column-like structure 50 ns from the current rise, similar to the results with a 3.0 mm interplanar gap. The structure appears to be forming from the anode traveling down to the cathode in a zipper-like manner. Figure 7.5(b) shows the evolution of this structure 6 ns later. The structure has completed its formation from anode to cathode and appears to be a well-structured

and uniform column, perhaps again a pre-cursor formation. Figure 7.5(c) shows the development of this structure from a parallel view, looking in between the planes, at approximately 52 ns. Again, the development forms from the anode and travels to the cathode, suggesting this behavior is reproducible. Figure 7.5(d) shows the progression of the structure 6 ns later and again a relatively uniform column has developed.

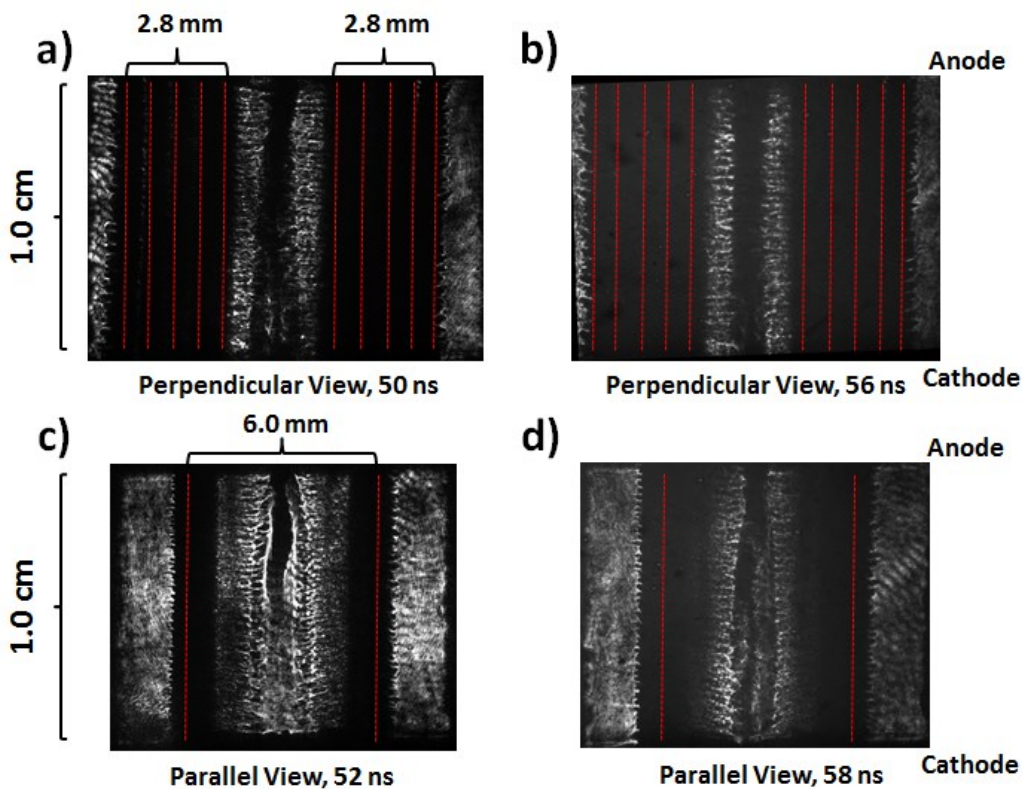


Figure 7.5. a) Shadowgraphy from a split double planar wire array 50 ns into the shot after current rise, seen from a perpendicular view. b) Shadowgraphy from same shot as in a) 6 ns later. c) Shadowgraphy from a split double planar wire array 52 ns into the shot after current rise, seen from a parallel view, in between the planes. d) Shadowgraphy from same shot as in c) 6 ns later. The red dotted lines indicated were the wires originally began.

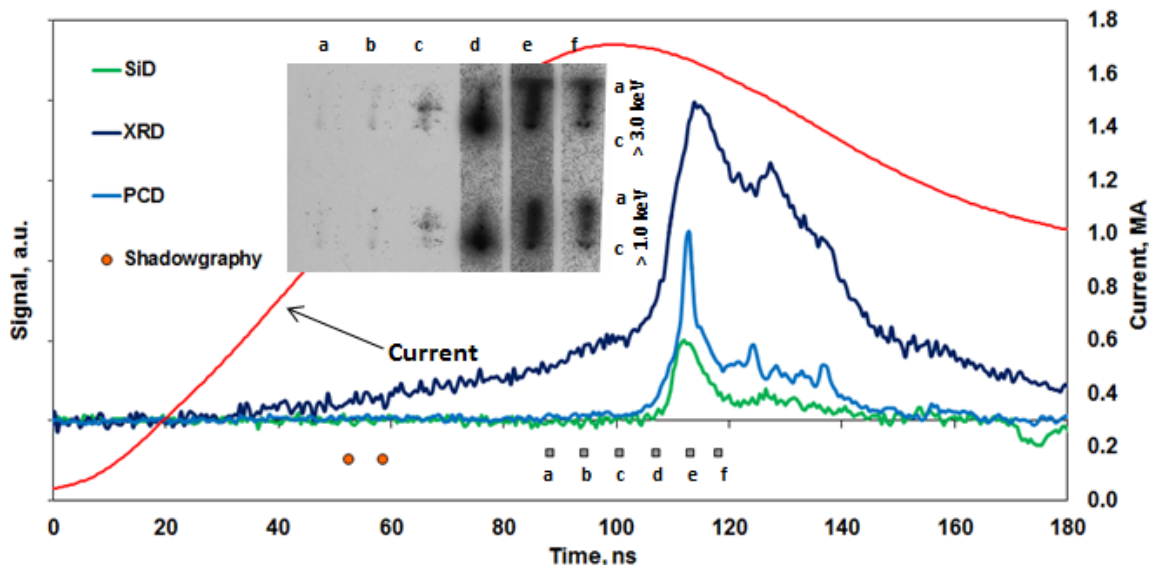


Figure 7.6. Signals and time-gated pinhole images from a Mo split double planar wire array with 6.0 mm interplanar gap on the 1.7 MA Zebra generator. The pinhole timings are shown with gray boxes and are listed “a-f” and are filtered at > 1.0 keV (bottom) and > 3.0 keV (top).

Figure 7.6 shows signals and TGPH images from the SDPWA with a 6.0 mm interplanar gap. The increased gap increased the implosion time from approximately 100 ns with a 3.0 mm gap to approximately 117 ns 6.0 mm gap. Frame (e) on the TGPH image was taken at maximum of the signals and indicates again a very uniform and column-like structure at implosion, similar to the experiments with a 3.0 mm gap.

The above data from the recent SDPWA experiments yield promising results of creating and controlling a plasma flow that could be ideal conditions for lasing. A few questions remain, namely the formation of the early column-like structure, which could be a precursor formation, and whether or not this early formation could produce plasma conditions that reach the necessary T_e and n_e for high gains. Precursor plasmas from cylindrical wire arrays (CWAs) have been a continual area of study using the Zebra

generator. These studies detailed the structure of the precursor column and approximated the precursor plasma conditions. Mid-atomic number materials (Ni, Cu, and Zn) were used to study precursor plasmas. Cu CWA precursor plasmas were shown to radiate at electron temperatures as high as 450 eV (Coverdale *et al.* 2009) using a non-LTE kinetic model.

The next step and future plans for the SDPWAs is to optimize load design through both WADM simulations and further experiments. Once the design, optimization, and implementation of the loads are finished, the experiments will be ready to move to the task of measuring the potential lasing lines. For Ne-like Mo, the lasing lines of interest radiate between 100 – 200 Å, so the use of calibrated EUV spectrometers will be necessary. To give the best chance of measuring lasing, two spectrometers will be utilized; one which will sit above the load for an axial view, and another will sit radially to view in between the planes. Figure 7.7 illustrates this idea. An important aspect of the load hardware for SDPWAs is the hole in the center of the anode and cathode plates that offer excellent axial diagnostic access. A picture of the hole is illustrated in figure 7.7.

If these experiments prove successful, and lasing lines of Ne-like Mo are measured, the next logical step would be to move onto Ag SDPWAs for experiments.

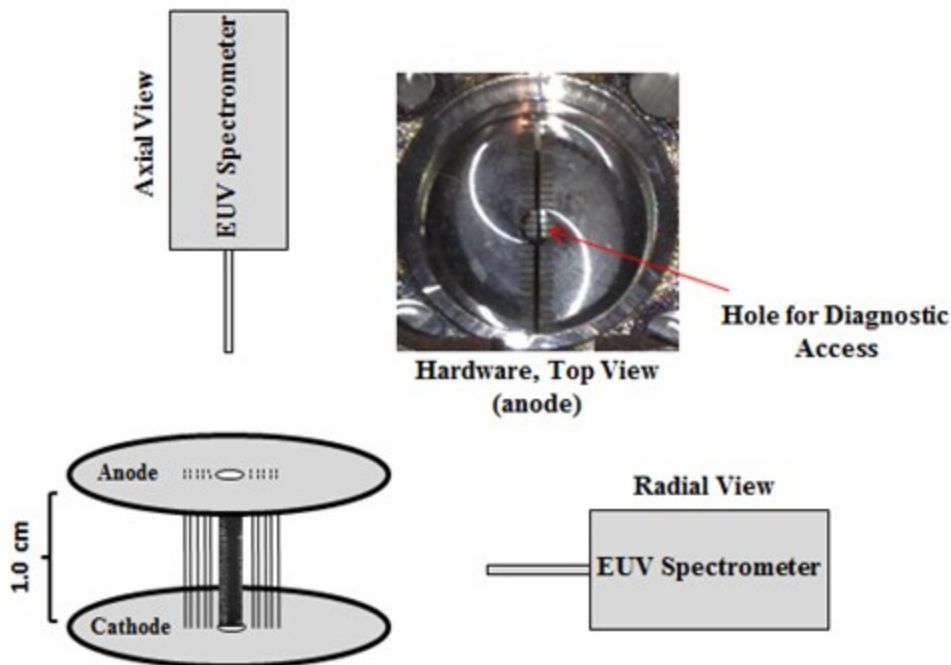


Figure 7.7. Illustrations of EUV Spectrometer locations for the split double planar wire array experiments. The picture in the upper right shows the physical anode plate hardware with a hole in the middle for diagnostic access for an EUV spectrometer measure potential lasing lines radiating axially.

7.4 Conclusions

The potential for lasing on the Zebra generator using Ag wires was explored. A total of fourteen transitions were included. The advantages and disadvantages of using z-pinch produced plasma sources for lasing were considered. It was shown that the Zebra generator may provide sufficient plasma conditions that yield gains as high as 6.6 cm^{-1} . A broad range of plasma conditions were also used to calculate gain and it was shown that for gains $> 1.0 \text{ cm}^{-1}$ plasma conditions need to be in the range of $1200 \text{ eV} \leq T_e \leq 3000 \text{ eV}$ and $10^{21} \text{ cm}^{-3} \leq n_e \leq 10^{23} \text{ cm}^{-3}$. Further experimental research is required to verify these results. It may be advantageous to point spectrometers in the proper spectral

range on-axis to look for these possible amplified soft x-ray lines. An on-axis view would provide 1-2 cm of plasma rather than a few mm of plasma looking in the radial view. A DPWA may be a good candidate for measuring gain, as it has been shown in this work to produce more uniform and stable pinches. Future work will focus on designing experiments and diagnostics to measure these potential gains, as well as exploring other properties of Ag plasmas that may further enhance overall efficiency, which is of importance for the possibility of observing significant lasing gain on a university scale z-pinch machine.

A new load, the split double planar wire array, was tested and analyzed for the first time. The initial results show promise in forming relatively uniform precursors which could provide a much needed medium in which lasing can occur in Ne-like plasmas. Future plans and goals were discussed for later experiments to optimize load design and utilize EUV spectrometers to try and measure lasing gain.

Chapter 8

Conclusions

This dissertation is focused on expanding the knowledge of high energy density plasmas predominately generated from z-pinchs using both theoretical and experimental tools. In Chapter 2, the theoretical tools were discussed and comprise of various non-LTE kinetic models including a new model for L-shell Ag, where dependencies were shown for electron temperature, electron density, and percentage of non-Maxwellian hot electrons. In addition, a new suite of codes from Prism have been implemented, including SPECT3D, which utilizes the atomic data from ATBASE to generate synthetic spectra to estimate non-LTE plasma conditions from many materials, and HELIOS-CR, which is a 1-D radiation hydrodynamics code that was used to simulate a Ag single wire z-pinch. A new experimental tool was designed, tested, and employed, the time-gated hard x-ray spectrometer, capable of attaining time resolution of spectra from 0.7 – 4.4 Å depending on various geometries and the crystal used (LiF or α -quartz). These new tools were applied in a variety of methods throughout the dissertation. The brunt of the dissertation concentrated on experiments from complex uniform and mixed wire arrays, ranging from more traditional nested cylindrical wire arrays to novel single, double, and triple planar wire arrays, with the goal of understanding the implosion and radiative dynamics and the continued search for higher efficient radiators.

With the above goals in mind, Chapter 3 looked into the results of uniform Mo and mixed with Al triple planar wire arrays performed Zebra with different interplanar gaps,

3.0 mm and 1.5 mm. The results showed that reducing the interplanar gap from 3.0 mm to 1.5 mm increased the total radiated energy output from ~16 kJ to ~25 kJ for the uniform Mo loads, and increased this efficiency for all mixed Mo and Al loads considered. For the mixed Mo and Al loads where Mo planes were on the outside and the Al plane was on the inside, L-shell Mo radiated from randomly generated bright spots while K-shell Al radiated optically thin lines and followed the Mo bright spot formations. For the opposite loads, where Al planes were on the outside and the Mo plane was on the inside, L-shell Mo again radiated from many bright spots while the most intense K-shell Al lines are optically thick and followed a column-like formation. The increased opacity in K-shell Al is likely from the initial placement of the Al wires and the twice increased initial mass. L-shell Mo spectra was modeled to radiate at electron temperatures between 900 - 1200 eV, while K-shell Al and Mg spectra was modeled to have electron temperatures between 300 – 500 eV, while the electron densities were estimated to be between 10^{19} and 10^{21} cm^{-3} . Results from these experiments were presented at the 8th International Conference on Dense Z-Pinches and submitted as Proceedings.

Chapter 4 discussed nested cylindrical wire arrays, in particular how the inner array radiates compared to how the outer array radiates. To answer this question, mixed brass and Al wires were used by keeping the outer array uniform brass and the inner array uniform Al for one set of experiments and then switching the materials for the next set of experiments. The results showed that the total radiated energy changed from ~15 kJ to ~17.5 kJ when the Al wires went from outside to the inside. The results also showed that the line intensities and opacity features changed dramatically, with higher intensities and opacities observed when the corresponding wires were placed on the outside compared to

when they were placed on the inside of the array. The overall conclusion is that the outer array contributes more to the total radiation than the inner array, likely due to increased kinetic energy the outer array develops as opposed to the inner array. Results from these experiments were presented at the Radiation from High Energy Density Plasmas International Conference in 2011 and published in the High Energy Density Physics journal (Weller *et al.* 2012a). Similar experiments were carried out with Mo and Al nested cylindrical wire arrays on both the Zebra and Cobra generators, with Al tracer wires used. The results showed similar trends as with the brass and Al NCWAs and produced plasmas with two different T_e , as with the Mo and Al TPWAs. An interesting result on the Cobra generator indicated that the Al tracer wires imploded before the Mo wires regardless of being placed in the inner or outer array, which may explain the early pre-pulse shape on the PCD at > 0.2 keV. These results of the Al tracer wires imploding before the Mo wires regardless of initial placement were reproduced with the WADM.

Chapter 5 explored EUV spectroscopy of Cu from two sets of experiments, one on the SSPX spheromak and the other on the laser plasma facility “Sparky”. The goal of studying EUV spectra from the SSPX spheromak experiments was to understand how impurities play a role in plasmas, such as sputtering of material from the walls of the chamber, or from various atmospheric contaminants, such as oxygen. The chamber itself was made of Cu, so M-shell Cu proved to be a prominent impurity. The results identified several Cu X – XIII transitions and modeled the M-shell Cu lines using Spect3D (Prism) giving results of $T_e = 35$ eV at $n_e = 10^{14}$ cm⁻³, while oxygen impurity lines were modeled to be cooler at $T_e \sim 15$ eV. The “Sparky” results indicated a two-temperature plasma of $T_e = 25$ and 90 eV, likely emitting from two locations, the cooler outer shell and the hotter

inner core. The results from these investigations not only gave new insight on the SSPX spheromak impurities and the plasma generated from “Sparky”, but also provided an excellent opportunity to study more challenging EUV Cu spectra compared to x-ray Cu spectra. The results were presented at the 19th Topical Conference on High Temperature Plasma Diagnostics in 2012 and published in the Review of Scientific Instruments journal (Weller *et al.* 2012b).

Chapter 6 focused on new results and applications of radiation from Ag high energy density plasmas. Planar wire arrays were chosen due to previous results of being very efficient radiators. The results showed that Ag planar wire arrays are some of the most efficient radiators on the Zebra generator at > 30 kJ. A comparison of uniform Ag single planar wire arrays and standard and enhanced currents and a mixed Ag and Al double planar wire array at standard current was accomplished. The new time-gated hard x-ray spectrometer was also utilized and measured cold L_{α} and L_{β} characteristic Ag lines for the first time, that likely correspond to electron beams. To further understand the implosion characteristics of double planar wire arrays, the interplanar gap was increased to 6 mm for uniform Ag and mixed with Al. Shadowgraphy and other x-ray diagnostics concluded that the individual planes in these proposed and performed experiments independently implode first, followed by a secondary implosion. Again, time-gated hard x-ray spectra measured cold L_{α} and L_{β} lines showing correlation to the SiD at > 9 keV. For the mixed Ag and Al loads, the Al planes were shown to implode first, though both Ag and Al planes indicated independent implosions first before the main implosion.

In Chapter 7, as an extension and application to the Ag planar wire arrays, a theoretical exercise was performed utilizing the new non-LTE kinetic model of Ag to

calculate population levels to estimate lasing gains in $3p \rightarrow 3s$ Ne-like transitions and the results showed that the Zebra generator may be providing suitable conditions for gains as high as 6 cm^{-1} . Results from these calculations and from the Ag single planar and mixed with Al double planar wire array were presented at the Radiation from High Energy Density Plasmas International Conference in 2013 and published in the *Physics of Plasmas* journal (Weller *et al.* 2014). As a first step in attaining lasing in wire array z-pinch the experimental results of a new load type, the split double planar wire array was shown as a potential load candidate to attain proper uniform plasma conditions as a medium for lasing to occur. Future plans will set out to optimize this load design and use EUV spectrometers both axially and radially to try and measure these lasing lines.

To conclude, the results of over six years of research has yielded participation in over 15 experimental campaigns on the Zebra generator, where I was responsible for all optical systems, and also played a key role in set up and take down of experimental diagnostics, including deep knowledge of the Load Current Multiplier and designing and fielding the new hard x-ray spectrometer. During these experimental campaigns, over 30 experiments were proposed and accomplished. The results were showcased in over 20 conferences scattered throughout the U.S. and abroad, which include 11 posters and 10 oral talks. I was the co-author in over 20 peer reviewed publications, 3 of which I was the first author, in addition to over 15 conference proceedings. I also helped in write several proposals for grants and was the mentor of three undergraduate students in writing their own senior thesis projects. I began as an experimentalist and branched out into the world of theoretical physics and the resulting work showcases a blend of both worlds.

Appendix

Appendix A1: Symbols

T_e = electron temperature

n_e = electron density

T_i = ion temperature

n_i = ion density

$X_{Z,\eta}$ = ion charge state

ε, E = energy

$\sigma(\varepsilon)$ = cross section

$\mathcal{F}(\varepsilon)$ = electron distribution

v = velocity

t = time

$\langle Z \rangle$ = average charge state

α = fraction of hot electrons

n = energy level

A_r = radiative decay rate

f = oscillator strength

g_i = statistical weight

λ = wavelength

$2d$ = atomic spacing

Λ = wavelength range

R = spectral resolution

I = electric current

G_n = ablation rate coefficient

W_{Th} = thermalized kinetic energy

ϕ = aspect ratio

Appendix A2: Constants

e = electron charge = $1.602176487 \times 10^{-19} \text{ C}$

m_e = mass of electron = $9.10938215 \times 10^{-31} \text{ kg} = 0.510999 \text{ MeV}/c^2$

c = speed of light in vacuum = 299792458 m/s

h = Planck's constant = $4.13566733 \times 10^{-15} \text{ eV}\cdot\text{s}$

$\hbar = h/2\pi = 6.58211899 \times 10^{-16} \text{ eV}\cdot\text{s}$

$\pi \approx 3.14159$

Ry = Rydberg's constant = $e^4 m_e / 2\hbar^2 = 13.605\,692 \text{ eV}$

Appendix B: Acronyms and Abbreviations

ICF = inertial confinement fusion

CWA = cylindrical wire array

NCWA = nested cylindrical wire array

PWA = planar wire array

SPWA = single planar wire array

DPWA = double planar wire array

TPWA = triple planar wire array

SDPWA = split double planar wire array

LTE = local thermodynamic equilibrium

UNR = University of Nevada, Reno

WADM = wire ablation dynamics model

WDM = wire dynamics model

SSPX = Sustained Spheromak Physics Experiment

EUV = extreme ultraviolet

TGSP = time-gated spectrometer

TISP = time-integrated spectrometer

TGHXR = time-gated hard x-ray spectrometer

TGPH = time-gated pinhole

TIPH = time-integrated pinhole

FAC = Flexible Atomic Code

SCRAM = Spectroscopic Collisional-Radiative Atomic Model

HULLAC = Hebrew University Lawrence Livermore Atomic Code

RMBPT = relativistic many-body perturbation theory

PROPACEOS = PRism OPACity and Equation Of State

NTF = Nevada Terawatt Facility

LCM = Load Current Multiplier

ICCD = intensified charge-coupled device

KAP = potassium hydrogen phthalate

MCP = microchannel plate

LLNL = Lawrence Livermore National Laboratory

SFFS = Silver Flat Field Spectrometer

FWHM = full width at half maximum

XRD = x-ray diode

PCD = photoconducting diode

References

O.A. Anderson, W.R. Baker, S.A. Colgate, J. Ise, R.V. Pyle, *Neutron Production in Linear Deuterium Pinches*, Physical Review **110**, 1375 (1958)

J.P. Apruzese and J. Davis, *Enhancement of x-ray gain in neon-like ions by direct collisional pumping with suprathermal electrons*, Physical Review A **28**, 3686-3688 (1983)

J.P. Apruzese, P.E. Pulsifer, J. Davis, R.W. Clark, K.G. Whitney, J.W. Thornhill, T.W.L. Sanford, G.A. Chandler, C. Deeney, D.L. Fehl, T.J. Nash, R.B. Spielman, W.A. Stygar, K.W. Struve, R.C. Mock, T.L. Gilliland, D.O. Jobe, J.S. McGurn, J.F. Seamen, J.A. Torres, and M. Vargas., *K-shell radiation physics in the ultrahigh optical depth pinches of the Z generator*, Physics of Plasmas **5**, 4476 (1998)

A. Bar-Shalom, M. Klapisch, and J. Oreg, *Electron collision excitations in complex spectra of ionized heavy atoms*, Physical Review A **38**, 1773 (1988)

B.S. Bauer, V.L. Kantsyrev, F. Winterberg, A.S. Shlyaptseva, R.C. Mancini, H. Li, A. Oxner, *The dense Z-pinch program at the University of Nevada, Reno*, AIP Conference Proceedings **409**, 153-156 (1997)

P. Beiersdorfer, S. von Goeler, M. Bitter, E. Hinnov, R. Bell, S. Bernabei, J. Felt, K.W. Hill, R. Hulse, J. Stevens, S. Suckewer, J. Timberlake, A. Wouters, M.H. Chen, J.H. Scofield, D.D. Dietrich, M. Gerassimenko, E. Silver, R.S. Walling, and P.L. Hagelstein, *X-ray transitions in highly charged neonlike ions*, Physical Review A **37**, 4153 (1988)

K.M. Chandler, S.A. Pikuz, T.A. Shelkovenko, M.D. Mitchell, D.A. Hammer, and J.P. Knauer, *Cross calibration of new x-ray films against direct exposure film from 1 to 8 keV using the X-pinch x-ray source*, Review of Scientific Instruments **76**, 113111 (2005)

A.S. Chuvatin, V.L. Kantsyrev, L.I. Rudakov, M.E. Cuneo, A.L. Astanovitskiy, R. Presura, A.S. Safronova, W. Cline, K.M. Williamson, I. Shrestha, G.C. Osborne, B. LeGalloudec, V. Nalajala, T.D. Pointon, and K.A. Mikkelsen, *Operation of a load current multiplier on a nanosecond mega-ampere pulse forming line generator*, Physical Review Special Topics - Accelerators and Beams **13**, 010401 (2010)

J. Clementson, P. Beiersdorfer, M.F. Gu, H.S. McLean, and R.D. Wood, *EUV spectroscopy on the SSPX spheromak*, Journal of Physics: Conference Series **130**, 012004 (2008)

C.A. Coverdale, C. Deeney, P.D. LePell, B. Jones, J. Davis, R.W. Clark, J.P. Apruzese, J.W. Thornhill, and K.G. Whitney, *Large diameter (45-80 mm) nested stainless steel wire arrays at the Z accelerator*, Physics of Plasmas **15**, 023107 (2008)

C.A. Coverdale, A.S. Safronova, V.L. Kantsyrev, N.D. Quart, A.A. Esaulov, C. Deeney, K.M. Williamson, G.C. Osborne, I. Shrestha, D.J. Ampleford, and B. Jones, *Observation of >400-eV Precursor Plasmas from Low-Wire-Number Copper Arrays at the I-MA Zebra Facility*, Physical Review Letters **102**, 155061 (2009)

R.D. Cowan, *The Theory of Atomic Structure and Spectra*, University of California Press, Berkeley (1981)

M.E. Cuneo, R.A. Vesey, D.B. Sinars, J.P. Chittenden, E.M. Waisman, R.W. Lemke, S.V. Lebedev, D.E. Bliss, W.A. Stygar, J.L. Porter, D.G. Schroen, M.G. Mazarakis, G.A. Chandler, and T.A. Mehlhorn, *Demonstration of Radiation Pulse Shaping with Nested-Tungsten-Wire-Array Z Pinches for High-Yield Inertial Confinement Fusion*, Physical Review Letters **95**, 185001 (2005)

M.E. Cuneo, D.B. Sinars, E.M. Waisman, D.E. Bliss, W.A. Stygar, R.A. Vesey, R.W. Lemke, I.C. Smith, P.K. Rambo, J.L. Porter, G.A. Chandler, T.J. Nash, M.G. Mazarakis,

R.G. Adams, E.P. Yu, K.W. Struve, T.A. Mehlhorn, S.V. Lebedev, J. P. Chittenden, and C.A. Jennings, *Compact single and nested tungsten-wire-array dynamics at 14–19 MA and applications to inertial confinement fusion*, Physics of Plasmas **13**, 056318 (2006)

J. Davis, R. Clark, J.P. Apruzese, and P.C. Kepple, *A Z-Pinch Neonlike X-Ray Laser*, IEEE Transactions on Plasma Science **16**, 482-490 (1988)

J. Davis, N.A. Gondarenko, and A.L. Velikovich, *Fast commutation of high current in double wire array Z-pinch loads*, Applied Physics Letters **70**, 170-172 (1997)

C. Deeney, M.R. Douglas, R.B. Spielman, T.J. Nash, D.L. Peterson, P. L'Eplattenier, G.A. Chandler, J.F. Seamen, and K.W. Struve, *Enhancement of X-Ray Power from a Z Pinch Using Nested-Wire Arrays*, Physical Review Letters **81**, 4883-4886 (1998)

C. Deeney, J.P. Apruzese, C.A. Coverdale, K.G. Whitney, J.W. Thornhill, and J. Davis, *Spectroscopic Diagnosis of Nested-Wire-Array Dynamics and Interpenetration at 7 MA*, Physical Review Letters **93**, 155001 (2004)

J.D. Douglass, S.A. Pikuz, T.A. Shelkovenko, D.A. Hammer, S.N. Bland, S.C. Bott, and R.D. McBride, *Structure of the dense cores and ablation plasmas in the initiation phase of tungsten wire-array Z pinches*, Physics of Plasmas **14**, 012704 (2007)

A.A. Esaulov, A.L. Velikovich, V.L. Kantsyrev, T.A. Mehlhorn, and M.E. Cuneo, *Wire dynamics model of the implosion of nested and planar wire arrays*, Physics of Plasmas **13**, 120701 (2006)

A.A. Esaulov, V.L. Kantsyrev, A.S. Safronova, K.M. Williamson, I. Shrestha, G.C. Osborne, M.F. Yilmaz, N.D. Quart, and M.E. Weller, *WADM and radiation MHD simulations of compact multi-planar and cylindrical wire arrays at 1 MA currents*, High Energy Density Physics **5**, 166-172 (2009)

D.J. Fields, R.S. Walling, G.M. Shimkaveg, B.J. MacGowan, L.B. Da Silva, J.H. Scofield, A.L. Osterheld, T.W. Phillips, M.D. Rosen, D.L. Matthews, W.H. Goldstein, and R.E. Stewart, *Observation of high gain in Ne-like Ag lasers*, Physical Review A **46**, 1606-1609 (1992)

A.H. Gabriel, *Dielectronic Satellite Spectra for Highly-charged Helium-like Ion lines*, Monthly Notices of the Royal Astronomical Society **160**, 99 (1972)

S. Glidden and H. Sanders, *COBRA High Current Generator Baseline Design*, Applied Pulsed Power, Inc. (2003)

A.T. Graf, S. Brockington, R. Horton, S. Howard, D. Hwang, P. Beiersdorfer, J. Clementson, D. Hill, M. May, H. McLean, R. Wood, M. Bitter, J. Rice, J. Terry, and W. L. Rowan, *Spectroscopy on magnetically confined plasmas using electron beam ion trap spectrometers*, Canadian Journal of Physics **86**, 307-313 (2008)

J.B. Greenly, J.D. Douglas, D.A. Hammer, B.R. Kusse, S.C. Glidden, and H.D.A. Sanders, *1 MA, variable risetime pulse generator for high energy density plasma research*, Review of Scientific Instruments **79**, 073501 (2008)

M.F. Gu, *The flexible atomic code*, Canadian Journal of Physics **86**, 675-689 (2008)

M.G. Haines, P.D. LePell, C.A. Coverdale, B. Jones, C. Deeney, and J.P. Apruzese, *Ion Viscous Heating in a Magnetohydrodynamically Unstable Z Pinch at over 2×10^9 Kelvin*, Physical Review Letters **96**, 075003 (2006)

S.B. Hansen, *Development and Application of L-shell Spectroscopic Modeling for Plasma Diagnostics*, Ph.D. Dissertation, University of Nevada, (2003)

S.B. Hansen, A.S. Safronova, J.P. Apruzese, P.D. LePell, C. Coverdale, C. Deeney, K.B.

Fournier, and U.I. Safronova, *Analysis of radially resolved spectra and potential for lasing in Mo wire array Z pinches*, Physics of Plasmas **12**, 094502 (2005)

B. Hudson, R.D. Wood, H.S. McLean, E.B. Hooper, D.N. Hill, J. Jayakumar, J. Moller, D. Montez, C.A. Romero-Talamás, T.A. Casper, J.A. Johnson III, L.L. LoDestro, E. Mezonlin, and L.D. Pearlstein, *Energy confinement and magnetic field generation in the SSPX spheromak*, Physics of Plasmas **15**, 056112 (2008)

B. Jones, C.A. Coverdale, C. Deeney, D.B. Sinars, E.M. Waisman, M.E. Cuneo, D.J. Ampleford, P.D. LePell, K.R. Cochran, J.W. Thornhill, J.P. Apruzese, A. Dasgupta, K. G. Whitney, R.W. Clark, and J.P. Chittenden, *Implosion dynamics and K-shell x-ray generation in large diameter stainless steel wire array Z pinches with various nesting configurations*, Physics of Plasmas **15**, 122703 (2008)

B. Jones, D.J. Ampleford, R.A. Vesey, M.E. Cuneo, C.A. Coverdale, E.M. Waisman, M.C. Jones, W.E. Fowler, W.A. Stygar, J.D. Serrano, M.P. Vigil, A.A. Esaulov, V.L. Kantsyrev, A.S. Safronova, K.M. Williamson, A.S. Chuvatin, and L.I. Rudakov, *Planar Wire-Array Z-Pinch Implosion Dynamics and X-Ray Scaling at Multiple-MA Drive Currents for a Compact Multisource Hohlraum Configuration*, Physical Review Letters **104**, 125001 (2010)

B. Jones, C.A. Jennings, J.E. Bailey, G.A. Rochau, Y. Maron, C.A. Coverdale, E.P. Yu, S.B. Hansen, D.J. Ampleford, P.W. Lake, G. Dunham, M.E. Cuneo, C. Deeney, D.V. Fisher, V.I. Fisher, V. Bernshtam, A. Starobinets, and L. Weingarten, *Doppler measurement of implosion velocity in fast Z-pinch x-ray sources*, Physical Review E **84**, 056408 (2011)

V.L. Kantsyrev, L.I. Rudakov, A.S. Safronova, D.A. Fedin, V.V. Ivanov, A.L. Velikovich, A.A. Esaulov, A.S. Chuvatin, K.M. Williamson, N.D. Quart, V. Nalajala, G.C. Osborne, I. Shrestha, M.F. Yilmaz, S. Pokala, P.J. Laca, and T.E. Cowan, *Planar*

Wire Array as Powerful Radiation Source, IEEE Transactions on Plasma Science **34**, 2295-2302 (2006)

V.L. Kantsyrev, A.S. Safronova, K.M. Williamson, P.G. Wilcox, N.D. Ouart, M.F. Yilmaz, K.W. Struve, D.L. Voronov, R.M. Feshchenko, I.A. Artyukov, and A.V. Vinogradov, *Extreme ultraviolet spectroscopy diagnostics of low-temperature plasmas based on a sliced multilayer grating and glass capillary optics*, Review of Scientific Instruments **79**, 10F542 (2008a)

V.L. Kantsyrev, L.I. Rudakov, A.S. Safronova, A.A. Esaulov, A.S. Chuvatin, C.A. Coverdale, C. Deeney, K.M. Williamson, M.F. Yilmaz, I. Shrestha, N.D. Ouart, and G.C. Osborne, *Double planar wire array as a compact plasma radiation source*, Physics of Plasmas **15**, 030704 (2008b)

V.L. Kantsyrev, A.S. Safronova, A.A. Esaulov, K.M. Williamson, I. Shrestha, F. Yilmaz, G.C. Osborne, M.E. Weller, N.D. Ouart, V.V. Shlyaptseva, L.I. Rudakov, A.S. Chuvatin, and A.L. Velikovich, *A review of new wire arrays with open and closed magnetic configurations at the 1.6 MA Zebra generator for radiative properties and opacity effects*, High Energy Density Physics **5**, 115-123 (2009)

V.L. Kantsyrev, A.S. Chuvatin, A.A. Esaulov, A.S. Safronova, L.I. Rudakov, A. Velikovich, K.M. Williamson, G.C. Osborne, I.K. Shrestha, M.E. Weller, and V.V. Shlyaptseva, *Anisotropy of radiation emitted from planar wire arrays*, Physics of Plasmas **20**, 070702 (2013)

J.P. Knauer, F.J. Marhall, B. Yaakobi, D. Anderson, B.A. Schmitt, K.M. Chandler, S.A. Pikuz, T.A. Shelkovenko, M.D. Mitchell, and D.A. Hammer, *Response model for Kodak Biomax-MS film to x rays*, Review of Scientific Instruments **77**, 10F331 (2006)

S.V. Lebedev, F.N. Beg, S.N. Bland, J.P. Chittenden, A.E. Dangor, M.G. Haines, K.H.

Kwek, S.A. Pikuz, and T.A. Shelkovenko, *Effects of discrete wires on the implosion dynamics of wire array Z pinches*, *Physics of Plasmas* **8**, 3734-3747 (2001)

S.V. Lebedev, F.N. Beg, S.N. Bland, J.P. Chittenden, A.E. Dangor, and M.G. Haines, *Snowplow-like behavior in the implosion phase of wire array Z pinches*, *Physics of Plasmas* **9**, 2293-2301 (2002)

M.A. Liberman, J.S. De Groot, A. Toor, R.B. Spielman, *Physics of High-Density Z-Pinch Plasmas*, Springer-Verlag (1999)

J.J. MacFarlane, I.E. Golovkin, and P.R. Woodruff, *HELIOS-CR – A 1-D radiation-magnetohydrodynamics code with inline atomic kinetics modeling*, *Journal of Quantitative Spectroscopy and Radiative Transfer* **99**, 381-397 (2006)

J.J. MacFarlane, I.E. Golovkin, P. Wang, P.R. Woodruff, and N.A. Pereyra, *SPECT3D – A Multi-Dimensional Collisional-Radiative Code for Generating Diagnostic Signatures Based on Hydrodynamics and PIC Simulation Output*, *High Energy Density Physics* **3**, 181-190 (2007)

B.J. MacGowan, M.D. Rosen, M.J. Echart, P.L. Hagelstein, D.L. Matthews, D.G. Nilson, T.W. Phillips, J.H. Scofield, G. Shimkaveg, J.E. Trebes, R.S. Walling, B.L. Whitten, and J.G. Woodworth, *Observation of soft x-ray amplification in neonlike molybdenum*, *Journal of Applied Physics* **61**, 5243-5248 (1987)

R.C. Mancini and C.F. Hooper, Jr., *Field-dependent dipole matrix elements and their application to the calculation of plasma-broadened line profiles*, *Review of Scientific Instruments* **59**, 1512 (1988)

J. Nilsen, J.A. Koch, J.H. Scofield, B.J. MacGowan, J.C. Moreno, and L.B. Da Silva, *Observation of Hyperfine Splitting on an X-Ray Laser Transition*, *Physical Review*

Letters **70**, 3713-3715 (1993)

N.D. Quart, M.F. Yilmaz, A.S. Safronova, V.L. Kantsyrev, A.A. Esaulov, K.M. Williamson, G.C. Osborne, I. Shrestha, M.E. Weller, R.D. McBride, P.F. Knapp, K.S. Bell, S.A. Pikuz, T.A. Shelkovenko, J.B. Greenly, D.A. Hammer, and B.R. Kusse, *Analysis of Compact Cylindrical Wire Array Implosions with Brass and also by Alternating Brass and Al wires on the 1-MA COBRA Generator*, AIP Conference Proceedings **1088**, 65-68 (2009)

N.D. Quart, *Radiative properties of Z-pinch and laser produced plasmas from mid-atomic-number materials*, Ph.D. Dissertation, University of Nevada, (2010a)

N.D. Quart, A.S. Safronova, V.L. Kantsyrev, A.A. Esaulov, K.M. Williamson, I. Shrestha, G.C. Osborne, and M.E. Weller, *Studies of Radiative and Implosion Characteristics From Brass Planar Wire Arrays*, IEEE Transactions on Plasma Science **38**, 631-638 (2010b)

N.D. Quart, A.S. Safronova, A.Ya. Faenov, T.A. Pikuz, S.V. Gasilov, F. Calegari, M. Nisoli, S.De. Silvesteri, S. Stagira, L. Poletto, and P. Villoresi, *Analysis of the simultaneous measurements of iron K- and L-shell radiation from ultrashort laser produced plasmas*, Journal of Physics B: Atomic, Molecular and Optical Physics **44**, 065602 (2011)

O. Peyrusse, P. Combis, M. Lousi-Jacquet, D. Naccache, C.J. Keane, B.J. MacGowan, and D.L. Matthews, *Spectroscopic diagnostics of an x-ray laser plasma by use of L-shell spectra*, Journal of Applied Physics **65**, 3802 (1989)

J.J. Rocca, F.G. Tomasel, M.C. Marconi, V.N. Shlyaptsev, J.L.A. Chilla, B.T. Szapiro, and G. Giudice, *Discharge-pumped soft-x-ray laser in neon-like argon*, Physics of Plasmas **2**, 2547-2554 (1995)

A.N. Ryabtsev, E.Ya. Kononov, and S.S. Churilov, *Spectrum of Calcium-Like Copper Cu X*, *Optics and Spectroscopy* **106**, 163-169 (2009)

A.S. Safronova, V.L. Kantsyrev, A.A. Esaulov, D. Fedin, N.D. Ouart, F. Yilmaz, G. Osborne, V. Nalajala, S. Pokala, I. Shrestha, A. Astanovisky, S. Batie, B. LeGalloudec, T. Cowan, B. Jones, C. Coverdale, C. Deeney, D. LePell, and J. Gradel, *Implosion dynamics and Spectroscopy of X-pinches and Wire arrays with doped Al wires on the UNR IMA Z-pinch generator*, *AIP Conference Proceedings* **808**, 149-152 (2006a)

A.S. Safronova, V.L. Kantsyrev, N.D. Ouart, F. Yilmaz, D. Fedin, A. Astanovitsky, B. LeGalloudec, S. Batie, D. Brown, V. Nalajala, S. Pokala, I. Shrestha, T.E. Cowan, B. Jones, C.A. Coverdale, C. Deeney, S.B. Hansen, P.D. LePell, D. Jobe, and D. Nielson, *Spectroscopic modeling of radiation from Cu and Mo X-pinches produced on the UNR I MA Zebra generator*, *Journal of Quantitative Spectroscopy & Radiative Transfer* **99**, 560-571 (2006b)

A.S. Safronova, V.L. Kantsyrev, M.F. Yilmaz, G. Osborne, N.D. Ouart, K. Williamson, I. Shrestha, V. Shlyaptseva, S. Batie, B. LeGalloudec, A. Astanovitsky, V. Nalajala, and W. McDaniel, *Radiative properties of implosions of combined X-pinches and planar wire arrays composed from different wire materials on the UNR I MA Z-pinch generator*, *High Energy Density Physics* **3**, 237-241 (2007)

A.S. Safronova, V.L. Kantsyrev, A.A. Esaulov, N.D. Ouart, M.F. Yilmaz, K.M. Williamson, V. Shlyaptseva, I. Shrestha, G.C. Osborne, C.A. Coverdale, B. Jones, and C. Deeney, *X-ray diagnostics of imploding plasmas from planar wire arrays composed of Cu and few tracer Al wires on the IMA pulsed power generator at UNR*, *Review of Scientific Instruments* **79**, 10E315 (2008a)

A.S. Safronova, V.L. Kantsyrev, A.A. Esaulov, N.D. Ouart, M.F. Yilmaz, K.M. Williamson, I. Shrestha, G.C. Osborne, J.B. Greenly, K.M. Chandler, R.D. McBride,

D.A. Chalenski, D.A. Hammer, B.R. Kusse, and P.D. LePell, *Spectroscopy and implosion dynamics of low wire number nested arrays on the 1 MA COBRA generator*, Physics of Plasmas **15**, 033302 (2008b)

A.S. Safronova, A.A. Esaulov, V.L. Kantsyrev, N.D. Ouart, V. Shlyaptseva, M.E. Weller, S.F. Keim, K.M. Williamson, I. Shrestha, and G.C. Osborne, *Searching for efficient X-ray radiators for wire array Z-pinch plasmas using mid-atomic-number single planar wire arrays on Zebra at UNR*, High Energy Density Physics **7**, 252-258 (2011)

A.S. Safronova, V.L. Kantsyrev, A.A. Esaulov, A.S. Chuvatin, M.E. Weller, V.V. Shlyaptseva, I. Shrestha, S.F. Keim, A. Stafford, C.A. Coverdale, J.P. Apruzese, N.D. Ouart, and J.L. Giuliani, *Radiation from mixed multi-planar wire arrays*, Physics of Plasmas **21**, 031205 (2014)

T.W.L. Sanford, M.E. Cuneo, D.E. Bliss, C.A. Jennings, R.C. Mock, T.J. Nash, W.A. Stygar, E.M. Waisman, J.P. Chittenden, M.G. Haines, and D.L. Peterson, *Demonstrated transparent mode in nested wire arrays used for dynamic hohlraum Z pinches*, Physics of Plasmas **14**, 052703 (2007)

J.H. Scofield and J. Nilsen, *Hyperfine splittings of neonlike lasing lines*, Physical Review A **49**, 2381-2388 (1994)

A.P. Shevelko, L.A. Shmaenok, S.S. Churilov, R.K.F.J. Bastiaensen, and F. Bijkerk, *Extreme Ultraviolet Spectroscopy of a Laser Plasma Source for Lithography*, Physica Scripta **57**, 276-282 (1998)

T. Shirai, T. Nakagaki, Y. Nakai, J. Sugar, K. Ishii, and K. Mori, *Spectral Data and Grotrian Diagrams for Highly Ionized Copper, Cu X-Cu XXIX*, Journal of Physical and Chemical Reference Data **20**, 1-81 (1991)

I. Shrestha, V.L. Kantsyrev, A.S. Safronova, A.A. Esaulov, K.M. Williamson, N.D. Quart, G.C. Osborne, M.E. Weller, and M.F. Yilmaz, *Study of Electron Beams in Wire Arrays at 1-MA Z-Pinch Generators*, IEEE Transactions on Plasma Science **38**, 658 (2010)

R.B. Spielman, C. Deeney, G.A. Chandler, M.R. Douglas, D.L. Fehl, M.K. Matzen, D.H. McDaniel, T.J. Nash, J.L. Porter, T.W. L. Sanford, J.F. Seamen, W.A. Stygar, K.W. Struve, S.P. Breeze, J.S. McGurn, J.A. Torres, D.M. Zagar, T.L. Gilliland, D.O. Jobe, J.L. McKenney, R.C. Mock, M. Vargas, T. Wagoner, and D.L. Peterson, *Tungsten wire-array Z-pinch experiments at 200 TW and 2 MJ*, Physics of Plasma **5**, 2105 (1998)

L. Spitzer Jr., *Physics of Fully Ionized Gases*, John Wiley and Sons (1962)

B.C. Stratton, M. Bitter, K.W. Hill, D.L. Hillis, and J.T. Hogan, *Passive Spectroscopic Diagnostics for Magnetically Confined Fusion Plasmas*, Fusion Science and Technology **53**, 431-486 (2008)

R.E. Terry, J. Davis, C. Deeney, and A.L. Velikovich, *Current Switching and Mass Interpenetration Offer Enhanced Power from Nested-Array Z Pinches*, Physical Review Letters **83**, 4305-4308 (1999)

A.L. Velikovich, F.L. Cochran, J. Davis, and Y.K. Chong, *Stabilized radiative Z-pinch loads with tailored density profiles*, Physics of Plasmas **5**, 3377-3388 (1998)

R.A. Vesey, M.C. Hermann, R.W. Lemke, M.P. Desjarlais, M.E. Cuneo, W.A. Stygar, G.R. Bennett, R.B. Campbell, P.J. Christenson, T.A. Mehlhorn, J.L. Porter, S.A. Slutz, *Target design for high fusion yield with the double Z-pinch-driven hohlraum*, Physics of Plasmas **14**, 056302 (2007)

M.E. Weller, A.S. Safronova, V.L. Kantsyrev, A.A. Esaulov, C.A. Coverdale, A.S.

Chuvatin, N.D. Ouart, K.M. Williamson, I. Shrestha, G.C. Osborne, V.V. Shlyaptseva, S.F. Keim, and A. Stafford, *Radiative properties of mixed nested cylindrical wire arrays on Zebra at UNR*, High Energy Density Physics **8**, 184 (2012a)

M.E. Weller, A.S. Safronova, J. Clementson, V.L. Kantsyrev, U.I. Safronova, P. Beiersdorfer, E.E. Petkov, P.G. Wilcox, and G.C. Osborne, *Extreme ultraviolet spectroscopy and modeling of Cu on the SSPX Spheromak and laser plasma "Sparky"*, Review of Scientific Instruments **83**, 10E101 (2012b)

M.E. Weller, A.S. Safronova, V.L. Kantsyrev, A.A. Esaulov, I. Shrestha, J.P. Apruzese, J.L. Giuliani, A.S. Chuvatin, A. Stafford, S.F. Keim, V.V. Shlyaptseva, G.C. Osborne, and E.E. Petkov, *Radiation from Ag high energy density Z-pinch plasmas and applications to lasing*, Physics of Plasmas **21**, 031206 (2014)

J. Wesson, *Tokamaks*, Oxford University Press (1997)

K.G. Whitney, J.W. Thornhill, J.P. Apruzese, J. Davis, C. Deeney, and C.A. Coverdale, *Enhanced energy coupling and x-ray emission in Z-pinch plasma implosions*, Physics of Plasmas **11**, 3700-3714 (2004)

P.G. Wilcox, A.S. Safronova, V.L. Kantsyrev, U.I. Safronova, K.M. Williamson, M.F. Yilmaz, J. Clementson, P. Beiersdorfer, and K.W. Struve, *Extreme ultraviolet spectroscopy of low-Z ion plasmas for fusion applications*, Review of Scientific Instruments **79**, 10F543 (2008)

K.M. Williamson, V.L. Kantsyrev, A.A. Esaulov, A.S. Safronova, N.D. Ouart, F.M. Yilmaz, I.K. Shrestha, V. Shlyaptseva, R.D. McBride, D.A. Chalenski, J.D. Douglass, J.B. Greenly, D.A. Hammer, and B.R. Kusse, *Ablation dominated implosion dynamics of aluminum and stainless steel nested cylindrical wire arrays*, Physics of Plasmas **16**, 012704 (2009)

K.M. Williamson, V.L. Kantsyrev, A.A. Esaulov, A.S. Safronova, P. Cox, I. Shrestha, G.C. Osborne, M.E. Weller, N.D. Ouart, and V.V. Shlyaptseva, *Implosion dynamics in double planar wire array Z pinches*, *Physics of Plasmas* **17**, 112705 (2010)

R.D. Wood, D.N. Hill, E.B. Hooper, H.S. McLean, D. Ryutov, and S. Woodruff, *Comparison of deuterium and hydrogen experiments in the Sustained Spheromak Physics Experiment*, *Journal of Nuclear Materials* **337-339**, 548-552 (2005a)

R.D. Wood, D.N. Hill, E.B. Hooper, S. Woodruff, H.S. McLean, and B.W. Stallard, *Improved operation of the SSPX spheromak*, *Nuclear Fusion* **45**, 1582-1588 (2005b)

M.F. Yilmaz, A.S. Safronova, V.L. Kantsyrev, A.A. Esaulov, K.M. Williamson, G.C. Osborne, I. Shrestha, and N.D. Ouart, *Spectroscopic features of implosions of Mo single- and double-planar wire arrays produced on the 1 MA Z-pinch generator*, *Journal of Quantitative Spectroscopy and Radiative Transfer* **109**, 2877- 2890 (2008)

M.F. Yilmaz, *Radiative properties of L-shell Mo and K-shell Al plasmas from planar and cylindrical wire arrays imploded at 1 MA Z-pinch generator*, Ph.D. Dissertation, University of Nevada, (2009)

B.K.F. Young, A.L. Osterheld, R.S. Walling, W.H. Golstein, T.W. Phillips, R.E. Stewart, G. Charatis, and Gar. E. Busch, *Measurement of density-sensitive electric quadrupole transition in neonlike laser-produced plasmas*, *Physical Review Letters* **62**, 1266 (1989)